Gas Diffusion Electrodes for Reduction of CO_2 to Formic Acid/Formate by Intermittent Energy and its Subsequent Chemical or Biological Upgrading

Dissertation

to attain the academic degree

"Doctor rerum naturalium" (Dr. rer. nat.)

in Chemistry

Faculty of Chemistry, Pharmaceutical Sciences,

Geography and Geosciences

Johannes Gutenberg University Mainz

by

Ida Dinges

born in Frankfurt am Main, Germany

Mainz, 2025

Dean:	Prof. Dr. Eva Rentschler
First Reviewer / Supervisor:	Prof. Dr. Siegfried R. Waldvogel
Second Reviewer:	PD Dr. Jonathan Bloh
Date of Defense:	08.01.2026

D77 (Johannes Gutenberg University Mainz)

Eigenständigkeitserklärung

Die experimentellen Arbeiten wurden im Zeitraum vom 07.12.2021-01.04.2025 am DECHEMA Forschungsinstitut (DFI, Frankfurt am Main / Deutschland) im Forschungsteam „Nachhaltige Elektrochemie“ von Dr. Markus Stöckl (DFI) durchgeführt. Die Arbeiten wurden von Prof. Dr. Siegfried R. Waldvogel (Max-Planck-Institut für Chemische Energiekonversion, ehemals Johannes Gutenberg-Universität Mainz) betreut.

Hiermit erkläre ich, Ida Dinges,
dass ich die vorliegende Arbeit mit dem Titel:

„Gas Diffusion Electrodes for Reduction of CO_2 to Formic Acid/Formate by Intermittent Energy and its Subsequent Chemical or Biological Upgrading“

selbstständig verfasst und keine anderen als die angegebenen Quellen und Hilfsmittel (dazu zählen auch KI-basierte Anwendungen oder Werkzeuge*) benutzt habe. Sämtliche wörtlichen oder sinngemäßen Übernahmen und Zitate sind kenntlich gemacht und nachgewiesen (dies gilt auch für Texte, die durch generative KI, wie Chat GPT erzeugt wurden). Ich versichere, dass ich keine Hilfsmittel verwendet habe, deren Nutzung die Prüferin oder der Prüfer explizit ausgeschlossen hat.

* Folgende KI-Tools wurden genutzt: DeepL Translate wurde über die gesamte Arbeit hinweg teilweise für sprachliche Überarbeitungen (Übersetzungen, sprachliche und grammatikalische Korrekturen) von selbst erzeugten Textentwürfen verwendet.

Mit Abgabe der vorliegenden Leistung übernehme ich die Verantwortung für das eingereichte Gesamtprodukt. Ich verantworte damit auch jegliche KI-generierten Inhalte, die ich in meine Arbeit übernommen habe. Die Richtigkeit übernommener (KI-generierter) Aussagen und Inhalte habe ich nach bestem Wissen und Gewissen geprüft.

Mir ist bekannt, dass ein Verstoß gegen die genannten Punkte prüfungsrechtliche Konsequenzen hat und insbesondere dazu führen kann, dass die Promotionsleistung als mit „nicht bestanden“ bewertet wird. Die Einschreibung kann für bis zu zwei Jahre widerrufen werden, wenn Studierende zweimal oder häufiger bei Prüfungsleistungen täuschen (§ 69 Abs. 4 und 5 HochSchG).

Mainz, 16.10.2025

Kurzzusammenfassung

Die zeitgenössische chemische Industrie muss aufgrund des anthropogenen Klimawandels und der begrenzten fossilen Ressourcen auf erneuerbare Energiequellen und nachhaltige Rohstoffe umsteigen. Vor diesem Hintergrund stellt die elektrochemische Reduktion von CO_2 eine vielversprechende Möglichkeit dar, mit der Kohlenstoff aus fossilen Quellen nachhaltig durch CO_2 ersetzt werden kann.

Im Rahmen dieser Dissertation wurde ein Prozesskonzept untersucht, bei dem intermittierende Energie aus erneuerbaren Quellen (z.B. Sonne und Wind) für die elektrochemische Reduktion von CO_2 zur leicht lagerbaren Ameisensäure genutzt wird, die dann ohne Aufbereitung zu weiteren Kohlenstoffprodukten umgesetzt wird. Dafür wurden Gasdiffusionselektroden mit kostengünstigen, relativ reichlich vorhandenen und ungiftigen Katalysatoren sowie einem skalierbaren Herstellungsverfahren entwickelt, die eine dezentrale Anwendung an Punktquellen erleichtern könnten. Die optimierten Gasdiffusionselektroden wurden erfolgreich für den flexiblen Betrieb bei variabler Stromdichte auf Basis intermittierender Elektrizität etabliert und zeigten dabei eine robuste und zuverlässig hohe Leistung.

Die Ameisensäure wurde in wässrigem Elektrolyt synthetisiert und erfolgreich ohne Verarbeitung (z.B. aufreinigen, aufkonzentrieren) als Edukt für weitere Umwandlung verwendet, um zusätzliche Kosten zu vermeiden. Einerseits wurde sie mittels Biosynthese in zweiter Generation zu dem Biopolymer Polyhydroxybutyrat, einem biologisch abbaubaren Thermoplast, umgesetzt. Andererseits wurde sie bei der Elektrosynthese von Wasserstoffperoxid verwendet, wobei das starke Oxidations- und Desinfektionsmittel Perameisensäure erhalten wurde. Die Ausbeute und Energiekosten der jeweiligen Gesamtprozesse wurden kritisch bewertet, womit ihre Eignung sowie Strategien zur Weiterentwicklung für eine potenzielle technische Nutzung ermittelt wurden.

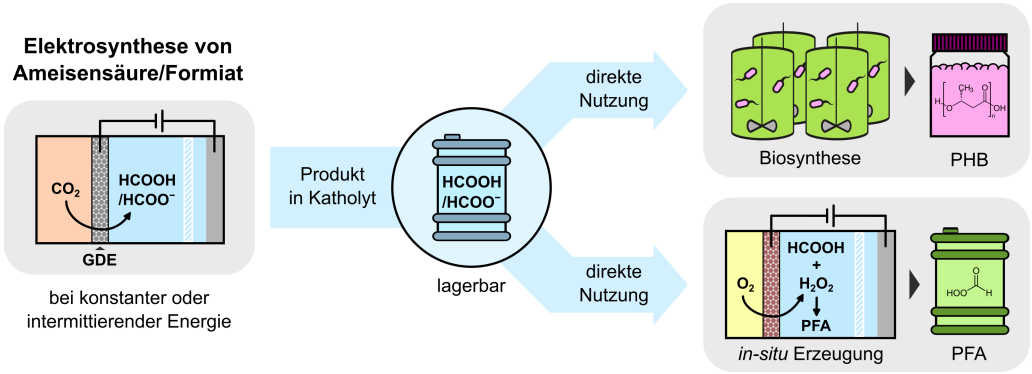

Abbildung 1 – Schematische Darstellung des im Rahmen dieser Arbeit untersuchten Prozesskonzeptes. Abkürzungen: GDE = Gasdiffusionselektrode, PHB = Polyhydroxybutyrat, PFA = Perameisensäure.

Abstract

Driven by anthropogenic climate change and limited fossil raw materials, the contemporary chemical industry needs a transition to renewable energy sources and sustainable feedstocks. In this context, the electrochemical reduction of CO_2 offers the attractive opportunity to sustainably replace carbon from fossil feedstock with CO_2.

This dissertation focused on a process concept in which intermittent energy from renewable sources (*e.g.* solar and wind) is used for electrochemical reduction of CO_2 to easily storable formic acid, which is then upgraded without any processing to value-added carbon products. Therefore, gas diffusion electrodes were developed with affordable, relatively abundant and non-toxic catalyst materials and a scalable fabrication method, which could facilitate decentralised implementation at point sources. The optimised gas diffusion electrodes were successfully established for flexible operation at current patterns based on intermittent electricity, demonstrating robust and reliably high performance.

The formic acid was obtained in aqueous electrolyte and successfully used as feedstock for chemical and biological synthesis routes without processing (*e.g.* purification, concentrating) to avoid additional costs. On the one hand, it was upgraded by biosynthesis in second generation to the biopolymer polyhydroxybutyrate, a biodegradable thermoplastic. On the other hand, it was upgraded to the strong oxidiser and disinfectant performic acid by using the feedstock in the electrosynthesis of hydrogen peroxide. The overall processes were critically assessed in terms of yield and energy costs, thereby demonstrating their feasibility as well as strategies for their future development towards a potential technical exploitation.

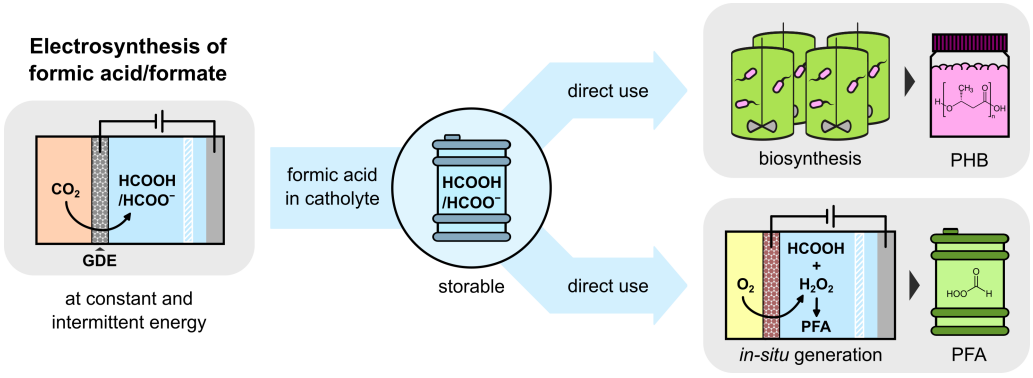

Figure 1 – Schematic illustration of the process concept this dissertation focused on. Abbreviations: GDE = gas diffusion electrode, PHB = polyhydroxybutyrate, PFA = performic acid.

Contents

Acronyms

BTX	benzene, toluene and mixed xylenes
CCS	carbon capture and storage
CCU	carbon capture and utilisation
CCUS	carbon capture, utilisation and storage
cf.	compare (Latin: confer)
C. necator	*Cupriavidus necator*
DAC	direct air capture
eCO$_2$RR	electrochemical CO_2 reduction reaction
eCORR	electrochemical CO reduction reaction
EE	energy efficiency
EEC	electric energy consumption
e.g.	for example (Latin: exempli gratia)
eO$_2$RR	electrochemical O_2 reduction reaction
et al.	and others (Latin: et alia)
FE	Faradaic efficiency
G	Gibbs free energy
GDE	gas diffusion electrode
GDL	gas diffusion layer
GHG	greenhouse gas
HER	hydrogen evolution reaction
ICP-OES	inductively coupled plasma optical emission spectroscopy
i.e.	that is / meaning (Latin: id est)
KPI	key performance indicator
MEA	membrane electrode assembly
OD	optical density
ODC	oxygen depolarised cathode
OER	oxygen evolution reaction
PCET	proton-concerted electron transfer
PFA	performic acid
PHB	polyhydroxybutyrate
PTFE	polytetrafluoroethylene
SEM	scanning electron microscopy
SPC	single-pass conversion
SPCE	single-pass carbon efficiency
SSE	solid-state electrolyte
TRL	technological readiness level

1 Introduction

Mitigating anthropogenic climate change is one of the most important challenges of the 21st century. It has mainly been driven by humanity's emissions of carbon dioxide (CO_2) through excessive exploitation of fossil resources since the beginning of the 20th century.[1] The increased atmospheric content of CO_2 traps heat and thus leads to global warming, which in turn disrupts weather patterns, melts glaciers and rises sea levels, posing a substantial threat to life on earth.

As countermeasure, the international community concluded the Paris Agreement in 2015.[2] It regulates CO_2 emissions to limit global warming to well below 2 °C compared to the pre-industrial level, preferably to 1.5 °C. Accordingly, the European Union initiated the European Green Deal, which aims to establish net-zero greenhouse gas (GHG) emissions until 2050.[3] Most abatable CO_2 emissions are generated by the sectors energy (*i.e.* electricity and heat), transportation, buildings, and industry through the combustion of fossil fuels for energy supply. To address this, the *power-to-X* strategy aims to replace fossil energy with electric energy from renewable sources and transfer it to various applications (*e.g.* X = energy carrier, heat, mobility).[4,5] However, unlike fossil fuels, the most important renewable energy sources (solar and wind) are intermittent. Therefore, sufficient energy storage is crucial to manage supply and demand of electric energy and capacities are currently being expanded.[6] Unlike other sectors, the chemical industry uses fossil resources not only for energy but also relies on them as feedstock and carbon source for primary chemicals, which serve as key building blocks. Consequently, substituting fossil carbon in the chemical industry poses a particular challenge.

1.1 Defossilisation of the Chemical Industry

The contemporary chemical industry is energy- and CO_2-intensive, it accounts for about 5% of global GHG emissions (direct and energy related emissions).[7] To address this, the *power-to-X* strategy can be implemented, in particular *power-to-heat* and *power-to-chemicals* technologies. Thereby, '*power-to-heat*' refers to the replacement of conventional process heat (based on the combustion of fossils) with heat through electricity generated by renewables.[8–10] In contrast, '*power-to-chemicals*' refers to the direct use of electric current for the synthesis of chemicals by electrolysis.[5,11] An important advantage of this approach is that it can be flexibly adapted to intermittent energy from renewable sources.[5,8,11] Consequently, *power-to-chemicals* offers the opportunity to store electric energy as chemical energy (*i.e.* transportable chemicals) and thus balance grids.[12]

Several *power-to-chemicals* processes have already been established on industrial scale.[13] One of the largest is the chlor-alkali process, which produced about 8 million tons of chlorine in Europe in 2024.[13,14] Besides, water electrolysis is becoming increasingly important to produce hydrogen as a renewable energy carrier to replace fossil fuels. Moreover, green hydrogen (produced using electricity from renewables) can be used to indirectly electrify and thus decarbonise the Haber-Bosch process for the synthesis of ammonia, one of the world's most important chemicals as precursor of nitrogen compounds.[15,16] Another important part of the *power-to-chemicals* concept and key research focus in recent years is organic electrosynthesis, in which electric current is used directly as traceless redox-agent for chemical transformations to obtain commodity and fine chemicals.[17–22] Thereby, organic electrosynthesis fulfils most of the principles of green chemistry (*e.g.* waste prevention, high atom economy, harmless auxiliaries) depending on its implementation.[23–25] Moreover, there already are examples of industrially established processes for organic electrosynthesis of adiponitrile (Monsanto), L-cysteine (Wacker) and Lysmeral (BASF).[18,21,26,27]

Besides ammonia, the value chain of the chemical industry is built on carbon compounds as primary chemicals derived from fossil resources: methanol, ethylene and propylene (light olefins), and benzene, toluene and mixed xylenes (BTX aromatics).[28] Methanol is produced from synthesis gas (CO and H_2), which is mostly obtained by steam reforming of methane (also a GHG).[29,30] Light olefins and BTX aromatics are mostly obtained by steam cracking of naphtha, a distillation fraction of crude oil.[29,30] Consequently, alternative and renewable carbon sources are necessary for the complete defossilisation of the chemical industry, ideally compatible with existing value chains to decrease implementation barriers. Furthermore, a circular carbon economy needs to be established to meet the ultimate target of net-zero emissions.

Renewable carbon encompasses all sources of carbon that avoid or substitute any additional fossil carbon from the geosphere.[31] This includes the recycling of carbon materials (technosphere) and the utilisation of biomass (biosphere) or carbon dioxide (atmosphere).[31] Regarding recycled carbon, plastic materials would be an attractive source as one of the major products of the chemical industry.[32,33] However, their variety and persistence make recycling difficult, meaning most plastic waste currently ends up in landfill, waste incineration and the environment.[34] Biomass, in which CO_2 has been assimilated via photosynthesis, can provide access to a wide variety of products[35–37] and already accounts for about 10%[38] of feedstock in the chemical industry. For example, primary biomass (*e.g.* corn or sugarcane) is used for the synthesis of biofuels such as ethanol and butanol.[38] However, expanding the use of primary biomass has limited potential, as it competes with food production, requires significant land and water resources and has a seasonal life cycle.[39] The utilisation of secondary biomass (*i.e.* organic waste materials) has therefore greater potential to support a

sustainable carbon cycle. Among these, lignocellulose is one of the most abundant and especially the electrochemical valorisation of its component lignin to value-added aromatic products such as vanillin has progressed greatly in recent years.[40–43]

Nonetheless, by far the most attractive source of renewable carbon would be carbon dioxide itself, as this would enable a closed, sustainable anthropogenic carbon cycle. This cycle can be based on both atmospheric CO_2 and process-related CO_2 emissions, which remain even when fossil resources have been completely replaced in direct and energy use (*e.g.* cement production, glass fabrication, biomass fermentation, waste incineration).[44] Such a cycle has been illustrated, and the technologies required are explained below (*cf.* figure 1.1).

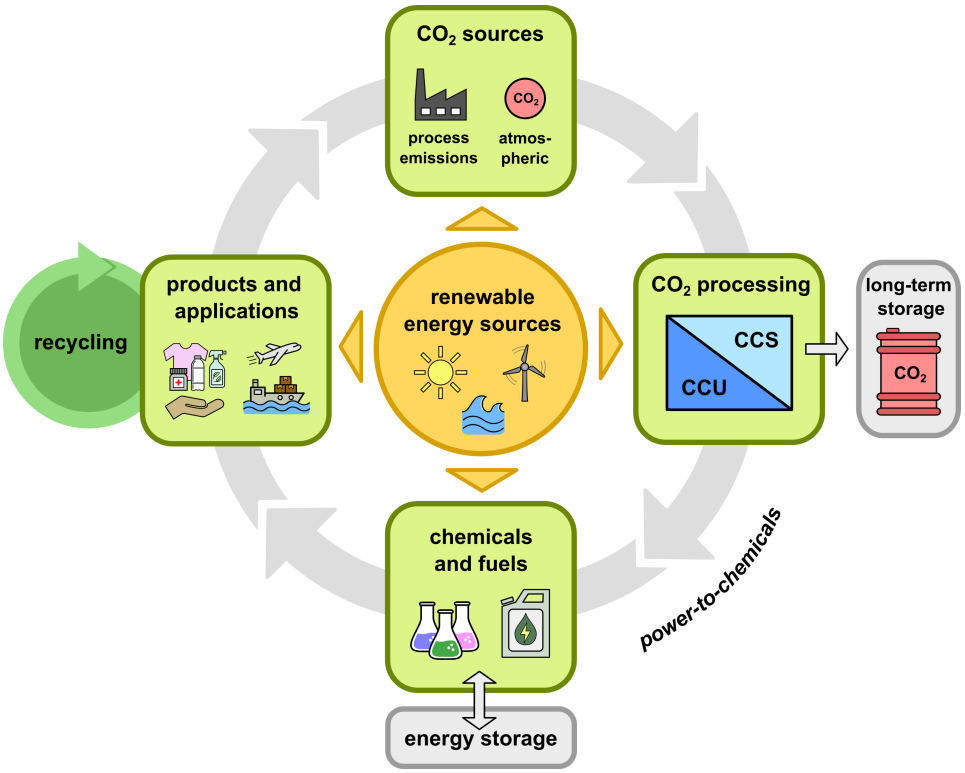

Figure 1.1 – Schematic illustration of an artificial anthropogenic carbon cycle incorporating the *power-to-X* strategy. Abbreviations: CCU = carbon capture and utilisation, CCS = carbon capture and storage.

To access unavoidable emissions, emissions until fossils are phased out and the increased content of CO_2 in the atmosphere as resource, the carbon capture, utilisation and storage (CCUS) concept is pursued.[45,46] Thereby, CO_2 is captured either at point sources or directly from air (direct air capture, DAC). To date, several technologies are in development for energy-efficient capture (*e.g.* absorption, adsorption, membrane separation), with some approaching high levels of technological readiness (TRL).[46,47] On the one hand, the captured CO_2 can then be stored in geological sites to take it out of the carbon cycle, thus preventing further accumulation in the atmosphere (carbon

capture and storage, CCS).[48,49] This is referred to as negative emissions, which are considered necessary by the European Union to achieve net-zero emissions by 2050.[45] On the other hand, the captured CO_2 can be utilised as resource for the synthesis of various chemicals or fuels (carbon capture and utilisation, CCU).[50,51] In particular, it can be converted to carbon monoxide through the thermochemical reverse water gas shift reaction using hydrogen and can thus be implemented into value chains based on synthesis gas (*cf.* equation 1.1).[52]

$$CO_2 + H_2 \rightleftharpoons CO + H_2O \tag{1.1}$$

This synthesis gas could either be used to produce methanol as platform chemical or various hydrocarbons (olefins, paraffins, oxygenates) by the Fischer-Tropsch process (*cf.* equations 1.2 and 1.3).[53]

$$CO + 2\,H_2 \rightarrow CH_3OH \tag{1.2}$$

$$(2n + 1)\,H_2 + n\,CO \rightarrow C_nH_{2n+2} + n\,H_2O \tag{1.3}$$

However, all these reactions occur at high pressures (>100 bar) and high temperatures (>250 °C), which in turn require large energy inputs.[54] To save hydrogen and avoid high energy inputs including energetic losses during multiple conversion steps, a single step process under mild conditions for transformation of CO_2 into value-added chemicals would be advantageous. This opportunity is offered by the electrochemical CO_2 reduction reaction (*eCO_2RR*) as part of the *power-to-chemicals* concept, whereby CO_2 is directly converted into chemical compounds using electric current.[55,56] In short, a variety of compounds can be obtained depending on the electrocatalyst, aqueous *eCO_2RR* works at ambient conditions and thus aligns with most principles of green chemistry, and it could be carried out decentralised at point sources to prevent emissions (*cf.* section 1.2). The opportunities and associated challenges are discussed in detail in the following section.

1.2 Electrochemical Reduction of CO_2

Since the first published report in 1870,[57] electrochemical reduction of CO_2 has evolved into a broad and diverse field of research. Especially in the last few decades, tremendous efforts have been undertaken in catalyst and system design to advance suitable products towards commercialisation.

After an introduction to the fundamentals, the key performance indicators and challenges of *eCO$_2$RR* processes towards industrial application are outlined. Finally, the prospects of the most promising reduction products are highlighted.

1.2.1 Fundamentals

CO_2 is a linear molecule with two carbon-oxygen double bonds, which results in high thermodynamic stability (the dissociation energy of a C=O bond in CO_2 is about 800 kJ mol^{-1}).[58] Therein, the carbon atom has its highest formal oxidation state of +IV. To transform CO_2 into more energetic products by the *eCO$_2$RR*, electrons need to be transferred to the carbon atom, reducing its oxidation state.

The *eCO$_2$RR* takes place in an electrochemical reactor, which can also be referred to as a cell or an electrolyser. A common and simple set-up consists of a power source, at least two electrodes (anode and cathode), a membrane as separator and a conductive water-based electrolyte that contains dissolved CO_2 (*cf.* figure 1.2).

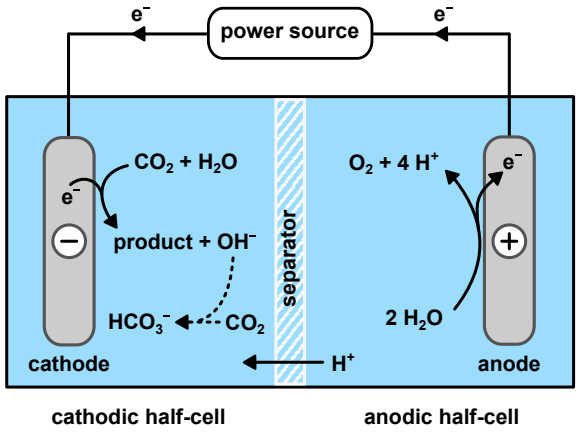

Figure 1.2 – Schematic illustration of an electrochemical cell for reduction of dissolved CO_2 in a water-based electrolyte.

The CO_2 is reduced at the catalyst surface of the cathode by electron transfer, which does not occur spontaneously ($\Delta G > 0$) and thus must be driven by a sufficient electrical potential applied with the power source. Thereby, the potential required for reduction exceeds the corresponding thermodynamic potential, partly due to the high stability of CO_2. This necessary excess is defined as overpotential, which is a kinetic effect that depends on various processes such as adsorption, charge transfer, desorption and mass transport (diffusion, migration and convection).[59] The electron transfer is accompanied by a proton transfer, whereby water or hydronium (H_3O^+) can serve as proton sources depending on the pH of the electrolyte. Consequently, the cathodic reaction of *eCO$_2$RR* has two general forms (*cf.* equations 1.4 and 1.5).

$$x\ CO_2 + (2x + y - z)\ H_2O + (4x + y - 2z)\ e^- \rightarrow C_xH_yO_z + (4x + y - 2z)\ OH^- \quad (1.4)$$

$$x\ CO_2 + (4x + y - 2z)\ H_3O^+ + (4x + y - 2z)\ e^- \rightarrow C_xH_yO_z + (6x + y - 3z)\ H_2O \quad (1.5)$$

The intrinsic need for protons/water to reduce CO_2 leads to the problem that they themselves can be reduced to hydrogen in the competing hydrogen evolution reaction (HER, *cf.* equations 1.6 and 1.7).

$$2\ H_2O + 2\ e^- \rightarrow H_2 + 2\ OH^- \quad (1.6)$$

$$2\ H^+ + 2\ e^- \rightarrow H_2 \quad (1.7)$$

Since the thermodynamic potentials of *eCO₂RR* to various products and HER are similar, it represents the most important side reaction, especially under acidic conditions.[54] To avoid HER, catalysts should have a high specific overpotential, respectively. Another important side reaction is the formation of carbonates by the chemical reaction of CO_2 with hydroxide in the electrolyte (*cf.* equations 1.8 and 1.9).

$$CO_2 + OH^- \rightarrow HCO_3^- \quad (1.8)$$

$$HCO_3^- + OH^- \rightarrow CO_3^{2-} + H_2O \quad (1.9)$$

These carbonates cannot be reduced at the cathode anymore and are considered carbon losses. Regarding the anode, *eCO₂RR* is usually paired with the oxygen evolution reaction (OER) as anodic reaction, which uses water as abundant feedstock to secure the proton supply of the cathodic reduction (*cf.* equation 1.10).

$$2\ H_2O \rightarrow O_2 + 4\ H^+ + 4\ e^- \quad (1.10)$$

However, the OER has a high positive thermodynamic potential and requires a relatively large overpotential despite appropriate catalysts (*e.g.* Pt, Ir) due to slow reaction kinetics.[60,61] This increases the energy demand of the anodic half-cell and thus the overall energy demand of both half-cells combined.

Since the reduction products of *eCO₂RR* have similar thermodynamic potentials, the product selectivity depends mostly on the catalyst material.

In general, a catalyst lowers the activation barrier (*i.e.* overpotential) so the reduction of CO_2 can occur at ambient conditions (low temperature and pressure), and it can

enhance selectivity by stabilising certain intermediates along the reduction pathway depending on its structural properties. Based on their behaviour and major final products, catalyst materials can be divided into three categories: (I) Formic acid/formate producing catalysts, (II) carbon monoxide producing catalysts and (III) hydrocarbon and oxygenate producing catalysts.[62] A simplified overview of the main reduction pathways has been illustrated based on a recent publication, which summarises the findings of numerous mechanistic studies (*cf.* figure 1.3).[63] The corresponding key steps and intermediates are discussed in the following.

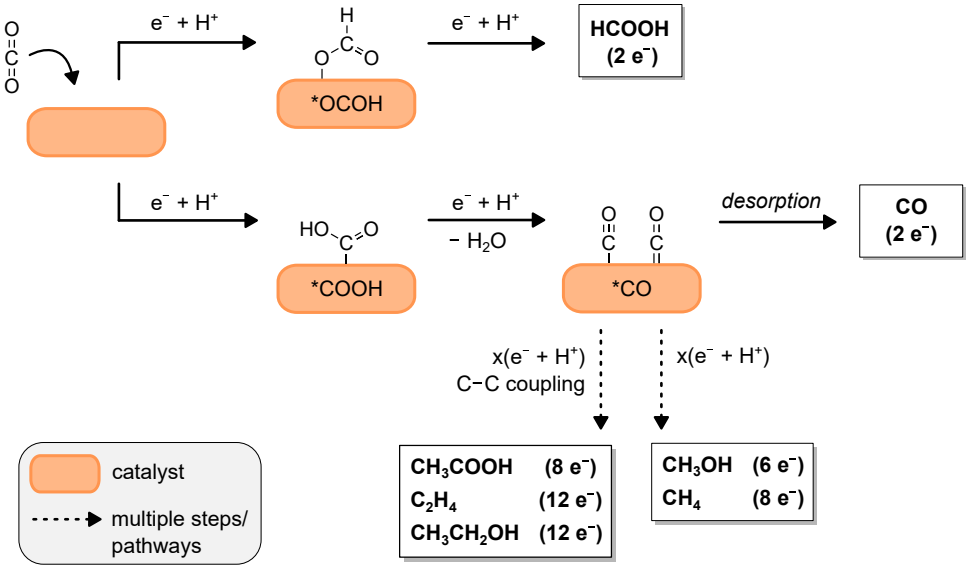

Figure 1.3 – Simplified mechanistic overview of the electrochemical reduction of CO_2 towards the most common and desired products, their key intermediates, and the number of required electrons for reduction (this figure was created based on *Seger et al.*[63]).

The initial step of the *eCO_2RR* is the adsorption of CO_2 onto the catalyst surface. This occurs by the transfer of a single electron, resulting in the surface bound radical anion of $CO_2^{\bullet-}$, which is quickly protonated. The transfer of electron and proton could also occur simultaneously, which is classified as a proton-concerted electron transfer (PCET). If the carbon atom is protonated, the intermediate *OCOH (whereby the * denotes the atom bound to the catalyst) is formed. This is the key intermediate for the category of catalysts selective for formic acid/formate, which includes metals such as Sn, In, Bi, Tl, Cd, and Hg.[62] These metals are relatively oxophilic, which most likely explains their preference to stabilise the oxygen-bound *OCOH intermediate. By transfer of another electron, this intermediate is then reduced to formate. As an anion, formate can be desorbed into the electrolyte from the negatively charged catalyst surface. Depending on the pH of the electrolyte, it is protonated to formic acid (pka = 3.75 at 25 °C).[64] In total, reduction of CO_2 to formic acid/formate requires two electrons and follows a relatively short and straight forward path. Consequently, production of formic acid/formate has

been reliably reported with high selectivity (>90%).[65,66]

In contrast, the other two categories of catalysts bind the activated CO_2 by the carbon atom as *COOH intermediate, in which the oxygen atom has been protonated. This is followed by a further PCET to the same oxygen (in acid or buffer) and elimination of H_2O or direct anionic desorption of OH-, which leaves *CO on the catalyst surface. In case of catalysts favouring carbon monoxide (*e.g.* Ag, Au, Zn),[62] the binding of *CO is weak, so carbon monoxide is quickly desorbed as final product. Like formic acid/formate, reduction to carbon monoxide requires only two electrons and follows a relatively short and straight forward path. This is also reflected in studies reporting *eCO_2RR* to carbon monoxide with high selectivity (>90%).[67]

In case of catalysts producing hydrocarbons and oxygenates, the *CO intermediate is not desorbed quickly. This category mainly consists of Cu, whose structural properties are unique as it binds *CO strongly enough for further reduction (>2 e^-), but not so strongly that the catalyst is deactivated by carbon monoxide poisoning.[68] Furthermore, Cu does not only allow further reduction but is the main catalyst that enables C–C coupling reactions.[68] Consequently, at least sixteen different products with up to three carbon atoms have been identified with Cu as catalyst: C_1 (carbon monoxide, formate, methanol, methane), C_2 (ethylene, ethanol, acetate, acetaldehyde, glyoxal, ethylene glycol, glycolaldehyde), and C_3 (acetone, hydroxyacetone, allyl alcohol, *n*-propanol, propionaldehyde).[69] These products require the transfer of up to 18 electrons. Thereby, the complexity generally increases with the number of transferred electrons, as there are more steps where reaction paths can diverge. This complexity combined with the broad spectrum of possible gaseous and liquid products can lead to complex mixtures, which should be avoided to prevent costly separation. To address this, many theoretical and experimental studies have been carried out to elucidate the mechanism of the different pathways and apply their principles to enhance the selectivity of Cu based materials towards the most desired products: methanol, methane, ethylene, ethanol and acetic acid.

Methanol and methane are both further reduced C_1 compounds that are attractive, for example, due to their high compatibility with existing infrastructure in the industry and energy sector. Although their mechanisms are still debated, they likely share commonalities.[70] By fine-tuning Cu based catalyst materials, relatively high selectivity (about 70-90%) could be achieved for methanol[71,72] as well as methane,[73,74] but only in few studies. Among the desired C_2 compounds, ethylene is the most important because it is the organic chemical with the highest annual production volume worldwide (about 170 Mt a^{-1}).[75] The mechanistic pathways of ethylene, ethanol and acetic acid are closely related and have been extensively studied from various perspectives (*e.g.* grain boundaries,[76] heterogenous/doped catalysts,[77,78] surface/interface tailoring,[79] role of surface oxophilicity,[80] surface hydrogen[81] and micro- and macro-environment[82,83]).

Even though the mechanism is still debated, relatively high selectivity (about 70-90%) could be achieved with highly engineered catalysts in few instances for ethylene,[79,84,85] ethanol,[86,87] and acetic acid.[88] Besides, another important approach to improve the synthesis of multi-carbon compounds is the tandem electrolysis, whereby the reduction of CO_2 to carbon monoxide is decoupled from further reduction.[89–91] Therefore, CO_2 is first selectively converted to carbon monoxide with a suitable catalyst (*e.g.* Ag, Au, Zn). Afterwards, this carbon monoxide is further reduced at a Cu based catalyst by the electrochemical CO reduction reaction (*eCORR*). This allows the conditions of both reactions to be optimised independently to increase overall process efficiency.

In summary, catalysts with high selectivity have been reported for all major products of the *eCO$_2$RR* (carbon monoxide, formic acid, methanol, methane, ethylene, ethanol and acetic acid). However, high selectivity needs to be achieved under industrially relevant conditions to allow industrial application. Therefore, certain criteria must be fulfilled, which are also referred to as key performance indicators or figures of merit.

1.2.2 Key Performance Indicators

In academic research and industrial development, the performance of *eCO$_2$RR* to any product can be assessed by the key performance indicators (KPI) outlined in this section.[92,93] Moreover, all these KPIs are commonly influenced by all cell components (*e.g.* catalyst, electrode architecture, electrolyte) and the electrolysis conditions.

Faradaic efficiency. The Faradaic efficiency (FE) describes the selectivity of an electrochemical process towards a particular product. It is defined as the ratio of the charge consumed to generate the product and the total charge passed during electrolysis. (*cf.* equation 1.11).

$$FE(x) = \frac{Q(x)}{Q(total)} = \frac{n \cdot z \cdot F}{I \cdot t} \tag{1.11}$$

with $FE(x)$ = Faradaic efficiency for product x, $Q(x)$ = amount of charge consumed for product x, $Q(total)$ = total amount of supplied charge, n = molar amount of product x, z = number of transferred electrons per equivalent of product x, F = Faraday constant, I = current, t = time.

In general, a FE of 100% is desired for any product of *eCO$_2$RR*, but this is challenging in aqueous electrolytes because of the competing HER (*cf.* section 1.2.1). However, a FE of at least 80% is considered a prerequisite for an industrial *eCO$_2$RR* process.[92,94]

Current density. The current density (j) is the total current (*i.e.* rate of electron flow) normalised to the geometrical surface area of the electrode (*cf.* equation 1.12).

$$j = \frac{I}{A} \tag{1.12}$$

with j = current density, I = current, A = geometrical surface area of the electrode.

Alternatively, the total current can also be normalised to the electrochemically active surface area to evaluate the activity of catalysts. Besides, partial current density represents the fraction of total current density used for the formation of a particular product and thus its synthesis rate (*cf.* equation 1.13).

$$j(x) = j \cdot FE(x) \tag{1.13}$$

with $j(x)$ = partial current density for product x, j = current density, $FE(x)$ = Faradaic efficiency for product x.

Consequently, high current density combined with high FE is necessary for high synthesis rates (*i.e.* space time yield) of products. To enable a high (partial) current density, mass transport of reactants and products to and from the electrode surface must be sufficient. This is particularly challenging in water-based *eCO$_2$RR*, as CO_2 has a low solubility in aqueous electrolytes (33 mmol L^{-1} at 298 K and 1 atm)[95,96] and its diffusion through bulk electrolyte is slow (diffusion coefficient = 0.00176 $mm^2\ s^{-1}$ at 20 °C).[97] To address this, suitable catalysts are applied with gas diffusion electrodes, which directly supply gaseous CO_2 to the reaction zone of the electrolyte-catalyst interface. This ensures sufficiently high mass transport of CO_2 at industrially relevant current densities. These electrodes are discussed in detail later (*cf.* section 1.3). Generally, most studies consider a current density of at least 200 mA cm^{-2} as the minimum required for industrial implementation.[92,94]

Energy efficiency, cell voltage and energy consumption. The energy efficiency (EE) describes the actual input of electric energy relative to the minimum amount required for the generation of a particular product based on standard redox potentials / thermodynamic potentials. It can be calculated for half-cells as well as full-cells, whereby the latter is more useful as it includes all sources of voltage losses (*cf.* equation 1.14).[21]

$$EE(x) = FE(x) \cdot \frac{U^0_{cell}}{U_{cell}} = FE(x) \cdot \frac{E^0_a - E^0_c}{E^0_a + \eta_a - E^0_c + |\eta_c| + I \cdot R_{cell}} \tag{1.14}$$

with $EE(x)$ = energy efficiency for product x, $FE(x)$ = Faradaic efficiency for product x, U^0_{cell} = thermodynamic cell voltage, U_{cell} = applied cell voltage, E^0_a = standard redox potential of anodic reaction, E^0_c = standard redox potential of cathodic reaction, η_a = anodic overpotential, η_c = cathodic overpotential, I = current, R_{cell} = cell resistance.

In addition to EE, the full-cell voltage is an important measure to calculate the overall electric energy consumption (EEC) and thus costs to conduct the electrolysis. The EEC can also be considered for products (*cf.* equation 1.15).[21]

$$EEC(x) = \frac{z \cdot F \cdot U_{cell}}{FE(x) \cdot M(x)} \tag{1.15}$$

with $EEC(x)$ = electric energy consumption for product x, z = number of transferred electrons per equivalent of product x, F = Faraday constant, U_{cell} = applied cell voltage, $FE(x)$ = Faradaic efficiency for product x, $M(x)$ = molar mass of product x.

In general, an EE of at least 50% is desired for a future industrial process.[92,94]

Carbon efficiency. In *eCO$_2$RR* literature, carbon efficiency is typically defined as the molar amount of CO_2 that is electrochemically converted to products, compared to the amount fed to the cell inlet (*cf.* equation 1.16). If unconverted CO_2 is not recycled to the inlet, carbon efficiency is also referred to as single-pass conversion (SPC) or single-pass carbon efficiency (SPCE).

$$\text{Carbon efficiency}(x) = \frac{a(x) \cdot n(x)}{n(CO_2)} \tag{1.16}$$

with $a(x)$ = number of carbon atoms per equivalent of product x, $n(x)$ = molar amount of product x, $n(CO_2)$ = total molar amount of consumed CO_2.

Other conversions of CO_2, such as the chemical formation of carbonates, are not included in the carbon efficiency but are considered carbon losses (*cf.* section 1.2.1). These carbon losses can be detrimental to an *eCO$_2$RR* process, as they change the composition and thus property of the electrolyte. They can form solid precipitates that block active sites and damage the usually porous cathodes and must be recovered in an additional process step by heating or acidification to reuse them.[98–101] Consequently, carbon losses / carbonate formation should be addressed to avoid additional process steps and the associated costs for industrial implementation. In general, the SPC should be as high as possible, but depends significantly on other parameters (*e.g.* current density), whose optimisation is a priority for improving the overall process.[102,103]

Stability. The stability of a catalyst, an electrolyser or an entire process is the duration in which they can be operated continuously while maintaining the same performance. Generally, the duration of stable performance significantly affects the costs of the entire process. To minimise the costs of material replacement, maintenance and downtime, stable performance should be achieved for at least 20000-50000 h (≙2.3-5.7 a).[92,104,105] As criteria for stable performance, decay rates of FE ($\frac{\Delta FE}{\Delta t} < 0.1\%$ per 1000 h) and cell voltage ($\frac{\Delta U_{cell}}{\Delta t} < 10\ \mu V\ h^{-1}$) have been suggested.[92,106] Besides some exceptions discussed later, stability of catalysts is not examined beyond 200 h of runtime in the majority of

literature. Consequently, sufficient long-term stability is one of the main challenges to be overcome towards commercialisation of the *eCO$_2$RR* technology. Thereby, a holistic approach is important to optimise any of the KPIs and thus the overall process, as they are interdependent and involve certain trade-offs.[92,93] For example, stability may not be improved at the maximum current density a catalyst can achieve while also maintaining high FE. Furthermore, the KPI benchmarks are based on data reported so far, most of which comes from laboratory scale or other industrially established electrolysis processes (*e.g.* H_2, Cl_2), and may therefore need to be reassessed once data sets from pilot plants become available. In addition to the presented KPI, more aspects of the overall process must be considered from an industrial point of view to advance the *eCO$_2$RR* technology towards application. They mainly concern the implementation and operation of a CO_2 electrolyser and are illustrated as well as discussed below (*cf.* figure 1.4).

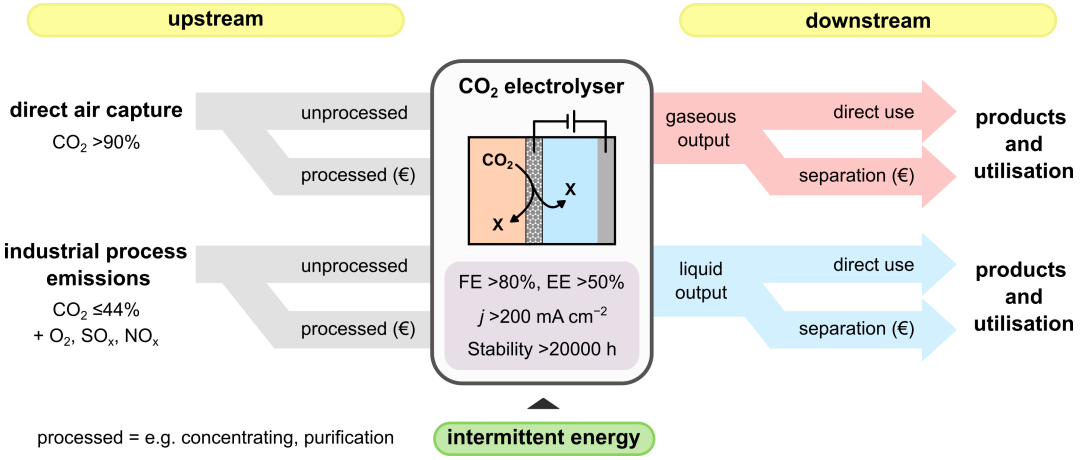

Figure 1.4 – Schematic illustration of the electrochemical CO_2 reduction, its key performance indicators and upstream/downstream processes (whereby € indicates additional costs) to implement a CO_2 electrolyser.

Anodic counter reaction. The oxidation of water (*i.e.* OER) commonly serves as anodic counter reaction of the *eCO$_2$RR*, as water is an abundant reactant and the reaction secures the supply of protons to the cathode. However, the thermodynamic potential as well as the overpotential of OER are relatively high and the required catalysts are expensive (*e.g.* Ir). Additionally, the generated oxygen does not have a particularly high value (about 30 € t^{-1})[60] but is mostly a safe product to vent. In other words, OER uses expensive catalysts and consumes a large amount of energy without generating a product of additional value to improve the economic feasibility of *eCO$_2$RR*. Consequently, alternative anodic reactions could be advantageous depending on the implementation and have been receiving attention in recent years.[107–110]

CO_2 source. Most studies evaluate the performance of catalysts and electrolysers using a highly pure CO_2 feed, but the two most significant future sources of CO_2 are

unavoidable process emissions and DAC (*cf.* section 1.1), both of which have lower concentrations of CO_2. DAC processes aim for >90%[111] of CO_2, whereas unprocessed industrial emissions usually have a maximum of 44%.[54] This dilution of CO_2 streams (*i.e.* a lower CO_2 partial pressure) needs to be considered as it can affect FE.[112–114] In addition, most industrial point sources contain reactive impurities such as oxygen, sulphur oxides, and nitrogen oxides, which compete with the *eCO₂RR* because their respective reduction has a more positive thermodynamic potential. Even at low concentrations, they can decrease the FE of *eCO₂RR* and negatively affect the stability of catalysts.[115–117] Consequently, the composition of CO_2 sources should be considered to develop compatible *eCO₂RR* processes to avoid additional costs of upstream processing (*e.g.* purification, concentrating). However, establishing a purification process for major CO_2 point sources (*e.g.* cement industry, waste incineration) might be more efficient than developing several different processes compatible with diluted and contaminated CO_2.

Product purity and downstream processing. Depending on their composition and intended use, output streams from CO_2 electrolysers must be processed downstream to either obtain or apply the products in high purity. Such downstream processing can significantly contribute to the overall cost of the process and especially complex product mixtures that require intensive separation should be avoided.[118–120] Even with selective catalysts to prevent product mixtures, gaseous products are usually diluted by unconverted CO_2 and liquid products by the electrolyte. Consequently, products should either be directly generated with high purity by adapted concepts or the diluted product streams should be compatible with their subsequent use to avoid expensive downstream processing.

Mode of operation. Electrolyses are usually performed in galvanostatic mode, meaning at constant current (density). The stability of catalysts and processes are thereby defined as decay rates of FE and cell voltage, as described above. However, electrolysis processes are also intended to store fluctuating energy from renewable resources (*e.g.* solar and wind) in chemical compounds. Consequently, the operation of *eCO₂RR* processes and stability of catalysts should be investigated at intermittent electricity to establish an overall robust process suitable for storing excess energy as available. Depending on the implementation, stable performance at intermittent electricity is at least advantageous, if not a prerequisite for industrial use. To date, only a few studies have been published on that regard with *eCO₂RR*, including two in which electricity patterns derived from solar panels were used to produce either carbon monoxide[121] or ethylene together with ethanol.[76]

Scalability. To be viable for industrial implementation, all components required for the respective *eCO₂RR* process must be scalable, meaning available in sufficient

quantities and functional in larger dimensions. Based on large-scale industrial chlor-alkali electrolysis,[122] an area of at least 2 m^2 can be assumed as a guideline for the size of electrodes. Consequently, development of catalysts/cathodes for reduction of CO_2 should be based on inexpensive, abundant raw materials and their large-scale fabrication should be reliable and cost-effective. This is particularly important if *eCO₂RR* processes are implemented decentralised on-site of point sources to keep the capital costs of electrolyser units as low as possible to avoid high investment barriers.

To achieve the KPI benchmarks, overcome the remaining challenges and thus close the gap between academic research and industrial requirements for adoption of the *eCO₂RR* technology, great efforts have been made in recent years. This includes exemplarily the development and evaluation of various catalyst materials for different products (*e.g.* carbon monoxide,[67] formic acid,[65,123,124] multi-carbon products[125–127]), reaction environments (*e.g.* electrolyte composition and pH[128–130]), and cell configurations (*e.g.* membrane electrode assemblies,[131] solid-state electrolyte cells[132]). As a result, performance of *eCO₂RR* processes have considerably improved over the last years, especially towards carbon monoxide, formic acid/formate and ethylene. Some of the respective highlights are compared below (*cf.* table 1.1). Thereby, sufficient FE is only achieved at relevant current density for carbon monoxide and formic acid/formate. Their respective energy efficiency, which is rarely reported to date, and their stability, which is rarely examined long-term, still need to be improved though. In addition, research efforts must be increased to transition from (large) laboratory scale to industrially relevant scale.

Table 1.1 – Overview of exemplary key performance indicators for electrochemical reduction of CO_2, their benchmark for industrial application, and state of the art / highlights on (large) laboratory scale for the reduction products carbon monoxide, formic acid and ethylene. Abbreviations: KPI = key performance indicator, FE = Faradaic efficiency, j = current density, EE = energy efficiency.

KPI	Benchmark	State of the art / Highlights		
		CO	HCOOH	C_2H_4
FE / %	>80[92,94]	90-98[133–137]	83-95[138–140]	65-75[141]
j / A cm^{-2}	>0.2[92,94]	0.3-0.6[133,137,142]	0.6-2.5[138–140,143]	1.3[141]
EE / %	>50[92,94]	40[144]	36-48.5[145]	20-34[146,147]
Stability / h	>20000[92,104,105]	1500-4000[133,137,148]	1000-5200[138,149]	1000[85]
Area[a)] / cm^2	>20000[122]	250-300[133,148]	25,[150] 1526[151]	30[85]

a) Refers to the geometrial surface area of the cathode.

Beyond academic research, several pilot-scale systems have been and continue to be developed for *eCO₂RR* by small start-ups and larger companies since 2010.[93] The TRL level of *eCO₂RR* to carbon monoxide was recently estimated to be at 8 for high-

temperature (T > 600 °C, solid-oxide electrolyser) and at 5-6 for low-temperature (T < 100 °C) processes.[105] In comparison, *eCO$_2$RR* to formic acid is estimated at 3-5 for low-temperature processes.[105] This is accompanied by the prediction *eCO$_2$RR* will become economically viable for both carbon monoxide and formic acid in the near future, but not for multi-carbon compounds.[102,104] In other words, only the simplest and least reduced single-carbon products are likely to be accessible with *eCO$_2$RR* technology in the foreseeable future. With this in mind, research has been exploring how carbon monoxide and formic acid themselves can be used to produce multi-carbon compounds.

1.2.3 Towards Multi-Carbon Compounds with Carbon Monoxide and Formic Acid

To obtain multi-carbon compounds with carbon monoxide and formic acid from *eCO$_2$RR*, their implementation into established chemical value chains can be considered first. As traditional building block, carbon monoxide can be used in synthesis gas to produce either BTX aromatics (via methanol) or various hydrocarbons by the Fischer-Tropsch process, although both options are energy-intensive (*cf.* section 1.1). In contrast, formic acid is not usually converted into multi-carbon compounds but is rather directly used as a reactant or in other industries (*e.g.* textiles, leather, food and medicine) as a preservative, antibacterial agent and pH regulator.[152]

Beyond established value chains, both carbon monoxide and formic acid can be used to obtain multi-carbon compounds in biosynthesis. Thereby, microorganisms serve as biocatalysts, which consume substrates in their metabolic pathways to produce a variety of products. This process is also referred to as fermentation and typically uses multi-carbon compounds (*e.g.* sugar) as substrate, but some species can also use carbon monoxide and formic acid as carbon and/or energy source. Depending on the specific microorganism, different products can be obtained with high selectivity. Additionally, suitable microorganisms can be further adapted for efficient biosynthesis by genetic and metabolic engineering. Overall, biocatalytic conversion is particularly attractive because it works at ambient conditions and can synthesise multi-carbon products in a single process step, which would otherwise require several steps in the traditional chemical industry.

Carbon monoxide is often used as a substrate with hydrogen as an (additional) energy source, which is referred to as syngas fermentation. Thereby, low solubility of both gases in aqueous growth media poses a general engineering challenge for sufficient mass transport. Exemplary multi-carbon products from syngas fermentation include alcohols (*e.g.* ethanol, isopropanol, butanol), carboxylic acids (*e.g.* acetic acid, propionic acid,

butyric acid) and even homologues with up to eight carbon atoms.[153,154] Moreover, this process is already used commercially to produce ethanol and 2,3-butanediol from waste gas streams containing CO, CO_2, and H_2 (LanzaTech).[155] Consequently, the use of carbon monoxide from *eCO_2RR* in microbial synthesis is a promising approach towards multi-carbon products. This approach has also been demonstrated in an exemplary manner by direct coupling of *eCO_2RR* with syngas fermentation on laboratory scale (*cf.* figure 1.5, left side).[156] Therefore, the synthesis gas was produced in an electrolyser by *eCO_2RR* to carbon monoxide (70% FE) and HER for hydrogen (30% FE) at industrially relevant current density (up to 300 mA cm^{-2}) with remarkable stability (over 1200 h). The gaseous output of the electrolyser (mixture of CO, CO_2 and H_2) was fed directly to a spatially separate fermenter in which a mixed culture of microorganisms produced the high value chemicals butanol and hexanol with high overall energy efficiency. In short, this report is an outstanding example of an energy efficient and scalable system, which highlights the prospects of directly combining *eCO_2RR* with versatile biosynthesis. Additionally, it shows gaseous outputs of *eCO_2RR* electrolysers can be used directly for biosynthesis without downstream processing, which is beneficial for the cost balance of electrolysis (*cf.* section 1.2.2).

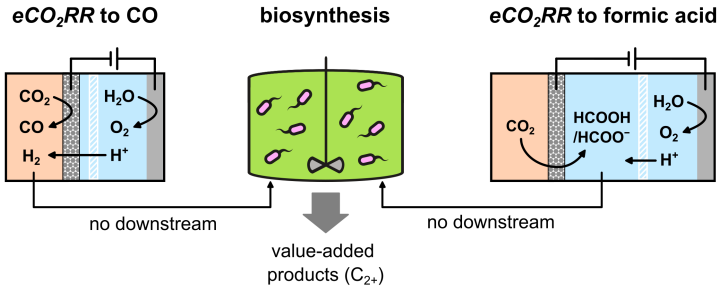

Figure 1.5 – Schematic illustration of coupling electrochemical reduction of CO_2 to either carbon monoxide (and hydrogen) or formic acid/formate with subsequent microbial conversion to value-added multi-carbon compounds without any intermediate downstream processing.

Formic acid/formate is typically used as the sole substrate, serving as both carbon and energy source. Unlike carbon monoxide (and hydrogen), it is highly soluble in aqueous growth media, which enables microbial conversion without the safety, transport, and mass transport challenges associated with gaseous feedstocks. Several native microorganisms have been reported to use formate as substrate.[157,158] Among them, *Cupriavidus necator* (*C. necator*) stands out as it can produce the biopolymer polyhydroxybutyrate (PHB), a biodegradable thermoplastic with commercial application.[159–161] Furthermore, *C. necator* can be genetically modified to also produce other multi-carbon compounds such as branched-chain alcohols (*e.g.* isobutanol, 3-methyl-1-butanol),[162] and organic acids (*e.g.* crotonic acid).[163] Since *C. necator* can be easily modified by genetic engineering, the product range is likely to be further expanded to establish a formate-based bioeconomy in the future.[164,165] Consequently, the use of formic

acid/formate from *eCO$_2$RR* in microbial synthesis is a promising approach towards multi-carbon compounds, like carbon monoxide. Besides, an initial direct coupling of *eCO$_2$RR* to formate with subsequent microbial conversion has already been carried out on small laboratory scale (*cf.* figure 1.5, right side).[166] The formate was electrochemically synthesised from CO_2 in a flow cell and accumulated in a biocompatible catholyte based on phosphates. This catholyte was then used as feedstock for microbial synthesis of PHB with *C. necator* in shake flasks without intermediate downstream processing. Although the yield of the combined processes was relatively low, this study demonstrates a viable concept for scalable coupling. Additionally, it highlights diluted liquid product streams from electrolysers can also be used for biosynthesis without further processing, which avoids additional costs (*cf.* section 1.2.2).

In summary, carbon monoxide and formic acid/formate from *eCO$_2$RR* processes can be utilised in biosynthesis to already produce a wide range of multi-carbon compounds. The coupling of these two processes combines the high energy efficiency of electrosynthesis with the high selectivity of biosynthesis and can upgrade CO_2 to value-added compounds in remarkably only two process steps. However, the high synthesis rates of electrolysis at industrially relevant conditions (*e.g.* current density > 200 mA cm^{-2}) are usually not compatible with the comparably lower rates of microbial substrate consumption.[157] Therefore, the two processes should be separated in terms of space (*i.e.* ex-cell process) and time. Consequently, formic acid would be the preferred substrate, as unlike carbon monoxide, it is a non-toxic liquid that can be easily stored. This also makes *eCO$_2$RR* to formic acid/formate particularly well suited for storing excess energy from fluctuating renewable energy sources. In short, excess energy can be stored as formic acid by *eCO$_2$RR* and then upgraded with biosynthesis to value-added multi-carbon compounds.

1.3 Gas Diffusion Electrodes

As briefly mentioned above, gas diffusion electrodes (GDE) are necessary for sufficient mass transport of CO_2 at industrially relevant current densities and are therefore a prerequisite for adoption of *eCO$_2$RR* technology (*cf.* section 1.2.2). This type of electrode was originally developed for fuel cells in the early 20$^{\text{th}}$ century,[167] and its adaption for *eCO$_2$RR* has become an important focus of research in recent years. This section explains their working principle, fabrication and operation in *eCO$_2$RR* processes.

When *eCO$_2$RR* is performed at regular planar electrodes, CO_2 is dissolved in the bulk electrolyte and supplied to the electrode surface by diffusion. Thereby, mass transport of CO_2 and thus current density of *eCO$_2$RR* is limited in aqueous electrolytes by its low solubility (33 mmol L^{-1} at 298 K and 1 atm)[95,96] and slow diffusion (diffusion coefficient = 0.00176 mm^2 s^{-1} at 20 °C).[97] These two limitations can be overcome by

GDEs, which are porous electrodes that can be operated with gaseous CO_2. During electrolysis (*i.e.* polarisation), electrolyte penetrates the pore structure because the solid catalyst becomes hydrophilic due to electrowetting.[96] This leads to an enlarged internal surface area in which gaseous CO_2 from one side of the GDE and liquid electrolyte from the other side of the GDE share a vast interface that allows high mass transport. Thereby, the main reaction zone of CO_2 reduction within the GDE was originally, and often still is, assumed to be a three-phase boundary between gaseous CO_2, liquid electrolyte and solid catalyst (*cf.* figure 1.6).

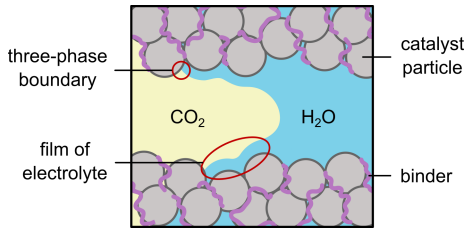

Figure 1.6 – Simplified schematic illustration of a pore in a gas diffusion electrode and its hypothesised phase boundaries.

However, studies in recent years indicate the interface of electrolyte and catalyst (*i.e.* two-phase boundary) to be the main reaction zone instead.[168–171] According to this, the polarised catalyst surface is coated by at least a film of electrolyte, which in turn shares an interface with gaseous CO_2. This results in relatively short diffusion pathways for bulk CO_2 in the pores through the electrolyte to the catalyst surface. Consequently, GDEs mitigate the low solubility of CO_2 and its slow diffusion in aqueous electrolytes by introducing gaseous CO_2 directly into the vicinity of the active sites and shortening the liquid diffusion pathways. This enables GDEs to achieve current densities approximately two orders of magnitude higher than those of planar electrodes in direct comparison.[172,173] Overall, theoretical and experimental research is ongoing to elucidate the exact nature of the reaction zone and the complex transport phenomena within the GDE governing its superior performance.[96,174]

There are two different designs for the construction of GDEs, which have been schematically illustrated (*cf.* figure 1.7).

The first and most common in academic research is a catalyst coated gas diffusion layer, also referred to as a multi-layer GDE.[175–177] It comprises a hydrophobic gas diffusion layer (GDL) onto which a catalyst layer has been deposited. Thereby, the GDL (about 100-300 µm) is usually a combination of a macro- and a microporous layer. The macroporous layer is formed by conductive carbon fibres (*e.g.* paper or cloth) and contains a small amount of hydrophobic polytetrafluoroethylene (PTFE), which ensures facile transport of CO_2 into the GDL. A thin microporous layer is coated on top and consists of carbon particles for conductivity, but with a high PTFE content to

prevent excessive flooding of the GDL, which would block gas diffusion pathways. The catalyst layer (about 5-50 µm) can be applied to the microporous layer with various methods (*e.g.* spray-coating, blade-coating, drop-casting, electrodeposition). In most cases, catalysts are immobilised as particles with an ionomer (*e.g.* Nafion) as binding agent. Consequently, the catalyst layer is likely more or less flooded during operation and supplied with gaseous CO_2 from the neighbouring pores of the GDL.[178] This design has the advantage of requiring only a relatively small amount of catalyst, but its manufacturing could be difficult on a larger scale.

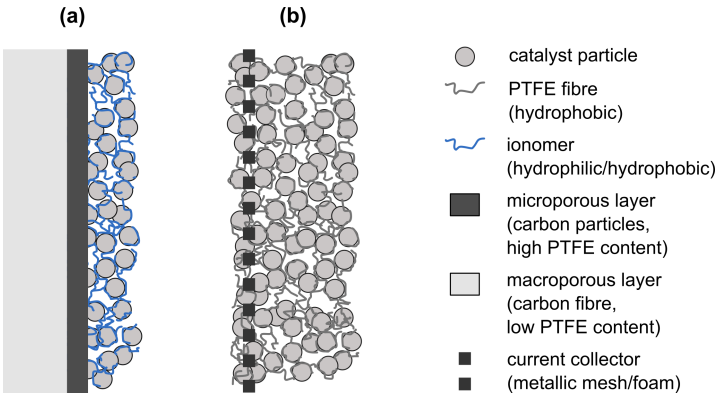

Figure 1.7 – Schematic illustration of the two types of gas diffusion electrodes in cross-section: (a) multi-layer (catalyst coated gas diffusion layer), (b) single layer (full catalyst). Abbreviations: PTFE = polytetrafluoroethylene.

The second configuration is a single layer (*i.e.* full catalyst) GDE, which is mostly known from the oxygen depolarised cathode (ODC) technology developed by Covestro.[122,179] The single layer is porous and consists of a homogenous mixture of catalyst and hydrophobic binding agent (mostly PTFE), which can be fixed onto a conductive support material (*e.g.* metallic mesh) to improve current distribution and mechanical stability. Consequently, the single layer acts as both catalyst and gas diffusion layer. The size and distribution of its pores mainly depend on the ratio of catalyst to binding agent, the size and shape of catalyst particles, and the fabrication method. The two main fabrication techniques are sintering and pressing.[179] In case of sintering, a wet or dry powder mixture of catalyst and PTFE is coated or pressed onto a support material, which is then treated at high temperature (about 340 °C).[179,180] The porosity of this GDE is significantly influenced by the protocols for drying and sintering. In case of pressing, a dry powder mixture of catalyst and PTFE is compressed by rollers known as calender, with or without a support material. Depending on the force applied during compression, the powder mixture is more or less compacted. Consequently, the porosity of the GDE can be adjusted to a certain extend by the amount of applied force. The porous structure can also be further tailored by pore forming agents or other additives. This fabrication process is also referred to as calendering and is a facile, industrially established method for fabrication of large-scale GDEs. It is used for the fabrication of

silver based ODCs (*i.e.* GDEs), which are applied for oxygen reduction to hydroxide in industrial chlor-alkali electrolysis.[122,179] Noticeably, such a GDE was also successfully applied for eCO_2RR to carbon monoxide with outstanding performance stability at high current density (300 mA cm^{-2}, >1200 h).[156]

To employ GDEs for eCO_2RR processes at ambient conditions with water oxidation at the anode, they are usually operated in flow cells with one of four different illustrated configurations (*cf.* figure 1.8).

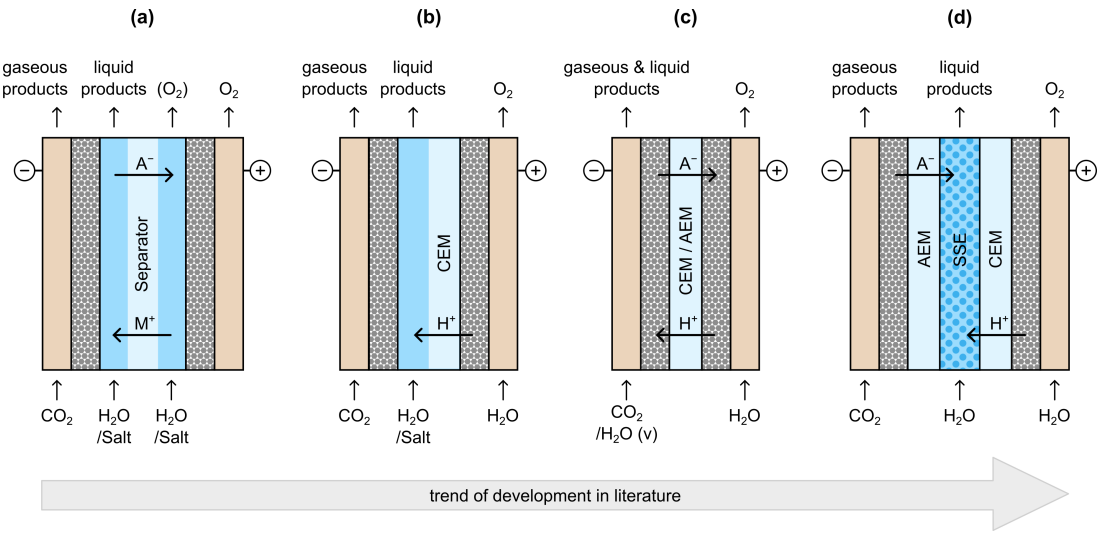

Figure 1.8 – Schematic illustration of different cell designs with gas diffusions electrodes (grey pattern) for eCO_2RR at ambient conditions: (a) Cell configuration with liquid electrolytes at the anode and cathode side, (b) cell configuration with liquid electrolyte at the cathode side and a zero gap anode, (c) Membrane electrode assembly (MEA) with CEM or AEM and no liquid electrolyte, but with humidified CO_2, (d) cell configuration with solid-state electrolyte purged by a flow of water or humidified inert gas, including AEM and CEM. Abbreviations: CEM = cation exchange membrane, AEM = anion exchange membrane, SSE = solid-state electrolyte (this figure was created based on *Stöckl et al.*[157] and extended).

The first configuration uses an aqueous electrolyte at both anode and cathode, which are divided by a separator. The separator can be a diaphragm in case of only gaseous products (*e.g.* carbon monoxide) or a cation-exchange membrane (CEM) in case of liquid products (*e.g.* formic acid/formate) to prevent crossover to the anode. Thereby, gaseous products are found in the output stream of CO_2, while liquid products leave the cell with the catholyte output. This set-up is common for initial evaluation of GDEs in flow cells because the individual components are not highly integrated and readily available. It also has the advantage that the interfaces within the GDE can be adjusted by regulating the ratio of gas and liquid pressure. However, the ohmic resistance of this cell can be relatively high due to the distance between the electrodes and especially in the anode compartment if bubbles of gaseous oxygen accumulate in the anolyte.

The second configuration is similar but uses a pure water fed anode in direct close

contact with a CEM.[181] This is also referred to as zero-gap anode or configuration and has two main advantages. On the one hand, it lowers ohmic resistance between anode and cathode by decreasing their distance and thus lowers the required cell voltage. On the other hand, it enhances mass transport of protons to the catholyte in which they are consumed by the *eCO$_2$RR*.

In the third configuration, both anode and cathode are in zero-gap configuration to either a CEM, an anion-exchange membrane (AEM) or a bipolar membrane.[131] The anode is fed with pure water, while the cathode is supplied with humidified CO_2. Thereby, both gaseous and liquid products are found in the gaseous output of the cathode. This configuration is referred to as membrane electrode assembly (MEA) and greatly reduces ohmic resistance between anode and cathode, which lowers cell voltage and thus energy costs. It is most advantageous for gaseous reduction products of CO_2, as liquid products can accumulate in the pores of the GDE and block gas diffusion paths.

The last configuration has emerged in recent years to obtain liquid products in acidic form (*e.g.* formic acid) and/or concentrated in pure water to avoid separation of supporting electrolytes.[132,139,145,182,183] Therefore, anode and cathode are separated by a conductive solid-state electrolyte (SSE). This SSE is purged by either pure water or humidified inert gas to obtain the liquid products. Additionally, anode and SSE are separated by a CEM to secure proton supply, while cathode and SSE are separated by an AEM to allow crossover of liquid products in anionic form to the SSE, where they are protonated.

In summary, GDEs can be designed, manufactured and integrated into electrolysers in various ways. This allows them to be developed in an application-oriented manner for different *eCO$_2$RR* processes, which is represented by a wide variety of reported GDEs.

2 Objectives

The electrochemical reduction of CO_2 would mitigate emissions and could be used to store fluctuating energy from renewable sources (*e.g.* solar, wind) as formic acid. This formic acid can be safely stored or transported and represents not only a source of hydrogen[184,185] but also a potential sustainable carbon feedstock. Since formic acid is not yet an established carbon feedstock in the contemporary chemical industry, new routes for its commercial integration would support the replacement of fossil feedstock.

To contribute to the substitution of fossil carbon with CO_2, this work focused on a process concept for *e*CO_2*RR* to formic acid/formate and its subsequent biological or chemical upgrading to value-added carbon products (*cf.* figure 2.1).

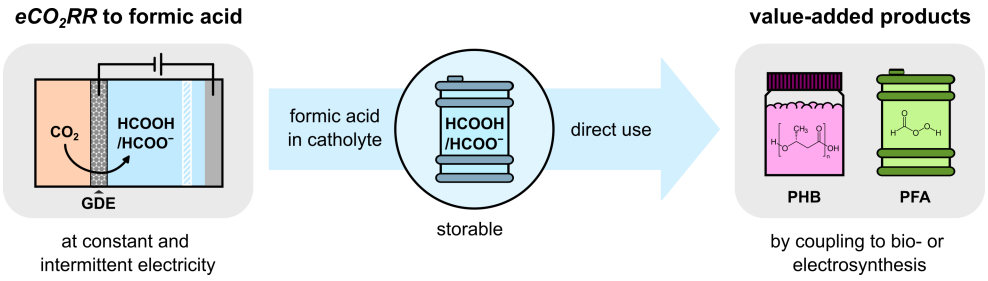

Figure 2.1 – Schematic illustration of *e*CO_2*RR* to formic acid/formate and its subsequent utilisation without downstream processing to obtain value-added carbon products.

This encompassed the development of GDEs for reliable operation at constant and intermittent electricity, which should be able to directly utilise surplus energy from renewables to generate formic acid. To facilitate cost-efficient and decentralised *e*CO_2*RR* at point sources (*e.g.* flue gas, DAC facilities), their design and fabrication should be based on the well-established and scalable ODC technology[122,179] and should use affordable as well as relatively abundant catalyst materials (*e.g.* Sn, Bi).

Since formic acid/formate can often be easily obtained in supporting electrolyte, its subsequent upgrading was to be explored without downstream processing to avoid additional costs (*e.g.* concentrating, purification). To this end, biological upgrading to the sustainable bioplastic polyhydroxybutyrate (PHB) and chemical upgrading to the promising disinfectant performic acid (PFA) via electrosynthesised hydrogen peroxide should be investigated with phosphate buffer as compatible supporting electrolyte. This was accompanied by the overarching goal to transparently balance the respective overall processes and critically evaluate their energy costs, which has often been neglected in the past.

3 Discussion of Results

Throughout this work, the development of single layer GDEs for *eCO$_2$RR* to formic acid/formate was an ongoing process with several stages. It was carried out in cooperation with Gaskatel (Kassel / Germany), a commercial fabricator of GDEs. All GDEs were based on commercially available materials and used inexpensive, relatively abundant and non-toxic catalysts (Sn, Bi, Bi_2O_3, all ≤200 € kg^{-1}). They were each evaluated in a custom designed divided flow cell[186] that corresponds to the most common cell configuration (*cf.* figure 1.8, a). The most important stages in the course of this work laid the foundation of all published manuscripts and are outlined below (*cf.* table 3.1, details are provided in appendix A).

Table 3.1 – Most important stages of GDE development with composition and fabrication of the single layer GDE and their key performance data in a screening set-up with a custom designed divided flow cell[186] (Electrolyte = 0.2 mol L^{-1} KH_2PO_4/K_2HPO_4, cathode = GDE (5 cm^2 geometrical area), anode = mixed Ir-Oxide, CEM = N117). Abbreviations: FE = Faradaic efficiency, j = current density, EEC = electric energy consumption, HP = heat press, CEM = cation exchange membrane.

Development stage	I[a)]	II	III	IV	V	VI
Catalyst	Sn	Sn	Sn	Bi	Bi_2O_3	Bi/Bi_2O_3 (80:20)
Support (Ni)	Mesh	Mesh	Foam	Foam	Foam	Foam
Fabrication	Calender	Calender	HP	HP	HP	HP
FE[b)] / %	54	58	80	86	86	90
c[b)] / mmol L^{-1}	94	312	441	505	501	501
j / mA cm^{-2}	50	100	150	150	150	150
EEC[b)] / kWh kg^{-1}	-	12.5	9.4	8.6	7.9	8.4[c)]
Runtime / h	5.25	30	22	22	22	21
Reference	[166]	-	[186]	-	[187]	[188]

a) The flow cell had a geometrical GDE surface of 10 cm^2.
b) Refers to formate and the values presented have been rounded for clarity (half round up).
c) Is higher compared to stage V, as a thicker CEM was used (N424 instead of N117).

The development started out from a Sn based GDE (90 wt% Sn, 5 wt% PTFE, 5 wt% activated carbon) with Ni mesh as support material supplied by Gaskatel (I). It was fabricated by them via calendering and applied for *eCO$_2$RR* to formate by *Stöckl et al.*[166] in a previous study. Thereby, a moderate overall FE (54%) was achieved at relatively low current density (50 mA cm^{-2}) in short runtime (5.25 h).

The second stage (II) was reached by adjusting the composition of the catalyst mixture (85 wt% Sn, 10 wt% PTFE, 5 wt% carbon black). At doubled current density (100 mA cm^{-2})

and increased runtime (30 h), a slightly higher overall FE (58%) was achieved (*cf.* appendix A, section 2.1). However, the course of FE was not stable and showed a decline (about 17%) throughout operation. Exemplary electrolyses at intervals with and without current suggested limited mass transport of formate within the GDE's pore system was responsible for the decline (*cf.* appendix A, section 2.2). To address this, pore-forming agents and porous support material were examined to improve porosity of the GDE. Exemplary pore-forming agents (*e.g.* NH_4HCO_3, KH_2PO_4/K_2HPO_4, *cf.* appendix A, section 2.3) did not lead to an improvement. In contrast, the course of FE could be stabilised with Ni foam as porous support material and became nearly constant with improved overall FE (69%, *cf.* appendix A, section 2.4). For the fabrication of GDEs with Ni foam, it was necessary to change from the calender to a stationary heat press, as the GDE blanks had to be pressed horizontally (available calender only allowed pressing in vertical orientation). This change of fabrication method did not significantly influence performance of GDE (*cf.* appendix A, section 2.5). Alongside, it was confirmed that the course of FE was stabilised by the Ni foam and not the adapted fabrication with the heat press. Nonetheless, calendering can still be used with Ni foam if the rollers press the GDE blank horizontally (verified by Gaskatel, *cf.* appendix A, section 2.6).

Using Ni foam as support and with an adjusted catalyst composition (87.5 wt% Sn, 12.5 wt% PTFE), the third stage (III) of development was reached. This GDE achieved an overall FE of 80% at 150 mA cm^{-2} in 22 h (or 77% FE at 100 mA cm^{-2} in 30 h, *cf.* appendix A, 2.7). The runtime was shortened at increased current density as high concentrations of formate (≥500 mmol L^{-1}) and depleted buffer capacity became limiting in longer runs for the screening protocol (*cf.* appendix A, section 2.8).

For the next stage (IV), Sn was substituted with Bi, whereby the catalyst to binder ratio remained the same. This GDE achieved an improved overall FE of 86% at 150 mA cm^{-2} in 22 h (*cf.* appendix A, section 2.9). Additionally, the EEC for formate was lower compared to the previous stage (about 8%).

In the subsequent stage (V), Bi was substituted with Bi_2O_3 and the catalyst to binding agent ratio was as before. Thereby, Bi_2O_3 acted as a precatalyst, which is predominantly reduced to Bi during initial polarisation.[187] This was hypothesised to improve the performance by increasing porosity and lowering the potential of the GDE (due to better interconnectivity of individual particles). While overall FE (86%) was comparable, EEC of formate could be lowered further (about 8%) compared to the previous stage.

The latest stage (VI) of GDE development was achieved with a mixture of Bi and Bi_2O_3 (80:20) as catalyst and an unchanged ratio to the binding agent. This GDE reached an improved overall FE of 90% at 150 mA cm^{-2} in 21 h. Notably, the EEC was higher than for the previous fifth stage (about 6%) as a thicker CEM was used (N424 instead of

N117). In direct comparison to the fourth and fifth stage at identical conditions, this GDE achieved the best EEC and the highest overall FE of formate.

Based on the outlined development of GDEs, three manuscripts were published and will be presented in the following. The first one concerns the latest stage (VI) of GDE development with mixtures of Bi and Bi_2O_3 as catalyst materials and their application at intermittent electricity (*cf.* section 3.1). The second and third one demonstrate the direct coupling of *e*CO_2*RR* to formate either with biosynthesis of PHB (stage III, *cf.* section 3.2) or with synthesis of PFA (via electrosynthesised hydrogen peroxide, stage V, *cf.* section 3.3). Although earlier versions of GDEs were used in both, the respective coupling should be fully compatible with the latest stage by design.

3.1 Bi based GDEs for Intermittent Energy

A manuscript was published on this section:

Ida Dinges, Siegfried R. Waldvogel, Markus Stöckl, CO_2 Reduction to Formic Acid/Formate by Intermittent Electricity at Bismuth Gas Diffusion Electrodes, *ChemSusChem* **2025**, e202501583.
DOI: 10.1002/cssc.202501583
The publication is reprinted within this section, according to the CC BY 4.0 license.[189]

Explanation of my contribution:
The project was conceptualised by S.R.W., M.S. and me. I performed all experimental work (fabrication and characterisation of GDEs, electrosynthesis of formate) and analysed the data. The manuscript was written by me with support of M.S. and S.R.W. The work was carried out under the supervision of M.S. and S.R.W.

The two most important renewable energy sources (*e.g.* solar and wind) are intermittent and must frequently be taken off the grid when they exceed demand as well as grid and storage capacity. As outlined above (*cf.* section 1.2.3), this surplus energy could be used instead with *eCO$_2$RR* to produce formic acid/formate as storable feedstock with versatile application (*e.g.* biosynthesis,[166,186,190] hydrogen source[184,185]). This requires catalysts suitable for operation at intermittent electricity, but most studies focus on catalysts in continuous operation at constant current. Thereby, great efforts have already been made in the development of Bi based catalysts for *eCO$_2$RR* to formic acid at high current density (0.5-2 A cm^{-2}) with high FE (≥90%).[191–194] However, most of these catalysts are highly engineered and thus relatively expensive, which could limit their decentralised application at point sources (*e.g.* flue gas, DAC facilities).

To address these aspects, GDEs based on affordable and commercially available Bi materials were developed for flexible operation at intermittent electricity. Elemental Bi was selected as base catalyst because it is the main product of global Bi production/refining. Bi_2O_3 was systematically added to enhance performance by acting as pore forming agent and reductive binder, as it is reduced to elemental Bi during cathodic polarisation.[187] This was based on the industrially established silver/silver oxide GDE in chlor-alkali electrolysis.[122,179] The single layer (*i.e.* full catalyst) GDEs were fabricated by heat pressing the catalyst mixture onto Ni foam as porous support material and current collector. The composition of catalyst was varied from pure elemental Bi (particle size ≤40 µm) to pure Bi_2O_3 (particle size ≈80 nm) in steps of 20 wt%, with PTFE serving as hydrophobic binding agent in constant ratio (12.5 wt%).

The six different types of GDE were characterised before and after electrosynthesis.

The homogeneity and distribution of particles in the catalyst layer were examined by bright-field microscopy of cross sections. This revealed particles were distributed rather evenly and particles of elemental Bi became slightly porous after electrolysis. Density measurements of the GDEs showed reduction of Bi_2O_3 to Bi decreased density and thus likely increased porosity, as expected.

For initial evaluation of the different GDEs, they were applied for electrosynthesis of formate at constant current density of 150 mA cm^{-2} for 21 h (n = 3, respectively). Electrosynthesis was carried out in a gas-fed flow cell (5 cm^2 GDE, anolyte and catholyte were circulated and separated by a CEM) using 0.2 mol L^{-1} KH_2PO_4 / K_2HPO_4 (equimolar, pH ≈ 6.67) as both anolyte and catholyte. Performance was assessed by total concentration and FE of formate, by comparing synthesis rates of formate after initial conditioning and the end of electrolysis, and energy demand. Thereby, energy demand was only suitable for comparison in relative terms, as the employed screening set-up was not optimised for energy efficiency. The stability of the catalyst materials was also evaluated by quantifying their amount dissolved in the catholyte after electrolysis by ICP-OES. Most criteria of performance were in a similar range for all GDEs, with no consistent trend or correlation with the systematic change in composition being observed. The best overall performance was achieved by the Bi/Bi_2O_3 (80:20) GDE, which was hypothesised to have a favourable porous structure to allow good mass transport. It reached the highest total concentration (501 ± 5 mmol L^{-1}) and FE (90.3 ± 1.2%) of formate, retained most of its initial synthesis rate (about 79%), and consumed the least amount of electric energy (8.37 ± 0.13 kWh kg^{-1} formate). Additionally, the loss of Bi catalyst was among the lowest and overall minor (109 ± 32 µg L^{-1}).

After identifying the best GDE, demonstrative patterns of current density were applied based on intermittent electricity from solar and wind power (n = 3, respectively). The first two patterns examined the repeated adjustment of current density to accommodate periods of low or no availability. Periods of low availability were simulated by repeated hourly alternation between full load (150 mA cm^{-2}) and half load (75 mA cm^{-2}), whereby FE (≈90%) and synthesis rate of formate remained reliably high and stable. This was also the case for similar alternations between full load (150 mA cm^{-2}) and zero load (0 mA cm^{-2}), which simulated periods of no availability. Consequently, electrosynthesis of formate could be flexibly adapted and also turned on and off as required by fluctuating renewable energy sources. The third and last pattern simulated the day-night cycle of electricity demand and generation. Electrosynthesis was carried out for 26 h, whereby full load (150 mA cm^{-2}) was decreased to night load (50 mA cm^{-2}) intermediately (16 h). Although FE and synthesis rate of formate decreased moderately at night load, high FE and stable synthesis rates were retained for intervals at full load. All in all, the developed Bi/Bi_2O_3 (80:20) GDEs showed robust performance with different current patterns, despite adjusting the current density with a steep ramp and without optimising other

operational parameters. However, alternating current generally impaired the stability of the catalyst as the dissolution of Bi was increased, but mostly if the electrosynthesis was shut down completely (0 mA cm^{-2}). This must be addressed to prevent loss of catalyst in the long-term. To this end, the results indicated either a flexible mode of operation with a lower limit of current density, or an optimisation of operational parameters at zero current for long term-stability at intermittent electricity.

ChemSusChem

Research Article
doi.org/10.1002/cssc.202501583

Chemistry Europe
European Chemical Societies Publishing

www.chemsuschem.org

CO_2 Reduction to Formic Acid/Formate by Intermittent Electricity at Bismuth Gas Diffusion Electrodes

Ida Dinges, Siegfried R. Waldvogel, and Markus Stöckl*

To avoid the waste of renewable energy resources beyond demand and grid capacity, innovative gas diffusion electrodes (GDE) for operation at intermittent electricity are presented. They are based on Bi as affordable and nontoxic electrocatalyst, to facilitate decentralized and cost-efficient reduction of CO_2 to formic acid. To develop flexible GDE materials, their catalyst composition is optimized by studying systematically inexpensive Bi/Bi_2O_3 mixtures. During initial evaluation at technically relevant current density (150 mA cm^{-2}, 21 h), the best composition achieve high Faradaic efficiency (FE) (≈90%) and the loss of catalyst is minor. In three demonstrative examples of realistic current patterns based on intermittent electricity, the performance and resilience of the optimized GDE is consistently very good in terms of high FE (≈90%) and stable synthesis rates of formate. However, loss of catalyst is partially increased, especially when GDEs are depolarized between electrolysis phases. Nonetheless, the GDE materials already show robust performances despite swift adjustments of current density (60 s) without any optimization of operational parameters so far. Based on these results, flexible operation of these GDE can be optimized to minimize cathodic corrosion of catalyst at long-term operation, and thus, ultimately evaluate their implementation to valorize intermittent electricity.

1. Introduction

Driven by anthropogenic climate change, the chemical industry needs a transition to renewable energy sources and sustainable feedstocks. Two of the most important renewable energy sources are solar and wind energy, but they only provide intermittent electricity depending on day-night cycles and/or weather conditions. Furthermore, electricity generation based on solar and wind power can exceed demand as well as grid and storage capacity. Therefore, photovoltaics and/or wind turbines have frequently to be taken off the grid, wasting potential energy resources instead of using this surplus of energy. Of course, progress has been made to improve energy storage (e.g., battery systems) and to increase storage capacities in general. However, another attractive option would be to use the fluctuating excess energy with flexible electrosynthesis systems, instead of shutting off renewable energy sources in order to stabilize the grid. This is also in line with the strategy of electrifying chemical processes.[1–3] Furthermore, electrosynthesis can be carried out decentralized at point sources of resources (e.g., local CO_2 emitters) and/or on-site on demand. This offers the unique and attractive opportunity to exploit intermittent electricity directly to generate feedstocks for the chemical industry, which would support its defossilization. To facilitate this, unit capital costs of systems for decentralized on-site applications should be as low as possible to avoid high investment barriers.

To purse this approach, electrochemical reduction of CO_2 is particularly promising, as it works at ambient conditions and would integrate CO_2 as sustainable carbon source toward a circular carbon economy. In addition, several point sources (e.g., flue gas) are available and their use would mitigate CO_2 emissions while avoiding the high costs of direct air capture.[4] Among numerous possible reduction products,[5] formic acid and formate are attractive due to their general importance in various areas, such as textile and leather industries, as preservatives and antibacterial agents and for biological/medical research.[6,7] Furthermore, their electrosynthesis is compelling due to their good storage and transport features, as well as their versatile subsequent applications (e.g., hydrogen source,[8,9] substrate for biosynthesis,[10–12] starting material for performic acid[13,14]). Moreover, electro-synthesized formic acid/formate is considered to become economically viable in the near future.[15,16] For efficient conversion of CO_2 at high current density, suitable electrocatalysts are employed with gas diffusion electrodes (GDE) circumventing the low solubility of CO_2 in aqueous electrolytes (33 mmol L^{-1} at 298 K and 1 atm).[17,18] Of several cathodic electrocatalysts selective for formic acid formation, Bi has received

I. Dinges, S. R. Waldvogel, M. Stöckl
Chemical Technology
DECHEMA Research Institute
Theodor-Heuss-Allee 25, 60486 Frankfurt am Main, Germany
E-mail: markus.stoeckl@dechema.de

I. Dinges, S. R. Waldvogel
Department for Electrosynthesis
Max-Planck-Institute for Chemical Energy Conversion
Stiftstraße 34-36, 45470 Mülheim an der Ruhr, Germany

S. R. Waldvogel
Karlsruhe Institute of Technology
Institute of Biological and Chemical Systems – Functional Molecular Systems (IBCS-FMS)
Kaiserstraße 12, 76131 Karlsruhe, Germany

Supporting information for this article is available on the WWW under https://doi.org/10.1002/cssc.202501583

increasing attention in numerous variations (e.g., nanoparticles, nanosheets, flakes, dendrites) in recent years.[19–21] Besides their selectivity, Bi-based electrocatalysts are promising because Bi is an affordable metal (95 € kg^{-1} standard ingot 15 kg)[22] and is considered nontoxic.[23] As Bi mainly occurs in small amounts in various ores and minerals, it is co-obtained as byproduct of commodity metals (e.g., W, Pb, Zn).[24,25] Global reserves were estimated at 370,000 t in 2017,[26] but Bi is often unreported in the prospection of ores and little data is reported. Consequently, more Bi seems to be available.[24] For some years now, the global production for Bi has been dominated by China and Vietnam.[27] For example, the European Union imported over 90% of Bi from China in 2024.[28] Since the production and export shares of Bi are highly concentrated, this metal is recognized as critical raw material by the European Commission, the United Kingdom, the United States, India, and Australia.[24,25] Nonetheless, there are Bi natural resources on every continent, and thus, sufficient reserves in case of geopolitical uncertainties.

So far, great efforts have already been made in the development of Bi-based catalysts to enable efficient CO_2 reduction to formic acid/formate at high current density (0.5–2 A cm^{-2}) with high Faradaic efficiency (FE) ($\geq$90%)[29–32] and toward continuous production.[33] Elaborate catalysts with finely tailored catalytic sides, facets, and grain boundaries have been developed.[34–36] Thereby, complex engineering of catalyst materials generally increases costs, which would increase unit costs for on-site, decentralized electrosynthesis. Moreover, most elaborate catalysts and electrode materials are developed for continuous operation at constant high current density, neglecting material stability under intermittent electricity/variable current density. However, the latter is prerequisite for the translation into application.

With this in mind, this study concerns the development of cost-efficient, mechanically durable, and chemically stable Bi-based GDEs for flexible operation at intermittent electricity. GDEs were developed systematically varying Bi to Bi_2O_3 ratio. Thereby, elemental Bi was selected because it is the primary version of Bi by refining. In addition, Bi_2O_3 was chosen as precursor (i.e., pore-forming agent) to enhance electrode material performance.[34–36] Details on design strategy are outlined below. As a result, GDEs with an optimized Bi/Bi_2O_3 composition were obtained and subsequently used in flexible electrolysis. Different realistic intermittent electricity scenarios were applied and the efficient and stable electrosynthesis of formate at high FE (≈90%) was successfully demonstrated at such variable current density.

2. Results and Discussion

To identify the best catalyst composition of Bi/Bi_2O_3-based GDEs for electrosynthesis of formate at variable current load, six different compositions were systematically investigated. All fabricated GDEs were first applied for electrosynthesis of formate at constant current density (150 mA cm^{-2}, 21 h) and characterized prior and upon electrolysis. The current density was based on the results of comparable previous studies.[12,14] Subsequently, the best performing GDE was applied for variable CO_2 reduction under various current conditions.

2.1. Fabrication and Characterization of GDE

For GDE design strategy, elemental Bi was selected because it is the main product of global Bi production/refining. Bi_2O_3 was added to it systematically as precatalyst and to act as reductive binder, as it is reduced to Bi during cathodic polarization.[14] Thereby, it will increase the conductivity of the Bi-based GDE by improving interconnectivity of the individual particles, and thus, lower the operational energy demand. This was based on the well-established silver/silver oxide based GDE in chlor-alkali electrolysis.[37,38] Furthermore, Bi_2O_3 likely acts as a pore-forming agent upon reduction,[39] which could also improve mass transport within the GDE. Moreover, Ni foam was chosen as porous support material instead of gas diffusion layers based on carbon, as these are vulnerable to degradation and thus flooding of the GDE.[40]

The full catalyst GDEs were fabricated by heat pressing Bi/Bi_2O_3 onto Ni foam as support material and current collector. This was based on the oxygen depolarized cathode technology developed by Covestro.[37] Each catalyst mixture had the same electrocatalyst to binder weight ratio (87.5:12.5). As relatively inexpensive electrocatalysts, Bi (particle size $\leq$ 40 μm, ≈50 € kg^{-1}) and/or Bi_2O_3 (particle size ≈80 nm, ≈200 € kg^{-1}) were used. Polytetrafluoroethylene (PTFE) powder served as hydrophobic binder (≈50 € kg^{-1}). All materials were used as commercially available (Supporting Information).

In total, three GDEs ($n = 3$) were fabricated for each of the six different compositions of electrocatalyst (Bi/Bi_2O_3). The composition was systemically varied in steps of 20 wt% from pure Bi (dark gray) to pure Bi_2O_3 (yellow). The catalyst loading b (67 ± 3 mg cm^{-2}, Table 2) and thickness d (507 ± 24 μm) of all GDEs were in the same range. Furthermore, no influence of minor variations of the predominantly manual steps of the fabrication method (e.g., distribution of catalyst mixture, handling of the GDE blank, cf. Supporting Information) on GDE performance was observed.

Taking contemporary costs into account, electrocatalyst cost of GDEs increased from 34.3 ± 0.1 € m^{-2} (pure Bi) to 130.5 ± 0.5 € m^{-2} (pure Bi_2O_3). All GDE types were characterized before and after electrolysis (21 h at 150 mA cm^{-2}) by bright-field microscopy of cross sections and measurement of density (**Figure 1**, cf. Supporting Information).

The microscopy images show the distribution of Bi particles (light color due to reflection) with various sizes ($\leq$40 μm) in PTFE binder and/or Bi_2O_3. As Bi_2O_3 particles were a magnitude smaller (≈80 nm), they cannot be distinguished at this resolution. However, areas rich in Bi_2O_3 of the mixed GDE as well as the pure Bi_2O_3 GDE appear relatively homogeneous prior to electrolysis. After electrolysis, most Bi_2O_3 (yellow) was reduced to Bi (dark gray).[14] The nontransparent white binder is visible as cloudy shadow. Noticeably, Bi particles seemed more porous upon

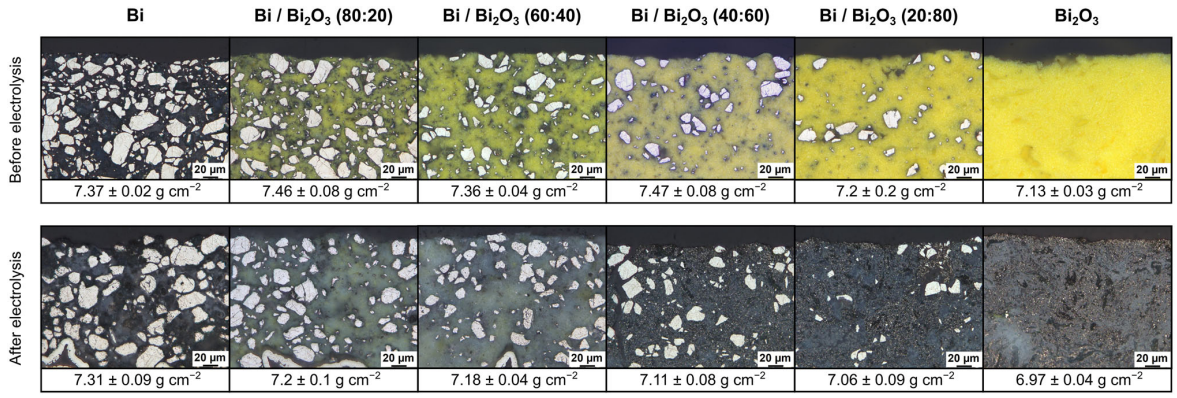

Figure 1. Cross section microscopy image of the catalyst layer and density of fabricated GDE with varying composition for electrosynthesis of formate before and after electrolysis.

electrolysis for each composition, which might indicate cathodic corrosion. Furthermore, some yellow (not reduced) Bi_2O_3 is still visible. This indicates some Bi_2O_3 could have been encapsulated in binder and was not accessible for electrolysis. Furthermore, different shades of gray in the catalyst layer indicate a small degree of inhomogeneity.

To examine stability and electrochemically induced changes of the GDE further, their density was determined with a gas pycnometer. In general, density was up to 4.9% lower after electrolysis. By reduction of Bi_2O_3 to Bi, a small decrease in density was expected. But unexpectedly, the GDE with the highest Bi_2O_3 content did not show the largest decrease in density (2.3%). Since density measurements after electrolysis were conducted with simply air-dried GDE, salt precipitations inside the porous GDE might have increased measured density. Furthermore, density could also have been decreased by loss of Bi due to cathodic corrosion. Hence, electrolytes were examined with inductively coupled plasma optical emission spectroscopy (ICP-OES) after electrolysis.

ICP-OES analysis revealed low concentrations of dissolved Bi and Ni in the catholyte for all catalyst compositions (**Table 1**).

Noticeably, the highest concentration of Bi occurred for GDE with pure Bi as starting material for the electrocatalyst. This agrees with observed cavities in the Bi particles, which made them seem more porous as described above. Consequently, pure Bi particles seemed more affected by cathodic corrosion than Bi originating from the reduction of Bi_2O_3. Furthermore, comparison of Bi/Bi_2O_3 (40:60) and Bi_2O_3 GDE show their cathodic corrosion of Bi was similar and therefore cannot explain the difference in density after electrolysis (4.9% vs. 2.3%). This suggests GDE densities may have been altered by salt precipitates in the GDE pore structures after electrolysis, as mentioned above.

Besides Bi, low concentrations of Ni were found in the catholyte for all catalyst compositions. This shows the GDE's support material Ni foam was in contact with catholyte and was slightly affected by cathodic corrosion, respectively. Noticeably, the highest concentration of Ni (Bi/Bi_2O_3, 20:80 GDE) did not coincide with the highest concentration of Bi (pure Bi GDE).

Nonetheless, the overall concentrations of Bi and Ni were rather low. Hence, no catalyst composition was significantly affected by cathodic corrosion and the respective catalyst was rather stable at the electrolysis conditions examined (21 h at 150 mA cm^{-2}). The GDEs' lifespan beyond the presented runtimes were not evaluated.

To summarize, density and cathodic corrosion of the six types of GDE were altogether similar, although their cross sections before and after electrolysis showed significant differences. Accordingly, greater differences in performance were expected during electrolysis. The electrolysis results are discussed in the following chapter to evaluate GDE performance.

Table 1. Concentrations of Bi^{3+} and Ni^{2+} in the catholyte after electrosynthesis of formate ($n = 3$) determined via ICP-OES.

Catalyst composition of GDE	$c(Bi^{3+})$ [µg L^{-1}]	$c(Ni^{2+})$ [µg L^{-1}]
Bi	342 ± 212[a)]	25 ± 6
Bi/Bi_2O_3 (80:20)	109 ± 32[a)]	20 ± 3
Bi/Bi_2O_3 (60:40)	101 ± 9	55 ± 7
Bi/Bi_2O_3 (40:60)	117 ± 13	60 ± 16
Bi/Bi_2O_3 (20:80)	86 ± 9	89 ± 20
Bi_2O_3	112 ± 14	52 ± 5

[a)] ($n = 2$), excluding outlier (see Supporting Information).

2.2. Electrosynthesis of Formate at Constant Current Density

Electrosynthesis of formate was carried out in a gas-fed flow reactor (5 cm^2 GDE, anolyte, and catholyte were circulated and separated by a cation exchange membrane, Section S1.3, Supporting Information) using 0.2 mol L^{-1} KH_2PO_4/K_2HPO_4 (equimolar, pH ≈ 6.67) as both anolyte and catholyte. Phosphate buffer was chosen as supporting electrolyte based on promising results in previous studies.[11,12,14] To evaluate performance of the six different GDE types, electrolyses were run 21 h at constant current density of 150 mA cm^{-2} ($n = 3$, respectively). The aim was to achieve and maintain high FE (>85%) and stable synthesis rates

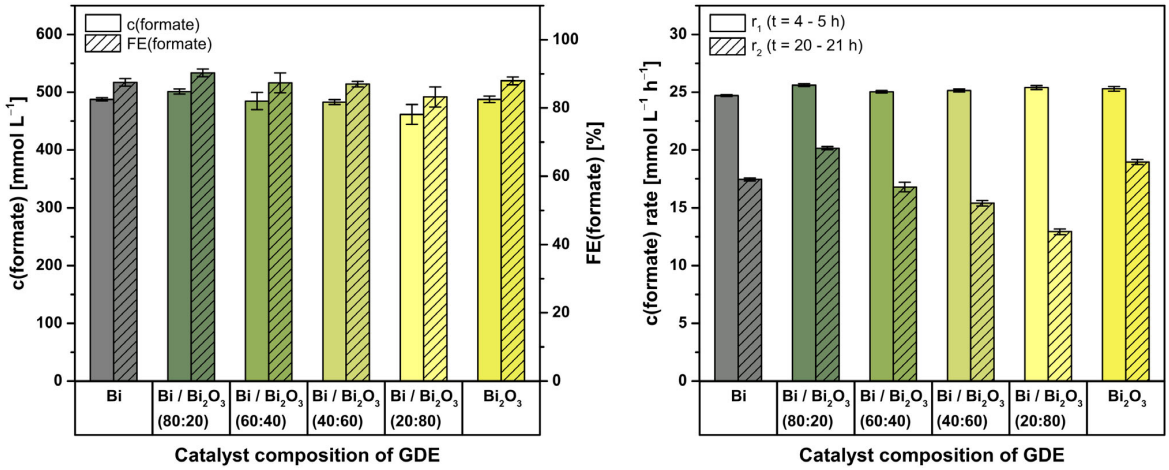

Figure 2. Final concentration and corresponding FE of formate (right) and formate synthesis rates (left) for the six different catalyst compositions of GDE ($n = 3$, respectively). Electrolysis parameters: Constant current density $j = 150$ mA cm^{-2}, runtime = 21 h (≙ 56 700 C), electrolyte = 0.2 mol L^{-1} KH_2PO_4/K_2HPO_4, initial V (catholyte, anolyte) = 500 mL each, membrane = Nafion 424, cathode (GDE, 5 cm^2) = 87.5 wt% Bi and/or Bi_2O_3 (composition specified in graph), 12.5 wt% PTFE on Ni foam, reference electrode = RHE, anode = mixed Ir-oxide on a Ti-grid (Platinode EP, Type 177, Umicore).

for formate. Catholyte samples were taken every hour to determine concentration and FE of formate and additionally every 15 min in two intervals to determine formate synthesis rates. The first interval (4–5 h) was after initial conditioning of the GDE to ensure electrochemical reduction of Bi_2O_3 was complete and electrowetting of the GDE was relatively stable. The second interval (20–21 h) was in the last hour of the electrolysis to assess stability of synthesis rates. Detailed courses of the individual electrolysis are provided in the Supporting Information Section S3.1. By screening the catalyst composition as described above, the least expensive composition for efficient electrosynthesis of formate was determined. The results of the six GDE types are summarized and discussed below.

Figure 2 depicts an overview of total concentration and FE after electrolysis and synthesis rates of formate (4–5 and 20–21 h, respectively) for the six different GDE types.

Generally, final concentration of formate was 484 ± 13 mmol L^{-1} for all different GDEs ($n = 18$), which was accompanied by corresponding FE of 87.3 ± 2.3%. Despite significant differences in characteristics before electrolysis (Figure 1), GDEs based on pure Bi (488 ± 3 mmol L^{-1}, 87.5 ± 1.1%) performed just as well as those based on pure Bi_2O_3 (488 ± 6 mmol L^{-1}, 88.0 ± 1.2%). However, mixtures of Bi and Bi_2O_3 yielded slightly different results. Thereby, no uniform trend or correlation of concentration and FE with the systematic change in composition was discernible. Of the four mixed catalyst compositions, three yielded lower concentrations, and thus, FE than pure Bi or Bi_2O_3 GDEs. Furthermore, results of Bi/Bi_2O_3 (60:40) and Bi/Bi_2O_3 (20:80) GDEs had relatively high standard deviations. This comparatively lower reproducibility could be due to the lower mechanical stability of these GDE compositions.

In contrast, Bi/Bi_2O_3 (80:20) GDEs achieved the best results in terms of total concentration (501 ± 5 mmol L^{-1}) and FE (90.3 ± 1.2%) of formate. In all instances, FE balance was most likely closed by the parasitic hydrogen evolution reaction (HER) as main side reaction, which is also favored by the increasingly acidic pH during electrolysis.[12,14]

To evaluate performance stability of the GDEs, synthesis rates of formate were compared after conditioning of the GDE ($t = 4$–5 h) and at the end of electrolysis ($t = 20$–21 h). Generally, synthesis rates of formate after conditioning (r_1) were relatively similar for all catalyst compositions (25.2 ± 0.4 mmol L^{-1} h^{-1}, $n = 18$). Thereby, synthesis rate (r_1) of Bi GDE was the lowest (24.71 ± 0.09 mmol L^{-1} h^{-1}), whereas Bi/Bi_2O_3 (80:20) GDE was the highest (25.62 ± 0.12 mmol L^{-1} h^{-1}). However, synthesis rates of formate (r_2) generally declined at the end of electrolysis (16.9 ± 2.6 mmol L^{-1} h^{-1}, $n = 18$) and differed significantly depending on the composition of the catalyst. In contrast to similar total concentration and FE of formate, the synthesis rate (r_2) of GDEs based on pure Bi (17.45 ± 0.14 mmol L^{-1} h^{-1}) was slightly lower than the one based on pure Bi_2O_3 (19.0 ± 0.3 mmol L^{-1} h^{-1}). As before, there was no uniform trend/correlation between synthesis rate (r_2) and systematic increase of Bi_2O_3 in the catalyst composition of the GDEs. Out of all catalyst compositions, Bi/Bi_2O_3 (80:20) GDEs (20.16 ± 0.14 mmol L^{-1} h^{-1}) had the highest synthesis rate (r_2) and thus maintained most of its initial performance (79%). The general decline in synthesis rate (r_1 vs. r_2) could be attributed to an increased influence of HER during electrolysis. This could be caused by, for example, either presumed formate mass transport limitations within the GDE's pore system or the increasingly acidic pH during electrolysis (Section S3.1, Supporting Information). Moreover, the employed set-up was optimized for screening and not yet for continuous synthesis of formate with concentrations above 500 mmol L^{-1}. However, the strong relative differences of r_2 could be attributed to presumably different pore structures due to varying content of Bi_2O_3 as pore-forming agent. Thereby, Bi/Bi_2O_3 (80:20) seemed to have the best porous

Table 2. Overview of catalyst loading, catalyst cost and energy demand for electrosynthesis of formate at constant current density (150 mA cm^{-2}, 21 h) with GDEs of variable catalyst composition ($n = 3$, respectively).

Catalyst composition of GDE	Catalyst loading[a] [mg cm^{-2}]	GDE catalyst[a] cost [€ m^{-2}]	U[b] [V]	E(GDE)[b] [V]	EEC [kWh kg^{-1}]
Bi	68.6 ± 0.2	34.3 ± 0.1	6.63 ± 0.06	-1.7 ± 0.1	8.84 ± 0.05
Bi/Bi_2O_3 (80:20)	69 ± 1	55.5 ± 0.1	6.48 ± 0.06	-1.6 ± 0.1	8.37 ± 0.13
Bi/Bi_2O_3 (60:40)	70 ± 2	76.6 ± 2.2	6.47 ± 0.01	-1.5 ± 0.1	8.6 ± 0.3
Bi/Bi_2O_3 (40:60)	67.1 ± 0.8	94.0 ± 1.1	6.44 ± 0.08	-1.7 ± 0.3	8.63 ± 0.15
Bi/Bi_2O_3 (20:80)	63.3 ± 1.1	107.7 ± 1.8	6.3 ± 0.2	-1.37 ± 0.14	8.79 ± 0.34
Bi_2O_3	65.3 ± 0.3	130.5 ± 0.5	6.4 ± 0.3	-1.52 ± 0.13	8.55 ± 1.5

[a]Bi and/or Bi_2O_3; [b]Average of 21 h runtime, without compensation for *iR* losses.

structure to allow good mass transport, as r_2 was highest here. In regard of total concentration, FE and synthesis rates of formate, Bi/Bi_2O_3 (80:20) was the most promising composition of catalyst for electrosynthesis of formate.

In addition to FE and synthesis rate, energy demand was also considered to determine the overall most efficient GDE (**Table 2**). Electrolyses were run with an average cell voltage of 6.46 ± 0.12 V for all different compositions of catalyst ($n = 18$). The generally relatively high cell voltage was mainly caused by ohmic losses in the anode compartment, as a nonzero gap anode (mixed Ir-oxide on a Ti-grid) was used for the oxygen evolution reaction as counter reaction of CO_2 reduction to formate (cf. Supporting Information). Accordingly, the average potential of GDEs was only -1.57 ± 0.14 V versus reversible hydrogen electrode (RHE) for all different compositions of catalyst ($n = 18$). Thereby, stepwise addition of Bi_2O_3 as a reductive binder did not lead to the presumed stepwise lowering of GDE potential/increase in conductivity of the GDE (Section S3.1, Supporting Information). Overall, the employed set-up was not yet optimized for energy efficiency, which offers opportunities to reduce the required cell voltage greatly (e.g., membrane electrode assembly[41,42]). Therefore, assessment of energy cost was mainly used to compare the different GDEs in relative terms herein. To determine the composition with the highest energy efficiency, electric energy consumption (EEC) for electrosynthesis of formate was calculated (Table S2 and Equation S2, Supporting Information). Generally, EEC of formate was 8.64 ± 0.17 k Wh kg^{-1} for all different compositions of catalyst ($n = 18$), which corresponded to an energy cost for formate of 1.55 ± 0.04 € kg^{-1} (no downstream processing etc., 0.1800 € kWh^{-1}[43]). The assessment revealed Bi/Bi_2O_3 (80:20) enabled the most energy efficient (8.37 ± 0.13 k Wh kg^{-1}) and thus least expensive (1.51 ± 0.03 € kg^{-1}) electrosynthesis of formate. In comparison, all energy costs of formate were higher than market prices for fossil-based concentrated formic acid, such as 0.37 and 0.69 € kg^{-1} (0.40[44] and 0.74 \$ kg^{-1},[45] respectively with 1 € ≙ 1.08 \$). However, they were already in a reasonable order of magnitude.

All in all, the variation of catalyst composition demonstrated mixtures of Bi/Bi_2O_3 can improve electrosynthesis of formate compared to pure Bi or Bi_2O_3 as electrocatalyst. Among the examined compositions, the second least expensive Bi/Bi_2O_3 (80:20) GDE was the best in terms of total concentration as well as FE of formate, stability of formate synthesis rate, and energy demand. Additionally, stability of these GDEs was sufficient as cathodic corrosion was minor at the applied conditions, as discussed previously (Table 1). Consequently, it was applied for the following electrolyses at variable current density to finally assess the possible use intermittent electricity.

2.3. Electrosynthesis of Formate at Variable Current Density

After identifying Bi/Bi_2O_3 (80:20) GDEs as most promising, their operation was investigated at variable current density based on realistic patterns of intermittent electricity (solar and wind power).[46] To utilize intermittent electricity with GDEs, they need to be reliably operated at variable current densities while maintaining high FE, and since intermittent electricity fluctuates on a fairly short time scale (≈20 min), GDEs should be robust enough to adjust current density quickly. Ideally, electrosynthesis could be turned on and off repeatedly without compromising GDE performance to accommodate periods of low availability. To examine whether Bi/Bi_2O_3 (80:20) GDEs meet these requirements or not, three patterns of variable current density were applied for electrosynthesis of formate ($n = 3$, respectively). Briefly, the first two concern the repeated adjustment of current density to low or no availability of solar and wind energy, whereas the third simulates the day–night cycle of solar energy.

Figure 3 depicts the first two courses of variable current density alongside total concentration/FE and synthesis rates of formate in the catholyte. In both cases, electrolysis was run at constant current density of 150 mA cm^{-2} (full load) for the first five hours to condition the GDE (as before during catalyst evaluation). Furthermore, the first synthesis rates of formate (r_1, $t = 4$–5 h) were compared after conditioning to ensure initial performance of the GDEs were comparable to those of the previous evaluation (Figure 2).

For the first pattern, current density was hourly alternated three times between half load (75 mA cm^{-2}) and full load (150 mA cm^{-2}) after 5 h conditioning (Figure 3, left). Thereby, current density was adjusted using a relatively fast current ramp (60 s). Moreover, no other operational parameters (e.g., CO_2 overpressure, electrolyte flow rate) were adjusted to examine the electrochemical and mechanical robustness of the GDE. The synthesis rate of formate started out from 25.43 ± 0.08 mmol L^{-1} h^{-1}

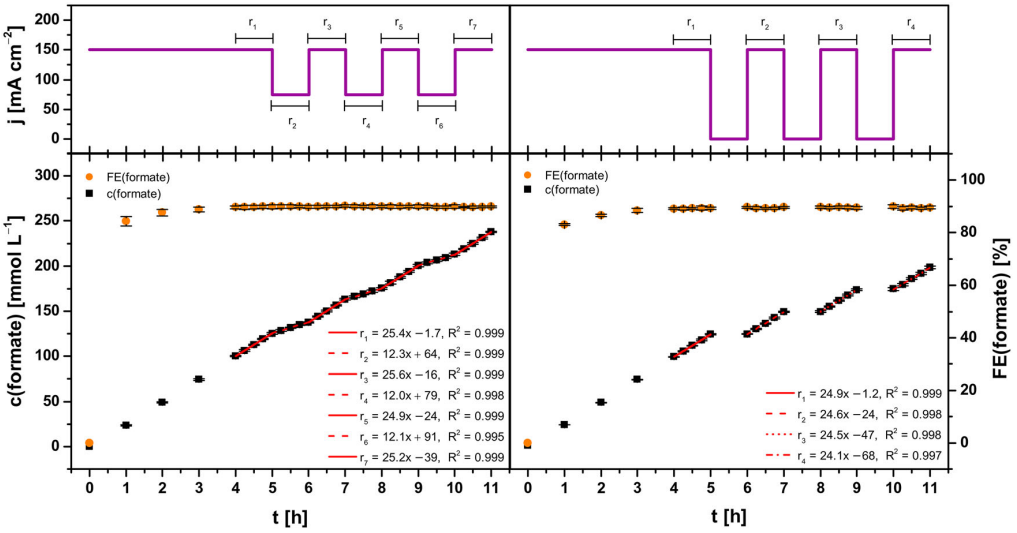

Figure 3. Concentration course and corresponding FE of formate during electrosynthesis at two variable current density patterns. The concentration course was fitted linearly in hourly intervals, respectively. Electrolysis parameters: runtime = 11 h, electrolyte = 0.2 mol L^{-1} KH_2PO_4/K_2HPO_4, initial *V* (catholyte, anolyte) = 500 mL each, membrane = Nafion 424, cathode (GDE, 5 cm^2) = 87.5 wt% Bi/Bi_2O_3 (80:20), 12.5 wt% PTFE on Ni foam, reference electrode = RHE, anode = mixed Ir-oxide on a Ti-grid (Platinode EP, Type 177, Umicore).

(r_1, $t = 4$–5 h) at full load and declined to 12.28 ± 0.12 mmol L^{-1} h^{-1} (r_2, $t = 5$–6 h) in the first interval at half load. Halving the load approximately halved the synthesis rate. In the subsequent interval at full load again, the synthesis rate increased back up to 25.6 ± 0.3 mmol L^{-1} h^{-1} (r_3, $t = 6$–7 h). Remarkably, comparable synthesis rates were also obtained with two further current load alternations.

Hence, alternating current density during electrosynthesis of formate between half (75 mA cm^{-2}) and full load (150 mA cm^{-2}) sustained the formate synthesis rate. This was accompanied by a relatively stable FE (≈90%) for formate throughout electrosynthesis after conditioning, which resulted in a total of 237.3 ± 1.5 mmol L^{-1} formate corresponding to an FE of 91.1 ± 0.5% for 11 h runtime ($n = 3$).

Regarding stability of the GDE, cathodic corrosion of Bi (electrocatalyst) and Ni (support material) were investigated as before using ICP-OES (**Table 3**). Analysis of the catholytes revealed the concentration of Bi was higher (≈55%) than for electrolyses at constant current density (Table 1). In terms of molar amounts (considering the increase in catholyte volume after electrolysis), 48% more Bi was dissolved from the GDE at alternating (full and half load) than at constant current density. Consequently, employing the first current density pattern for GDE operation led to more cathodic corrosion of Bi, although absolute values remained relatively low. In contrast, concentration and molar amount of Ni were similar to the results at constant current density. Overall, electrosynthesis of formate maintained consistently high FE and stable synthesis rates despite switching between full and half load repeatedly, while cathodic corrosion of Bi was slightly increased.

Table 3. Concentration of Bi^{3+} and Ni^{2+} in the catholyte after electrosynthesis of formate ($n = 3$) using Bi/Bi_2O_3 (80:20) based GDE at variable current load determined via ICP-OES.

Current density [mA cm^{-2}]	c(Bi^{3+}) [µg L^{-1}]	c(Ni^{2+}) [µg L^{-1}]
150 ⇌ 75	168 ± 37	27 ± 5
150 ⇌ 0	4416 ± 97	411 ± 97
150 → 50 → 150	134 ± 17	143 ± 63

For the second pattern, current density was hourly alternated three times between zero (0 mA cm^{-2}) and full load (150 mA cm^{-2}) after conditioning (Figure 3, right). As above, current density was adjusted with a steep current ramp (60 s) while no other operational parameters were adjusted throughout. The synthesis rate of formate started out from 24.94 ± 0.07 mmol L^{-1} h^{-1} (r_1, $t = 4$–5 h) at full load. After the first interval at zero load, the synthesis rate increased back up to 24.6 ± 0.5 mmol L^{-1} h^{-1} (r_2, $t = 6$–7 h) at full load again. After the second and third interval at zero load, the synthesis rate declined slightly from 24.5 ± 0.4 mmol L^{-1} h^{-1} (r_3, $t = 8$–9 h) to 24.1 ± 0.7 mmol L^{-1} h^{-1} (r_4, $t = 10$–11 h). Comparing the first and last synthesis rate, the decline was only about 3%. Hence, alternating current density between zero (0 mA cm^{-2}) and full load (150 mA cm^{-2}) impacted the synthesis rate of formate only slightly. Furthermore, FE for formate remained relatively stable throughout electrosynthesis (≈90%) after conditioning. This resulted in a total of 198.1 ± 1.7 mmol L^{-1} formate, which corresponded to 91.0 ± 0.8% FE for 11 h runtime ($n = 3$).

Regarding stability of the GDE, dissolution of Bi and Ni was greatly increased by alternating between zero and full load. The concentration of dissolved Bi in the catholyte (4416 ± 97 µg L^{-1}) was about factor 27 higher than for the first pattern of variable load and factor 40 for electrolyses at constant current density (Table 1). Likewise, the concentration/amount of

dissolved Ni was increased by about factor 20 in comparison to electrolyses without current alternation (Table 1). However, results of the alternation between half and full load indicate the intervals without any current are responsible for the increased dissolution of Bi and Ni instead of cathodic corrosion during full load. Consequently, degradation of the unpolarized GDE occurred most likely and the results cannot be attributed to cathodic corrosion alone.

Nevertheless, the second pattern of current (zero and full load) was suitable for formate electrosynthesis with high FE and relatively constant synthesis rates as well, but demonstrated stability and resilience of GDE could be an important issue in long-term operation.

The third and final pattern of electric current was based on the day–night cycle of electricity generation/demand. **Figure 4** depicts the corresponding course of current density alongside total concentration, FE, and synthesis rates of formate in the catholyte. First, electrolyses were run at constant current density of 150 mA cm^{-2} (full load) for the first five hours as before to condition the GDE. Afterwards, current density was reduced to 50 mA cm^{-2} (night load) for 16 h throughout the night. Finally, current density was increased back up to 150 mA cm^{-2} (full load) until the end of electrolyses. As before, current density was adjusted using a steep current ramp (60 s) while no other operational parameters were adjusted.

The synthesis rate of formate started out from 24.93 ± 0.16 mmol L^{-1} h^{-1} (r_1, $t = 4$–5 h) at full load. Thereby, total FE amounted to 88.6 ± 0.7% for the first interval of runtime at full load ($t = 0$–5 h). After switching to night load ($t = 5$–21 h), the synthesis rate of formate declined to 8.1 ± 0.3 mmol L^{-1} h^{-1} (r_2, $t = 5$–6 h). This was about one third of the previous rate (r_1), as expected at one third of current density. However, the synthesis rate declined throughout 16 h at night load about 20% to

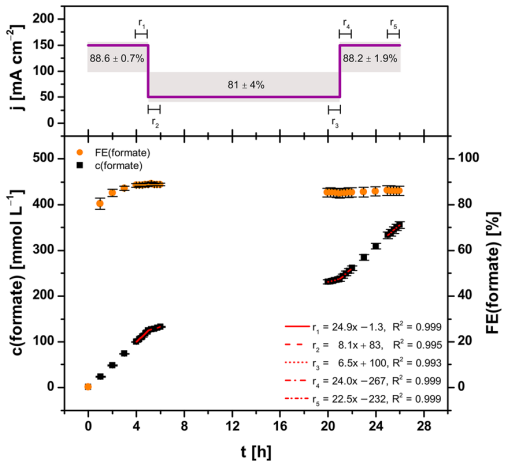

Figure 4. Concentration course and corresponding FE of formate during electrosynthesis at variable current density. The concentration course was fitted linearly in several intervals (r_1 = 4–5 h, r_2 = 5–6 h, r_3 = 20–21 h, r_4 = 21–22 h, r_5 = 25–26 h). Electrolysis parameters: runtime = 26 h, electrolyte = 0.2 mol L^{-1} KH_2PO_4/K_2HPO_4, initial V (catholyte, anolyte) = 500 mL each, membrane = Nafion 424, cathode (GDE, 5 cm^2) = 87.5 wt% Bi/Bi_2O_3 (80:20), 12.5 wt% PTFE on Ni foam, reference electrode = RHE, anode = mixed Ir-oxide on a Ti-grid (Platinode EP, Type 177, Umicore).

6.5 ± 0.3 mmol L^{-1} h^{-1} (r_3, $t = 20$–21 h). Consequently, total FE for the interval at night load was 81 ± 4%, almost 10% lower than for the previous interval at full load. Nonetheless, synthesis rate of formate increased back up to 23.97 ± 0.07 mmol L^{-1} h^{-1} (r_4, $t = 21$–22 h) in the subsequent interval at full load. Taking an increase in catholyte volume throughout runtime into account, r_4 was about the same as the initial r_1. Hence, performance of the GDE at full load remained as good as before, even though it had been operated at lower efficiencies with night load. After a further five hours of operation at full load, the synthesis rate had declined about 6% to 22.5 ± 0.3 mmol L^{-1} h^{-1} (r_5, $t = 25$–26 h). This was attributed to an increased influence of HER, as the buffer capacity was depleted and pH decreased from ≈6.67 to 5.59 ± 0.13 ($n = 3$) during this last interval (Section S3.2, Supporting Information). Since buffer capacity was a systematic limitation of the employed screening set-up, its optimization for continuous electrosynthesis of formate could most likely prevent the decline of synthesis rates. Despite the slight decline of synthesis rate, the total FE for this interval was 88.2 ± 1.9%, which was comparable to the first interval at full load. It follows that operation at full load was not significantly impaired by shifting to night load intermediately for 16 h. However, a decrease in GDE performance was observed during night load, as described above. On the one hand, it could suggest there is a minimum current density for operation of GDE with stable synthesis rates of formate. On the other hand, no operational parameters were adjusted together with current density. Therefore, optimization of operating parameters during night load could possibly stabilize synthesis rates. Nonetheless, the whole electrosynthesis reached a total concentration of 355 ± 8 mmol L^{-1} for formate, which corresponded to a total FE of 85.9 ± 2.1% ($n = 3$).

Regarding stability of the GDE, dissolution of Bi for the day–night cycle was the lowest among all variable current patterns, but slightly higher than at constant current density. In contrast, the concentration of dissolved Ni was the second highest among the current patterns, and about factor 7 higher than at constant current density. Consequently, Ni appeared to be more affected by cathodic corrosion at 50 mA cm^{-2} than Bi, possibly due a probable change of the electrowetting state/three-phase boundary position.

Overall, the third pattern of current (day–night cycle) was suitable for electrosynthesis of formate with high FE (≈88%) and relatively stable synthesis rates, particularly in intervals at full load. Although FE was slightly lower in the night interval and the synthesis rate declined, the GDE performance of the subsequent day interval was as high as before at full load. Furthermore, cathodic corrosion of Bi was only increased slightly by shifting between full and night load.

All in all, the different current patterns demonstrated that Bi/Bi_2O_3 (80:20) GDEs had an overall robust performance as they maintained high FE and relatively stable formate synthesis rates despite alternating current densities. The rapid adjustment of current density with a steep ramp (60 s) did not appear to affect their performance. However, alternating current density generally increased dissolution of Bi, but mostly if the electrolysis was

turned on and completely off again. This suggests either an alternating mode of operation with a lower limit for current density, or an optimization of operational parameters at zero current to prevent loss of catalyst material in the long-term. Additionally, a lower limit for current density was also indicated by the moderate loss of efficiency during night load (50 mA cm^{-2}). Alternatively, the addition of ionomers to the GDE has recently been demonstrated to improve catalyst stability.[47] To examine stability of the GDE at variable current density in the long-term, time-dependent studies should be carried out with a set-up optimized for continuous electrosynthesis of formate employing real intermittent electricity patterns. Thereby, the flexible operation of GDE could be optimized to evaluate an implementation of decentralized utilization of intermittent electricity for CO_2 reduction.

3. Conclusion

To avoid wasting renewable energy resources beyond demand and grid capacity, GDEs for flexible operation at intermittent electricity were successfully established. The GDE materials were based on Bi as inexpensive and relatively abundant electrocatalyst, to facilitate decentralized electrochemical reduction of CO_2 to formic acid. This formic acid or formate can be stored and has versatile applications.

The catalyst composition of the GDE was optimized to Bi/Bi_2O_3 (80:20). It achieved the highest total FE/concentration of formate and the most stable synthesis rates of formate. Additionally, cathodic corrosion of Bi was minor. Without adaption of operational parameters, demonstrative current patterns based on intermittent electricity were applied. The GDE showed overall robust performance despite swift current adjustment. At repeated hourly alternation between full load (150 mA cm^{-2}) and half load (75 mA cm^{-2}), FE and synthesis rate of formate remained reliably high and stable. This was also the case for similar alternations between full load (150 mA cm^{-2}) and zero load (0 mA cm^{-2}). Consequently, electrolysis could be turned on and off flexibly as required by fluctuating renewable energy sources. Furthermore, electrolysis was also adapted to a day–night cycle of energy demand/generation. It was demonstrated for 26 h, whereby, full load (150 mA cm^{-2}) was decreased to night load (50 mA cm^{-2}) intermediately (16 h). Even though performance decreased moderately at night load, the GDE maintained high FE and stable synthesis rates of formate for intervals at full load. Noticeably, dissolution of Bi was only increased if the electrolysis was shut down completely (zero load). This needs to be addressed to prevent loss of catalyst in the long-term. Overall, this study successfully demonstrates the flexible operation of GDE for the reduction of CO_2 and thus hands out their future implementation to use intermittent electricity, support grid stability and a sustainable chemical industry.

Acknowledgements

The authors gratefully acknowledge the Federal Ministry of Research, Technology and Space (03XP0615C and 031B1398F) for financial support. Special thanks go to Daniela Hasenpflug for preparing the cross sections of the GDE.

Open Access funding enabled and organized by Projekt DEAL.

Conflict of Interest

The authors declare no conflict of interest.

Data Availability Statement

The data that support the findings of this study are available in the supplementary material of this article.

Keywords: bismuth · cathode · CO_2 valorization · flexible electricity consumption · formic acid

[1] a) A. Wiebe, T. Gieshoff, S. Möhle, E. Rodrigo, M. Zirbes, S. R. Waldvogel, Electrifying Organic Synthesis, *Angew. Chem. Int. Ed.* **2018**, *57*, 5594; b) A. Wiebe, T. Gieshoff, S. Möhle, E. Rodrigo, M. Zirbes, S. R. Waldvogel, *Angew. Chem.* **2018**, *130*, 5694.
[2] a) S. Möhle, M. Zirbes, E. Rodrigo, T. Gieshoff, A. Wiebe, S. R. Waldvogel, Modern Electrochemical Aspects for the Synthesis of Value-Added Organic Products, *Angew. Chem. Int. Ed.* **2018**, *57*, 6018; b) S. Möhle, M. Zirbes, E. Rodrigo, T. Gieshoff, A. Wiebe, S. R. Waldvogel, *Angew. Chem.* **2018**, *130*, 6124.
[3] D. Pollok, S. R. Waldvogel, Electro-Organic Synthesis – a 21st Century Technique, *Chem. Sci.* **2020**, *11*, 12386.
[4] B. Belsa, L. Xia, V. Golovanova, B. Polesso, A. Pinilla-Sánchez, L. San Martín, J. Ye, C.-T. Dinh, F. P. García De Arquer, Materials Challenges on the path to Gigatonne CO_2 Electrolysis, *Nat. Rev. Mater.* **2024**, *9*, 535.
[5] K. P. Kuhl, E. R. Cave, D. N. Abram, T. F. Jaramillo, New Insights into the Electrochemical Reduction of Carbon Dioxide on Metallic Copper Surfaces, *Energy Environ. Sci.* **2012**, *5*, 7050.
[6] V. Theußl, S. Sanz, K. Von Foerster, B. Rutjens, H. Weinrich, H. Tempel, R. A. Eichel, Technological Advances in the Electroreduction of CO_2 to HCOOH: The Impact of Catalyst, Gas Diffusion Electrode, and Cell Design, *Electrochem. Sci. Adv.* **2024**, e202400014, https://doi.org/10.1002/elsa.202400014.
[7] J. Hietala, A. Vuori, P. Johnsson, I. Pollari, W. Reutemann, H. Kieczka, *ULLMANN'S Encyclopedia Of Industrial Chemistry*, 1st ed, Wiley, Weinheim **2016**, pp. 1–22.
[8] K. Tedsree, T. Li, S. Jones, C. W. Chan, K. M. Yu, P. A. Bagot, E. A. Marquis, G. D. Smith, S. C. Tsang, Hydrogen Production from Formic Acid Decomposition at Room Temperature using a Ag–Pd Core–Shell Nanocatalyst, *Nat. Nanotechnol.* **2011**, *6*, 302.
[9] M. Grasemann, G. Laurenczy, Formic Acid as A Hydrogen Source – Recent Developments and Future Trends, *Energy Environ. Sci.* **2012**, *5*, 8171.
[10] R. Hegner, K. Neubert, C. Kroner, D. Holtmann, F. Harnisch, Coupled Electrochemical and Microbial Catalysis for the Production of Polymer Bricks, *ChemSusChem* **2020**, *13*, 5295.
[11] M. Stöckl, S. Harms, I. Dinges, S. Dimitrova, D. Holtmann, From CO_2 to Bioplastic – Coupling the Electrochemical CO_2 Reduction with a Microbial Product Generation by Drop-in Electrolysis, *ChemSusChem* **2020**, *13*, 4086.
[12] I. Dinges, I. Depentori, L. Gans, D. Holtmann, S. R. Waldvogel, M. Stöckl, Coupling of CO_2 Electrolysis with Parallel and Semi-Automated Biopolymer Synthesis – Ex-Cell and without Downstream Processing, *ChemSusChem* **2024**, *17*, e202301721.
[13] S. Schneider, M. Stöckl, General Route to Indirect and On-Demand Electrosynthesis of (Various) Peroxy Acids via In Situ Generated Hydrogen Peroxide on a Gas Diffusion Electrode, *ACS Sustainable Chem. Eng.* **2024**, *12*, 5160.
[14] I. Dinges, M. Pyschik, J. Schütz, S. Schneider, E. Klemm, S. R. Waldvogel, M. Stöckl, All Electrochemical Synthesis of Performic Acid Starting from CO_2, O_2, and H_2O, *ChemSusChem* **2025**, *18*, e202500180.

[15] M. G. Kibria, J. P. Edwards, C. M. Gabardo, C. T. Dinh, A. Seifitokaldani, D. Sinton, E. H. Sargent, Electrochemical CO_2 Reduction into Chemical Feedstocks: From Mechanistic Electrocatalysis Models to System Design, *Adv. Mater.* **2019**, *31*, 1807166.
[16] H. Shin, K. U. Hansen, F. Jiao, Techno-economic Assessment of Low-Temperature Carbon Dioxide Electrolysis, *Nat. Sustainability* **2021**, *4*, 911.
[17] S. Malkhandi, B. S. Yeo, Electrochemical Conversion of Carbon Dioxide to High Value Chemicals Using Gas-Diffusion Electrodes, *Curr. Opin. Chem. Eng.* **2019**, *26*, 112.
[18] B. J. M. Etzold, U. Krewer, S. Thiele, A. Dreizler, E. Klemm, T. Turek, Understanding the Activity Transport Nexus in Water and CO_2 Electrolysis: State of the Art, Challenges and Perspectives, *Chem. Eng. J.* **2021**, *424*, 130501.
[19] X.-D. Liang, N. Tian, S.-N. Hu, Z.-Y. Zhou, S.-G. Sun, Recent Advances of Bismuth-Based Electrocatalysts for CO_2 Reduction: Strategies, Mechanism and Applications, *Mater. Rep. Energy* **2023**, *3*, 100191.
[20] N. Sabouhanian, J. Lipkowski, A. Chen, Unveiling the Potential of Bismuth-Based Catalysts for Electrochemical CO_2 Reduction, *Ind. Chem. Mater.* **2025**, *3*, 131.
[21] D. Song, S. Zhang, M. Zhou, M. Wang, R. Zhu, H. Ning, M. Wu, Advances in the Stability of Catalysts for Electroreduction of CO_2 to Formic Acid, *ChemSusChem* **2024**, *17*, e202301719.
[22] Haines & Maassen Metallhandelsgesellschaft Personal communication **2025**.
[23] R. Mohan, *Nat. Chem.* **2010**, *2*, 336.
[24] X. Liu, S. Handschuh-Wang, Bismuth – Production, Market and Price Development, and Applications, *Can. Metall. Q.* **2025**, 1, https://doi.org/10.1080/00084433.2025.2465085.
[25] E. Deady, C. Moon, K. Moore, K. M. Goodenough, R. K. Shail, Bismuth: Economic Geology and Value Chains, *Ore Geol. Rev.* **2022**, *143*, 104722.
[26] Bismuth Statistics and Information | U.S. Geological Survey, https://www.usgs.gov/centers/national-minerals-information-center/bismuth-statistics-and-information, (accessed: May 2025)
[27] British Geological Survey - Latest mineral production statistics for 2019 to 2023, https://www.bgs.ac.uk/news/latest-mineral-production-statistics-for-2019-to-2023-released/, (accessed: May 2025)
[28] UN Comtrade, https://comtradeplus.un.org/TradeFlow?Frequency=A&Flows=M&CommodityCodes=810600&Partners=0&Reporters=all&period=2024&AggregateBy=none&BreakdownMode=plus, (accessed: May 2025)
[29] Z. Jiang, S. Ren, X. Cao, Q. Fan, R. Yu, J. Yang, J. Mao, pH-Universal Electrocatalytic CO_2 Reduction with Ampere-Level Current Density on Doping-Engineered Bismuth Sulfide, *Angew. Chem. Int. Ed.* **2024**, *63*, e202408412.
[30] Q. Huang, Z. Qian, N. Ye, Y. Tan, M. Li, M. Luo, S. Guo, In Situ Reconstructed Hydroxyl-Rich Atomic-Thin $Bi_2O_2CO_3$ Enables Ampere-Scale Synthesis of Formate from CO_2 with Activated Water Dissociation, *Adv. Mater.* **2025**, *37*, 2415639.
[31] S. He, F. Ni, Y. Ji, L. Wang, Y. Wen, H. Bai, G. Liu, Y. Zhang, Y. Li, B. Zhang, H. Peng, The p-Orbital Delocalization of Main-Group Metals to Boost CO_2 Electroreduction, *Angew. Chem. Int. Ed.* **2018**, *57*, 16114.
[32] T. Fan, W. Ma, M. Xie, H. Liu, J. Zhang, S. Yang, P. Huang, Y. Dong, Z. Chen, X. Yi, Achieving High Current Density for Electrocatalytic Reduction of CO_2 to Formate on Bismuth-Based Catalysts, *Cell Rep. Phys. Sci.* **2021**, *2*, 100353.
[33] K. Fernández-Caso, G. Díaz-Sainz, M. Alvarez-Guerra, A. Irabien, Electroreduction of CO_2: Advances in the Continuous Production of Formic Acid and Formate, *ACS Energy Lett.* **2023**, *8*, 1992.
[34] L. Li, D.-K. Ma, F. Qi, W. Chen, S. Huang, Bi Nanoparticles/Bi_2O_3 Nanosheets with Abundant Grain Boundaries for Efficient Electrocatalytic CO_2 Reduction, *Electrochim. Acta* **2019**, *298*, 580.
[35] L. Li, S. Yao, Y. Feng, Z. Gao, J. Wang, P. Yin, H. Liu, Z. Zhang, Grain Boundary-Induced Stabilization of Bi^{3+}/Bi^0 Coexistence in β-Bi_2O_3 for Highly Efficient Electrochemical CO_2 Reduction to Formate, *Appl. Catal. B Environ. Energy* **2025**, *372*, 125302.
[36] P. Lei, S. Liu, Q. Wen, J. Y. Wu, S. Wu, X. Wei, R. Feng, X. Z. Fu, J. L. Luo, "Two-in-One" Strategy for High-Rate Electrocatalytic CO_2 Reduction to Formate, *Angew. Chem. Int. Ed.* **2025**, *64*, e202415726.
[37] J. Kintrup, M. Millaruelo, V. Trieu, A. Bulan, E. S. Mojica, Gas Diffusion Electrodes for Efficient Manufacturing of Chlorine and Other Chemicals, *Electrochem. Soc. Interface* **2017**, *26*, 73.
[38] A. Bulan, J. Kintrup, R. Weber, Gas diffusion electrode and method for its production, EP2398101 **2011**.
[39] Y. Pang, R. Xie, H. Xie, S. Lan, T. Jiang, G. Chai, Porous Bi Nanosheets Derived from β-Bi_2O_3 for Efficient Electrocatalytic CO_2 Reduction to Formate, *ACS Appl. Mater. Interfaces* **2024**, *16*, 42109.
[40] H. Rabiee, B. Ma, Y. Yang, F. Li, P. Yan, Y. Wu, X. Zhang, S. Hu, H. Wang, L. Ge, Z. Zhu, Advances and Challenges of Carbon-Free Gas-Diffusion Electrodes (GDEs) for Electrochemical CO_2 Reduction, *Adv. Funct. Mater.* **2025**, *35*, 2411195.
[41] Z. Zhang, X. Huang, Z. Chen, J. Zhu, B. Endrődi, C. Janáky, D. Deng, Membrane Electrode Assembly for Electrocatalytic CO_2 Reduction: Principle and Application, *Angew. Chem. Int. Ed.* **2023**, *62*, e202302789.
[42] M. Stöckl, N. Claassens, S. Lindner, E. Klemm, D. Holtmann, Coupling Electrochemical CO_2 Reduction to Microbial Product Generation – Identification of the Gaps and Opportunities, *Curr. Opin. Biotechnol.* **2022**, *74*, 154.
[43] Electricity prices for non-household customers: Germany, half-years, annual consumption classes, price types, https://www-genesis.destatis.de/datenbank/online/statistic/61243/table/61243-0005, (accessed: May 2025)
[44] M. Solakidou, A. Gemenetzi, G. Koutsikou, M. Theodorakopoulos, Y. Deligiannakis, M. Louloudi, Cost Efficiency Analysis of H_2 Production from Formic Acid by Molecular Catalysts, *Energies* **2023**, *16*, 1723.
[45] M. Jouny, W. Luc, F. Jiao, General Techno-Economic Analysis of CO_2 Electrolysis Systems, *Ind. Eng. Chem. Res.* **2018**, *57*, 2165.
[46] SMARD | Market data visuals, provided by the German Federal Network Agency for Electricity, Gas, Telecommunications, Posts and Railway, https://www.smard.de/en, (accessed: January 2025)
[47] J. A. Abarca, L. Warmuth, A. Rieder, A. Dutta, S. Vesztergom, P. Broekmann, A. Irabien, G. Díaz-Sainz, GDE Stability in CO_2 Electroreduction to Formate: The Role of Ionomer Type and Loading, *ACS Catal.* **2025**, *15*, 8753.

Manuscript received: July 24, 2025
Revised manuscript received: August 20, 2025
Version of record online:

3.2 Formate for Biosynthesis of Polyhydroxybutyrate

A manuscript was published on this section:

Ida Dinges, Ina Depentori, Lisa Gans, Dirk Holtmann, Siegfried R. Waldvogel, Markus Stöckl, Coupling of CO_2 Electrolysis with Parallel and Semi-Automated Biopolymer Synthesis – Ex-Cell and without Downstream Processing, *ChemSusChem* **2024**, *17*, e202301721.
DOI: 10.1002/cssc.202301721

Explanation of my contribution:

The project was conceptualised by M.S., D.H. and me. I performed the experimental work to generate formate feedstock (fabrication of GDEs, optimisation experiments, electrosynthesis of formate, ICP-OES and HPLC measurements) and analysed the data. I.D. performed the experimental work regarding biosynthesis of PHB (optimisation experiments, operation of the bioreactors, analysis of PHB). L.G. supported I.D. in establishing the bioreactor set-up. I analysed all data and carried out the process evaluation. The manuscript was written by me with support of M.S., D.H. and S.R.W. The work was carried out under the supervision of M.S. and S.R.W.

As discussed above (*cf.* section 1.2.3), *eCO$_2$RR* to formic acid/formate can be coupled with microbial synthesis of PHB by *C. necator* without intermediate processing of the formate feedstock. This was initially demonstrated by *Stöckl et al.*[166] on small laboratory scale, but with relatively low yields for both subprocesses and thus the overall process (about 12%). The formate was electrosynthesised by *eCO$_2$RR* at low current density (50 mA cm^{-2}) and accumulated in a biocompatible catholyte based on phosphates, achieving relatively low concentration (≈94 mmol L^{-1}) and FE (≈50%). This catholyte was then used as incubation medium without processing for microbial synthesis of PHB with *C. necator* (wildtype) in shake flasks, leading to complete consumption of its formate content with a low yield of PHB (≈24%).

To improve the overall process and transfer biosynthesis to a scalable system, both *eCO$_2$RR* and microbial synthesis of PHB were optimised and their coupling harmonised. Therefore, three biocompatible phosphate buffers with different contents of K^+ and Na^+ were examined as both supporting electrolyte and incubation medium: (A) KH_2PO_4 / K_2HPO_4, (B) NaH_2PO_4 / K_2HPO_4, and (C) NaH_2PO_4 / Na_2HPO_4, (equimolar and 0.2 mol L^{-1}, respectively). They were derived from the initial coupling and the usual incubation medium of *C. necator* (wildtype).

Electrosynthesis of formate was mainly optimised by application of further developed GDEs based on Sn (*cf.* table 3.1, stage III). They were fabricated by heat pressing catalyst mixture onto Ni foam as support material. Electrosynthesis was carried out at 150 mA cm^{-2} for 22 h in a gas-fed flow cell (5 cm^2 GDE, anolyte and catholyte were circulated and separated by a CEM) using either phosphate buffer (A), (B) or (C) as both anolyte and catholyte ($n \geq 3$, respectively). Formate was accumulated in the catholyte, which was intended as a concentrated feed for semi-automated synthesis of PHB. Both phosphate buffer (A) and (B) resulted in similar high concentration (≥441 mmol L^{-1}) and FE (≥76%) of formate, whereas results for (C) were noticeably lower (≈358 mmol L^{-1}, 63%). Gas chromatography detected hydrogen from HER as main byproduct in all instances, which probably closed FE balances. In addition, the stability of the GDE was relatively high as only minor concentrations of Sn were detected by ICP-OES in all different catholytes after electrosynthesis. Therefore, no negative effects on microbial synthesis of PHB were expected. Compared to the initial coupling,[166] concentration and FE of formate could be significantly improved at tripled current density while maintaining biocompatible electrolytes.

Microbial synthesis of PHB with *C. necator* (wildtype) was first optimised in shake flasks by systematically varying the formate concentration in range of 0-100 mmol L^{-1} in all three phosphate buffers (n = 3, respectively). The range of formate concentration was selected based on previous results.[166] Thereby, criteria for evaluation were the total concentration of PHB and the amount of PHB per consumed formate in 4 h of incubation at low optical density (OD ≙ turbidity as measure for concentration of microorganisms). The highest concentration of PHB (43.8 ± 3.0 mg L^{-1} OD^{-1}) coincided with the highest amount of PHB per formate (18.6 ± 1.0 mg g^{-1}) and was achieved in buffer (B) with 21 mmol L^{-1} formate. Consequently, buffer (B) was chosen for the next generation coupling of *eCO₂RR* to formate with microbial synthesis of PHB (at 21 mmol L^{-1} formate).

The next generation coupling was carried out on larger laboratory scale in four parallelised semi-automated bioreactors (increased by factor ≈10 compared to shake flasks) with continuous feed of formate-containing catholyte. The catholyte was generated by six individual electrolyses with both high concentration (441 ± 9 mmol L^{-1}) and FE (76.6 ± 1.4%) of formate. The incubations were conducted with *C. necator* (wildtype) and were entirely based on formate from electrosynthesis. Throughout 7.5 h of incubation, the concentration of formate strongly deviated from the target concentration (21 mmol L^{-1}), as the feed could only be adjusted hourly due to time-consuming offline analysis of samples. This must be addressed to ensure optimal availability of formate for PHB synthesis in the future. Nevertheless, a relatively high concentration of PHB (63 ± 6 mg L^{-1} OD^{-1}) and amount of PHB per formate (16.5 ± 4.0 mg g^{-1}) were achieved at one of the highest synthesis rates reported at that time (8.4 ± 2.1 mg L^{-1} OD^{-1} h^{-1}). According to the metabolism of *C. necator*,[195] the

yield of PHB was relatively low (29.1 ± 7.1%), probably due to the challenging feed adjustment, but slightly improved compared to the initial coupling.

Finally, the overall process was balanced and critically assessed in terms of yield and energy cost. The improved yields in electrosynthesis (76.6 ± 1.4%) and synthesis of PHB (29.1 ± 7.1%) resulted in an almost doubled yield for the overall process (22.3 ± 5.5%) compared to the initial coupling (12%). The costs of electric energy of formate (1.88 ± 0.08 € kg^{-1}) and PHB (114 ± 19 € kg^{-1}) were assessed under recent and realistic assumptions (0.182 € kWh^{-1}[196]). On the one hand, this showed the energy costs of formate were already in the right order of magnitude but still need to be improved compared to the market prices for fossil-based formic acid, which are about 3-5 times lower and already include all costs beyond electricity. On the other hand, this highlighted the model organism *C. necator* must be either genetically modified or replaced with a more efficient production strain to improve formate-based synthesis of PHB and thus its energy cost. The critical assessment of the entire process also showed coupling *eCO_2RR* to formate with biosynthesis of PHB in a scalable system is feasible without intermediate processing of the formate feed and should be explored further.

ChemSusChem

Research Article
doi.org/10.1002/cssc.202301721

Chemistry Europe
European Chemical Societies Publishing

www.chemsuschem.org

Coupling of CO_2 Electrolysis with Parallel and Semi-Automated Biopolymer Synthesis – Ex-Cell and without Downstream Processing

Ida Dinges,[a, b] Ina Depentori,[a] Lisa Gans,[a] Dirk Holtmann,[c] Siegfried R. Waldvogel,[b, d] and Markus Stöckl*[a]

Important improvements have been achieved in developing the coupling of electrochemical CO_2 reduction to formate with its subsequent microbial conversion to polyhydroxybutyrate (PHB) by *Cupriavidus necator*. The CO_2 based formate electrosynthesis was optimised by electrolysis parameter adjustment and application of Sn based gas diffusion electrodes reaching almost 80% Faradaic efficiency at 150 mA cm^{-2}. Thereby, catholyte with the high formate concentration of 441 ± 9 mmol L^{-1} was generated as feedstock without intermediate downstream processing for semi-automated formate feeding into a fed-batch reactor system. Moreover, microbial formate conversion to PHB was studied further, optimised, and successfully scaled from shake flasks to semi-automated bioreactors. Therein, a PHB per formate ratio of 16.5 ± 4.0 mg g^{-1} and a PHB synthesis rate of 8.4 ± 2.1 mg L^{-1} OD^{-1} h^{-1} were achieved. By this process combination, an almost doubled overall process yield of 22.3 ± 5.5% was achieved compared to previous reports. The findings allow a detailed evaluation of the overall CO_2 to PHB conversion, providing the basis for potential technical exploitation.

Introduction

The contemporary global chemical industry relies upon fossil resources as energy source and feedstock for basic chemicals. However, the world's fossil resources are ultimately limited, and their use leads to high CO_2 emissions, accelerating the climate change. Consequently, the chemical industry needs to replace fossil resources with renewable energy sources and secure alternative access to basic chemicals. Thereby, the electrification of chemical processes will represent one of the main building blocks in the future.[1–3]

With this in mind, the electrochemical CO_2 reduction reaction (*eCO$_2$RR*) offers the promising opportunity to convert CO_2 into higher value chemicals using renewable electricity.[4,5] In general, the reduction of gaseous CO_2 at technically relevant current densities (> 100 mA cm^{-2},[6–8] strongly depended on the electrolysis product) requires gas diffusion electrodes (GDE),[9–11] as gaseous CO_2 has a low solubility in aqueous electrolytes (33 mmol L^{-1} at 298 K and 1 atm).[12,13] Besides the *eCO$_2$RR* to carbon monoxide,[14–16] the electrosynthesis of formic acid/formate represents a far developed reaction, which has been reported in numerous studies with outstanding performance indicators such as current density up to 1.8 A cm^{-2},[17] Faradaic efficiency (FE) above 90%,[9,18] long-time process stability of 1000 h[19] and high product concentration (20 wt% formic acid).[20]

Based on this tremendous scientific effort, formic acid/formate originating from *eCO$_2$RR* is considered to become economically viable in the near future.[7] However, it has to be pointed out that for a successful substitution of fossil feedstock, more complex and more reduced carbon based chemicals are demanded, and an upgrade, e.g. based on formate, is required. An elegant option to transform formate into more complex and higher value products is its use as substrate in biotechnological syntheses.[21–23] This kind of process combination is exemplarily illustrated in Figure 1 (Section 1).

Several organisms such as *Acetobacterium woodii*, *Eubacterium limosum* or *Methylobacterium extroquens* have been reported as possible biocatalysts for a formate based bioeconomy.[21,23] Within this study, the well-established formatotrophic model organism *Cupriavidus necator* (*C. necator*) was used, which has been shown to produce a variety of products, ranging from polyhydroxybutyrate[24,25] (PHB) in the wildtype

[a] I. Dinges, I. Depentori, L. Gans, Dr. M. Stöckl
Chemical Technology
DECHEMA Research Institute
Theodor-Heuss-Allee 25, 60486 Frankfurt am Main, Germany
E-mail: markus.stoeckl@dechema.de

[b] I. Dinges, Prof. Dr. S. R. Waldvogel
Department of Chemistry
Johannes Gutenberg University Mainz
Duesbergweg 10–14, 55128 Mainz, Germany

[c] Prof. Dr. Ing. D. Holtmann
Institute of Process Engineering in Life Sciences
Karlsruhe Institute of Technology
Fritz-Haber-Weg 4, 76131 Karlsruhe, Germany

[d] Prof. Dr. S. R. Waldvogel
Institute of Biological and Chemical, Systems – Functional Molecular Systems (IBCS-FMS)
Karlsruhe Institute of Technology
Kaiserstraße 12, 76131 Karlsruhe, Germany.

Supporting information for this article is available on the WWW under https://doi.org/10.1002/cssc.202301721

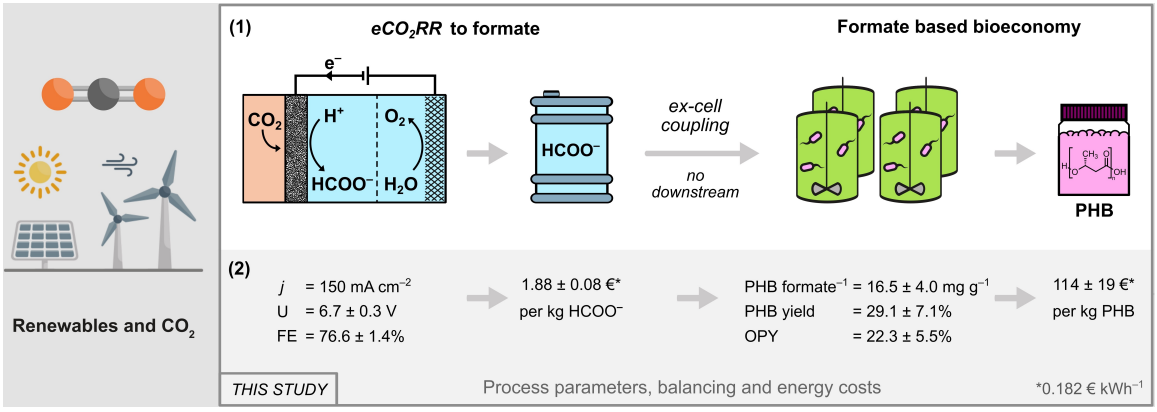

Figure 1. Schematic illustration of the overall process combination of the electrochemical CO_2 reduction reaction (*eCO₂RR*) to formate with a formate based bioeconomy using renewable energy sources. (1) Ex-cell coupling of *eCO₂RR* to formate with its subsequent microbial conversion to polyhydroxybutyrate (PHB) by *Cupriavidus necator* without intermediate downstream processing. (2) Key process data as well as resulting costs for formate and PHB based on a recent energy price[35] achieved in this study. Abbreviations: *j* = Current density, U = Average terminal voltage, FE = Faradaic efficiency for formate, OPY = Overall process yield.

strain to solvents,[26–29] organic acids[30,31] and terpenes[32,33] with genetically modified strains.

Even though the combination of the *eCO₂RR* and the subsequent biosynthesis of higher value products is a promising route to substitute fossil raw materials, the technical combination of the latter processes is challenging. In general, a suitable process combination can be realised by an "in-cell" or "ex-cell" coupling. In in-cell processes (or secondary microbial electrochemical technologies),[34] *eCO₂RR* to formate and its subsequent microbial conversion would take place in the same reactor (system), whereas an ex-cell coupling keeps both subprocesses separated in both space and time. To the authors' point of view, the ex-cell coupling of *eCO₂RR* and biosynthesis provides a variety of advantages, since it allows their process parameters to be optimised and operated more independently.

In previous work,[25] the initial coupling of *eCO₂RR* to formate with its subsequent microbial conversion to PHB by *C. necator* was demonstrated, but several challenges were not solved: Both subprocesses were kept spatially separated. Formate was electrochemically synthesised from CO_2 in a flow reactor with a Sn based GDE in 0.2 M KH_2PO_4/K_2HPO_4 as a biocompatible electrolyte. Back then, a FE for formate of 49.7 ± 0.9% at 50 mA cm^{-2} was achieved. The biocompatible catholyte containing electrosynthesised formate (e-formate) was used as substrate for microbial PHB synthesis with *C. necator* in shake flasks without intermediate downstream processing, leading to a final PHB concentration of 56 mg L^{-1} solely on e-formate and an overall FE of 4% for the coupled processes. Herein, very important challenges were solved by the improvement of individual subprocesses and harmonisation of the coupling based on previous findings, and an overall process was established and evaluated (Figure 1, Section 1 and 2).

Results and Discussion

The CO_2 based formate electrosynthesis (first subprocess) was mainly optimised by application of self-fabricated GDEs. Thereby, catholyte with high e-formate concentration was produced as feedstock for *C. necator*. Moreover, microbial formate conversion to PHB (second subprocess) was examined and successfully transferred as well as scaled from shake flasks to a fed-batch reactor system with a semi-automated e-formate feed. Three different phosphate buffers were examined for both subprocesses, they only differ in their K^+ and Na^+ contents. They were derived from the physiological, biocompatible 0.2 M phosphate buffer employed for the initial successful coupling. This is in turn an adaption of Sydow et al.,[36] who developed an electrolysis-compatible cultivation medium for *C. necator* based on phosphates. To avoid any intermediate downstream processing, all buffer compositions were examined for both subprocesses individually.

Gas Diffusion Electrodes

GDEs were fabricated by heat pressing the catalyst mixture onto support material. Sn powder of inexpensive origin (approx. 95 € kg^{-1}) with particle sizes ≤ 20 µm was used as electrocatalyst and polytetrafluoroethylene (PTFE) powder served as hydrophobic binder in the catalyst mixture. Both materials were homogenised and pressed onto Ni foam, which served as support material and current collector. Taking current prices into account, material cost of GDE fabrication was estimated at approx. 436 € m^{-2}, of which Ni foam accounts for 79%. In total, twelve GDEs were fabricated for the herein presented electrolyses using a relatively inexpensive electrocatalyst by a fast, easy, and scalable fabrication method. The reproducibility of this predominantly manual fabrication method was sufficient and no influence of the minor fabrication variation on GDE

performance was observed (Sn loading b (Sn, wt%) = 90 ± 4 mg cm^{-2} and thickness d = 558 ± 15 µm, n = 12). Further details and photographs are provided in the Supporting Information (SI, Section 1.2 and 3.2).

Formate Electrosynthesis

Electrochemical CO_2 reduction was carried out in a gas-fed flow reactor with three different phosphate-based electrolytes regarding microbial PHB synthesis optimisation: (A) 0.2 M KH_2PO_4/K_2HPO_4, (B) 0.2 M NaH_2PO_4/K_2HPO_4 and (C) 0.2 M NaH_2PO_4/Na_2HPO_4 (equimolar, respectively), with pH values of 6.67 ± 0.05 (A, n = 3), 6.61 ± 0.05 (B, n = 6) and 6.53 ± 0.05 (C, n = 3). To use formate-containing catholyte as feedstock in semi-automated bioreactors, the aim was to achieve the highest possible formate concentration at high FE produced with a high energy efficiency. For this purpose, all electrolyses were run for 22 h, maintaining current density at 150 mA cm^{-2} after an initial ramp (12.5 mA cm^{-2} increase every 5 min). Figure 2 compares FE and concentration of formate in the catholyte obtained during electrolysis for the different electrolytes.

Generally, all three FE courses showed a decrease during the 22 h runtime. This was accompanied by a deterioration of formate production rates between the first and second fitted intervals (Interval 1 = 1–6 h, interval 2 = 19–22 h). These deteriorations were attributed to presumed formate mass transport limitations within the GDE's pore system increasing the influence of the parasitic hydrogen evolution reaction (HER). This hypothesis was supported by gas chromatography (GC) analysis, as hydrogen was detected as sole byproduct for all electrolyses (SI, Section 1.8). Final formate FE's of 79.8 ± 1.3% (A, n = 3), 76.6 ± 1.4% (B, n = 6) and 63 ± 2% (C, n = 3) were achieved. These were accompanied by catholyte formate concentrations of 458 ± 7 mmol L^{-1} (A, n = 3), 441 ± 9 mmol L^{-1} (B, n = 6) and 358 ± 11 mmol L^{-1} (C, n = 3). Consequently, electrolysis results of electrolyte (A) and (B) were relatively similar, while those of (C) were significantly inferior. Furthermore, electrolyses with electrolyte (A) and (B) were more energy efficient compared to electrolyte (C). In electrolyte (A), electrolyses required an average terminal voltage (U) of 6.38 ± 0.15 V (n = 3) and consumed 104 ± 3 Wh (n = 3) of electric energy. Similarly, electrolyses with (B) were run at 6.7 ± 0.3 V (n = 6) with an electric energy consumption (EEC) of 110 ± 4 Wh (n = 6). In contrast, using electrolyte (C) resulted in 7.54 ± 0.14 V (n = 3) combined with an EEC of 123 ± 3 Wh (n = 3).

Taking everything into account, electrolyte (A) containing only K^+ as alkali cation yielded the best results among the examined electrolytes. Results for electrolyte (B) with Na^+/K^+ (1 : 2) were only slightly lower, whereas electrolyte (C) led to the lowest electrolysis performance of all three. It was hypothesised that the electrolytes decreasing conductivity from (A, 24.0 mS cm^{-1} at 23.4 °C) over (B, 21.8 mS cm^{-1} at 23.5 °C) to (C, 17.1 mS cm^{-1} at 23.4 °C) was responsible for this. Lower conductivity leads to a higher terminal voltage necessary to maintain the set current density, which resulted in a higher GDE potential favouring HER. Averaged for electrolysis duration and referenced to a reversible hydrogen electrode (RHE), the GDE potentials were −1.79 ± 0.14 V (A, n = 3), −1.74 ± 0.06 V (B, n = 6) and −1.86 ± 0.13 V (C, n = 3). Nonetheless, all electrolysis systems presented herein outperform the preceding study,[25] on which this study was based. Back then, only 49.7 ± 0.9% formate FE were achieved at 50 mA cm^{-2} employing electrolyte (A). This shows that the optimised Sn based GDEs with adjusted electrolysis conditions achieved an over 25% higher formate FE in the same electrolyte at tripled current density.

As mentioned in the introduction, higher FE (90%)[9] and higher current densities (1.8 A cm^{-2})[17] than those described here have already been published. However, the combination of the achieved FE of almost 80% at 150 mA cm^{-2} in 22 h of electrolysis with a final formate concentration around 450 mmol L^{-1} was achieved directly in a biocompatible electrolyte, which is suitable for the direct application as feed for the microbial PHB synthesis. Recently, Lim et al.[37] carried out a similar coupling, in which they reported slightly lower values of 66% FE for formate at 120 mA cm^{-2}.

Besides the herein improved FE and constant current density, the initial current density ramp of the electrolysis start-

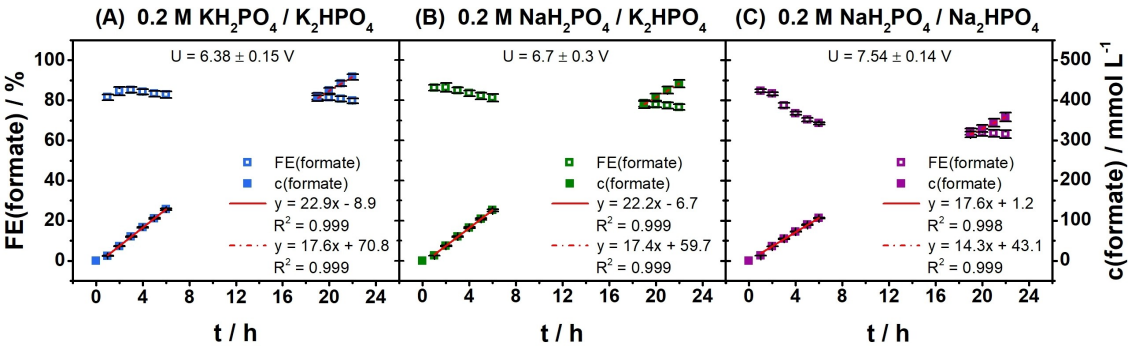

Figure 2. Faradaic efficiency (FE) and concentration course of formate in the catholyte of CO_2 electrolyses with different electrolytes: (A) 0.2 M KH_2PO_4/K_2HPO_4 (n = 3, blue), (B) 0.2 M NaH_2PO_4/K_2HPO_4 (n = 6, green) and (C) 0.2 M NaH_2PO_4/Na_2HPO_4 (n = 3, purple). Formate concentration courses were fitted linearly in two intervals: t = 1–6 h (red, solid line) and t = 19–22 h (red, dash dot line). Electrolysis parameters: Initial ramp (12.5 mA cm^{-2} increase every 5 min), Constant current density j = 150 mA cm^{-2} (after ramp), Runtime = 22 h (≙ 58162.5 C), Initial V (catholyte, anolyte) = 500 mL each, Cathode (GDE): 87.5% Sn, 12.5% PTFE on Ni foam, Reference electrode: Reversible hydrogen electrode (RHE), Anode: Mixed Ir-oxide on a Ti-grid (Platinode EP, Type 177, Umicore).

up procedure demonstrated that the GDE's performance was relatively stable at different current densities until at least the final 150 mA cm^{-2}. This is an advantage, as fluctuating electric energy originating from renewable sources could be compensated by adjusting current density of the electrolysis, which would be enabled by flexibly operable GDEs.

Catholyte Characterisation

After electrolysis, the three catholytes intended as e-formate feedstock were further characterised. On the one hand, their Sn^{2+} content was determined via inductively coupled plasma atomic emission spectroscopy (ICP-OES) to investigate cathodic corrosion[38] of the self-fabricated GDEs. On the other hand, the concentrations of Na^+, K^+ an PO_4^{3-} were determined by ion chromatography (IC) to examine possible differences compared to their initial concentrations. The cation analysis data of the catholyte characterisation are summarised in Table 1.

ICP-OES analysis showed that only traces of dissolved electrocatalyst were found in the catholyte for all three electrolytes after 22 h electrolysis. Consequently, the GDEs were not particularly susceptible to cathodic corrosion at the applied electrolysis conditions. They were most stable in contact with electrolyte (B), followed by electrolyte (A) and then electrolyte (C). As all catholyte's Sn^{2+} concentrations were relatively low, no negative effects on the microbial PHB synthesis were expected for any of them. Details on ICP-OES analysis as well as before and after scanning electron microscope (SEM) images of all GDEs are supplied in the SI (Section 1.6 and 3.3).

IC analysis revealed that initial and final PO_4^{3-} concentrations after electrolysis differed only slightly in all experiments (SI, Section 1.7). In contrast to PO_4^{3-}, the final concentrations of Na^+ and/or K^+ increased compared to their initial concentrations for all three electrolytes. At the same time, the concentrations in the respective anolytes decreased accordingly (SI, section 1.7). Nearly all alkali cations from both catholyte and anolyte are found in the catholyte after electrolysis. Therefore, their concentrations should have nearly doubled in the catholyte. However, the catholytes increased in volume during electrolysis due to osmosis. This results in concentrations slightly below doubling, whereas the total molar amounts were constant. All IC analysis results are provided in the SI (Section 1.7).

Although an increase of final cation concentrations was induced by electrolysis, the catholytes could still serve as e-formate feed in a fed-batch reactor system, as these higher concentrations do not alter the main incubation's cation concentration significantly at herein examined feeding times.

Microbial PHB synthesis with *C. necator*

The three phosphate buffers were also investigated for microbial PHB synthesis with *C. necator*. Additionally, it was deduced from previous results[25] that a formate concentration below 100 mmol L^{-1} could be advantageous for PHB synthesis. Consequently, PHB synthesis was carried out with the three respective phosphate buffers at different formate concentrations in a range from 0 to 100 mmol L^{-1}. The aim was to identify the most suitable buffer composition alongside the formate concentration that should be maintained for PHB synthesis in bioreactors with a semi-automated e-formate feed. Hence, preliminary incubations for PHB synthesis were designed accordingly.

All incubations were conducted with *C. necator* (wildtype) resting cells. The resting cells were acquired by raising *C. necator* cells from cryo stock in a first preculture in Lysogeny broth (LB), followed by a second preculture in formate-based minimal medium. The bioconversion of formate to PHB was carried out in shake flasks for 4 h. The target value of the initial OD_{600} was 0.2, which was intentionally low to prevent large changes in formate concentration during incubation as formate is consumed for PHB synthesis. The real OD_{600} after the inoculation was measured and differed slightly, therefore the results were normalised to the actual initial OD_{600}. Figure 3 compares the achieved PHB concentrations as well as the amount of PHB per consumed formate for all three phosphate buffers and the respective formate concentrations.

Each incubation series was performed in triplets ($n = 3$) and 0 mmol L^{-1} formate was examined to ensure the determined PHB content was synthesised on formate. The resting cells already contained PHB from pre-cultivation, which was subtracted from all incubation data. For some incubations, especially with 0 mmol L^{-1}, negative PHB concentrations were observed, since the cells could neither synthesise new PHB nor had they formate to sustain their energy demand, so the PHB originating from pre-cultivation was consumed instead.

Besides, the results show that the highest PHB concentration occurred at different initial formate concentrations for each phosphate buffer. This is also true for the highest amount of PHB per consumed formate. Generally, the highest PHB

Table 1. Comparison of cation concentrations in the catholyte before and after formate electrosynthesis (22 h, 150 mA cm^{-2}) for three phosphate buffers as electrolytes: (A) 0.2 M KH_2PO_4/K_2HPO_4, (B) 0.2 M NaH_2PO_4/K_2HPO_4 and (C) 0.2 M NaH_2PO_4/Na_2HPO_4. Sn^{2+} concentration was quantified via ICP-OES, Na^+ and K^+ concentrations via IC.

Buffer	c(Na^+)[a]/mmol L^{-1}	c(K^+)[a]/mmol L^{-1}	c(Na^+)[b]/mmol L^{-1}	c(K^+)[b]/mmol L^{-1}	c(Sn^{2+})[b]/µmol L^{-1}
A ($n = 3$)	3.0[c]	289.3[c]	5.5 ± 0.3	535 ± 2	11 ± 3
B ($n = 6$)	102.2[c]	192.1[c]	187 ± 1	355 ± 3	8.7 ± 1.6
C ($n = 3$)	297.2[c]	1.4[c]	536 ± 2	2.5 ± 0.6	20 ± 6

[a] Before electrolysis. [b] After electrolysis. [c] Measured $n = 1$.

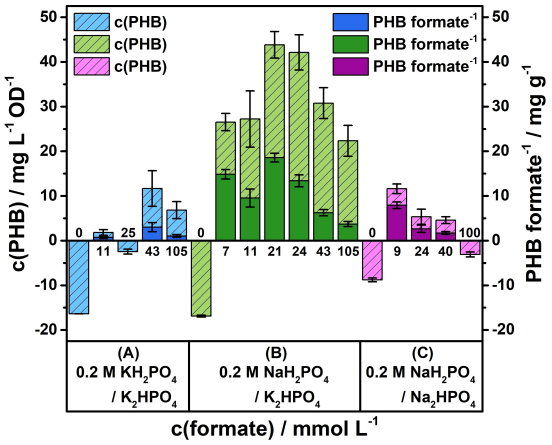

Figure 3. Comparison of PHB concentration normalised to initial OD_{600} (column, line pattern) and PHB per formate (column, solid) during PHB synthesis with *C. necator* resting cells in shake flasks with variable initial formate concentrations specified at the columns in different phosphate buffers: (A) 0.2 M KH_2PO_4/K_2HPO_4 (blue), (B) 0.2 M NaH_2PO_4/K_2HPO_4 (green), (C) 0.2 M NaH_2PO_4/Na_2HPO_4 (purple). Incubation conditions ($n=3$), Initial $OD_{600} \approx 0.2$, V = 75 mL, Duration = 4 h, T = 30 °C, Shaking = 180 rpm.

concentration coincided with the highest amount of PHB per formate for all three buffer compositions. To optimise formate conversion to PHB and thereby process efficiency, the amount of PHB per consumed formate was the main evaluation criterion.

In incubations with phosphate buffer (A), the highest achieved PHB concentration was 11.7 ± 4.0 mg L^{-1} OD^{-1} ($n=3$) with 3.0 ± 1.1 mg g^{-1} ($n=3$) PHB per formate at a starting formate concentration of 43 mmol L^{-1}. The corresponding average formate consumption rate was 21.5 ± 0.2 mmol L^{-1} h^{-1} OD^{-1} ($n=3$). In contrast, the best results in phosphate buffer (B) were obtained at 21 mmol L^{-1} formate. PHB concentration reached 43.8 ± 3.0 mg L^{-1} OD^{-1} ($n=3$) and 18.6 ± 1.0 mg g^{-1} ($n=3$) PHB per formate with an average formate consumption rate of 13.1 ± 0.2 mmol L^{-1} h^{-1} OD^{-1} ($n=3$). Finally, incubations in phosphate buffer (C) were best at 9 mmol L^{-1} formate. They reached 11.6 ± 1.1 mg L^{-1} OD^{-1} ($n=3$) PHB corresponding to 7.9 ± 0.8 mg g^{-1} ($n=3$) PHB per formate at an average formate consumption of 8.2 ± 0.2 mmol L^{-1} h^{-1} OD^{-1} ($n=3$).

The comparison of each buffer's best results revealed that the most efficient PHB synthesis had been achieved with buffer (B) regarding both the total PHB concentration and the amount of synthesised PHB per consumed formate. It follows that the presence of both Na^+ and K^+ is beneficial for PHB synthesis since neither solely Na^+ nor K^+ containing buffer allowed proper PHB synthesis. Although this was not the focus of this work and was not investigated further, it could be assumed that the absence of either K^+ or Na^+ might result in an overall decreased biological activity, possibly related to membrane potentials inside the cells. Besides the 1:2 ratio of Na^+/K^+ of buffer (B), the inverse Na^+/K^+ ratio of 2:1 has also been investigated but did not provide a higher PHB per formate ratio (SI, section 3.4). Consequently, the Na^+/K^+ ratio (1:2) of buffer (B) was preferred.

All in all, phosphate buffer (B) with 21 mmol L^{-1} formate was chosen for PHB synthesis in parallelised bioreactors with semi-automated e-formate feed. Thereby, 21 mmol L^{-1} formate has to be maintained within a relatively narrow window, as examined formate concentrations above and below (11 and 24 mmol L^{-1}) already have lower PHB to formate ratios. It is assumed that with increasing formate concentrations the substrate toxicity/stress caused by formate could play a role, which might lead to a decreased PHB to formate ratio. Nevertheless, compared to the starting point,[25] buffer adaption with lower formate concentration has improved PHB synthesis considerably.

Process Coupling

For the process coupling using phosphate buffer (B), six electrolyses were performed generating approximately 3 L of catholyte containing 441 mmol L^{-1} e-formate as feedstock. Afterwards, four incubations were carried out simultaneously in semi-automated bioreactors in the so called DASGIP® fermentation system. They were conducted with *C. necator* (wildtype) resting cells as before, which were obtained following the procedure described earlier. However, this time the second formate-based preculture was already grown on e-formate. Thus, the entire incubation process is based on formate originating from electrosynthesis.

The bioreactor incubations started with an initial OD_{600} of 1.80 in 340 mL of buffer (B) 0.2 M NaH_2PO_4/K_2HPO_4 containing 21 mmol L^{-1} e-formate. From then on, the cells were incubated for 7.5 h with hourly adapted e-formate feed rates from the stock solution to maintain 21 mmol L^{-1} e-formate. Samples for formate analysis by high-performance liquid chromatography (HPLC) were taken every 30 min for all bioreactors. However, only samples from two reactors every hour in the range of 0.5 h to 6.5 h of the incubation duration could be analysed instantly to adjust the catholyte feed at every full hour to maintain a constant formate concentration. Samples for PHB analysis were taken every two hours and at the incubation's end for all reactors, respectively. All changes in volume caused by sampling and e-formate feed were considered for result calculations, especially for normalising all results to the initial OD_{600}. Figure 4 relates e-formate concentration and its consumption to PHB synthesis during the incubation process.

Section 1 of Figure 4 shows that the e-formate concentration deviated significantly from the target e-formate concentration of 21 mmol L^{-1} throughout incubation. This was caused by the only available formate quantification method, samples had to be analysed off-line via HPLC and a single measurement took 25 min. Therefore, the hourly e-formate feed had to be extrapolated based on the e-formate consumption rate determined within the first half of each feeding interval. Nonetheless, the microorganisms always had e-formate to feed on as its concentration never fell to zero. Despite the variation in concentration, e-formate was consumed continuously with an average consumption rate of 10.2 ± 2.3 mmol L^{-1} h^{-1} OD^{-1} ($n=$

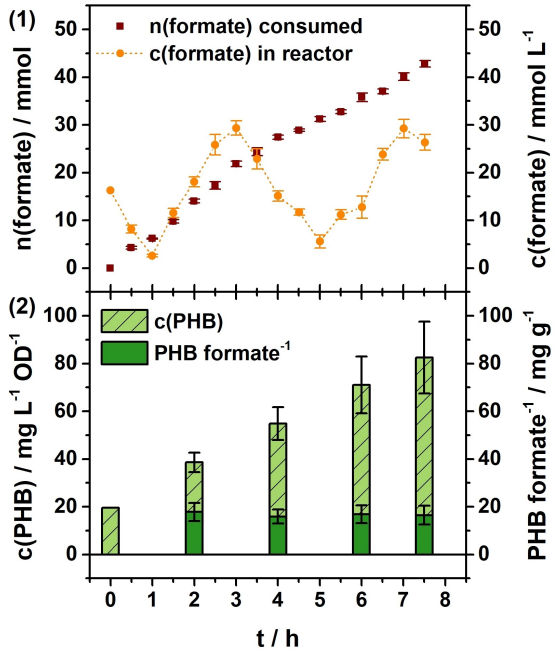

Figure 4. PHB synthesis of *C. necator* resting cells in semi-automated bioreactors with e-formate stock solution feed ($n=4$). (1) Consumed formate and formate concentration within the reactor during incubation. (2) PHB concentration normalised to initial OD_{600} (column, light green, line pattern) and continuous PHB formate^{-1} (column, green, solid). Incubation conditions ($n=4$): Medium = 0.2 M NaH_2PO_4/K_2HPO_4 (equimolar), Initial $OD_{600}=1.80$, Initial V = 340 mL, T = 30 °C, c(e-formate) of feed = 441 mmol L^{-1}, Initial e-formate feed = 6.9 mL h^{-1} (adjusted during runtime), Runtime = 7.5 h.

4). Thereby, the highest observed consumption rate was 13.1 ± 0.9 mmol L^{-1} h^{-1} OD^{-1} ($n=4$) in the third hour.

Equally important, PHB concentration increased continuously as well and reached 83 ± 16 mg L^{-1} OD^{-1} (≙ 110 ± 20 mg L^{-1}, $n=4$) at the end of incubation (Figure 4, Section 2). Considering that the cells already contained PHB from pre-cultivation, 63 ± 16 mg L^{-1} OD^{-1} ($n=4$) PHB were synthesised during bioreactor incubation with an average PHB synthesis rate of 8.4 ± 2.1 mg L^{-1} OD^{-1} h^{-1} ($n=4$). This corresponds to a final overall PHB per formate ratio of 16.5 ± 4.0 mg g^{-1} ($n=4$). Moreover, this ratio was also relatively constant throughout incubation despite the changes in e-formate concentration.

Compared to the shake flask incubation, the incubation results of the bioreactors were different. Their average formate consumption rate was 10.2 ± 2.3 mmol L^{-1} h^{-1} OD^{-1} ($n=4$), which was lower than the 13.1 ± 0.2 mmol L^{-1} h^{-1} OD^{-1} ($n=3$) in the shake flasks. Nevertheless, a similar consumption rate of 13.1 ± 0.9 mmol L^{-1} h^{-1} OD^{-1} ($n=4$) was reached in the third hour. Apart from that, the final PHB concentration obtained in the bioreactors of 63 ± 16 mg L^{-1} OD^{-1} ($n=4$) was higher compared to 43.8 ± 3.0 mg L^{-1} OD^{-1} ($n=3$) in the shake flasks. However, this is most probably due to the longer incubation time (7.5 h instead of 4 h) and a higher formate availability. Furthermore, the PHB amount per formate shows that PHB synthesis was marginally more efficient in shake flasks. These incubations resulted in 18.6 ± 1.0 mg g^{-1} ($n=3$) PHB per formate whereas the bioreactors yielded 16.5 ± 4.0 mg g^{-1} ($n=4$). This was mainly attributed to the challenging adjustment of the e-formate feed described above, as the target e-formate concentration could not be maintained throughout the complete incubation. The shake flask results for formate concentrations above and below 21 mmol L^{-1} support this hypothesis further, as they showed a lower PHB to formate ratio. Even though PHB synthesis was marginally more efficient in shake flasks, it was successfully transferred to the semi-automated, parallel fermenter system. Furthermore, the initial OD_{600} was increased approximately by factor 10 while reaching a similar PHB per formate ratio, which is crucial for the space-time yield of the process. All discussed deviations were mainly attributed to limitations of the e-formate feed control, which could be addressed by establishing an alternative, on-line formate analysis method in the future. All in all, transfer and scale-up of the microbial PHB synthesis were successfully demonstrated.

In the predecessor study,[25] an average PHB synthesis rate of 3.2 mg L^{-1} OD^{-1} h^{-1} was obtained. Thus, a significant improvement to 8.4 ± 2.1 mg L^{-1} OD^{-1} h^{-1} ($n=4$) was achieved herein. Moreover, the PHB per formate ratio was increased to 16.5 ± 4.0 mg g^{-1} ($n=4$) in the bioreactors compared to 14.1 mg g^{-1} achieved in the shake flasks back then. Recently, Lim et al.[37] reported 11.5 mg h^{-1} as highest PHB synthesis rate on e-formate at the time. Normalised to their starting OD_{600} (0.9) and initial incubation volume (2 L), this equals a PHB synthesis rate of 6.4 mg L^{-1} OD^{-1} h^{-1}, which is below the rate achieved herein now. Given the difference in incubation time and conditions, these rates have limited comparability though.

Process Balancing

The overarching aim of this study was to demonstrate the excell coupling of the subprocesses *eCO$_2$RR* to formate and PHB biosynthesis as well as to use the process data to conduct a transparent process balancing and evaluation under current and realistic assumptions. The authors would like to encourage others to do the same alongside an analysis under predicted future conditions, as it is currently underrepresented and could help draw attention to the main realisation barriers.

Hence, after demonstrating the coupling of formate electrosynthesis to microbial PHB synthesis on a larger and semi-automated lab scale, the resulting overall process was evaluated. For this purpose, the overall process yield was calculated based on the yields of both subprocesses. The yield of formate electrosynthesis (first subprocess) is equivalent to the formate FE discussed earlier. All electrolyses carried out for e-formate feedstock production resulted in a formate FE of 76.6 ± 1.4 % ($n=6$). To calculate the microbial PHB synthesis yield (second subprocess), a theoretical PHB yield based on the microorganism's metabolism was determined. Referring to Vlaeminck et al.,[39] *C. necator* uses 33 equivalents formic acid/formate to synthesise a single equivalent PHB monomer unit. Based on this stoichiometric ratio, a PHB yield of 29.1 ± 7.1 % ($n=4$) was obtained in the bioreactors. Thus, an overall process yield of

22.3 ± 5.5 % was achieved. All equations for yield calculations are provided in the Experimental Section.

For comparison with the initial coupled process,[25] PHB and overall process yield were calculated from the aforementioned study in the same manner because previously only an overall FE (4 %) had been considered. Consequently, 49.7 ± 0.9 % formate FE and 24.1 % PHB yield resulted in an overall process yield of 12 %. This shows that the overall process yield has been nearly doubled herein, especially due to the improved formate FE. In contrast, the current PHB yield is only about five percent higher than the former and still relatively low. Therefore, the main opportunity for further optimisation lies within the PHB synthesis. On the one hand, the PHB yield could potentially be optimised by lowering the salt/phosphate load, which is currently a compromise between the *eCO$_2$RR* and the PHB synthesis. On the other hand, more fundamental approaches such as evolutionary engineering, as it has been shown for *C. necator* and formate,[40] or genetic metabolism optimisation[41] would most likely increase the PHB yield. The need for an optimisation in this sense becomes even clearer if one takes economic aspects into account. Figure 1 (Section 2) contains an energy cost assessment for the overall process with PHB as final product alongside key process data.

Formate electrosynthesis from CO_2 required 10.3 ± 0.5 kWh kg^{-1} of electric energy. According to the Federal Statistical Office of Germany, 0.182 € kWh^{-1} were the average electricity costs for non-households in the first half of 2023 (excluding taxes, fees, levies and charges).[35] Consequently, electrosynthesised formate would cost 1.88 ± 0.08 € kg^{-1}, which is higher than exemplary market prices for formic acid of 0.37 € kg^{-1} and 0.69 € kg^{-1} (0.40 $ kg^{-1}[42] and 0.74 $ kg^{-1},[43] respectively with 1 € ≙ 1.08 $). With the achieved PHB per formate ratio, the final cost for PHB from CO_2 would amount to 114 ± 19 € kg^{-1}. Even with a quantitative PHB yield according to *C. necator's* metabolism,[39] PHB cost would be 34 € kg^{-1} based on the electric energy costs mentioned above, which is currently far off an economic price range.

In regard of this data, lowering the average terminal voltage required for formate electrosynthesis has great potential to lower overall energy costs. This could be achieved by flow reactor optimisation, for example by integration of a membrane assembled anode. However, the main cause increasing final PHB energy costs is the inefficient formate conversion pathway[39] of *C. necator*. This microorganism was chosen for this study as it remains a robust and reliable model system for demonstrating the coupling of formate electrosynthesis from CO_2 to microbial PHB synthesis. Nonetheless, either *C. necator* needs to be optimised, as has been reported by Claassens et al.[41] by replacing the rather inefficient Calvin cycle with the reductive glycine pathway, or *C. necator* needs to get substituted with a production strain harbouring a more efficient metabolism to move towards realisation of the demonstrated coupling on larger scale.

Conclusions

In this study, the *eCO$_2$RR* to formate has been coupled to microbial PHB synthesis in parallelised bioreactors with a semi-automated formate feed without intermediate downstream feed purification or concentrating. Beforehand, three biocompatible phosphate-based buffers were examined as both electrolytes and incubation buffers, with 0.2 M NaH_2PO_4/K_2HPO_4 allowing the most efficient coupling.

The formate feedstock solution was generated as catholyte by electrochemical CO_2 reduction at GDE. The GDE incorporated relatively inexpensive Sn (approx. 95 € kg^{-1}) as electrocatalyst and were self-fabricated by a fast, easy, reproducible and scalable fabrication method. They were reliably operated at 150 mA cm^{-2} for 22 h and no significant cathodic corrosion was observed. The catholyte used as feed contained 441 ± 9 mmol L^{-1} (n = 6) formate, which corresponded to an overall formate FE of 76.6 ± 1.4 % (n = 6).

The subsequent PHB synthesis was carried out with *C. necator* (wildtype), based on preliminary experiments evaluating the ideal formate concentration with regards to maximum PHB production and highest PHB per formate ratio in semi-automated bioreactors. Despite challenging formate feed adjustment during incubation, 63 ± 16 mg L^{-1} OD^{-1} (n = 4) PHB was reached. This corresponds to an average PHB synthesis rate of 8.4 ± 2.1 mg L^{-1} OD^{-1} h^{-1}, which is among the highest reported in literature so far to the best of the authors' knowledge. According to *C. necator's* metabolism,[39] a PHB yield of 29.1 ± 7.1 % (n = 4) was obtained. Consequently, the coupling of both subprocesses resulted in a considerably improved overall process yield of 22.3 ± 5.5 %.

Finally, energy costs of the demonstrated overall process were assessed for formate (1.88 ± 0.08 € kg^{-1}) and PHB (114 ± 19 € kg^{-1}) under current and realistic assumptions (0.182 € kWh^{-1}[35]). The assessment revealed that although the concept is promising, its realisation depends on further development of both subprocesses as well as the availability of inexpensive, renewable energy in the future.[44]

Experimental Section

Gas Diffusion Electrodes

The gas diffusion electrodes (GDE) were fabricated by pressing a Sn based catalyst mixture onto Ni foam as support material and current collector with a heating press. The catalyst mixture (30.00 g) consisted of Sn (87.5 wt%, 26.25 g, particle size ≤ 20 µm, Metallpulver24, Sankt Augustin, Germany) and polytetrafluoroethylene (PTFE) powder (12.5 wt%, 3.75 g, Dyneon™ PTFE TF 2072Z, 3M, Saint Paul, USA). The catalyst mixture was homogenised in a knife mill, the mixing (30 s, 25000 rpm) lead to a temperature increase of the mixture (T > 35 °C). After cooling to room temperature (RT), the catalyst mixture (4.00 g) was equally distributed onto Ni foam (d = 1.4 cm, 3.5 cm×4.0 cm ≙ 14 cm^2, Ni-5763, density 420–450 g m^{-2}, Recemat BV, Dodewaard, Netherlands) with a sieve and a stencil (Cut-out 3.5 cm×4.0 cm). The GDE blank was placed in between two pieces of ordinary baking sheet in the heating press and compressed (plate temperature 120 °C, pressure 10 bar, duration

60 s). After compressing, any excess material was removed. The GDE's catalyst loading *b* was determined by differential weighing and its thickness *d* was measured at the centre point. GDE photographs are provided in the SI (Section 3.2)

Electrolysis flow reactor set-up

The electrochemical reduction of CO_2 to formate was performed in a custom designed, gas-fed flow reactor (Figure 5). It consisted of three different compartments made from PEEK (polyetheretherketone), one for gaseous CO_2, followed by a catholyte and an anolyte compartment, respectively. The CO_2 compartment (2.0 cm×2.5 cm×1 mm, flow field) was separated from the catholyte compartment by the GDE (3.5 cm×4.0 cm, accessible geometrical surface area 2.0 cm×2.5 cm ≙ 5 cm^2). The GDE was placed in between two silicone gaskets (thickness 0.5 cm) to prevent fluid leakage and enable application of CO_2 overpressure. The following catholyte compartment frame (thickness 3 mm) had spatial cut-outs to allow equal distribution of catholyte flow and a port to incorporate a reversible hydrogen electrode (RHE, Mini HydroFlex, Gaskatel GmbH, Kassel, Germany) as reference electrode. Catholyte and anolyte compartment were separated by a proton exchange membrane (2.5 cm×3.0 cm, Nafion™, PFSA 117, DuPont, Wilmington, USA) sealed in between two silicone gaskets (thickness 0.5 cm). The anolyte compartment (2.0 cm×2.5 cm×2.0 cm) had spatial cut-outs like the catholyte compartment and contained a titanium mesh coated with Ir mixed oxide as an anode (PLATINODE® EP, 2.0 cm×2.5 cm, mesh type F, anode type 177, Umicore, Brussels, Belgium). The assembled reactor was enclosed in between two steel plates (d = 8 mm) to ensure an equal distribution of compacting pressure.

The CO_2 was fed into the reactor through a water-filled bubble counter to saturate the CO_2 with water at RT. It flowed top-down through the gas compartment to prevent fluid accumulation within.

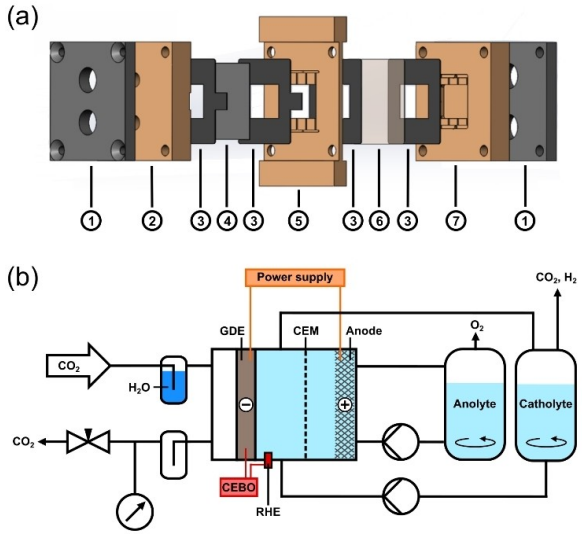

Figure 5. (a) Schematic illustration of the custom designed, gas-fed flow reactor fabricated by the DECHEMA workshop composed of: (1) Stainless-steel plate, (2) CO_2 compartment with flow-field, (3) silicone gasket, (4) GDE (5 cm^2 geometrically accessible), (5) catholyte compartment with a reversible hydrogen electrode (RHE) port, (6) cation exchange membrane (CEM), (7) anolyte compartment (incorporating the anode). (b) Schematic set-up for the operation of the electrolysis flow reactor for the electrosynthesis of formate with gaseous CO_2 as starting material (CEBO = Data logger).

The CO_2 outlet of the reactor's gas compartment was followed by a collecting vessel (500 mL) to collect any electrolyte potentially breaking through the GDE. The CO_2 overpressure was adjusted at the end of the CO_2 line with a regulating valve as well a differential pressure sensor combined with a pressure meter.

Catholyte and anolyte were circulated between the respective reactor compartments and reservoir with a peristaltic pump. To prevent gas entrapment and maintain fluid coverage of the electrodes, both anolyte and catholyte were passed through the reactor bottom-up. Further details can be found in the SI (Section 1.3).

Formate electrosynthesis

All electrosyntheses were performed for 22 h. A power supply unit (NGP804, Rohde & Schwarz GmbH & Co. KG, Munich, Germany) was employed to run the electrolysis, it recorded terminal voltage, current and power. Furthermore, the electrode potential of the GDE was referenced to RHE and recorded. The electrosynthesis started with a current ramp in the first hour, in which the current density was increased in steps of 12.5 mA cm^{-2} every 5 min until it reached 150 mA cm^{-2} (750 mA in total), which was kept constant for the remaining 21 h runtime.

CO_2 was supplied to the GDE in the gas compartment at a flow rate of 15–20 mL min^{-1} and an initial overpressure of approx. 100 mbar relative to ambient pressure. The pressure was recorded continuously during the running electrolysis. Gas samples were collected in the last hour of the electrolysis (t = 21 h) at the exhaust of the catholyte reservoir, where gas mainly bubbled through (approx. 50 mL in 5 min) and analysed by gas chromatography (SI, section 1.8).

Three different phosphate-based buffers were used as electrolyte: (A) 0.2 M KH_2PO_4/K_2HPO_4, (B) 0.2 M NaH_2PO_4/K_2HPO_4 and (C) 0.2 M NaH_2PO_4/Na_2HPO_4 (equimolar, respectively), with pH values of 6.67 ± 0.05 (A, n = 3), 6.61 ± 0.05 (B n = 6) and 6.53 ± 0.05 (C, n = 3). For each electrolysis, anolyte and catholyte had a starting volume of 500 mL (volumetric flask, ISO 1042). Anolyte and catholyte were circulated continuously at a flow rate of 40 mL min^{-1} between flow reactor compartment and reservoir, respectively. During the electrolysis, catholyte samples (1 mL) were taken hourly in the first six (t = 0–6 h) and the last four (t = 19–22 h) hours to monitor pH value, formate concentration and calculate the corresponding FE. After electrolysis, the respective anolyte and catholyte volume was determined by its weight and density. Therefore, the density was calculated by taking samples (1 mL) and weighing them (n = 3). Catholyte containing electrochemically generated formate (e-formate) was stored at −20 °C until its application for microbial PHB synthesis. The GDE was rinsed with H_2O and dried at RT. Further details can be found in the SI (section 1.4).

Sn quantification by inductively coupled plasma optical emission spectrometry (ICP-OES)

ICP-OES measurements were performed in radial viewing mode on Agilent 5800 ICP-OES equipped with an SPS 4 Autosampler, a borosilicate double-pass spray chamber and a Seaspray concentric glass nebulizer.

The wavelength for Sn determination was 283.998 nm and the Ar wavelength 420.067 nm served as an internal standard, for which errors less than 5% were accepted. All electrolyte samples had to be diluted by factor 4 to meet the internal standard criterion. The catholyte's Sn content was quantified via standard addition of a stock solution containing 1 ppm Sn. The stock solution was

prepared from a Sn standard (1000 ppm, Single-Element ICP-Standard-Solution, Lot N. 83131639, Carl Roth GmbH + Co. KG) via a dilution series by factor 10 using volumetric flasks (100 mL, ISO 1042).

For each sample, four different aliquots of stock solution (0.5, 1.0, 1.5, 2 mL) were added to the undiluted sample (1 mL). The analyte spiked samples were filled up to 4 mL with H_2O, respectively. Hence, five points were measured for each sample. Linear fits with $R^2 \geq 0.995$ were accepted due to the limited available sample volumes and several signals being close to the lower limit of detection (LOD, approx. 0.2 ppm for Sn at 283.998 nm) resulting out of the necessary dilution factor.

Cation analysis by ion chromatography (IC)

IC measurements to determine cation concentrations were performed on Dionex™ ICS-5000$^+$ DC (Pre column = Dionex™ IonPac CG17, Column = Dionex™ IonPacTM CS17, Analytical 2×250 mm, Suppressor = CERS 500, 2 mm). Methanesulphonic acid (MSA) served as eluent with a gradient method (steps 1–4: 1. −5–0 min, 1.5 mmol L^{-1} MSA (preparation step), 2. 0–25 min, 1.5–2.1 mmol L^{-1} MSA, 3. 25–40 min, 6 mmol L^{-1} MSA, 4. 40–60 min, 1.5 mmol L^{-1} MSA) at 0.1 mL min^{-1} flow rate. Samples were diluted by factor 200 or 400, Na^+ (retention time = 29.1 min) and K^+ (retention time = 35.1 min) were detected with a conductivity cell.

Standards to determine the concentrations of Na^+ and K^+ were prepared by a dilution series of a stock solution. The stock solution was prepared with NaCl (3.254 g ≙ 1280 ppm Na^+) and KCl (2.441 g ≙ 1280 ppm K^+) in a volumetric flask (1 L, ISO 1042). All combined standards (1, 2, 4, 8, 16, 32, 64 ppm) were measured (n = 1) and their signal areas fitted (R^2 = 0.9999, linear fit forced through zero).

Formate quantification by high-performance liquid chromatography (HPLC)

Formate concentration in both electrolysis and incubation samples were determined via HPLC (LC-20AD, SIL-20AC HT, CBM-20 A, CTO-20AC, SPD-M20A – Shimadzu, Kyoto, Japan). Samples from incubations were centrifuged (14100×g, 5 min) prior to analysis to remove all cells.

The HPLC unit was equipped with a Rezex ROA – Organic Acid (8%) column (300 mm×7.8 mm, Phenomenex, California, USA) and the following method parameters were employed: 5 mmol L^{-1} H_2SO_4, 0.6 mL min^{-1}, 30 °C, 30 ± 1 bar, photodiode array detector (λ = 194 nm), 15.3 min (retention time), 25 min (duration).

Formate standards were prepared by a dilution series from a stock solution. The stock solution was prepared with HCOONa (3.482 g, 51.2 mmol) in a volumetric flask (100 mL, ISO 1042). All formate standards (8, 16, 32, 64, 128, 256, 512 mmol L^{-1}) were measured (n = 3) and their signal areas fitted linearly (R^2 = 0.9999, fit forced through zero).

PHB quantification by high-performance liquid chromatography (HPLC)

PHB was depolymerised to its monomer unit crotonic acid for quantitative analysis. Sample preparation was conducted as follows: Samples were taken from the cultivation broth (10 or 30 mL, depending on the available volume). They were centrifuged (6000×g, 30 min) and the supernatant was discarded. The cell pellet was resuspended in 1 mL H_2O. The resulting cell suspension was transferred into a 2 mL centrifuge tube and centrifuged (14100×g, 5 min). The supernatant was discarded, and the cell pellet was dried overnight (100 °C). The dried cell pellet was mixed with 1 mL of concentrated H_2SO_4 and incubated (99 °C, 500 rpm, 60 min). The resulting solution was diluted 1:50 with H_2O and subsequently used for HPLC analysis.

It was performed on an HPLC-Unit (LC-20AD, SIL-20AC HT, CBM-20 A, CTO-20AC, SPD–M20 A – Shimadzu, Kyoto, Japan) equipped with the Rezex ROA – Organic Acid (8%) column (300 mm ×7.8 mm, Phenomenex, California, USA). Crotonic acid was analysed with the following method parameters: 5 mmol L^{-1} H_2SO_4, 0.6 mL min^{-1}, 40 °C, 27 ± 1 bar, photodiode array detector (λ = 207 nm), 29.2 min (retention time), 40 min (duration).

PHB standards were prepared by a dilution series from a stock solution. For preparation of the stock solution, PHB (7.45 mg) was weighed in a 2 mL centrifuge tube. The PHB was depolymerised in the same manner as described for the dried cell pellets above. Hence, the PHB was mixed with 1 mL of concentrated H_2SO_4, incubated (99 °C, 500 rpm, 60 min) and afterwards diluted 1:50 with H_2O. All PHB standards (25, 50, 100, 250, 500, 1000 μg) were measured (n = 3) and their signal areas fitted linearly (R^2 = 0.9997, fit forced through zero).

Microorganisms

The bioconversion of either commercial or electrosynthesised formate (e-formate) was demonstrated with *Cupriavidus necator* wildtype (DSM-428, DSMZ, Braunschweig, Germany), which produces PHB from formate under NH_4^+ limitation.

Growth media

The cultivation and incubation of *C. necator* was carried out with the different growth media following below.

Lysogeny broth (LB): Yeast extract (5 g L^{-1}), tryptone (10 g L^{-1}) and NaCl (5 g L^{-1}) in deionized water, the pH was set to 7.0 with NaOH (2 M) and HCl (2 M).

Minimal medium with commercially available formate: HCOONa (6.801 g L^{-1}), Na_2HPO_4 (2.895 g L^{-1}), $NaH_2PO_4 \cdot 2\ H_2O$ (3.980 g L^{-1}), K_2SO_4 (0.171 g L^{-1}), $MgSO_4 \cdot H_2O$ (0.390 g L^{-1}), $(NH_4)_2SO_4$ (0.980 g L^{-1}), $CaSO_4 \cdot 2\ H_2O$ (0.097 g L^{-1}) and trace element solution (350 μL L^{-1}). All media components were prepared sterile as separate stock solutions and combined prior to each experiment. The pH value was set to 7.0 with sterile H_2SO_4 (2 M) and NaOH (2 M).

Trace element solution: $FeSO_4 \cdot 7\ H_2O$ (15.00 g L^{-1}), $MnSO_4 \cdot H_2O$ (1.46 g L^{-1}), $ZnSO_4 \cdot 7\ H_2O$ (2.40 g L^{-1}), $CuSO_4 \cdot 5\ H_2O$ (0.48 g L^{-1}), $Na_2MoO_4 \cdot 2\ H_2O$ (1.80 g L^{-1}), $NiSO_4 \cdot 6\ H_2O$ (1.50 g L^{-1}), $CoSO_4 \cdot 7\ H_2O$ (0.04 g L^{-1}) dissolved in 0.1 M HCl.

Minimal medium with e–formate: The calculated volume of the catholyte (depending on the e-formate concentration) for 100 mmol L^{-1} e-formate was mixed with the ingredients of the minimal medium described above, except for HCOONa, Na_2HPO_4 and NaH_2PO_4, which were not added in this case.

Formate-containing buffer for resting cells: The phosphate buffer was either (A) 0.2 M KH_2PO_4/K_2HPO_4, (B) 0.2 M NaH_2PO_4/K_2HPO_4 or (C) 0.2 M NaH_2PO_4/Na_2HPO_4. The different formate concentrations were adjusted with either commercially available formate (HCOONa or HCOOK) or e-formate feedstock originating from electrosynthesis.

Cultivation and incubation of *C. necator*

All experiments were conducted using a first preculture raised in LB and a second preculture raised in minimal medium before the main incubation in formate-containing buffer. All incubations were carried out at 30 °C. All shake flask and test tube incubations were shaken at 180 rpm (shaking diameter of 25 mm). The second precultures (in minimal medium) were conducted in shake flasks of varying sizes depending on the required volume for the main incubation with filling volumes of 25 % of the nominal volume. All samples taken during the incubation were frozen at −20 °C until further analysis.

One or several *C. necator* precultures (depending on the required volume for further cultivation steps) were raised from a cryo stock in 5 mL LB in test tubes. After 22–24 h of incubation, cells were harvested by centrifugation (5 min, 5000×g), washed with fresh minimal medium, centrifuged again (5 min, 5000×g), resuspended and added to the required volume of prepared minimal medium to reach a starting OD_{600} of 0.05. After 24 h the second precultures were harvested by centrifugation (7 min, 5000×g), washed with fresh sterilised buffer, centrifuged again (7 min, 5000×g) and used for inoculation of the main incubation of resting cells in formate-containing buffer.

Incubation in shake flasks: Incubation of resting cells in buffer (A) 0.2 M KH_2PO_4/K_2HPO_4, (B) 0.2 M NaH_2PO_4/K_2HPO_4 or (C) 0.2 M NaH_2PO_4/Na_2HPO_4 with different formate concentrations were performed in 300 mL shaking flasks with a filling volume of 75 mL. Main cultures were inoculated with the calculated cell amount for an initial OD_{600} of 0.2, whereby the actual initial OD_{600} could slightly deviate. All incubation conditions were run in triplicates.

Incubation in semi-automated parallelised bioreactors: Main incubations of resting cells in semi-automated bioreactors were performed in the DASGIP® Parallel Bioreactor System (DASGIP AG, Jülich, Germany, Modules: Gas supply system = MX4/4, Temperature control system/Speed control system = TC4/SC4, Multipump module = MP8, Sensor amplifier = PH4PO4, DO-Sensor = InPro6820/12/220 from Mettler Toledo, pH electrode = 405-DPAS-SC-K8 S/225 from Mettler Toledo, PTFE air filter = Midisart® 2000 from Sartorius) in quadruplets. The initial incubation volume was 340 mL of buffer (B) 0.2 M NaH_2PO_4/K_2HPO_4, the initial OD_{600} was 1.80. The stirring frequency was set to 800 rpm, the pH value was measured and when reaching values above 7.2 regulated by automated adding of H_2SO_4 (1 M). All bioreactors were gassed with 6 sl min^{-1} compressed air. The initial feed of the catholyte containing 441 mmol L^{-1} e-formate was regulated to 6.9 mL h^{-1}. Samples (1 mL) for formate analysis by HPLC were taken every 30 min for all bioreactors. However, only samples of reactor 1 and 4 at 0.5 h, 1.5 h, 2.5 h, 3.5 h, 4.5 h, 5.5 h, 6.5 h of the incubation duration were analysed instantly to adjust the catholyte feed every full hour. At 0 h, 2 h, 4 h, 6 h and 7.5 h samples for PHB analysis were taken (10 mL).

Calculations

The FE for formate was calculated based on the determined amount of electrosynthesised formate using equation (1).

$$FE = \frac{F \cdot z \cdot n}{I \cdot t} \cdot 100\,\% \tag{1}$$

With FE = Faradaic efficiency of formate electrosynthesis/%, F = Faraday constant/A s mol^{-1}, z = Number of transferred electrons (z = 2), n = Amount of synthesised formate/mol, I = Current/A, t = Electrolysis runtime/s.

The results for each different phosphate-based electrolyte were averaged and their standard deviation was provided as uncertainty.

The PHB yield was calculated based on the determined amount of PHB using equation (2), (3) and (4).[39]

$$PHB\ yield = \frac{m(PHB)}{m(PHB,\ theo)} \cdot 100\,\% \tag{2}$$

With $PHB\ Yield$ = Yield of the microbial PHB synthesis based on e-formate, $m(PHB)$ = Mass of synthesised PHB/mg, $m(PHB,\ theo)$ = Theoretical mass of PHB at quantitative conversion of the consumed formate according to *C. necator's* metabolism[39]/mg.

$$m(PHB,\ theo) = M(CA) \cdot \frac{n(con.\ formate)}{33} \tag{3}$$

With $m(PHB,\ theo)$ = Theoretical mass of PHB at quantitative conversion of the consumed formate according to *C. necator's* metabolism[39]/mg, $M(CA) = 86.09$ g mol^{-1} (crotonic acid), $n(con.\ formate)$ = Total amount of formate consumed in the bioreactor/mol.

$$33\ HCOOH + 12\ O_2 \rightarrow C_4H_6O_2 + 30\ H_2O + 29\ CO_2 \tag{4}$$

The results for each different bioreactor were averaged and their standard deviation was provided as uncertainty.

The overall process yield (OPY) was calculated based on the yields of the two subprocesses using equation (5) and (6).

$$OPY = FE \cdot PHB\ Yield \cdot 100\,\% \tag{5}$$

$$\Delta(OPY) = \sqrt{\begin{matrix}(PHB\ Yield)^2 \cdot (\Delta FE)^2 \\ +(FE)^2 \cdot (\Delta PHB\ Yield)^2\end{matrix}} \cdot 100\,\% \tag{6}$$

With OPY = Overall process yield, $\Delta(OPY)$ = Uncertainty of the overall process yield, FE = Faradaic efficiency of formate electrosynthesis/%, ΔFE = Standard deviation of the formate synthesis (n = 6)/%, $PHB\ Yield$ = Yield of the microbial PHB synthesis based on e-formate/%, $\Delta PHB\ Yield$ = Standard deviation of the PHB yield (n = 4)/%. All variables in equation (5) and (6) were divided by 100 % prior to implementation for OPY and $\Delta(OPY)$ calculation.

Supporting Information

Supporting Information is available from the Wiley Online Library or from the corresponding author.

Acknowledgements

The authors are very grateful to the German Federal Ministry of Education and Research for their financial support (033RC031A and 033RC031B). Special thanks go to Dr. Nicky Bogolowski and Dr. Hans Joachim Kohnke (Gaskatel GmbH) for their support during GDE development. Furthermore, the authors would like to express their gratitude to Robin Kupec for his support in reactor design and to the DECHEMA Research Institute work-

shop, especially to Yvonne Hohmann, for construction of the custom electrolysis reactor. Finally, the authors would like to thank Jürgen Schuster and Jacqueline Patzsch for IC measurements as well as Alexander Langsdorf for sharing optimisations of the PHB analysis method. Open Access funding enabled and organized by Projekt DEAL.

Conflict of Interests

The authors declare no conflict of interest.

Data Availability Statement

The data that support the findings of this study are available in the supplementary material of this article.

Keywords: biosynthesis · CO_2 reduction · *Cupriavidus necator* · electrochemistry · polyhydroxybutyrate

[1] D. Pollok, S. R. Waldvogel, *Chem. Sci.* **2020**, *11*, 12386–12400.
[2] A. Wiebe, T. Gieshoff, S. Möhle, E. Rodrigo, M. Zirbes, S. R. Waldvogel, *Angew. Chem. Int. Ed.* **2018**, *57*, 5594–5619; *Angew. Chem.* **2018**, *130*, 5694–5721.
[3] S. Möhle, M. Zirbes, E. Rodrigo, T. Gieshoff, A. Wiebe, S. R. Waldvogel, *Angew. Chem. Int. Ed.* **2018**, *57*, 6018–6041; *Angew. Chem.* **2018**, *130*, 6124–6149.
[4] M. G. Kibria, J. P. Edwards, C. M. Gabardo, C. Dinh, A. Seifitokaldani, D. Sinton, E. H. Sargent, *Adv. Mater.* **2019**, *31*, 1807166.
[5] S. A. Al-Tamreh, M. H. Ibrahim, M. H. El-Naas, J. Vaes, D. Pant, A. Benamor, A. Amhamed, *ChemElectroChem* **2021**, *8*, 3207–3220.
[6] T. Haas, R. Krause, R. Weber, M. Demler, G. Schmid, *Nat. Catal.* **2018**, *1*, 32–39.
[7] R. I. Masel, Z. Liu, H. Yang, J. J. Kaczur, D. Carrillo, S. Ren, D. Salvatore, C. P. Berlinguette, *Nat. Nanotechnol.* **2021**, *16*, 118–128.
[8] J. Jörissen, T. Turek, R. Weber, *Chem. Unserer Zeit* **2011**, *45*, 172–183.
[9] D. Kopljar, A. Inan, P. Vindayer, N. Wagner, E. Klemm, *J. Appl. Electrochem.* **2014**, *44*, 1107–1116.
[10] D. Kopljar, N. Wagner, E. Klemm, *Chem. Eng. Technol.* **2016**, *39*, 2042–2050.
[11] M. Stöckl, T. Lange, P. Izadi, S. Bolat, N. Teetz, F. Harnisch, D. Holtmann, *Biotechnol. Bioeng.* **2023**, *120*, 1465–1477.
[12] S. Malkhandi, B. S. Yeo, *Curr. Opin. Chem. Eng.* **2019**, *26*, 112–121.
[13] B. J. M. Etzold, U. Krewer, S. Thiele, A. Dreizler, E. Klemm, T. Turek, *Chem. Eng. J.* **2021**, *424*, 130501.
[14] Z. Liu, H. Yang, R. Kutz, R. I. Masel, *J. Electrochem. Soc.* **2018**, *165*, J3371–J3377.
[15] C.-T. Dinh, F. P. García De Arquer, D. Sinton, E. H. Sargent, *ACS Energy Lett.* **2018**, *3*, 2835–2840.
[16] R. B. Kutz, Q. Chen, H. Yang, S. D. Sajjad, Z. Liu, I. R. Masel, *Energy Technol.* **2017**, *5*, 929–936.
[17] A. Löwe, M. Schmidt, F. Bienen, D. Kopljar, N. Wagner, E. Klemm, *ACS Sustainable Chem. Eng.* **2021**, *9*, 4213–4223.
[18] X. Wang, S. Liu, H. Zhang, S. Zhang, G. Meng, Q. Liu, Z. Sun, J. Luo, X. Liu, *Chem. Commun.* **2022**, *58*, 7654–7657.
[19] H. Yang, J. J. Kaczur, S. D. Sajjad, R. I. Masel, *J. CO2 Util.* **2020**, *42*, 101349.
[20] H. Yang, J. J. Kaczur, S. D. Sajjad, R. I. Masel, *J. CO2 Util.* **2017**, *20*, 208–217.
[21] N. J. Claassens, C. A. R. Cotton, D. Kopljar, A. Bar-Even, *Nat. Catal.* **2019**, *2*, 437–447.
[22] O. Yishai, S. N. Lindner, J. Gonzalez De La Cruz, H. Tenenboim, A. Bar-Even, *Curr. Opin. Chem. Biol.* **2016**, *35*, 1–9.
[23] M. Stöckl, N. Claassens, S. Lindner, E. Klemm, D. Holtmann, *Curr. Opin. Biotechnol.* **2022**, *74*, 154–163.
[24] D. Jendrossek, D. Pfeiffer, *Environ. Microbiol.* **2014**, *16*, 2357–2373.
[25] M. Stöckl, S. Harms, I. Dinges, S. Dimitrova, D. Holtmann, *ChemSusChem* **2020**, *13*, 4086–4093.
[26] N. Teetz, D. Holtmann, F. Harnisch, M. Stöckl, *Angew. Chem. Int. Ed.* **2022**, *61*, e202210596.
[27] H. Li, P. H. Opgenorth, D. G. Wernick, S. Rogers, T.-Y. Wu, W. Higashide, P. Malati, Y.-X. Huo, K. M. Cho, J. C. Liao, *Science* **2012**, *335*, 1596–1596.
[28] L. Garrigues, L. Maignien, E. Lombard, J. Singh, S. E. Guillouet, *New Biotechnol.* **2020**, *56*, 16–20.
[29] J. Lu, C. J. Brigham, C. S. Gai, A. J. Sinskey, *Appl. Microbiol. Biotechnol.* **2012**, *96*, 283–297.
[30] J. S. Chen, B. Colón, B. Dusel, M. Ziesack, J. C. Way, J. P. Torella, *PeerJ* **2015**, *3*, e1468.
[31] M. Raberg, E. Volodina, K. Lin, A. Steinbüchel, *Crit. Rev. Biotechnol.* **2018**, *38*, 494–510.
[32] T. Krieg, A. Sydow, S. Faust, I. Huth, D. Holtmann, *Angew. Chem. Int. Ed.* **2018**, *57*, 1879–1882; *Angew. Chem.* **2018**, *130*, 1897–1900.
[33] S. Milker, D. Holtmann, *Microb. Cell Fact.* **2021**, *20*, 89.
[34] U. Schröder, F. Harnisch, L. T. Angenent, *Energy Environ. Sci.* **2015**, *8*, 513–519.
[35] "Electricity prices for non-household customers: Germany, half-years, annual consumption classes, price types," can be found under https://www-genesis.destatis.de/datenbank/beta/statistic/61243/table/61243-0005, **2023**, (accessed: 11.10.2023).
[36] A. Sydow, T. Krieg, R. Ulber, D. Holtmann, *Eng. Life Sci.* **2017**, *17*, 781–791.
[37] J. Lim, S. Y. Choi, J. W. Lee, S. Y. Lee, H. Lee, *Proc. Nat. Acad. Sci.* **2023**, *120*, e2221438120.
[38] T. Wirtanen, T. Prenzel, J.-P. Tessonnier, S. R. Waldvogel, *Chem. Rev.* **2021**, *121*, 10241–10270.
[39] E. Vlaeminck, K. Quataert, E. Uitterhaegen, K. De Winter, W. K. Soetaert, *J. Biotechnol.* **2022**, *343*, 102–109.
[40] C. H. Calvey, V. Sànchez I Nogué, A. M. White, C. M. Kneucker, S. P. Woodworth, H. M. Alt, C. A. Eckert, C. W. Johnson, *Metab. Eng.* **2023**, *75*, 78–90.
[41] N. J. Claassens, G. Bordanaba-Florit, C. A. R. Cotton, A. De Maria, M. Finger-Bou, L. Friedeheim, N. Giner-Laguarda, M. Munar-Palmer, W. Newell, G. Scarinci, J. Verbunt, S. T. De Vries, S. Yilmaz, A. Bar-Even, *Metab. Eng.* **2020**, *62*, 30–41.
[42] M. Solakidou, A. Gemenetzi, G. Koutsikou, M. Theodorakopoulos, Y. Deligiannakis, M. Louloudi, *Energies* **2023**, *16*, 1723.
[43] M. Jouny, W. Luc, F. Jiao, *Ind. Eng. Chem. Res.* **2018**, *57*, 2165–2177.
[44] J. Seidler, J. Strugatchi, T. Gärtner, S. R. Waldvogel, *MRS Energy Sustainability* **2020**, *7*, 42.

Manuscript received: November 21, 2023
Revised manuscript received: December 12, 2023
Accepted manuscript online: January 5, 2024
Version of record online: January 19, 2024

3.3 Formate for Synthesis of Performic Acid

A manuscript was published on this section:

Ida Dinges, Markus Pyschik, Julian Schütz, Selina Schneider, Elias Klemm, Siegfried R. Waldvogel, Markus Stöckl, All Electrochemical Synthesis of Performic Acid Starting from CO_2, O_2, and H_2O, *ChemSusChem* **2025**, *18*, e202500180.
DOI: 10.1002/cssc.202500180

Explanation of my contribution:
The project was conceptualised by M.S., S.Sch., M.P., E.K. and me. I performed the experimental work to generate formate feedstock (fabrication and characterisation of GDEs, electrosynthesis of formate). M.P. performed the experimental work with support of J.S. for electrosynthesis of hydrogen peroxide (fabrication and characterisation of GDEs, electrosynthesis of hydrogen peroxide, PFA analysis). I performed further analytical measurements with support of M.P. (ICP-OES, contact angle) and analysed the data. The manuscript was written by me with support of M.S., E.K. and S.R.W. The work was carried out under the supervision of M.S. and S.R.W.

Recently, Schneider and Stöckl[197] published the indirect and on-demand electrosynthesis of peroxy acids. They carried out the electrochemical oxygen reduction reaction (*eO$_2$RR*) to hydrogen peroxide at commercial carbon GDEs in presence of various carboxylic acids, whereby the corresponding peroxy acid was generated *in-situ* in a chemical equilibrium reaction. Among these, performic acid (PFA) is an attractive disinfectant for several sectors such as food industry, healthcare and wastewater treatment, as it is already very effective at low concentration ($<20\,mg\,L^{-1} \mathrel{\hat{=}} 0.32\,mmol\,L^{-1}$).[198–201] The use of formic acid from *eCO$_2$RR* offers the opportunity of producing PFA exclusively from CO_2, O_2, H_2O and renewable electricity. Exploring this opportunity, the first complete (indirect) electrosynthesis of PFA was achieved by coupling *eCO$_2$RR* to formate with *eO$_2$RR* to hydrogen peroxide without any intermediate downstream processing.

Both Bi_2O_3 based GDE for *eCO$_2$RR* and carbon-based GDE for *eO$_2$RR* were self-fabricated by heat pressing catalyst mixture onto support material. They were characterised before and after electrolysis by contact angle measurement, density measurement and scanning electron microscopy (SEM). After electrolysis, density of the Bi_2O_3 based GDE was decreased due to reduction of Bi_2O_3 to Bi, its surface became relatively hydrophilic and showed new dendritic structures. The carbon-based GDE remained largely unchanged, but became slightly less hydrophobic after electrolysis.

The formate feed for subsequent electrosynthesis of hydrogen peroxide and thus PFA formation was generated as catholyte by *eCO$_2$RR* with Bi_2O_3 based GDEs (*cf.* table 3.1, stage V). They were operated at 150 mA cm^{-2} for 22 h in a gas-fed flow cell (5 cm^2 GDE, anolyte and catholyte were circulated and separated by a CEM) using 0.2 mol L^{-1} KH_2PO_4 / K_2HPO_4 (equimolar, pH ≈ 6.67) as both anolyte and catholyte (n = 3). Thereby, the catholyte reached a high concentration of formate (500.7 ± 0.6 mmol L^{-1}) and an acidic pH (4.12). This corresponded to a high overall FE (86.3 ± 0.3%), while higher peak FE (up to 90%) was achieved during electrolysis. Furthermore, stability of the GDE was relatively high as only minor concentrations of Bi^{3+} (catalyst) and Ni^{2+} (support material) were detected in the catholyte by ICP-OES. The catholyte was also screened for other metallic impurities that could potentially decompose hydrogen peroxide / PFA and traces of Cr^{3+} and Fe^{3+} originating from the supporting electrolyte were found.

The subsequent *eO$_2$RR* to hydrogen peroxide was carried out directly using the formate feed as catholyte with carbon-based GDEs in the same flow cell (n = 4). They were operated at 150 mA cm^{-2} for 6 h, whereby hydrogen peroxide reached high total concentration (1.27 ± 0.06 mol L^{-1}) and overall FE (85.3 ± 5.4%). PFA was formed *in-situ* with a relatively low yield (16.3 ± 2.2%), but in a concentration (82 ± 11 mmol L^{-1}) that exceeds those sufficient for disinfection. This represents the first benchmark for an all-electrochemical synthesis of PFA to the best of the authors' knowledge. To improve concentration and yield of PFA in future, the chemical equilibrium can be adjusted (*e.g.* concentration and ratio of reactants). In addition, stability of the carbon-based GDE was examined and the amount of metallic impurities (Cr^{3+}, Fe^{3+}, Ni^{2+}) was slightly increased due to cathodic corrosion of its support material (stainless steel). Nonetheless, their overall low concentration did not seem to have compromised hydrogen peroxide / PFA generation, especially in the presence of phosphate ions acting as possible chelating agents.[202]

To evaluate if catholyte from *eCO$_2$RR* impairs electrosynthesis of hydrogen peroxide and PFA generation, it was also carried out with a comparable feed containing formate of commercial origin. This demonstrated that formate feed from *eCO$_2$RR* results in slight improvements instead of performance losses for electrosynthesis of hydrogen peroxide and PFA generation.

Finally, the electric energy costs of the overall process were assessed for formate (1.35 ± 0.05 € kg^{-1}), hydrogen peroxide (1.53 ± 0.11 € kg^{-1}) and hydrogen peroxide / PFA (2.88 ± 0.13 € kg^{-1}) under recent and realistic assumptions (0.1723 € kWh^{-1}[203]). These costs were up to 3 times higher than fossil-based market prices for formic acid and hydrogen peroxide, which already include all costs beyond electricity (no comparison possible for PFA, as it is not a commercial product). Consequently, the energy demand of both *eCO$_2$RR* to formate and *eO$_2$RR* to hydrogen peroxide must be addressed alongside yield and concentration of PFA. Nonetheless, an all-electrochemical synthesis of PFA is a feasible approach to generate value-added compounds with formic acid from *eCO$_2$RR*.

ChemSusChem

Research Article
doi.org/10.1002/cssc.202500180

Chemistry Europe
European Chemical Societies Publishing

www.chemsuschem.org

All Electrochemical Synthesis of Performic Acid Starting from CO_2, O_2, and H_2O

Ida Dinges, Markus Pyschik, Julian Schütz, Selina Schneider, Elias Klemm, Siegfried R. Waldvogel, and Markus Stöckl*

Driven by anthropogenic climate change, innovative approaches to defossilize the chemical industry are required. Herein, the first all-electrochemical feasibility study for the complete electrosynthesis of the strong oxidizer and effective disinfectant performic acid is presented. Its synthesis is achieved solely from CO_2, O_2, and H_2O in a two-step process. Initially, CO_2 is electrochemically reduced to formate employing Bi_2O_3-based gas diffusion electrodes in a phosphate-buffered electrolyte. Thereby, high formate concentration (500.7 ± 0.6 mmol L^{-1}) and high Faradaic efficiency ($86.3 \pm 0.3\%$) are achieved at technically relevant current density (150 mA cm^{-2}). Subsequently, the formate acts as (storable) feed electrolyte for the second electrolysis step. Employing carbon-based gas diffusion electrodes, O_2 is reduced to H_2O_2 and performic acid is directly formed in situ. As before, high H_2O_2 concentration (1.27 ± 0.06 mol L^{-1}) and high Faradaic efficiency ($85.3 \pm 5.4\%$) are achieved. Furthermore, performic acid concentration suitable for disinfection is obtained (82 ± 11 mmol L^{-1}). In summary, this innovative feasibility study highlights the potential of combining electrochemical CO_2 reduction with H_2O_2 electrosynthesis, which could provide sustainable access to performic acid in the future.

1. Introduction

The pressing need for a transition to renewable energy sources and sustainable feedstocks has led to increased research into alternative chemical production processes. Electrochemical processes, in particular, are emerging as a promising route for achieving this goal, enabling the direct conversion of renewable electricity into value-added chemical products.[1–4] Such approaches offer not only a reduction in process emissions, but also the potential to integrate decentralized, onsite manufacturing that can complement renewable energy and systems.

One of the most compelling areas of electrochemical synthesis is the reduction of carbon dioxide (CO_2) and its implementation as a renewable feedstock in the chemical industry. Among the various products generated by the electrochemical CO_2 reduction reaction (eCO_2RR), formic acid and formate represent attractive intermediates due to their good storage and transport properties, as well as their versatile applications.[5–9] Thereby, the aqueous eCO_2RR can be performed efficiently using gas diffusion electrodes (GDEs), allowing high current densities up to 1.8 A cm^{-2},[10] Faradaic efficiencies (FE) exceeding 90%,[11–14] and operational times of 1000 h.[15]

Beyond its immediate use, formic acid/formate can serve as versatile platform chemical for synthesizing higher-value products combining subsequent chemical and biological processes. Exemplarily, the use as a feedstock in microbial synthesis offers the option to produce more complex and attractive products,[16–19] which has been demonstrated exemplarily for the synthesis of the biopolymer polyhydroxybutyrate (PHB) without the need for further downstream processing between eCO_2RR and the biosynthesis.[8,9] Another pathway for formic acid/formate is its utilization for the synthesis of the strong oxidizer and disinfectant performic acid (PFA),[20–23] which is obtained in the equilibrium reaction of formic acid and hydrogen peroxide. PFA is an attractive disinfectant for several sectors such as the food industry, healthcare, and wastewater treatment, as it is already very effective at low concentrations (<20 mg $L^{-1} \triangleq 0.32$ mmol L^{-1}).[24–27] It is also environmentally friendly, especially compared to halogen-based disinfectants. Decomposition leads to CO_2, O_2 and H_2O whereas the formation of harmful disinfection byproducts is largely unlikely.[27–31] The downside of its high reactivity is that it is not stable and safe enough for storage and needs to be produced onsite shortly before use from formic acid and H_2O_2.[26,31–35]

I. Dinges, M. Pyschik, J. Schütz, S. Schneider, M. Stöckl
Chemical Technology
DECHEMA Research Institute
Theodor-Heuss-Allee 25, 60486 Frankfurt am Main, Germany
E-mail: markus.stoeckl@dechema.de

I. Dinges, S. R. Waldvogel
Department for Electrosynthesis
Max Planck Institute for Chemical Energy Conversion
Stiftstraße 34-36, 45470 Mülheim an der Ruhr, Germany

E. Klemm
Institute of Technical Chemistry
University of Stuttgart
Pfaffenwaldring 55, 70569 Stuttgart, Germany

S. R. Waldvogel
Institute of Biological and Chemical Systems – Functional Molecular Systems (IBCS-FMS)
Karlsruhe Institute of Technology
Kaiserstraße 12, 76131 Karlsruhe, Germany

Supporting information for this article is available on the WWW under https://doi.org/10.1002/cssc.202500180

The traditional industrial anthraquinone process for H_2O_2 production is energy intensive, generates organic waste, and is associated with significant CO_2 emissions.[36] Facing these challenges, H_2O_2 syntheses via the two-electron oxygen reduction reaction (eO_2RR) using GDEs has emerged as an alternative approach to the anthraquinone process. Thereby, FE above 90%,[37–39] current densities up to 0.5 A cm^{-2},[39] and operational times in range of 200–1000 h[40–42] have been already reported.

If H_2O_2 is synthesized electrochemically in the presence of carboxylic acids such as formic acid, PFA is generated in situ. Recently, Schneider and Stöckl[23] published a comprehensive approach to the indirect and on-demand electrosynthesis of various peroxy acids via in situ generated H_2O_2 on GDEs, including PFA. After 24 h of electrosynthesis in a buffered system with 1 wt% H_3PO_4, 1.47 mol L^{-1} H_2O_2, and 0.24 mol L^{-1} PFA have been obtained with FEs of 37.5% and 6.1% (combined FE = 43.6%), respectively.

With this study, the first innovative all-electrochemical feasibility study for the complete electrosynthesis of PFA from CO_2, O_2, and H_2O through a two-step process utilizing GDEs is presented (cf. **Figure 1**). In the first step, CO_2 is electrochemically reduced to formate, which then acts as (storable) feed electrolyte in the second step, where O_2 is reduced to H_2O_2 and PFA is formed in situ. The authors thereby continue the findings of their previous study, where it was shown that phosphate ions/phosphoric acid and a buffered electrolyte are beneficial for PFA synthesis,[23] leading to the initial eCO_2RR in a phosphate-buffered electrolyte solution.

This approach not only highlights the potential of combining CO_2 reduction with H_2O_2 synthesis, but demonstrates the advantages of electrochemical processes like decentralized and on-demand production using the example of PFA, a highly effective oxidant and disinfectant that is not stable and safe enough for storage.

2. Results and Discussion

2.1. GDE Fabrication and Characterization for eCO_2RR and eO_2RR

GDEs for eCO_2RR were fabricated by heat pressing a catalyst mixture onto Ni foam as support material and current collector according to the oxygen-depolarized cathode (ODC) technology developed by Covestro.[43] The catalyst mixture consisted of Bi_2O_3 nanopowder (≈200 € kg^{-1}) as electrocatalyst and polytetrafluoroethylene (PTFE, ≈50 € kg^{-1}) powder as a hydrophobic binder. Taking contemporary costs into account, the GDE's material cost was estimated at 474 € m^{-2}, of which Ni foam (≈338 € m^{-2}) accounts for 71.3%. In total, three GDEs ($n = 3$) were fabricated for formate feed generation via eCO_2RR. The reproducibility of the predominantly manual fabrication method was sufficient, resulting in GDEs with catalyst loading b (Bi_2O_3, wt%) = 65.7 ± 0.7 mg cm^{-2} and thickness $d = 523 \pm 11$ µm ($n = 3$). Furthermore, no influence of minor fabrication variations on GDE performance was observed.

GDEs for eO_2RR were fabricated in a similar manner as described above, their composition and part of the pressing protocol (excluding sintering at 340 °C) was based on Kopljar et al.[44] The catalyst mixture consisted of acetylene black powder (≈320 € kg^{-1}) as carbon-based electrocatalyst and PTFE powder as binder. The mixture was pressed onto stainless steel mesh (≈10 € m^{-2}) using a cylindrical mask. Afterward, GDEs were treated in a heat press to improve their mechanical stability. In total, eight GDEs ($n = 8$) were fabricated with a catalyst loading of $b = 26.1 \pm 0.5$ mg cm^{-2} and a thickness of $d \approx 600 \pm 10$ µm. Based on recent prices, the GDE's material cost was estimated at 62 € m^{-2}.

Both fabricated GDE types were characterized before and after electrolysis by contact angle measurement, density measurement, and scanning electron microscopy (SEM). Exemplary results are summarized in **Figure 2**.

The pristine Bi_2O_3 GDE was bright yellow in color, had a contact angle of 136.2 ± 0.3° ($n = 2$) and a density of 7.060 ± 0.002 g cm^{-3}

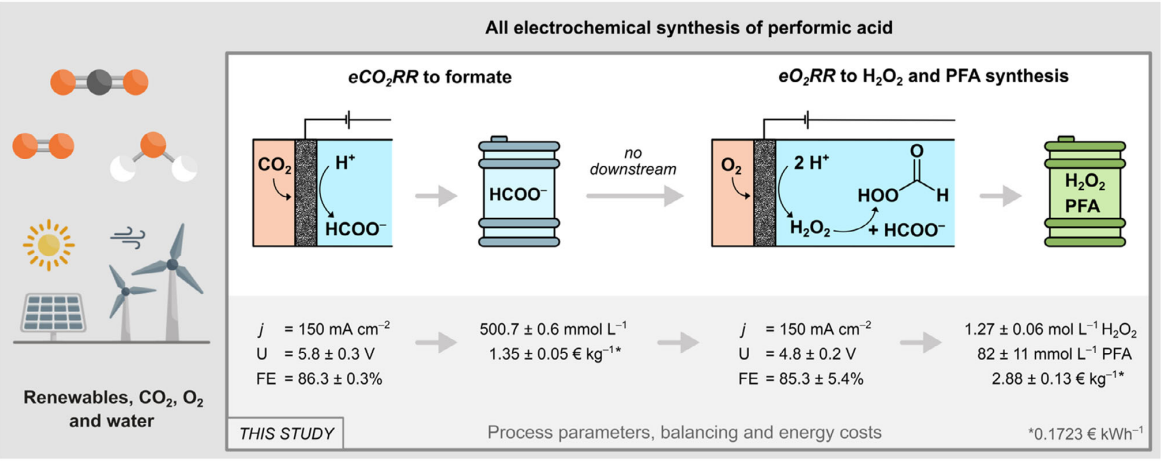

Figure 1. Schematic illustration and key process data of the overall process combination of the electrochemical CO_2 reduction reaction (eCO_2RR) to formate with the electrochemical O_2 reduction reaction (eO_2RR) to H_2O_2 to synthesize PFA using renewable energy sources. Resulting costs for formate and H_2O_2/PFA were based on a recent energy price.[47] Abbreviations: j = current density, U = average cell voltage, FE = Faradaic efficiency.

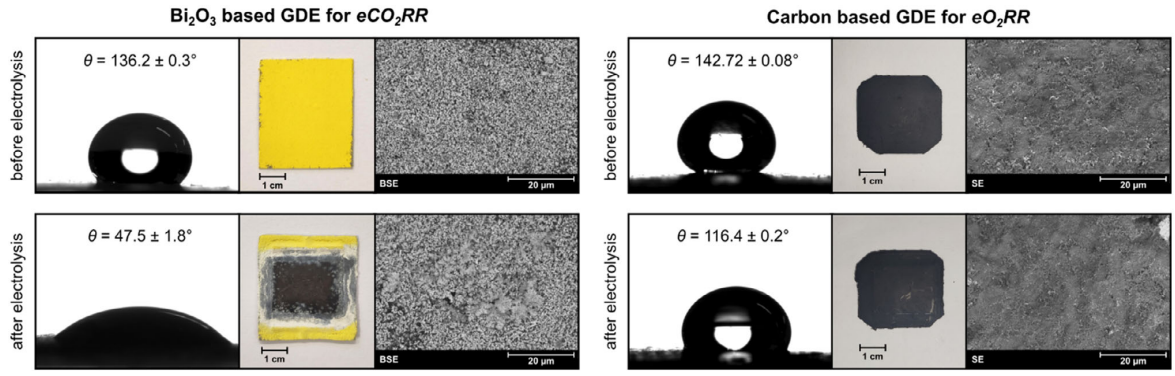

Figure 2. Fabricated GDE for eCO_2RR (left) and eO_2RR (right) and their characterization before and after electrolysis using SEM imaging (BSE = back scattering electrons, SE = secondary electrons) and contact angle measurements.

($n = 3$), and showed evenly distributed, mostly round Bi_2O_3 particles in the SEM (back-scattering electrons) image. After electrolysis, the GDE showed a black discoloration of the area exposed in the flow cell during electrolysis. This was attributed to the reduction of Bi_2O_3 to elemental Bi at the beginning of the electrolysis, which was supported by X-ray diffraction results (cf. Supporting Information). Accordingly, the discolored GDE area had a lower density of $6.631 \pm 0.004\ g\ cm^{-3}$ ($n = 3$). The discoloration was further examined using SEM, whereby new dendritic structures were observed. Alongside or in addition to Bi_2O_3 reduction, cathodic corrosion[45] could have contributed to the change in the GDE's surface structure. Therefore, GDE stability was investigated and will be discussed later regarding feed characterization. Apart from optical changes, the GDE's contact angle decreased significantly to $47.5 \pm 1.8°$ ($n = 2$) after electrolysis. It therefore became relatively hydrophilic during electrolysis, which was expected due to electrowetting.

The carbon GDE for eO_2RR did not show significant optical differences or changes in the GDE surface via SEM either before or after electrolysis. However, the contact angle changed from $142.72 \pm 0.08°$ ($n = 2$) to $116.4 \pm 0.2°$ ($n = 2$) after electrolysis. Consequently, this GDE type was also wetted during electrolysis but remained relatively hydrophobic compared to Bi_2O_3 GDEs. Moreover, the initial GDE density of $3.094 \pm 0.004\ g\ cm^{-3}$ ($n = 3$) increased to $3.270 \pm 0.001\ g\ cm^{-3}$ ($n = 3$). This density increase might have been caused by salt residues within the GDE, although no significant GDE swelling was observed.

2.2. eCO_2RR to Formate

To generate the formate feed for subsequent H_2O_2 electrosynthesis and PFA generation, eCO_2RR was carried out with Bi_2O_3 GDEs in a gas-fed flow reactor (divided cell, cf. Experimental Section) using $0.2\ mol\ L^{-1}$ KH_2PO_4/K_2HPO_4 (equimolar, pH ≈ 6.67) as both anolyte and catholyte. Phosphate buffer was chosen as a supporting electrolyte based on the results from Schneider and Stöckl[23] for peroxy acid synthesis using electrochemically generated H_2O_2. Furthermore, promising results were obtained using this electrolyte with Sn-based GDE.[9] Generally, the aim was to generate a feed with high formate concentration (>0.5 mol L^{-1}) at high FE (>85%). For this purpose, all electrolyses were run 22 h at $150\ mA\ cm^{-2}$. **Figure 3** contains the courses of formate concentration and FE in the catholyte.

Formate concentration increased linearly over time, its course was fitted in two intervals to obtain the respective formate production rate. It shows the rate declined about 20% from $24.4 \pm 0.2\ mmol\ L^{-1}\ h^{-1}$ (interval 1 = 1–5 h, ≙$113 \pm 1\ mg\ h^{-1}\ cm^{-2}$) to $19.5 \pm 0.7\ mmol\ L^{-1}\ h^{-1}$ (interval 2 = 20–22 h, ≙$89.8 \pm 3.2\ mg\ h^{-1}\ cm^{-2}$) during runtime. This decline could be attributed to presumed formate mass transport limitations within the GDE's pore system, which would increase the influence of the parasitic hydrogen evolution reaction (HER). Additionally, the decline could also be caused by a possible decrease in the

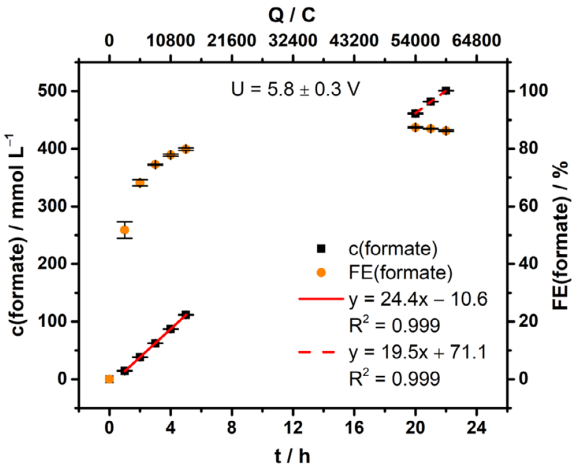

Figure 3. Concentration and FE course of formate for formate electrosynthesis ($n = 3$). The formate concentration course was fitted linearly in two intervals: $t = 1$–5 h (red, solid line) and $t = 20$–22 h (red, dashed line). Electrolysis parameters: constant current density $j = 150\ mA\ cm^{-2}$, runtime = 22 h (≙59,400 C), electrolyte = 0.2 mol L^{-1} KH_2PO_4/K_2HPO_4, initial V (catholyte, anolyte) = 500 mL each, cathode (GDE) = 87.5 wt% Bi_2O_3, 12.5 wt% PTFE on Ni-foam, reference electrode = reversible hydrogen electrode (RHE), anode = mixed Ir-oxide on a Ti-grid (Platinode EP, Type 177, Umicore).

GDE's stability during electrolysis (cf. feed characterization). Nonetheless, a final formate concentration of 500.7 ± 0.6 mmol L^{-1} ($n = 3$) was achieved.

Moreover, formate FE shows a nonlinear increase in the first 5 h runtime, especially the FE at 1 h is rather low with 52 ± 3% ($n = 3$). On the one hand, this is likely caused by partial consumption of supplied charge to reduce Bi_2O_3 to Bi. On the other hand, the GDE's electrowetting behavior could have contributed to the low initial FE. Nonetheless, to reach an overall FE of 79.9 ± 0.5% ($n = 3$) during the first 5 h, the FE per hour must have been close to 90% after the initial first hour. Consequently, the Bi_2O_3 type GDEs fabricated herein have a peak FE performance of close to 90%. Overall, 86.3 ± 0.3% ($n = 3$) was achieved as final formate FE in 22 h runtime.

Regarding energy demand, electrolyses were run with an average cell voltage of 5.8 ± 0.3 V ($n = 3$). This relatively high cell voltage was mainly caused by ohmic losses in the anode chamber, as a nonzero-gap anode was used for the oxygen evolution reaction (OER) as counter reaction, the GDEs' average potential was only −1.21 + 0.03 V versus RHE ($n = 3$, cf. Supporting Information). However, the GDEs' potential is also relatively high, possibly due to bismuth's low electric conductivity (0.936×10^6 S m^{-1} at 298 K).[46] In total, electrolyses consumed 96 ± 4 Wh ($n = 3$) of electric energy. Hence, formate electrosynthesis required 7.9 ± 0.3 kWh kg^{-1}, which corresponds to 1.35 ± 0.05 € kg^{-1} formate (no downstream processing etc., 0.1723 € kWh^{-1},[47] cf. Figure 1). This is higher than market prices for fossil-based concentrated formic acid such as 0.37 and 0.69 € kg^{-1} (0.40 $ kg^{-1}[48] and 0.74 $ kg^{-1},[49] respectively with 1 € ≙ 1.08 $). Consequently, lowering cell voltage and thereby energy demand of *eCO₂RR* are essential to compete with current fossil-based market prices. As discussed above, the integration of a zero-gap anode could lower cell voltage significantly.

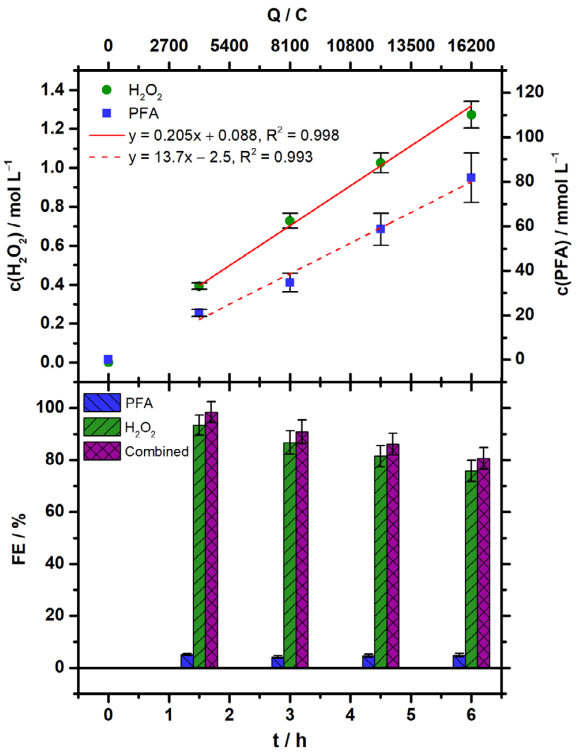

Figure 4. Concentration and FE course of H_2O_2 and PFA for H_2O_2 electrosynthesis and PFA generation ($n = 4$). Electrolysis parameters: constant current density $j = 150$ mA cm^{-2}, runtime = 6 h (≙16,200 C), catholyte = formate containing catholyte originating from *eCO₂RR* to formate (50 mL), anolyte = 0.5 mol L^{-1} $HClO_4$ (50 mL), cathode (GDE) = 65.5 wt% acetylene black, 34.5 wt% PTFE on stainless steel mesh, reference electrode = reversible hydrogen electrode (RHE), anode = mixed Ir-oxide on a Ti-grid (Platinode EP, Type 177, Umicore).

2.3. *eO₂RR* to H_2O_2 and PFA Synthesis

In the next step, the generated formate feed (pH ≈ 4.12, formic acid $pK_a = 3.75$ at 25 °C)[50] was used as catholyte for H_2O_2 electrosynthesis and PFA generation. It was carried out with the same flow cell setup as above, but employing carbon-based GDEs.

All electrolyses were run 6 h at 150 mA cm^{-2}, catholyte samples were taken every 1.5 h to determine H_2O_2 and PFA ($pK_a = 7.3$ at 25 °C)[50] concentrations by two-step titration[51] (H_2O_2 was first quantified by cerimetry and then PFA by iodometry, $n = 3$ for each sample). Direct FE for H_2O_2 and indirect FE for PFA were calculated based on their determined amounts and under the assumption that H_2O_2 and formate react equimolar with each other to form PFA (cf. Equation (2), Experimental Section). A rapid adjustment of the reaction's equilibrium was assumed based on Schneider and Stöckl[23] results. The combined FE therefore corresponds to the actual FE of H_2O_2 electrosynthesis. **Figure 4** summarizes the concentration and corresponding FE courses obtained during electrolysis ($n = 4$).

H_2O_2 concentration increased linearly over time up to 1.27 ± 0.06 mol L^{-1} ($n = 4$) in 6 h. After initial GDE conditioning, a production rate of 20.5 ± 0.9 mmol L^{-1} h^{-1} (≙6.97 ± 0.31 mg h^{-1} cm^{-2}) was reached ($t = 1.5$–6 h). This was accompanied by a continuous increase in PFA concentration (13.7 ± 1.2 mmol L^{-1} h^{-1}, $t = 1.5$–6 h) to finally 82 ± 11 mmol L^{-1} ($n = 4$). Despite the concentration's increase, H_2O_2 FE declined by about 17% from initially 93 ± 4% ($n = 4$) down to 76 ± 5% ($n = 4$) during runtime (50 mL catholyte volume assumed). This also applies to the combined FE, so the actual H_2O_2 FE, as the PFA's indirect FE remains nearly constant at 4–5% due to its reaction equilibrium. However, the final H_2O_2 FE had to be corrected to account for an observed increase in catholyte volume after electrolysis. Thereby, a combined H_2O_2 FE of 85.3 ± 5.4% ($n = 4$) was achieved in 6 h runtime. The FE balance is most likely closed by parasitic HER, but four-electron oxygen reduction to H_2O and/or H_2O_2 decomposition during electrolysis cannot be fully excluded. However, significant decomposition of H_2O_2/PFA after electrolysis was not indicated (e.g., gas evolution/titration results, cf. Supporting Information).

Electrolyses were run with an average cell voltage of 4.8 ± 0.2 V ($n = 4$) consuming 21.5 ± 0.6 Wh ($n = 4$) of electric energy. As before, this is a relatively high cell voltage caused by the ohmic losses due to OER at the nonzero-gap anode, the GDEs' potential was only −1.4 + 0.5 V versus RHE ($n = 4$, cf. Supporting Information). Consequently, H_2O_2 required 8.9 ± 0.6 kWh kg^{-1}

($n = 4$) corresponding to 1.53 ± 0.11 € kg^{-1} as electric energy cost (no downstream processing etc., 0.1723 € kWh^{-1},[47] cf. Figure 1). In comparison, fossil-based market prices for concentrated H_2O_2 are in the range of 0.64–1.1 € kg^{-1} (700–1200 \$ t^{-1}, with 1 ≙ 1.08 \$).[52] For the target byproduct PFA, a yield of $16.3 \pm 2.2\%$ ($n = 4$) was obtained. To achieve higher PFA concentrations/yields, higher concentrations of H_2O_2 and formate are necessary. This is also supported by Greenspan's[53] results on PFA formation. Taking presumed formate and H_2O_2 energy costs into account, the H_2O_2/PFA product solution cost added up to 2.88 ± 0.13 € kg^{-1} ($n = 4$). As PFA is usually generated onsite of its application, no commercial price was available as reference.

For comparison, H_2O_2 electrosynthesis for PFA generation was also performed with a reference electrolyte (R) based on the formate feed generated via *eCO₂RR*. It was prepared from commercially available compounds and contained 0.2 mol L^{-1} KH_2PO_4/K_2HPO_4 (equimolar) and 0.5 mol L^{-1} HCOOK/HCOOH (equimolar) in 1 wt% H_3PO_4. It was adjusted to $pH = 4.13 \pm 0.05$ with KOH. Using (R) as catholyte, H_2O_2 and PFA showed concentration and FE courses similar to the results presented above, whereas overall values were slightly lower. In short, a combined H_2O_2 FE of $78 \pm 7\%$ ($n = 4$) was obtained in combination with $13.7 \pm 0.8\%$ ($n = 4$) PFA yield. Hence, the formate feed can be generated via *eCO₂RR* with slight improvements instead of performance losses for H_2O_2 electrosynthesis and PFA generation. Details are provided (Section S3.2.2, Supporting Information).

So far, only a few results have been published on (indirect) electrochemical PFA synthesis. Recently, Sun et al.[54] conceptually reported an all-electrochemical PFA synthesis with parallel *eCO₂RR* and *eO₂RR* using their trifunctional indium-based catalyst/electrolysis system. Furthermore, Kolyagin et al.[20] used 1.5 mol L^{-1} formic acid (+0.2 mol L^{-1} K_2SO_4 and 0.05 mol L^{-1} H_2SO_4) as electrolyte solution for *eO₂RR* to H_2O_2 with a carbon-based GDE. Thereby, they achieved 1.8 mol L^{-1} H_2O_2 (55% FE) and 6.5 mmol L^{-1} PFA in 7 h electrolysis at 100 mA cm^{-2}.

Schneider and Stöckl[23] recently published a new benchmark for the indirect electrosynthesis of PFA among various peroxy acids via in situ generated H_2O_2 on commercial carbon black GDEs, as mentioned in the introduction. Thereby, 0.77 mol L^{-1} H_2O_2 (69% FE) and 0.14 mol L^{-1} PFA (13% FE) were achieved in 6 h at 100 mA cm^{-2} with 1 mol L^{-1} HCOOH/HCOOK (+1 wt% H_3PO_4) as electrolyte solution. This corresponded to a combined FE of 82% for H_2O_2 electrosynthesis. Compared to these previous results, H_2O_2 concentration (1.27 ± 0.06 mol L^{-1}) and combined FE ($85.3 \pm 5.4\%$) were improved at increased current density (150 mA cm^{-2}) herein. In contrast, PFA concentration (82 ± 11 mmol L^{-1}) was lower, which is most probably attributed to the lower initial formate concentration of the formate feed used as electrolyte solution. Nonetheless, 82 ± 11 mmol L^{-1} PFA represents the first benchmark for an all-electrochemical approach to PFA synthesis using CO_2, O_2, and H_2O to the best of the authors' knowledge. Even though there is space for improvement in terms of electrolysis and reaction/equilibrium adjustment to reach higher PFA concentrations, the obtained PFA/H_2O_2 mixture could most likely already be applied for disinfection. On the one hand, far lower PFA concentrations (<20 mg L^{-1} ≙ 0.32 mmol L^{-1})[24,26,27] have been reported as sufficient for disinfection. On the other hand, a mixture of H_2O_2, formic acid, and PFA could be advantageous, as synergistic effects have been reported for comparable mixtures.[55]

2.4. Feed Characterization/GDE Evaluation

After electrolysis, both formate feed and H_2O_2/PFA product solution were further examined for characterization and to evaluate GDE stability. On the one hand, K^+ and PO_4^{3-} concentrations were determined by ion chromatography (IC) to examine possible differences compared to their initial concentrations. These results were also used to prepare reference electrolyte (R) as formate feed substitute for H_2O_2 electrosynthesis and PFA generation. On the other hand, all solutions were screened via inductively coupled plasma atomic emission spectroscopy (ICP-OES) for metal ions originating from the GDEs as well as other impurities that could decompose H_2O_2/PFA. Detected target elements were Bi (electrocatalyst *eCO₂RR*), Ni (support material *eCO₂RR*/*eO₂RR*), Cr and Fe (support material *eO₂RR*, respectively). Hence, their concentrations were quantified via calibration to investigate cathodic corrosion[45] and thus GDE stability. The characterization results are summarized in **Table 1**.

IC analysis revealed the formate feed's PO_4^{3-} concentration was slightly lower (7%) than the initial phosphate buffer, which is due to an increase in volume by osmosis during electrolysis. Moreover, PO_4^{3-} concentration decreases further by about 20% during *eO₂RR*. This decrease cannot be explained solely by a volume increase or by losses due to a concentration gradient to the anolyte ($HClO_4$), as the anolyte's phosphate concentrations remained below 0.8 mmol L^{-1} (cf. Section S1.12, Supporting Information).

Besides, K^+ concentration was almost doubled after *eCO₂RR*. Nearly all K^+ ions are found in the formate feed due to migration, their molar amount in the electrolyte system was constant. In contrast, K^+ concentration was about 22% lower in the H_2O_2/PFA product solution. Some K^+ was found in the anolyte (12.6 ± 1.8 mmol L^{-1}, $n = 3$) but its molar amount was not constant.

Although no GDE swelling was observed, it was presumed both K^+ and PO_4^{3-} discrepancies were caused by salt precipitation

Table 1. Catholyte/feed composition before and after formate as well as H_2O_2 electrosynthesis for PFA generation. K^+ and PO_4^{3-} concentrations were determined via IC and Bi^{3+}, Cr^{3+}, Fe^{3+}, and Ni^{2+} concentrations were quantified via ICP-OES.

	$c(K^+)$ [mmol L^{-1}]	$c(PO_4^{3-})$ [mmol L^{-1}]	$c(Bi^{3+})$ [μmol L^{-1}]	$c(Cr^{3+})$ [μmol L^{-1}]	$c(Fe^{3+})$ [μmol L^{-1}]	$c(Ni^{2+})$ [μmol L^{-1}]
0.2 mol L^{-1} KH_2PO_4/K_2HPO_4 ($n = 1$)	286.2	197.5	0	0.270 ± 0.013	2.71 ± 0.05	0.13 ± 0.04
Formate feed ($n = 3$)	542 ± 6	183.4 ± 0.4	0.6 ± 0.4	0.224 ± 0.004	1.67 ± 0.15	0.41 ± 0.17
H_2O_2/PFA solution ($n = 4$)	423 ± 28	147 ± 10	0.18 ± 0.06	0.23 ± 0.04	1.83 ± 0.14	0.55 ± 0.19

within the carbon-based GDE. This hypothesis is supported by the GDEs' increased density after eO_2RR as discussed previously.

For ICP-OES analysis, the phosphate buffer was examined before characterization of formate feed and product solution. It already contained traces of the identified target elements Cr, Fe, and Ni, which originate from the compounds used for electrolyte preparation. Besides, ICP-OES analysis found only traces of dissolved Bi in the formate feed after eCO_2RR. Its concentration was even lower after eO_2RR due to dilution, as expected for carbon-based GDEs. In general, these traces were above detection but below quantification limit, which resulted in relatively high standard deviations (30–40%). Furthermore, quantification was challenging due to strong matrix effects, as it was observed that Bi^{3+} partly precipitated as $BiPO_4$ in standards containing matrix (cf. Section S1.11, Supporting Information). Consequently, most $BiPO_4$ could have already precipitated during electrolysis, although no precipitates were observed. Therefore, the extent of Bi's cathodic corrosion cannot be fully assessed but is most likely overall very low, as other studies on Bi as electrocatalyst also suggest.[56] Additionally, the previously discussed possible loss of GDE stability can neither be confirmed nor ruled out as explanation for performance decline during electrolysis. However, as the formate feed's Bi^{3+} concentration was at least below 1 μmol L^{-1}, a significant influence on H_2O_2/PFA generation seemed unlikely. Moreover, the feed's Cr^{3+} and Fe^{3+} concentrations were lower compared to their initial ones due to dilution. In contrast, Ni^{2+} concentration was increased by 32% to 0.41 ± 0.17 μmol L^{-1} ($n = 3$). This shows the Bi_2O_3 GDE's support material Ni foam was in contact with catholyte solution and was slightly affected by cathodic corrosion.

Further analysis of the H_2O_2/PFA solution after eO_2RR revealed Cr^{3+} concentration remained relatively constant, while Fe^{3+} and Ni^{2+} concentrations increased slightly. As the feed is diluted during electrolysis (≈5%), molar amounts of all three elements were increased by cathodic corrosion of the stainless steel mesh (1.4301) serving as support material. Nonetheless, all concentrations were rather low and did not seem to have compromised H_2O_2/PFA generation, especially in the presence of phosphate ions acting as possible chelating agents.[57]

However, the future aim should be to minimize overall metal ion impurities to avoid potential efficiency losses, as these could potentially catalyze H_2O_2/PFA decomposition.[31,58–60]

Furthermore, Schneider and Stöckl[23] hypothesized that leached Ni may have affected their H_2O_2 electrosynthesis for PFA generation. Although only a total of 0.55 ± 0.19 μmol L^{-1} Ni was leached from the self-fabricated GDEs presented, future GDEs should ideally be realized without metallic support material (without compromising performance and stability).

3. Conclusion

In this study, the first all-electrochemical PFA synthesis has been achieved by coupling eCO_2RR to formate with eO_2RR to H_2O_2 without any intermediate downstream processing.

The formate feed was generated as catholyte by electrochemical CO_2 reduction using Bi_2O_3 GDEs (474 € m^{-2}), which were self-fabricated by a fast, facile, and reproducible fabrication method. The GDEs were operated at 150 mA cm^{-2} for 22 h to generate a feed containing 500.7 ± 0.6 mmol L^{-1} ($n = 3$) formate with a pH of 4.12. Thereby, an overall formate FE of $86.3 \pm 0.3\%$ ($n = 3$) was achieved, while a peak FE up to 90% was reached. Furthermore, no significant cathodic corrosion was observed for the GDEs, Bi^{3+} concentration was at least below 1 μmol L^{-1}, and Ni^{2+} concentration was below 0.6 μmol L^{-1}.

The subsequent eO_2RR to H_2O_2 was carried out with the formate feed as catholyte at self-fabricated, inexpensive carbon GDEs (62 € m^{-2}). They were operated at 150 mA cm^{-2} for 6 h without significant cathodic corrosion, whereby 1.27 ± 0.06 mol L^{-1} ($n = 4$) H_2O_2 and 82 ± 11 mmol L^{-1} ($n = 4$) PFA were reached. This corresponded to an overall H_2O_2 FE of $85.3 \pm 5.4\%$ ($n = 4$) and a PFA yield of $16.3 \pm 2.2\%$ ($n = 4$). The achieved PFA concentration represents the first benchmark for an all-electrochemical PFA synthesis to the best of the authors' knowledge. Furthermore, it already exceeds concentrations suitable for disinfection (<20 mg L^{-1} ≙ 0.32 mmol L^{-1}).[24,26,27]

Finally, electric energy costs of the overall process were assessed for formate (1.35 ± 0.05 € kg^{-1}), H_2O_2 (1.53 ± 0.11 € kg^{-1}), and H_2O_2/PFA (2.88 ± 0.13 € kg^{-1}) under recent and realistic assumptions (0.1723 € kWh^{-1}[47]). These costs were ≈2–3 times higher than fossil-based market prices for formic acid and H_2O_2, which already include all costs beyond electricity. Consequently, the energy demand for eCO_2RR to formate and eO_2RR to H_2O_2 must be reduced in the future. Nonetheless, this feasibility study demonstrates that an all-electrochemical PFA synthesis from CO_2, O_2, and H_2O is a promising approach for new sustainable chemical production processes, which should be investigated further to evaluate potential technical exploitation.

4. Experimental Section

Gas Diffusion Electrodes: Bi_2O_3-Based GDE

The GDEs were fabricated by pressing the catalyst mixture onto Ni foam as support material. The catalyst mixture (30.00 g) consisted of Bi_2O_3 (87.5 wt%, 26.25 g, purity 99.9%, particle size ≈80 nm, US Research Nanomaterials, Houston, USA) and polytetrafluoroethylene (PTFE) powder (12.5 wt%, 3.75 g, Dyneon PTFE TF 2072Z, 3M, Saint Paul, USA). The mixture was homogenized in a knife mill (30 s, 25,000 rpm, 2×). Afterward, it (4.00 g) was equally distributed onto Ni foam ($d = 1.4$ cm, 3.5 cm × 4.0 cm × 14 cm^2, Ni-5763, density 420–450 g m^{-2}, Recemat BV, Dodewaard, Netherlands) with a sieve and a stencil (cut-out 3.5 cm × 4.0 cm). The GDE blank was placed in between ordinary baking sheet and compressed in a heat press (plate temperature 120 °C, pressure 10 bar, duration 60 s). Excess material was removed, the GDE's catalyst loading b was determined by differential weighing, and its thickness d was measured at the center point.

Gas Diffusion Electrodes: Carbon-Based GDE

The GDEs were fabricated by pressing catalyst mixture consisting of carbon catalyst (65.5 wt%, 1.97 g, acetylene black, 100% compressed, >99.9%, Alfa Aesar, Haverhill, USA) and PTFE powder (34.5 wt%, 1.03 g, as above) onto a stainless steel mesh (Material 1.4301, mesh size = 0.5 cm, $d = 240$ μm, 3.2 cm × 3.2 cm, Haver & Boecker, Oelde, Germany) as support material. The catalyst mixture was homogenized (as above) and placed (500 mg) in a cylindrical mask ($d = 40$ mm) containing stainless steel mesh. The GDE blank was

compressed in a hydraulic press (pressure 3.5 t, 60 s, RT followed by pressure 7 t, 180 s, RT). Afterward, the GDEs were treated in a heat press (plate temperature 120 °C, pressure 10 bar, duration 180 s) to improve their mechanical stability. Catalyst loading *b* and thickness *d* of the GDEs were determined as described above.

Gas Diffusion Electrodes: Scanning Electron Microscopy

SEM imaging was performed on Flex SEM 1000 II (Hitachi, Tokyo, Japan) using the following conditions: 15 kV (accelerating voltage), ×2000 (magnification), 6–8 mm (viewing height), 40 (spot size), and SE and BSE (detector). All images were taken at the GDE's geometrical center point.

Gas Diffusion Electrodes: Contact Angles

Contact angles were determined with the OCA 15 plus (DataPhysics Instruments, Filderstadt, Germany). Using the sessile drop method, a droplet of H_2O (50 μL) was placed at the GDE's center point. Contact angles were calculated by fitting the droplet edges with a Young–Laplace model.

Gas Diffusion Electrodes: Density

GDE densities were determined with the gas pycnometer BELPYCNO L (Microtrac Retsch, Haan, Germany) using helium as probing gas. Samples were measured ($n = 3$) at 20 °C in sample chamber S (20 cm^3) using glass beads as filler volume (≈50%).

Formate Electrosynthesis

The same electrochemical flow reactor (divided cell with a cation exchange membrane) and electrolysis setup as described in Dinges et al.[9] were used for formate electrosynthesis.

All formate electrosyntheses were performed for 22 h at 150 mA cm^{-2} (750 mA in total) using a power supply unit (NGP804, Rohde & Schwarz, Munich, Germany), which recorded cell voltage, current, and power. The GDE's electrode potential was referenced to RHE without compensation for *iR* losses.

CO_2 (N4.5) was supplied to the GDE at a flow rate of 10–15 mL min^{-1} and an initial overpressure in the range of 110–150 mbar relative to ambient pressure.

The buffer 0.2 mol L^{-1} KH_2PO_4/K_2HPO_4 (equimolar) served as electrolyte, both anolyte and catholyte had a starting volume of 500 mL (volumetric flask, ISO 1042). They were circulated continuously at a flow rate of ≈40 mL min^{-1} between the flow reactor and reservoir, respectively. During electrolysis, catholyte samples (1 mL) were taken hourly in the first five ($t = 0$–5 h) and the last three ($t = 20$–22 h) hours to monitor formate concentration and calculate the corresponding FE. After electrolysis, the catholyte volume was determined by its weight and density ($n = 3$). Catholyte-containing formate was stored at 5 °C until its application for H_2O_2 electrosynthesis and PFA generation. The GDE was rinsed with H_2O and dried at RT. Further details are provided (Section S1.4, Supporting Information).

Formate Quantification by High-Performance Liquid Chromatography

Formate concentrations were determined via HPLC (LC-20AD, SIL-20AC HT, CBM-20A, CTO-20AC, SPD-M20A - Shimadzu, Kyoto, Japan).

The HPLC unit was equipped with a Rezex ROA-Organic Acid (8%) column (300 mm × 7.8 mm, Phenomenex, Torrance, USA) and the following method parameters were employed: 5 mmol L^{-1} H_2SO_4, 0.6 mL min^{-1}, 30 °C, 30 ± 1 bar, photodiode array detector ($\lambda = 194$ nm), 14.9 min (retention time), 25 min (duration).

Formate standards were prepared by a dilution series from a stock solution, which was prepared with HCOONa (3.482 g, 51.2 mmol) in a volumetric flask (100 mL, ISO 1042). All formate standards (8, 16, 32, 64, 128, 256, 512 mmol L^{-1}) were measured ($n = 3$) and their signal areas fitted linearly ($R^2 = 0.9999$, fit forced through zero).

H_2O_2 Electrosynthesis for PFA Generation

The same flow reactor and electrolysis setup were used for H_2O_2 electrosynthesis as for formate electrosynthesis.

All electrolyses were performed for 6 h at 150 mA cm^{-2} (750 mA in total) using a power supply unit (HMC8043, Rohde & Schwarz, Munich, Germany), which recorded cell voltage and current. The GDE's electrode potential was referenced to RHE, without compensation of *iR* losses.

O_2 (N4.6) was supplied to the GDE with a flow rate of 20 mL min^{-1} and an initial overpressure of ≈90 mbar relative to ambient pressure.

Catholyte (Formate feed) and anolyte (0.5 mol L^{-1} $HClO_4$) had a starting volume of 50 mL each (measuring cylinder, 100 mL, ISO 4788) and were continuously circulated at a flow rate of ≈40 mL min^{-1} between the flow reactor and the reservoir. $HClO_4$ was selected as an anolyte to ensure sufficient proton supply to the catholyte. During electrolysis, electrolytes were sampled (1 mL) every 1.5 h to determine H_2O_2/PFA concentrations and calculate their corresponding FE. The catholyte's volume was determined after electrolysis in the same manner as described above. Further details are provided (Section S1.5, Supporting Information).

H_2O_2/PFA Quantification by Titration

The concentrations of H_2O_2 and PFA were determined using a two-step titration method derived from the procedure described by Greenspan and Mackellar.[51] First, the concentration of H_2O_2 was determined by cerimetry using $Ce(SO_4)_2$ ($c = 0.01$ mol L^{-1}). For this purpose, 5 drops of H_2SO_4 ($c = 5$ mol L^{-1}) and 70 μL ferroin ($c = 0.025$ mol L^{-1} in ethanol) as an indicator were added to the sample solution. The orange solution was titrated until a light blue color was observed. The concentration of PFA was then determined via iodometry with $Na_2S_2O_3$ ($c = 0.01$ mol L^{-1}). To the light blue solution, 0.1 mL of a KI solution ($c = 0.48$ mol L^{-1}) and a spatula tip of $(NH_4)_6Mo_7O_{24}{\cdot}4H_2O$ were added. After 15 min, the resulting reddish-brown suspension was slowly titrated until the color changed to light brown. Then 2–3 drops of starch solution (1 wt% v^{-1}) were added and titration continued until the color changed back to orange and no precipitate remained. The sample volumes were 0.2 mL (after 1.5 h), 0.1 mL (after 3.0 h), and 0.075 mL (after 4.5 and 6.0 h). Each titration was carried out in triplicates ($n = 3$) for the specified time and experiment.

Catholyte/Feed Characterization: Ion Chromatography

IC measurements to determine K^+ concentrations were performed on Dionex ICS-5000$^+$ DC (Pre column = Dionex IonPac CG17, Column = Dionex IonPac CS17, Analytical 2 × 250 mm, Suppressor = CERS 500, 2 mm, Thermo Fisher Scientific, Waltham, USA). Methanesulfonic acid (MSA) served as eluent with a gradient method (steps 1–4: 1. −5–0 min, 1.5 mmol L^{-1} MSA (preparation step); 2. 0–25 min, 1.5–2.1 mmol L^{-1} MSA; 3. 25–40 min, 6 mmol L^{-1} MSA; 4. 40–60 min, 1.5 mmol L^{-1} MSA) at 0.1 mL min^{-1} flow rate. Samples were diluted by factor 500 and K^+ (retention time = 34.9 min) was detected with a conductivity cell.

Standards were prepared by a dilution series of a stock solution. The stock solution was prepared with KCl (1.221 g ≙ 640 mg K^+) in a volumetric flask (1 L, ISO 1042). All standards (2, 4, 8, 16, 32, 64 ppm) were measured ($n = 3$) and their signal areas fitted linearly ($R^2 = 0.999$, fit forced through zero).

IC measurements to determine PO_4^{3-} concentrations were performed on Dionex Aquion system (Pre column = Dionex IonPac AS22, 4 × 50 mm, Column = Dionex IonPac AS22, 4 × 250 mm, Suppressor = ACRS 500 Suppressor, 4 mm).

The following isocratic method was used: 4.5 mmol L^{-1} Na_2CO_3/1.4 mmol L^{-1} $NaHCO_3$ (eluent), 1.2 mL min^{-1} (flow rate), 250 µL (injection volume), 15 min (duration), 9.3 min (retention time), conductivity cell (detector). Samples were diluted by factor 250.

PO_4^{3-} standards were prepared by a dilution series from a stock solution, which was prepared from an anion multielement standard (10 mL, Certipur, Anion multielement standard I, 1000 ppm F^-, PO_4^{3-}, Br^-, Merck, HC17168637) in a volumetric flask (50 mL, ISO 1042).

All PO_4^{3-} standards (25, 50, 100 mg L^{-1}) were measured ($n = 1$) and their signal areas fitted linearly ($R^2 = 0.999$, fit forced through zero).

Catholyte/Feed Characterization: Inductively Coupled Plasma Optical Emission Spectroscopy

ICP-OES measurements were performed in axial viewing mode on Agilent 5800 ICP-OES equipped with an SPS 4 Autosampler, a borosilicate double-pass spray chamber, and a Seaspray concentric glass nebulizer (Agilent Technologies, Santa Clara, USA).

All catholyte samples were measured without dilution except for acidification to 2 wt% HNO_3 (using 69 wt% HNO_3).

Standards to determine the concentrations of Bi^{3+} ($\lambda = 223.061$ nm), Cr^{3+} ($\lambda = 205.560$ nm), Fe^{3+} ($\lambda = 238.204$ nm), and Ni^{2+} ($\lambda = 231.604$ nm) were prepared by a dilution series of a stock solution (16 mg L^{-1}). The stock solution was prepared by combining the respective standards (10 mL each, 1000 mg L^{-1}, Single Element ICP-Standard-Solution, Carl Roth) in a volumetric flask (100 mL, ISO 1042) using 2 wt% HNO_3 for dilution. Afterward, the solution was diluted further with 2 wt% HNO_3 to 16 mg L^{-1} in a volumetric flask (50 mL, ISO 1042). This was followed by a dilution series by factor 2. Finally, each standard (0.125, 0.25, 0.5, 1, 2, 4, 8, 16 mg L^{-1}) was diluted again by factor 2 with a matrix solution (0.4 mol L^{-1} KH_2PO_4/K_2HPO_4, 0.5 mol L^{-1} HCOOH, 0.5 mol L^{-1} HCOOK in 2 wt% HNO_3). Thereby, a set of standards with a matrix based on the catholyte's composition was obtained. They were measured ($n = 5$) and their signal areas fitted linearly ($R^2 \geq 0.997$, fit forced through zero). Further details are provided (Section S1.11, Supporting Information).

Calculations

The FE for formate and H_2O_2 were calculated based on the determined amount of electrosynthesized components using Equation (1).

$$FE = \frac{F \cdot z \cdot n}{I \cdot t} \times 100\% \quad (1)$$

with FE = Faradaic efficiency, %; F = Faraday constant, A s mol^{-1}; z = number of transferred electrons ($z = 2$); n = amount of synthesized formate or H_2O_2, mol; I = current, A; t = electrolysis runtime, s.

The results for the different catholytes were averaged and their standard deviation was provided as uncertainty.

The indirect *FE* for PFA was determined under the assumption formic acid reacted equimolar in a chemical reaction with the electrochemically generated H_2O_2 to PFA using Equation (2).

$$H_2O_2 + HCOOH \rightleftharpoons HCOOOH + H_2O \quad (2)$$

The combined concentrations and *FE* of H_2O_2 and PFA were calculated by the addition of the individual mean values. The errors were determined using their standard deviations and Gaussian error propagation using Equation (3).

$$\sigma_{combined} = \sqrt{\sigma_{H_2O_2}{}^2 + \sigma_{PFA}{}^2} \quad (3)$$

Acknowledgements

The authors gratefully acknowledge the Federal Ministry of Food and Agriculture (2220NR113X) and the Federal Ministry of Education and Research (03XP0615C) for their financial support. Special thanks go to Jacqueline Patzsch and Abdelkarim Zaim for their support on IC measurements.

Open Access funding enabled and organized by Projekt DEAL.

Conflict of Interest

The authors declare no conflict of interest.

Data Availability Statement

Data available in article supplementary material.

Keywords: electrochemistry · formic acid · gas diffusion electrode · hydrogen peroxide · peroxides

[1] D. Pollok, S. R. Waldvogel, *Chem. Sci.* **2020**, *11*, 12386.
[2] a) A. Wiebe, T. Gieshoff, S. Möhle, E. Rodrigo, M. Zirbes, S. R. Waldvogel, *Angew. Chem., Int. Ed.* **2018**, *57*, 5594; b) A. Wiebe, T. Gieshoff, S. Möhle, E. Rodrigo, M. Zirbes, S. R. Waldvogel, *Angew. Chem.* **2018**, *130*, 5694.
[3] a) S. Möhle, M. Zirbes, E. Rodrigo, T. Gieshoff, A. Wiebe, S. R. Waldvogel, *Angew. Chem., Int. Ed.* **2018**, *57*, 6018; b) S. Möhle, M. Zirbes, E. Rodrigo, T. Gieshoff, A. Wiebe, S. R. Waldvogel, *Angew. Chem.* **2018**, *130*, 6124.
[4] N. Teetz, D. Holtmann, F. Harnisch, M. Stöckl, *Angew. Chem., Int. Ed.* **2022**, *61*, e202210596.
[5] K. Tedsree, T. Li, S. Jones, C. W. A. Chan, K. M. K. Yu, P. A. J. Bagot, E. A. Marquis, G. D. W. Smith, S. C. E. Tsang, *Nat. Nanotechnol.* **2011**, *6*, 302.
[6] M. Grasemann, G. Laurenczy, *Energy Environ. Sci.* **2012**, *5*, 8171.
[7] R. Hegner, K. Neubert, C. Kroner, D. Holtmann, F. Harnisch, *ChemSusChem* **2020**, *13*, 5295.
[8] M. Stöckl, S. Harms, I. Dinges, S. Dimitrova, D. Holtmann, *ChemSusChem* **2020**, *13*, 4086.
[9] I. Dinges, I. Depentori, L. Gans, D. Holtmann, S. R. Waldvogel, M. Stöckl, *ChemSusChem* **2024**, *17*, e202301721.
[10] A. Löwe, M. Schmidt, F. Bienen, D. Kopljar, N. Wagner, E. Klemm, *ACS Sustainable Chem. Eng.* **2021**, *9*, 4213.
[11] D. Kopljar, A. Inan, P. Vindayer, N. Wagner, E. Klemm, *J. Appl. Electrochem.* **2014**, *44*, 1107.
[12] X. Wang, S. Liu, H. Zhang, S. Zhang, G. Meng, Q. Liu, Z. Sun, J. Luo, X. Liu, *Chem. Commun.* **2022**, *58*, 7654.
[13] N. Han, P. Ding, L. He, Y. Li, Y. Li, *Adv. Energy Mater.* **2020**, *10*, 1902338.
[14] L. Li, Z. Liu, X. Yu, M. Zhong, *Angew. Chem., Int. Ed.* **2023**, *62*, e202300226.
[15] H. Yang, J. J. Kaczur, S. D. Sajjad, R. I. Masel, *J. CO2 Util.* **2020**, *42*, 101349.
[16] N. J. Claassens, C. A. R. Cotton, D. Kopljar, A. Bar-Even, *Nat. Catal.* **2019**, *2*, 437.
[17] O. Yishai, S. N. Lindner, J. Gonzalez De La Cruz, H. Tenenboim, A. Bar-Even, *Curr. Opin. Chem. Biol.* **2016**, *35*, 1.

[18] M. Stöckl, N. Claassens, S. Lindner, E. Klemm, D. Holtmann, *Curr. Opin. Biotechnol.* **2022**, *74*, 154.
[19] M. Stöckl, T. Lange, P. Izadi, S. Bolat, N. Teetz, F. Harnisch, D. Holtmann, *Biotechnol. Bioeng.* **2023**, *120*, 1465.
[20] G. A. Kolyagin, I. S. Vasil'eva, V. L. Kornienko, *Russ. J. Electrochem.* **2010**, *46*, 957.
[21] G. A. Kolyagin, V. L. Kornienko, *Russ. J. Electrochem.* **2015**, *51*, 185.
[22] M. Prieschl, S. B. Ötvös, C. O. Kappe, *ACS Sustainable Chem. Eng* **2021**, *9*, 5519.
[23] S. Schneider, M. Stöckl, *ACS Sustainable Chem. Eng.* **2024**, *12*, 5160.
[24] H. Heinonen-Tanski, H. Miettinen, *J. Food Process Eng.* **2010**, *33*, 1159.
[25] M. Mora, A.-M. Veijalainen, H. Heinonen-Tanski, *Sustainability* **2018**, *10*, 4116.
[26] P. Ragazzo, N. Chiucchini, V. Piccolo, M. Spadolini, S. Carrer, F. Zanon, R. Gehr, *Water Res.* **2020**, *184*, 116169.
[27] T. Karpova, P. Pekonen, R. Gramstad, U. Öjstedt, S. Laborda, H. Heinonen-Tanski, A. Chávez, B. Jiménez, *Water Sci. Technol.* **2013**, *68*, 2090.
[28] R. Gehr, D. Chen, M. Moreau, *Water Sci. Technol.* **2009**, *59*, 89.
[29] P. Ragazzo, D. Feretti, S. Monarca, L. Dominici, E. Ceretti, G. Viola, V. Piccolo, N. Chiucchini, M. Villarini, *Water Res.* **2017**, *116*, 44.
[30] J. Wang, J. Xu, J. Kim, C.-H. Huang, *Environ. Sci. Technol.* **2023**, *57*, 18898.
[31] C. Nabintu Kajoka, J. Gasperi, S. Brosillon, E. Caupos, E. Mebold, M. Oliveira, V. Rocher, G. Chebbo, J. Le Roux, *ACS ES&T Water* **2023**, *3*, 3121.
[32] D. Swern, *Chem. Rev.* **1949**, *45*, 1.
[33] P. Ragazzo, N. Chiucchini, V. Piccolo, M. Ostoich, *Water Sci. Technol.* **2013**, *67*, 2476.
[34] T. Luukkonen, S. O. Pehkonen, *Crit. Rev. Environ. Sci. Technol.* **2017**, *47*, 1.
[35] F. Ebrahimi, E. Kolehmainen, P. Oinas, V. Hietapelto, I. Turunen, *Chem. Eng. J.* **2011**, *167*, 713.
[36] a) J. M. Campos-Martin, G. Blanco-Brieva, J. L. G. Fierro, *Angew. Chem., Int. Ed.* **2006**, *45*, 6962; b) J. M. Campos-Martin, G. Blanco-Brieva, J. L. G. Fierro, *Angew. Chem.* **2006**, *118*, 7116.
[37] G. O. S. Santos, P. J. M. Cordeiro-Junior, I. Sánchez-Montes, R. S. Souto, M. S. Kronka, M. R. V. Lanza, *Curr. Opin. Electrochem.* **2022**, *36*, 101124.
[38] J. Xie, J. Jing, J. Gu, J. Guo, Y. Li, M. Zhou, *J. Environ. Chem. Eng.* **2022**, *10*, 107882.
[39] S. M. Bashir, E. L. Gyenge, *Chem. Eng. J.* **2024**, *494*, 152854.
[40] P. Cao, X. Quan, K. Zhao, X. Zhao, S. Chen, H. Yu, *ACS Catal.* **2021**, *11*, 13797.
[41] E. Zhao, G. Xia, Y. Li, J. Zhan, G. Yu, Y. Wang, *ACS ES&T Eng.* **2023**, *3*, 1800.
[42] E. Zhao, S. Wang, G. Yu, Y. Wang, *Electrochim. Acta* **2024**, *502*, 144835.
[43] J. Kintrup, M. Millaruelo, V. Trieu, A. Bulan, E. S. Mojica, *Electrochem. Soc. Interface* **2017**, *26*, 73.
[44] D. Kopljar, N. Wagner, E. Klemm, *Chem. Eng. Technol.* **2016**, *39*, 2042.
[45] T. Wirtanen, T. Prenzel, J.-P. Tessonnier, S. R. Waldvogel, *Chem. Rev.* **2021**, *121*, 10241.
[46] A. F. Holleman, N. Wiberg, E. Wiberg, *Lehrbuch Der Anorganischen Chemie*, Walter De Gruyter, Berlin **2007**.
[47] Electricity Prices for Non-Household Customers: Germany, Half-Years, Annual Consumption Classes, Price Types, https://www-genesis.destatis.de/datenbank/online/statistic/61243/table/61243-0005, (accessed: December 2024).
[48] M. Solakidou, A. Gemenetzi, G. Koutsikou, M. Theodorakopoulos, Y. Deligiannakis, M. Louloudi, *Energies* **2023**, *16*, 1723.
[49] M. Jouny, W. Luc, F. Jiao, *Ind. Eng. Chem. Res.* **2018**, *57*, 2165.
[50] E. Santacesaria, V. Russo, R. Tesser, R. Turco, M. Di Serio, *Ind. Eng. Chem. Res.* **2017**, *56*, 12940.
[51] F. P. Greenspan, D. G. MacKellar, *Anal. Chem.* **1948**, *20*, 1061.
[52] R. Ciriminna, L. Albanese, F. Meneguzzo, M. Pagliaro, *ChemSusChem* **2016**, *9*, 3374.
[53] F. P. Greenspan, *J. Am. Chem. Soc.* **1946**, *68*, 907.
[54] Y. Sun, L. Dai, N. L. D. Sui, Y. Li, M. Tian, J. Duan, S. Chen, J.-M. Lee, *Proc. Natl. Acad. Sci.* **2024**, *121*, e2409620121.
[55] H. Martin, P. Maris, *J. Appl. Microbiol.* **2012**, *113*, 578.
[56] Q. Chen, A. Kube, D. Schonvogel, D. Kopljar, E. Klemm, K. A. Friedrich, *Chem. Eng. J.* **2023**, *476*, 146486.
[57] J. R. Van Wazer, C. F. Callis, *Chem. Rev.* **1958**, *58*, 1011.
[58] I. A. Salem, M. El-Maazawi, A. B. Zaki, *Int. J. Chem. Kinet.* **2000**, *32*, 643.
[59] G. U. Greene, *Trans. Electrochem. Soc.* **1939**, *76*, 391.
[60] J. Wang, J. Kim, J. Li, C. Krall, V. K. Sharma, D. C. Ashley, C.-H. Huang, *Environ. Sci. Technol.* **2024**, *58*, 17157.

Manuscript received: January 27, 2025
Revised manuscript received: March 24, 2025
Version of record online: April 23, 2025

4 Summary of Results

To contribute to the replacement of fossil carbon with CO_2, this work has advanced a process concept in which intermittent energy from renewable sources (*e.g.* solar and wind) is used for electrochemical reduction of CO_2 to easily storable formic acid, which is then upgraded without any processing to value-added carbon products.

A key aspect was the development of cost-efficient GDEs with sufficiently high and stable performance for electrosynthesis of formic acid/formate. Their design (*i.e.* single layer) and fabrication by pressing was therefore based on the well-established and scalable ODC technology.[122,179] In addition, inexpensive and relatively abundant Sn or Bi materials of commercial origin ($\leq$200 € kg^{-1}) were used as catalysts instead of highly engineered materials. The performance of GDEs was continuously improved in several stages of development, in particular through the use of Ni foam as a support material and the replacement of Sn with Bi as a more efficient catalyst.

The latest stage of development was reached by systematically studying mixtures of Bi and Bi_2O_3 as catalyst.[188] The catalyst composition was optimised to Bi/Bi_2O_3 (80:20), which achieved high concentration ($\approx$500 mmol L^{-1}) and FE ($\approx$90%) of formate during evaluation at technically relevant current density (150 mA cm^{-2}). In addition, stability of the catalyst was high as the loss of Bi was minor. This GDE was then successfully established for flexible operation at intermittent electricity. Therefore, three demonstrative current patterns were applied based on solar and wind power. The first two patterns simulated periods of low or no availability by repeated hourly alternation of current density between full load (150 mA cm^{-2}) and half load (75 mA cm^{-2}) or zero load (0 mA cm^{-2}). In both cases, FE ($\approx$90%) and synthesis rates of formate remained reliably high and stable. The third pattern simulated a day-night cycle of energy demand and generation by intermediately lowering current density from full load (150 mA cm^{-2}) to night load (50 mA cm^{-2}). High FE ($\approx$90%) and stable synthesis rates were retained for intervals at full load, even though both moderately decreased at night load. In addition, alternating current density generally impaired the stability of the catalyst as the dissolution of Bi was increased, but mostly if the GDEs were depolarised in phases of zero load. Nonetheless, the GDEs already showed robust and high performance at intermittent electricity despite swift adjustments of current density without any optimisation of operational parameters so far.

For the second step of the process concept, either a biological or a chemical approach was successfully used to apply formic acid/formate from CO_2 reduction as feedstock without any processing and upgrade it into two different value-added carbon products.

The first product was the commercially relevant biopolymer polyhydroxybutyrate (PHB), which was obtained by microbial synthesis with *C. necator* (wildtype) using formate as substrate.[186] To this end, the coupling of electrosynthesis of formate with microbial synthesis of PHB was advanced to a second generation based on previous results.[166] This was achieved by adjusting the content of K^+ and Na^+ in biocompatible phosphate buffer, which served as both supporting electrolyte and incubation medium. The formate feedstock was generated as catholyte with a Sn based GDE (stage III, *cf.* table 3.1) and achieved high concentration (≈441 mmol L^{-1}) and FE (≈77%) of formate at technically relevant current density (150 mA cm^{-2}). The microbial synthesis of PHB was first optimised in shake flasks by identifying the ideal concentration of formate (21 mmol L^{-1}) with regards to maximising concentration of PHB and amount of PHB per formate. Afterwards, synthesis of PHB was scaled (about factor 10) to semi-automated bioreactors with continuous feed of formate-containing catholyte. Despite challenging adjustment of the formate feed during incubation, PHB was obtained with relatively high concentration (≈63 mg L^{-1} OD^{-1}) and amount per formate (≈16.5 mg g^{-1}) at one of the highest synthesis rates (≈8.4 mg L^{-1} OD^{-1} h^{-1}) reported at that time. The overall process was balanced and achieved a nearly doubled yield (≈22%) compared to the first generation coupling. Furthermore, the balancing allowed the assessment of energy costs for formate (≈1.88 € kg^{-1}) and PHB (≈114 € kg^{-1}) under recent and realistic assumptions (0.182 € kWh^{-1}[196]). This revealed the coupling was generally feasible but needs to be further improved by lowering energy demand of electrosynthesis and especially by increasing the efficiency of the model microorganism by genetic engineering or substitution.

The second product and final part of this thesis was the strong oxidiser and promising disinfectant performic acid (PFA).[187] Based on the indirect and on-demand electrosynthesis of peroxy acids by Schneider and Stöckl,[197] synthesis of PFA was achieved by coupling CO_2 reduction to formate with O_2 reduction to hydrogen peroxide. Therefore, formate feed was generated as catholyte by CO_2 reduction with Bi_2O_3 based GDEs (stage V, *cf.* table 3.1), which achieved high concentration (≈500 mmol L^{-1}) and FE (≈86%) of formate at technically relevant current density (150 mA cm^{-2}). The formate feed was subsequently used as catholyte for electrosynthesis of hydrogen peroxide by O_2 reduction at carbon-based GDEs, which reached high concentration (≈1.3 mol L^{-1}) and overall FE (≈85%) for hydrogen peroxide at the same current density (150 mA cm^{-2}). Thereby, PFA was generated *in-situ* by a chemical equilibrium reaction of formic acid and hydrogen peroxide in relatively low yield (≈16%) and concentration (≈82 mmol L^{-1}). This represents the first benchmark for a complete (indirect) electrosynthesis of PFA to the best of the authors' knowledge. The overall process was balanced and the electric energy costs were assessed for formate (≈1.35 € kg^{-1}), hydrogen peroxide (≈1.53 € kg^{-1}) and hydrogen peroxide/PFA (≈2.88 € kg^{-1}) under recent and realistic assumptions (0.1723 € kWh^{-1}[203]). They were up to three times higher than fossil-based market

prices for formic acid and hydrogen peroxide, which already include all costs beyond electricity. This demonstrated that an all-electrochemical synthesis of PFA was generally feasible, but energy demand of both electrosynthesis steps should be lowered alongside improved yield and concentration of PFA.

Overall, the objectives for further developing the process concept, which were the focus of this work, were successfully pursued. GDEs for reduction of CO_2 to formic acid were developed with relatively inexpensive catalyst materials and a scalable fabrication method. They were also established for flexible operation at intermittent electricity, enabling the use of surplus energy to generate storable formic acid in supporting electrolyte as feedstock. This feedstock was successfully applied without any intermediate downstream processing to exemplarily obtain the biopolymer PHB and the strong organic oxidiser PFA. The overall processes were critically evaluated in terms of yield and energy costs, identifying limiting factors and measures to address them.

5 Outlook

Within this thesis, a process concept for the intermittent electrosynthesis of formic acid and the direct (decentralised) utilisation towards a fossil free chemical industry was examined. However, for a successful transformation of the process concept into the chemical industry, substantial effort is needed to further develop and to evaluate the potential of using formic acid from electrochemical reduction of CO_2 by surplus energy as carbon feedstock for a technical exploitation.

With regard to the electrosynthesis of formic acid, the next step should be to investigate the performance of the established GDEs on a larger scale by transferring them from the screening set-up (5 cm^2 area) to a large laboratory set-up (100 cm^2 area). Thereby, a zero-gap anode should be integrated to lower the cell voltage and thus electric energy consumption for formate. The scaled set-up could be constructed as feed-and-bleed system in which catholyte with a constantly high concentration of formate would be continuously generated as feedstock. This would allow the GDEs to be adapted further with regards to operational challenges accompanying larger scale electrolysers, which is mandatory for the further development and GDE integration into pilot plants to demonstrate and examine the CO_2 electrolysis under industrial conditions. In addition, their performance should be examined at actual patterns of intermittent electricity, with a focus on long-term stability of the catalyst materials, as alternating current density generally increased the loss of catalyst in the demonstration examples.

With regard to the utilisation of the formate feedstock without any intermediate processing, the application needs to be optimised further for both the demonstrated upgrade processes as well as a broadening of the feedstock application. In case of the biosynthesis of PHB, the model organism *C. necator* (wildtype) should either be genetically modified or replaced to improve the metabolic conversion efficiency of formate to PHB and thus reduce its production costs. Furthermore, this approach can also be transferred to other appropriately modified microorganisms to obtain value-added carbon products beyond PHB. This would enable a biological production platform based on formate from electrochemical reduction of CO_2 and thereby offer a flexible and non-fossil-based production route for complex and high-value products. In case of the first demonstrated all-electrochemical synthesis of PFA, the chemical equilibrium of its formation should be adjusted to increase the concentration and yield of PFA. This could be achieved by a second generation in which both electrosynthesis of formate and electrosynthesis of hydrogen peroxide reach higher concentration with an adapted ratio.

Ultimately, the further optimised and scaled process concept would provide suitable data for more detailed balancing and evaluation of the respective coupling to determine its realisation potential, and thus might contribute to the transformation towards a sustainable chemical industry.

6 Bibliography

[1] IPCC, 2023: Climate Change 2023: Synthesis Report. Contribution of Working Groups I, II and III to the Sixth Assessment Report of the Intergovernmental Panel on Climate Change [Core Writing Team, H. Lee and J. Romero (eds.)]. IPCC, Geneva, Switzerland. 184 pp., DOI: 10.59327/IPCC/AR6-9789291691647.

[2] United Nations, “Paris Agreement”, can be found under https://treaties.un.org/Pages/ViewDetails.aspx?src=TREATY&mtdsg_no=XXVII-7-d&chapter=27&clang=_en, **2015** (accessed: 06.08.2025).

[3] European Commission, "Communication from the Commission to the European Parliament, the European Council, the Council, the European Economic and Social Committee and the Committee of the Regions - The European Green Deal", can be found under https://eur-lex.europa.eu/legal-content/EN/TXT/?uri=celex:52019DC0640, **2019** (accessed: 06.08.2025).

[4] A. Sternberg, A. Bardow, Power-to-What? – Environmental assessment of energy storage systems, *Energy Environ. Sci.* **2015**, *8*, 389–400.

[5] S. R. Foit, I. C. Vinke, L. G. J. de Haart, R.-A. Eichel, Power-to-Syngas: An Enabling Technology for the Transition of the Energy System?, *Angew. Chem. Int. Ed.* **2017**, *56*, 5402–5411; *Angew. Chem.* **2017**, *129*, 5488–5498.

[6] European Commission, "Report from the Commission to the European Parliament and the Council - Progress on competitiveness of clean energy technologies", can be found under https://eur-lex.europa.eu/legal-content/EN/TXT/?uri=celex:52025DC0074, **2025** (accessed: 31.07.2025).

[7] P. Gabrielli, L. Rosa, M. Gazzani, R. Meys, A. Bardow, M. Mazzotti, G. Sansavini, Net-zero emissions chemical industry in a world of limited resources, *One Earth* **2023**, *6*, 682–704.

[8] K. M. Van Geem, V. V. Galvita, G. B. Marin, Making chemicals with electricity, *Science* **2019**, *364*, 734–735.

[9] S. T. Wismann, J. S. Engbæk, S. B. Vendelbo, F. B. Bendixen, W. L. Eriksen, K. Aasberg-Petersen, C. Frandsen, I. Chorkendorff, P. M. Mortensen, Electrified methane reforming: A compact approach to greener industrial hydrogen production, *Science* **2019**, *364*, 756–759.

[10] K. M. Van Geem, B. M. Weckhuysen, Toward an e-chemistree: Materials for electrification of the chemical industry, *MRS Bull.* **2021**, *46*, 1187–1196.

[11] M. Sterner, F. Bauer, F. Crotogino, F. Eckert, C. von Olshausen, D. Teichmann, M. Thema in *Energiespeicher - Bedarf, Technologien, Integration*, (Eds.: M. Sterner, I. Stadler), Springer Berlin Heidelberg, Berlin, Heidelberg, **2017**, pp. 327–493.

[12] J. W. Ager, A. A. Lapkin, Chemical storage of renewable energy, *Science* **2018**, *360*, 707–708.

[13] G. G. Botte, Electrochemical Manufacturing in the Chemical Industry, *Electrochem. Soc. Interface* **2014**, *23*, 49–55.

[14] Euro Chlor, "Chlor-Alkali Industry Review 2024/2025", can be found under https://www.chlorineindustryreview.com/wp-content/uploads/2025/09/Chlor-Alkali-Industry-Review-2024_2025.pdf, (accessed: 09.10.2025).

[15] M. Fasihi, R. Weiss, J. Savolainen, C. Breyer, Global potential of green ammonia based on hybrid PV-wind power plants, *Appl. Energy* **2021**, *294*, 116170.

[16] B. Lee, L. R. Winter, H. Lee, D. Lim, H. Lim, M. Elimelech, Pathways to a Green Ammonia Future, *ACS Energy Lett.* **2022**, *7*, 3032–3038.

[17] M. Yan, Y. Kawamata, P. S. Baran, Synthetic Organic Electrochemical Methods Since 2000: On the Verge of a Renaissance, *Chem. Rev.* **2017**, *117*, 13230–13319.

[18] S. Möhle, M. Zirbes, E. Rodrigo, T. Gieshoff, A. Wiebe, S. R. Waldvogel, Modern Electrochemical Aspects for the Synthesis of Value-Added Organic Products, *Angew. Chem. Int. Ed.* **2018**, *57*, 6018-6041; *Angew. Chem.* **2018**, *130*, 6124–6149.

[19] A. Wiebe, T. Gieshoff, S. Möhle, E. Rodrigo, M. Zirbes, S. R. Waldvogel, Electrifying Organic Synthesis, *Angew. Chem. Int. Ed.* **2018**, *57*, 5594–5619; *Angew. Chem.* **2018**, *130*, 5694–5721.

[20] D. Pollok, S. R. Waldvogel, Electro-organic synthesis – a 21st century technique, *Chem. Sci.* **2020**, *11*, 12386–12400.

[21] J. Seidler, J. Strugatchi, T. Gärtner, S. R. Waldvogel, Does electrifying organic synthesis pay off? The energy efficiency of electro-organic conversions, *MRS Energy Sustain.* **2020**, *7*, 42.

[22] J. L. Röckl, D. Pollok, R. Franke, S. R. Waldvogel, A Decade of Electrochemical Dehydrogenative C,C-Coupling of Aryls, *Acc. Chem. Res.* **2020**, *53*, 45–61.

[23] P. Anastas, N. Eghbali, Green Chemistry: Principles and Practice, *Chem. Soc. Rev.* **2010**, *39*, 301–312.

[24] H. J. Schäfer, Contributions of organic electrosynthesis to green chemistry, *C. R. Chim.* **2011**, *14*, 745–765.

[25] B. A. Frontana-Uribe, R. D. Little, J. G. Ibanez, A. Palma, R. Vasquez-Medrano, Organic electrosynthesis: a promising green methodology in organic chemistry, *Green Chem.* **2010**, *12*, 2099.

[26] N. Aust in *Encyclopedia of Applied Electrochemistry* (Eds.: G. Kreysa, K. Ota, R. F. Savinell), Springer New York, New York, **2014**, pp. 1392–1397.

[27] E. K. Oehl, M. S. Lenhard, S. R. Waldvogel in *Encyclopedia of Green Chemistry*, Elsevier, Amsterdam, **2025**, pp. 364–381.

[28] G. Lopez, D. Keiner, M. Fasihi, T. Koiranen, C. Breyer, From fossil to green chemicals: sustainable pathways and new carbon feedstocks for the global chemical industry, *Energy Environ. Sci.* **2023**, *16*, 2879–2909.

[29] A. Behr, D. W. Agar, A. J. Vorholt, J. Jörissen, *Einführung in die Technische Chemie*, Springer Berlin Heidelberg, Berlin, Heidelberg, **2025**, pp. 221–238.

[30] P. G. Levi, J. M. Cullen, Mapping Global Flows of Chemicals: From Fossil Fuel Feedstocks to Chemical Products, *Environ. Sci. Technol.* **2018**, *52*, 1725–1734.

[31] M. Carus, L. Dammer, A. Raschka, P. Skoczinski, Renewable carbon: Key to a sustainable and future-oriented chemical and plastic industry: Definition, strategy, measures and potential, *Greenhouse Gas Sci Technol.* **2020**, *10*, 488–505.

[32] A. Rahimi, J. M. García, Chemical recycling of waste plastics for new materials production, *Nat. Rev. Chem.* **2017**, *1*, 0046.

[33] J.-P. Lange, Towards circular carbo-chemicals – the metamorphosis of petrochemicals, *Energy Environ. Sci.* **2021**, *14*, 4358–4376.

[34] R. Geyer, J. R. Jambeck, K. L. Law, Production, use, and fate of all plastics ever made, *Sci. Adv.* **2017**, *3*, e1700782.

[35] B. Kamm, Production of Platform Chemicals and Synthesis Gas from Biomass, *Angew. Chem. Int. Ed.* **2007**, *46*, 5056–5058.

[36] A. Corma, S. Iborra, A. Velty, Chemical Routes for the Transformation of Biomass into Chemicals, *Chem. Rev.* **2007**, *107*, 2411–2502.

[37] T. Khandaker, T. Islam, A. Nandi, M. A. A. M. Anik, M. S. Hossain, M. K. Hasan, M. S. Hossain, Biomass-derived carbon materials for sustainable energy applications: a comprehensive review, *Sustainable Energy Fuels* **2025**, *9*, 693–723.

[38] D. T. Troiano, T. Hofmann, S. Brethauer, M. H.-P. Studer, Toward optimal use of biomass as carbon source for chemical bioproduction, *Curr. Opin. Biotechnol.* **2023**, *81*, 102942.

[39] O. Arodudu, B. Holmatov, A. Voinov, Ecological impacts and limits of biomass use: a critical review, *Clean Techn. Environ. Policy* **2020**, *22*, 1591–1611.

[40] M. Garedew, F. Lin, B. Song, T. M. DeWinter, J. E. Jackson, C. M. Saffron, C. H. Lam, P. T. Anastas, Greener Routes to Biomass Waste Valorization: Lignin Transformation Through Electrocatalysis for Renewable Chemicals and Fuels Production, *ChemSusChem* **2020**, *13*, 4214–4237.

[41] J. Klein, R. Kupec, M. Stöckl, S. R. Waldvogel, Degradation of Lignosulfonate to Vanillic Acid Using Ferrate, *Adv. Sustainable Syst.* **2023**, *7*, 2200431.

[42] M. Zirbes, T. Graßl, R. Neuber, S. R. Waldvogel, Peroxodicarbonate as a Green Oxidizer for the Selective Degradation of Kraft Lignin into Vanillin, *Angew. Chem. Int. Ed.* **2023**, *62*, e202219217; *Angew. Chem.* **2023**, *135*, e202219217.

[43] T. Rücker, T. Pettersen, H. Graute, B. Wittgens, T. Graßl, S. R. Waldvogel, Pilot Scale Electrolysis of Peroxodicarbonate as an Oxidizer for Lignin Valorization, *ACS Sustainable Chem. Eng.* **2024**, *12*, 11283–11296.

[44] A. R. Alagu, C. Boumrifak, L. F. López González, Report: Carbon for Power-to-X Suitable CO_2 sources and integration in PtX value chains, can be found under https://dechema.de/Themen/Studien+und+Positionspapiere/2024+04+Carbon+for+Power_to_X+-+Suitable+CO2+sources+and+integration+in+PtX+value+chains-p-20480537/_/CO2-R_03-04-24_f.pdf, **2024** (accessed: 31.07.2025).

[45] European Parliament and the Council, "Regulation (EU) 2024/1735 of the European Parliament and of the Council of 13 June 2024 on establishing a framework of measures for strengthening Europe's net-zero technology manufacturing ecosystem and amending Regulation (EU) 2018/1724", can be found under https://eur-lex.europa.eu/eli/reg/2024/1735/oj/eng, **2024** (accessed: 11.08.2025).

[46] European Commission, Joint Research Centre, Martinez Castilla, G., Tumara, D., Mountraki, A., Letout, S., Jaxa-Rozen, M., Schmitz, A., Ince, E. and Georgakaki, A., *Clean Energy Technology Observatory: Carbon Capture, Utilisation and Storage in the European Union - 2024 Status Report on Technology Development, Trends, Value Chains and Markets*, Publications Office of the European Union, Luxembourg, **2024**, https://data.europa.eu/doi/10.2760/0287566, JRC139285.

[47] J. Z. Y. Tan, J. M. Uratani, S. Griffiths, J. M. Andresen, M. M. Maroto-Valer, Chemistry advances driving industrial carbon capture technologies, *Nat. Rev. Chem.* **2025**, *9*, 656–671.

[48] IPCC, 2005: IPCC Special Report on Carbon Dioxide Capture and Storage. Prepared by Working Group III of the Intergovernmental Panel on Climate Change [Metz, B., O. Davidson, H. C. de Coninck, M. Loos, and L. A. Meyer (eds.)]. Cambridge University Press, Cambridge, United Kingdom and New York, NY, USA, 442 pp.

[49] R. S. Haszeldine, Carbon Capture and Storage: How Green Can Black Be?, *Science* **2009**, *325*, 1647–1652.

[50] M. Aresta, A. Dibenedetto, A. Angelini, Catalysis for the Valorization of Exhaust Carbon: from CO_2 to Chemicals, Materials, and Fuels. Technological Use of CO_2, *Chem. Rev.* **2014**, *114*, 1709–1742.

[51] Z. Zhang, S.-Y. Pan, H. Li, J. Cai, A. G. Olabi, E. J. Anthony, V. Manovic, Recent advances in carbon dioxide utilization, *Renew. Sustain. Energy Rev.* **2020**, *125*, 109799.

[52] M. González-Castaño, B. Dorneanu, H. Arellano-García, The reverse water gas shift reaction: a process systems engineering perspective, *React. Chem. Eng.* **2021**, *6*, 954–976.

[53] J. Ye, N. Dimitratos, L. M. Rossi, N. Thonemann, A. M. Beale, R. Wojcieszak, Hydrogenation of CO_2 for sustainable fuel and chemical production, *Science* **2025**, *387*, eadn9388.

[54] C. P. O'Brien, R. K. Miao, A. Shayesteh Zeraati, G. Lee, E. H. Sargent, D. Sinton, CO_2 Electrolyzers, *Chem. Rev.* **2024**, *124*, 3648–3693.

[55] D. T. Whipple, P. J. A. Kenis, Prospects of CO_2 Utilization via Direct Heterogeneous Electrochemical Reduction, *J. Phys. Chem. Lett.* **2010**, *1*, 3451–3458.

[56] J. Wyndorps, H. Ostovari, N. von der Assen, Is electrochemical CO_2 reduction the future technology for power-to-chemicals? An environmental comparison with H_2-based pathways, *Sustainable Energy Fuels* **2021**, *5*, 5748–5761.

[57] M. Royer, Réduction de l'acide carbonique en acide formique, *Compt. rend* **1870**, *1870*, 731–732.

[58] G. Glockler, Carbon–Oxygen Bond Energies and Bond Distances, *J. Phys. Chem.* **1958**, *62*, 1049–1054.

[59] D. M. Heard, A. J. J. Lennox, Electrode Materials in Modern Organic Electrochemistry, *Angew. Chem. Int. Ed.* **2020**, *59*, 18866–18884.

[60] Á. Vass, A. Kormányos, Z. Kószó, B. Endrődi, C. Janáky, Anode Catalysts in CO_2 Electrolysis: Challenges and Untapped Opportunities, *ACS Catal.* **2022**, *12*, 1037–1051.

[61] Y. Zhao, D. P. Adiyeri Saseendran, C. Huang, C. A. Triana, W. R. Marks, H. Chen, H. Zhao, G. R. Patzke, Oxygen Evolution/Reduction Reaction Catalysts: From *In Situ* Monitoring and Reaction Mechanisms to Rational Design, *Chem. Rev.* **2023**, *123*, 6257–6358.

[62] A. Bagger, W. Ju, A. S. Varela, P. Strasser, J. Rossmeisl, Electrochemical CO_2 Reduction: A Classification Problem, *ChemPhysChem* **2017**, *18*, 3266–3273.

[63] B. Seger, G. Kastlunger, A. Bagger, S. B. Scott, A Perspective on the Reaction Mechanisms of CO_2 Electrolysis, *ACS Energy Lett.* **2025**, *10*, 2212–2227.

[64] E. Santacesaria, V. Russo, R. Tesser, R. Turco, M. Di Serio, Kinetics of Performic Acid Synthesis and Decomposition, *Ind. Eng. Chem. Res.* **2017**, *56*, 12940–12952.

[65] N. Han, P. Ding, L. He, Y. Li, Y. Li, Promises of Main Group Metal–Based Nanostructured Materials for Electrochemical CO_2 Reduction to Formate, *Adv. Energy Mater.* **2020**, *10*, 1902338.

[66] S. A. Al-Tamreh, M. H. Ibrahim, M. H. El-Naas, J. Vaes, D. Pant, A. Benamor, A. Amhamed, Electroreduction of Carbon Dioxide into Formate: A Comprehensive Review, *ChemElectroChem* **2021**, *8*, 3207–3220.

[67] S. Jin, Z. Hao, K. Zhang, Z. Yan, J. Chen, Advances and Challenges for the Electrochemical Reduction of CO_2 to CO: From Fundamentals to Industrialization, *Angew. Chem. Int. Ed.* **2021**, *60*, 20627–20648.

[68] S. Nitopi, E. Bertheussen, S. B. Scott, X. Liu, A. K. Engstfeld, S. Horch, B. Seger, I. E. L. Stephens, K. Chan, C. Hahn, J. K. Nørskov, T. F. Jaramillo, I. Chorkendorff, Progress and Perspectives of Electrochemical CO_2 Reduction on Copper in Aqueous Electrolyte, *Chem. Rev.* **2019**, *119*, 7610–7672.

[69] K. P. Kuhl, E. R. Cave, D. N. Abram, T. F. Jaramillo, New insights into the electrochemical reduction of carbon dioxide on metallic copper surfaces, *Energy Environ. Sci.* **2012**, *5*, 7050–7059.

[70] K. P. Kuhl, T. Hatsukade, E. R. Cave, D. N. Abram, J. Kibsgaard, T. F. Jaramillo, Electrocatalytic Conversion of Carbon Dioxide to Methane and Methanol on Transition Metal Surfaces, *J. Am. Chem. Soc.* **2014**, *136*, 14107–14113.

[71] H. Lee, N. Park, T.-H. Kong, S. Kwon, S. Shin, S. G. Cha, E. Lee, J. Cha, S. Sultan, Y. Kwon, Advancements in electrochemical methanol synthesis from CO_2: Mechanisms and catalyst developments, *Nano Energy* **2024**, *130*, 110099.

[72] I. Hussain, H. Alasiri, W. Ullah Khan, K. Alhooshani, Advanced electrocatalytic technologies for conversion of carbon dioxide into methanol by electrochemical reduction: Recent progress and future perspectives, *Coord. Chem. Rev.* **2023**, *482*, 215081.

[73] J. Cai, Q. Zhao, W.-Y. Hsu, C. Choi, Y. Liu, J. M. P. Martirez, C. Chen, J. Huang, E. A. Carter, Y. Huang, Highly Selective Electrochemical Reduction of CO_2 into Methane on Nanotwinned Cu, *J. Am. Chem. Soc.* **2023**, *145*, 9136–9143.

[74] F. Huang, H. Sun, S. He, X. Chen, D. Wei, A. Xu, B. Wang, X. Yin, J. Xu, H. He, Progress and Perspectives for Efficient Electrochemical Carbon Dioxide Reduction to Methane, *ChemSusChem* **2025**, *18*, e202402568.

[75] A. Tullo, The search for greener ethylene, *C&EN* **2021**, *99*, 20–22.

[76] Z. Chen, T. Wang, B. Liu, D. Cheng, C. Hu, G. Zhang, W. Zhu, H. Wang, Z.-J. Zhao, J. Gong, Grain-Boundary-Rich Copper for Efficient Solar-Driven Electrochemical CO_2 Reduction to Ethylene and Ethanol, *J. Am. Chem. Soc.* **2020**, *142*, 6878–6883.

[77] T. K. Todorova, M. W. Schreiber, M. Fontecave, Mechanistic Understanding of CO_2 Reduction Reaction (CO2RR) Toward Multicarbon Products by Heterogeneous Copper-Based Catalysts, *ACS Catal.* **2020**, *10*, 1754–1768.

[78] S. You, J. Xiao, S. Liang, W. Xie, T. Zhang, M. Li, Z. Zhong, Q. Wang, H. He, Doping engineering of Cu-based catalysts for electrocatalytic CO_2 reduction to multi-carbon products, *Energy Environ. Sci.* **2024**, *17*, 5795–5818.

[79] Z. Zhang, L. Bian, H. Tian, Y. Liu, Y. Bando, Y. Yamauchi, Z.-L. Wang, Tailoring the Surface and Interface Structures of Copper-Based Catalysts for Electrochemical Reduction of CO_2 to Ethylene and Ethanol, *Small* **2022**, *18*, 2107450.

[80] M. Li, N. Song, W. Luo, J. Chen, W. Jiang, J. Yang, Engineering Surface Oxophilicity of Copper for Electrochemical CO_2 Reduction to Ethanol, *Adv. Sci.* **2023**, *10*, 2204579.

[81] Y. Ouyang, L. Shi, X. Bai, C. Ling, Q. Li, J. Wang, Selectivity of Electrochemical CO_2 Reduction toward Ethanol and Ethylene: The Key Role of Surface-Active Hydrogen, *ACS Catal.* **2023**, *13*, 15448–15456.

[82] Y. Guan, Y. Li, Z. Li, Y. Hou, L. Lei, B. Yang, Promotion of C–C Coupling in the CO_2 Electrochemical Reduction to Valuable C_{2+} Products: From Micro-Foundation to Macro-Application, *Adv. Mater.* **2025**, *37*, 2417567.

[83] H. H. Heenen, H. Shin, G. Kastlunger, S. Overa, J. A. Gauthier, F. Jiao, K. Chan, The mechanism for acetate formation in electrochemical $CO_{(2)}$ reduction on Cu: selectivity with potential, pH, and nanostructuring, *Energy Environ. Sci.* **2022**, *15*, 3978–3990.

[84] W. Liu, P. Zhai, A. Li, B. Wei, K. Si, Y. Wei, X. Wang, G. Zhu, Q. Chen, X. Gu, R. Zhang, W. Zhou, Y. Gong, Electrochemical CO_2 reduction to ethylene by ultrathin CuO nanoplate arrays, *Nat. Commun.* **2022**, *13*, 1877.

[85] X. She, L. Zhai, Y. Wang, P. Xiong, M. M.-J. Li, T.-S. Wu, M. C. Wong, X. Guo, Z. Xu, H. Li, H. Xu, Y. Zhu, S. C. E. Tsang, S. P. Lau, Pure-water-fed, electrocatalytic CO_2 reduction to ethylene beyond 1,000 h stability at 10 A, *Nat. Energy* **2024**, *9*, 81–91.

[86] H. Xu, D. Rebollar, H. He, L. Chong, Y. Liu, C. Liu, C.-J. Sun, T. Li, J. V. Muntean, R. E. Winans, D.-J. Liu, T. Xu, Highly selective electrocatalytic CO_2 reduction to ethanol by metallic clusters dynamically formed from atomically dispersed copper, *Nat. Energy* **2020**, *5*, 623–632.

[87] W. Xia, Y. Xie, S. Jia, S. Han, R. Qi, T. Chen, X. Xing, T. Yao, D. Zhou, X. Dong, J. Zhai, J. Li, J. He, D. Jiang, Y. Yamauchi, M. He, H. Wu, B. Han, Adjacent Copper Single Atoms Promote C–C Coupling in Electrochemical CO_2 Reduction for the Efficient Conversion of Ethanol, *J. Am. Chem. Soc.* **2023**, *145*, 17253–17264.

[88] H. Wang, J. Xue, C. Liu, Z. Chen, C. Li, X. Li, T. Zheng, Q. Jiang, C. Xia, CO_2 electrolysis toward acetate: A review, *Curr. Opin. Electrochem.* **2023**, *39*, 101253.

[89] M. Jouny, G. S. Hutchings, F. Jiao, Carbon monoxide electroreduction as an emerging platform for carbon utilization, *Nat. Catal.* **2019**, *2*, 1062–1070.

[90] Y. Chen, X.-Y. Li, Z. Chen, A. Ozden, J. E. Huang, P. Ou, J. Dong, J. Zhang, C. Tian, B.-H. Lee, X. Wang, S. Liu, Q. Qu, S. Wang, Y. Xu, R. K. Miao, Y. Zhao, Y. Liu, C. Qiu, J. Abed, H. Liu, H. Shin, D. Wang, Y. Li, D. Sinton, E. H. Sargent, Efficient multicarbon formation in acidic CO_2 reduction via tandem electrocatalysis, *Nat. Nanotechnol.* **2024**, *19*, 311–318.

[91] T. Möller, M. Filippi, S. Brückner, W. Ju, P. Strasser, A CO_2 electrolyzer tandem cell system for CO_2-CO co-feed valorization in a Ni-N-C/Cu-catalyzed reaction cascade, *Nat. Commun.* **2023**, *14*, 5680.

[92] D. Segets, C. Andronescu, U.-P. Apfel, Accelerating CO_2 electrochemical conversion towards industrial implementation, *Nat. Commun.* **2023**, *14*, 7950.

[93] B. Belsa, L. Xia, F. P. García De Arquer, CO_2 Electrolysis Technologies: Bridging the Gap toward Scale-up and Commercialization, *ACS Energy Lett.* **2024**, *9*, 4293–4305.

[94] M. G. Kibria, J. P. Edwards, C. M. Gabardo, C.-T. Dinh, A. Seifitokaldani, D. Sinton, E. H. Sargent, Electrochemical CO_2 Reduction into Chemical Feedstocks: From Mechanistic Electrocatalysis Models to System Design, *Adv. Mater.* **2019**, *31*, 1807166.

[95] S. Malkhandi, B. S. Yeo, Electrochemical conversion of carbon dioxide to high value chemicals using gas-diffusion electrodes, *Curr. Opin. Chem. Eng.* **2019**, *26*, 112–121.

[96] B. J. Etzold, U. Krewer, S. Thiele, A. Dreizler, E. Klemm, T. Turek, Understanding the activity transport nexus in water and CO_2 electrolysis: State of the art, challenges and perspectives, *Chem. Eng. J.* **2021**, *424*, 130501.

[97] A. Tamimi, E. B. Rinker, O. C. Sandall, Diffusion Coefficients for Hydrogen Sulfide, Carbon Dioxide, and Nitrous Oxide in Water over the Temperature Range 293-368 K, *J. Chem. Eng. Data* **1994**, *39*, 330–332.

[98] J. A. Rabinowitz, M. W. Kanan, The future of low-temperature carbon dioxide electrolysis depends on solving one basic problem, *Nat. Commun.* **2020**, *11*, 5231.

[99] M. Sassenburg, M. Kelly, S. Subramanian, W. A. Smith, T. Burdyny, Zero-Gap Electrochemical CO_2 Reduction Cells: Challenges and Operational Strategies for Prevention of Salt Precipitation, *ACS Energy Lett.* **2023**, *8*, 321–331.

[100] J. Biemolt, J. Singh, G. Prats Vergel, H. M. Pelzer, T. Burdyny, Preventing Salt Formation in Zero-Gap CO_2 Electrolyzers by Quantifying Cation Accumulation, *ACS Energy Lett.* **2025**, *10*, 807–814.

[101] W. Lai, Y. Qiao, Y. Wang, H. Huang, Stability Issues in Electrochemical CO_2 Reduction: Recent Advances in Fundamental Understanding and Design Strategies, *Adv. Mater.* **2023**, *35*, 2306288.

[102] H. Shin, K. U. Hansen, F. Jiao, Techno-economic assessment of low-temperature carbon dioxide electrolysis, *Nat. Sustain.* **2021**, *4*, 911–919.

[103] S. C. Da Cunha, J. Resasco, Maximizing single-pass conversion does not result in practical readiness for CO_2 reduction electrolyzers, *Nat. Commun.* **2023**, *14*, 5513.

[104] M. Jouny, W. Luc, F. Jiao, General Techno-Economic Analysis of CO_2 Electrolysis Systems, *Ind. Eng. Chem. Res.* **2018**, *57*, 2165–2177.

[105] R. J. Detz, C. J. Ferchaud, A. J. Kalkman, J. Kemper, C. Sánchez-Martínez, M. Saric, M. V. Shinde, Electrochemical CO_2 conversion technologies: state-of-the-art and future perspectives, *Sustainable Energy Fuels* **2023**, *7*, 5445–5472.

[106] R. I. Masel, Z. Liu, H. Yang, J. J. Kaczur, D. Carrillo, S. Ren, D. Salvatore, C. P. Berlinguette, An industrial perspective on catalysts for low-temperature CO_2 electrolysis, *Nat. Nanotechnol.* **2021**, *16*, 118–128.

[107] H. Chen, C. Ding, C. Kang, J. Zeng, Y. Li, Y. Li, Y. Li, C. Li, J. He, The design of alternative anodic reactions paired with electrochemical CO_2 reduction, *Green Chem.* **2023**, *25*, 5320–5337.

[108] W. Xie, B. Li, L. Liu, H. Li, M. Yue, Q. Niu, S. Liang, X. Shao, H. Lee, J. Y. Lee, M. Shao, Q. Wang, D. O'Hare, H. He, Advanced systems for enhanced CO_2 electroreduction, *Chem. Soc. Rev.* **2025**, *54*, 898–959.

[109] E. Pérez-Gallent, S. Turk, R. Latsuzbaia, R. Bhardwaj, A. Anastasopol, F. Sastre-Calabuig, A. C. Garcia, E. Giling, E. Goetheer, Electroreduction of CO_2 to CO Paired with 1,2-Propanediol Oxidation to Lactic Acid. Toward an Economically Feasible System, *Ind. Eng. Chem. Res.* **2019**, *58*, 6195–6202.

[110] X. V. Medvedeva, J. J. Medvedev, S. W. Tatarchuk, R. M. Choueiri, A. Klinkova, Sustainable at both ends: electrochemical CO_2 utilization paired with electrochemical treatment of nitrogenous waste, *Green Chem.* **2020**, *22*, 4456–4462.

[111] M. Erans, E. S. Sanz-Pérez, D. P. Hanak, Z. Clulow, D. M. Reiner, G. A. Mutch, Direct air capture: process technology, techno-economic and socio-political challenges, *Energy Environ. Sci.* **2022**, *15*, 1360–1405.

[112] M. Moradzaman, C. S. Martínez, G. Mul, Effect of partial pressure on product selectivity in Cu-catalyzed electrochemical reduction of CO_2, *Sustainable Energy Fuels* **2020**, *4*, 5195–5202.

[113] B. Kim, S. Ma, H.-R. Molly Jhong, P. J. Kenis, Influence of dilute feed and pH on electrochemical reduction of CO_2 to CO on Ag in a continuous flow electrolyzer, *Electrochim. Acta* **2015**, *166*, 271–276.

[114] B.-U. Choi, Y. C. Tan, H. Song, K. B. Lee, J. Oh, System Design Considerations for Enhancing Electroproduction of Formate from Simulated Flue Gas, *ACS Sustainable Chem. Eng.* **2021**, *9*, 2348–2357.

[115] Y. Xu, J. P. Edwards, J. Zhong, C. P. O'Brien, C. M. Gabardo, C. McCallum, J. Li, C.-T. Dinh, E. H. Sargent, D. Sinton, Oxygen-tolerant electroproduction of C_2 products from simulated flue gas, *Energy Environ. Sci.* **2020**, *13*, 554–561.

[116] W. Luc, B. H. Ko, S. Kattel, S. Li, D. Su, J. G. Chen, F. Jiao, SO_2-Induced Selectivity Change in CO_2 Electroreduction, *J. Am. Chem. Soc.* **2019**, *141*, 9902–9909.

[117] B. H. Ko, B. Hasa, H. Shin, E. Jeng, S. Overa, W. Chen, F. Jiao, The impact of nitrogen oxides on electrochemical carbon dioxide reduction, *Nat. Commun.* **2020**, *11*, 5856.

[118] J. B. Greenblatt, D. J. Miller, J. W. Ager, F. A. Houle, I. D. Sharp, The Technical and Energetic Challenges of Separating (Photo)Electrochemical Carbon Dioxide Reduction Products, *Joule* **2018**, *2*, 381–420.

[119] H.-L. Zhu, J.-R. Huang, M.-D. Zhang, C. Yu, P.-Q. Liao, X.-M. Chen, Continuously Producing Highly Concentrated and Pure Acetic Acid Aqueous Solution via Direct Electroreduction of CO_2, *J. Am. Chem. Soc.* **2024**, *146*, 1144–1152.

[120] T. Alerte, J. P. Edwards, C. M. Gabardo, C. P. O'Brien, A. Gaona, J. Wicks, A. Obradović, A. Sarkar, S. A. Jaffer, H. L. MacLean, D. Sinton, E. H. Sargent, Downstream of the CO_2 Electrolyzer: Assessing the Energy Intensity of Product Separation, *ACS Energy Lett.* **2021**, *6*, 4405–4412.

[121] A. A. Samu, A. Kormányos, E. Kecsenovity, N. Szilágyi, B. Endrődi, C. Janáky, Intermittent Operation of CO_2 Electrolyzers at Industrially Relevant Current Densities, *ACS Energy Lett.* **2022**, *7*, 1859–1861.

[122] J. Kintrup, M. Millaruelo, V. Trieu, A. Bulan, E. S. Mojica, Gas Diffusion Electrodes for Efficient Manufacturing of Chlorine and Other Chemicals, *Electrochem. Soc. Interface* **2017**, *26*, 73–76.

[123] M. F. Liu, C. Zhang, J. Wang, X. Han, W. Hu, Y. Deng, Recent research progresses of Sn/Bi/In-based electrocatalysts for electroreduction CO_2 to formate, *Chem. Eur. J.* **2024**, *30*, e202303711.

[124] Z. Yang, Y. Jin, Z. Feng, P. Luo, C. Feng, Y. Zhou, X. An, X. Hao, A. Abudula, G. Guan, Rational Strategies for Preparing Highly Efficient Tin-, Bismuth- or Indium-Based Electrocatalysts for Electrochemical CO_2 Reduction to Formic acid/Formate, *ChemSusChem* **2025**, *18*, e202401181.

[125] Y. Xue, Y. Guo, H. Cui, Z. Zhou, Catalyst Design for Electrochemical Reduction of CO_2 to Multicarbon Products, *Small Methods* **2021**, *5*, 2100736.

[126] J. Yu, J. Wang, Y. Ma, J. Zhou, Y. Wang, P. Lu, J. Yin, R. Ye, Z. Zhu, Z. Fan, Recent Progresses in Electrochemical Carbon Dioxide Reduction on Copper-Based Catalysts toward Multicarbon Products, *Adv. Funct. Mater.* **2021**, *31*, 2102151.

[127] A. R. Woldu, Z. Huang, P. Zhao, L. Hu, D. Astruc, Electrochemical CO_2 reduction (CO_2RR) to multi-carbon products over copper-based catalysts, *Coord. Chem. Rev.* **2022**, *454*, 214340.

[128] M. Moura De Salles Pupo, R. Kortlever, Electrolyte Effects on the Electrochemical Reduction of CO_2, *ChemPhysChem* **2019**, *20*, 2926–2935.

[129] J. Resasco, Y. Lum, E. Clark, J. Z. Zeledon, A. T. Bell, Effects of Anion Identity and Concentration on Electrochemical Reduction of CO_2, *ChemElectroChem* **2018**, *5*, 1064–1072.

[130] A. S. Varela, M. Kroschel, T. Reier, P. Strasser, Controlling the selectivity of CO_2 electroreduction on copper: The effect of the electrolyte concentration and the importance of the local pH, *Catal. Today* **2016**, *260*, 8–13.

[131] Z. Zhang, X. Huang, Z. Chen, J. Zhu, B. Endrődi, C. Janáky, D. Deng, Membrane Electrode Assembly for Electrocatalytic CO_2 Reduction: Principle and Application, *Angew. Chem. Int. Ed.* **2023**, *62*, e202302789.

[132] T. Chen, Z. Zhao, S. Zhang, B. Ding, D. Chen, G. Chen, Y. Zhu, X. Zhang, Recent Progress in Solid-State Electrolyte for Electrocatalytic CO_2 Reduction, *Adv. Energy Mater.* **2025**, 2502092.

[133] R. Krause, D. Reinisch, C. Reller, H. Eckert, D. Hartmann, D. Taroata, K. Wiesner-Fleischer, A. Bulan, A. Lueken, G. Schmid, Industrial Application Aspects of the Electrochemical Reduction of CO_2 to CO in Aqueous Electrolyte, *Chem. Ing. Tech.* **2020**, *92*, 53–61.

[134] B. Endrődi, E. Kecsenovity, A. Samu, F. Darvas, R. V. Jones, V. Török, A. Danyi, C. Janáky, Multilayer Electrolyzer Stack Converts Carbon Dioxide to Gas Products at High Pressure with High Efficiency, *ACS Energy Lett.* **2019**, *4*, 1770–1777.

[135] R. B. Kutz, Q. Chen, H. Yang, S. D. Sajjad, Z. Liu, I. R. Masel, Sustainion Imidazolium-Functionalized Polymers for Carbon Dioxide Electrolysis, *Energy Technol.* **2017**, *5*, 929–936.

[136] C.-T. Dinh, F. P. García De Arquer, D. Sinton, E. H. Sargent, High Rate, Selective, and Stable Electroreduction of CO_2 to CO in Basic and Neutral Media, *ACS Energy Lett.* **2018**, *3*, 2835–2840.

[137] Z. Liu, H. Yang, R. Kutz, R. I. Masel, CO_2 Electrolysis to CO and O_2 at High Selectivity, Stability and Efficiency Using Sustainion Membranes, *J. Electrochem. Soc.* **2018**, *165*, J3371–J3377.

[138] W. Fang, W. Guo, R. Lu, Y. Yan, X. Liu, D. Wu, F. M. Li, Y. Zhou, C. He, C. Xia, H. Niu, S. Wang, Y. Liu, Y. Mao, C. Zhang, B. You, Y. Pang, L. Duan, X. Yang, F. Song, T. Zhai, G. Wang, X. Guo, B. Tan, T. Yao, Z. Wang, B. Y. Xia, Durable CO_2 conversion in the proton-exchange membrane system, *Nature* **2024**, *626*, 86–91.

[139] C. Zhang, X. Hao, J. Wang, X. Ding, Y. Zhong, Y. Jiang, M.-C. Wu, R. Long, W. Gong, C. Liang, W. Cai, J. Low, Y. Xiong, Concentrated Formic Acid from CO_2 Electrolysis for Directly Driving Fuel Cell, *Angew. Chem. Int. Ed.* **2024**, *63*, e202317628.

[140] C. Peng, S. Yang, G. Luo, S. Yan, N. Chen, J. Zhang, Y. Chen, X. Wang, Z. Wang, W. Wei, T.-K. Sham, G. Zheng, Ampere-level CO_2-to-formate electrosynthesis using highly exposed bismuth(110) facets modified with sulfur-anchored sodium cations, *Chem* **2023**, *9*, 2830–2840.

[141] F. P. García De Arquer, C.-T. Dinh, A. Ozden, J. Wicks, C. McCallum, A. R. Kirmani, D.-H. Nam, C. Gabardo, A. Seifitokaldani, X. Wang, Y. C. Li, F. Li, J. Edwards, L. J. Richter, S. J. Thorpe, D. Sinton, E. H. Sargent, CO_2 electrolysis to multicarbon products at activities greater than 1 A cm^{-2}, *Science* **2020**, *367*, 661–666.

[142] S. Heuser, L. Hoof, K. Pellumbi, J. N. Oberndorf, L. Krämer, D. Blaudszun, K. J. Puring, M. Prokein, N. Mölders, A. Kilzer, M. Petermann, U.-P. Apfel, Differential pressure CO_2 electrolysis opens the way for direct coupling to industrial processes, *Chem Catal.* **2025**, 101393.

[143] A. Löwe, M. Schmidt, F. Bienen, D. Kopljar, N. Wagner, E. Klemm, Optimizing Reaction Conditions and Gas Diffusion Electrodes Applied in the CO_2 Reduction Reaction to Formate to Reach Current Densities up to 1.8 A cm^{-2}, *ACS Sustainable Chem. Eng.* **2021**, *9*, 4213–4223.

[144] A. Ozden, J. Li, S. Kandambeth, X.-Y. Li, S. Liu, O. Shekhah, P. Ou, Y. Zou Finfrock, Y.-K. Wang, T. Alkayyali, F. Pelayo García de Arquer, V. S. Kale, P. M. Bhatt, A. H. Ip, M. Eddaoudi, E. H. Sargent, D. Sinton, Energy- and carbon-efficient CO_2/CO electrolysis to multicarbon products via asymmetric ion migration–adsorption, *Nat. Energy* **2023**, *8*, 179–190.

[145] C. Xia, P. Zhu, Q. Jiang, Y. Pan, W. Liang, E. Stavitski, H. N. Alshareef, H. Wang, Continuous production of pure liquid fuel solutions via electrocatalytic CO_2 reduction using solid-electrolyte devices, *Nat. Energy* **2019**, *4*, 776–785.

[146] F. Li, A. Thevenon, A. Rosas-Hernández, Z. Wang, Y. Li, C. M. Gabardo, A. Ozden, C. T. Dinh, J. Li, Y. Wang, J. P. Edwards, Y. Xu, C. McCallum, L. Tao, Z.-Q. Liang, M. Luo, X. Wang, H. Li, C. P. O'Brien, C.-S. Tan, D.-H. Nam, R. Quintero-Bermudez, T.-T. Zhuang, Y. C. Li, Z. Han, R. D. Britt, D. Sinton, T. Agapie, J. C. Peters, E. H. Sargent, Molecular tuning of CO_2-to-ethylene conversion, *Nature* **2020**, *577*, 509–513.

[147] C.-T. Dinh, T. Burdyny, M. G. Kibria, A. Seifitokaldani, C. M. Gabardo, F. P. García De Arquer, A. Kiani, J. P. Edwards, P. De Luna, O. S. Bushuyev, C. Zou, R. Quintero-Bermudez, Y. Pang, D. Sinton, E. H. Sargent, CO_2 electroreduction to ethylene via hydroxide-mediated copper catalysis at an abrupt interface, *Science* **2018**, *360*, 783–787.

[148] J. J. Kaczur, H. Yang, Z. Liu, S. D. Sajjad, R. I. Masel, Carbon Dioxide and Water Electrolysis Using New Alkaline Stable Anion Membranes, *Front. Chem.* **2018**, *6*, 263.

[149] H. Yang, J. J. Kaczur, S. D. Sajjad, R. I. Masel, Performance and long-term stability of CO_2 conversion to formic acid using a three-compartment electrolyzer design, *J. CO2 Util.* **2020**, *42*, 101349.

[150] Y. Chen, A. Vise, W. E. Klein, F. C. Cetinbas, D. J. Myers, W. A. Smith, T. G. Deutsch, K. C. Neyerlin, A Robust, Scalable Platform for the Electrochemical Conversion of CO_2 to Formate: Identifying Pathways to Higher Energy Efficiencies, *ACS Energy Lett.* **2020**, *5*, 1825–1833.

[151] A. G. Fink, F. Navarro-Pardo, J. R. Tavares, U. Legrand, Scale-up of electrochemical flow cell towards industrial CO_2 reduction to potassium formate, *ChemCatChem* **2024**, *16*, e202300977.

[152] J. Hietala, A. Vuori, P. Johnsson, I. Pollari, W. Reutemann, H. Kieczka in *Ullmann's Encyclopedia of Industrial Chemistry*, Wiley, Weinheim, **2016**, pp. 1–22.

[153] X. Sun, H. K. Atiyeh, R. L. Huhnke, R. S. Tanner, Syngas fermentation process development for production of biofuels and chemicals: A review, *Bioresour. Technol. Rep.* **2019**, *7*, 100279.

[154] A. S. Neto, S. Wainaina, K. Chandolias, P. Piatek, M. J. Taherzadeh, Exploring the Potential of Syngas Fermentation for Recovery of High-Value Resources: A Comprehensive Review, *Curr. Pollut. Rep.* **2024**, *11*, 7.

[155] R. Takors, M. Kopf, J. Mampel, W. Bluemke, B. Blombach, B. Eikmanns, F. R. Bengelsdorf, D. Weuster-Botz, P. Dürre, Using gas mixtures of CO, CO_2 and H_2 as microbial substrates: the do's and don'ts of successful technology transfer from laboratory to production scale, *Microb. Biotechnol.* **2018**, *11*, 606–625.

[156] T. Haas, R. Krause, R. Weber, M. Demler, G. Schmid, Technical photosynthesis involving CO_2 electrolysis and fermentation, *Nat. Catal.* **2018**, *1*, 32–39.

[157] M. Stöckl, N. Claassens, S. Lindner, E. Klemm, D. Holtmann, Coupling electrochemical CO_2 reduction to microbial product generation – identification of the gaps and opportunities, *Curr. Opin. Biotechnol.* **2022**, *74*, 154–163.

[158] N. J. Claassens, C. A. R. Cotton, D. Kopljar, A. Bar-Even, Making quantitative sense of electromicrobial production, *Nat. Catal.* **2019**, *2*, 437–447.

[159] D. Jendrossek, D. Pfeiffer, New insights in the formation of polyhydroxyalkanoate granules (carbonosomes) and novel functions of poly(3-hydroxybutyrate), *Environ. Microbiol.* **2014**, *16*, 2357–2373.

[160] A. A. Alves, E. C. Siqueira, M. P. S. Barros, P. E. C. Silva, L. M. Houllou, Polyhydroxyalkanoates: a review of microbial production and technology application, *Int. J. Environ. Sci. Technol.* **2023**, *20*, 3409–3420.

[161] F. W. Lichtenthaler in *Ullmann's Encyclopedia of Industrial Chemistry*, Wiley, Weinheim, **2010**, n05_n07.

[162] H. Li, P. H. Opgenorth, D. G. Wernick, S. Rogers, T.-Y. Wu, W. Higashide, P. Malati, Y.-X. Huo, K. M. Cho, J. C. Liao, Integrated Electromicrobial Conversion of CO_2 to Higher Alcohols, *Science* **2012**, *335*, 1596–1596.

[163] F. Collas, B. B. Dronsella, A. Kubis, K. Schann, S. Binder, N. Arto, N. J. Claassens, F. Kensy, E. Orsi, Engineering the biological conversion of formate into crotonate in Cupriavidus necator, *Metab. Eng.* **2023**, *79*, 49–65.

[164] O. Yishai, S. N. Lindner, J. Gonzalez De La Cruz, H. Tenenboim, A. Bar-Even, The formate bio-economy, *Curr. Opin. Chem. Biol.* **2016**, *35*, 1–9.

[165] S. Donati, C. W. Johnson, Optimizing Cupriavidus necator H16 as a host for aerobic C1 conversion, *Curr. Opin. Biotechnol.* **2025**, *93*, 103306.

[166] M. Stöckl, S. Harms, I. Dinges, S. Dimitrova, D. Holtmann, From CO_2 to Bioplastic – Coupling the Electrochemical CO_2 Reduction with a Microbial Product Generation by Drop-in Electrolysis, *ChemSusChem* **2020**, *13*, 4086–4093.

[167] J. H. Reid, Process of generating electricity, US736016A, **1903**.

[168] T. Burdyny, W. A. Smith, CO_2 reduction on gas-diffusion electrodes and why catalytic performance must be assessed at commercially-relevant conditions, *Energy Environ. Sci.* **2019**, *12*, 1442–1453.

[169] N. T. Nesbitt, T. Burdyny, H. Simonson, D. Salvatore, D. Bohra, R. Kas, W. A. Smith, Liquid–Solid Boundaries Dominate Activity of CO_2 Reduction on Gas-Diffusion Electrodes, *ACS Catal.* **2020**, *10*, 14093–14106.

[170] T. Moore, X. Xia, S. E. Baker, E. B. Duoss, V. A. Beck, Elucidating Mass Transport Regimes in Gas Diffusion Electrodes for CO_2 Electroreduction, *ACS Energy Lett.* **2021**, *6*, 3600–3606.

[171] F. Bernasconi, A. Senocrate, P. Kraus, C. Battaglia, Enhancing $C_{\geq 2}$ product selectivity in electrochemical CO_2 reduction by controlling the microstructure of gas diffusion electrodes, *EES Catal.* **2023**, *1*, 1009–1016.

[172] L.-C. Weng, A. T. Bell, A. Z. Weber, Modeling gas-diffusion electrodes for CO_2 reduction, *Phys. Chem. Chem. Phys.* **2018**, *20*, 16973–16984.

[173] F. Bienen, D. Kopljar, A. Löwe, P. Aßmann, M. Stoll, P. Rößner, N. Wagner, A. Friedrich, E. Klemm, Utilizing Formate as an Energy Carrier by Coupling CO_2 Electrolysis with Fuel Cell Devices, *Chem. Ing. Tech.* **2019**, *91*, 872–882.

[174] S. Brosch, E. Häger, O. Frank, P. Scholz, W. Plischka, M. Wessling, Visualization of CO formation at the triple-phase boundary in gas diffusion electrodes for ecCO_2RR, *Chem* **2025**, 102582.

[175] T. N. Nguyen, C.-T. Dinh, Gas diffusion electrode design for electrochemical carbon dioxide reduction, *Chem. Soc. Rev.* **2020**, *49*, 7488–7504.

[176] D. Wakerley, S. Lamaison, J. Wicks, A. Clemens, J. Feaster, D. Corral, S. A. Jaffer, A. Sarkar, M. Fontecave, E. B. Duoss, S. Baker, E. H. Sargent, T. F. Jaramillo, C. Hahn, Gas diffusion electrodes, reactor designs and key metrics of low-temperature CO_2 electrolysers, *Nat. Energy* **2022**, *7*, 130–143.

[177] A. Gawel, T. Jaster, D. Siegmund, J. Holzmann, H. Lohmann, E. Klemm, U.-P. Apfel, Electrochemical CO_2 reduction - The macroscopic world of electrode design, reactor concepts & economic aspects, *iScience* **2022**, *25*, 104011.

[178] Z. Xing, L. Hu, D. S. Ripatti, X. Hu, X. Feng, Enhancing carbon dioxide gas-diffusion electrolysis by creating a hydrophobic catalyst microenvironment, *Nat. Commun.* **2021**, *12*, 136.

[179] A. Bulan, J. Kintrup, R. Weber, Gas diffusion electrode and method for its production, EP2398101, **2011**.

[180] D. Kopljar, A. Inan, P. Vindayer, N. Wagner, E. Klemm, Electrochemical reduction of CO_2 to formate at high current density using gas diffusion electrodes, *J. Appl. Electrochem.* **2014**, *44*, 1107–1116.

[181] M. Oßkopp, A. Löwe, C. M. Lobo, S. Baranyai, T. Khoza, M. Auinger, E. Klemm, Producing formic acid at low pH values by electrochemical CO_2 reduction, *J. CO2 Util.* **2021**, *56*, 101823.

[182] H. Yang, J. J. Kaczur, S. D. Sajjad, R. I. Masel, Electrochemical conversion of CO_2 to formic acid utilizing Sustainion™ membranes, *J. CO2 Util.* **2017**, *20*, 208–217.

[183] A. Elgazzar, P. Zhu, F.-Y. Chen, S. Hao, T.-U. Wi, C. Qiu, V. Okatenko, H. Wang, Electrochemical CO_2 Reduction to Formic Acid with High Carbon Efficiency, *ACS Energy Lett.* **2025**, *10*, 450–458.

[184] K. Tedsree, T. Li, S. Jones, C. W. A. Chan, K. M. K. Yu, P. A. J. Bagot, E. A. Marquis, G. D. W. Smith, S. C. E. Tsang, Hydrogen production from formic acid decomposition at room temperature using a Ag–Pd core–shell nanocatalyst, *Nature Nanotech.* **2011**, *6*, 302–307.

[185] M. Grasemann, G. Laurenczy, Formic acid as a hydrogen source – recent developments and future trends, *Energy Environ. Sci.* **2012**, *5*, 8171–8181.

[186] I. Dinges, I. Depentori, L. Gans, D. Holtmann, S. R. Waldvogel, M. Stöckl, Coupling of CO_2 Electrolysis with Parallel and Semi-Automated Biopolymer Synthesis – Ex-Cell and without Downstream Processing, *ChemSusChem* **2024**, *17*, e202301721.

[187] I. Dinges, M. Pyschik, J. Schütz, S. Schneider, E. Klemm, S. R. Waldvogel, M. Stöckl, All Electrochemical Synthesis of Performic Acid Starting from CO_2, O_2, and H_2O, *ChemSusChem* **2025**, *18*, e202500180.

[188] I. Dinges, S. R. Waldvogel, M. Stöckl, CO_2 Reduction to Formic Acid/Formate by Intermittent Electricity at Bismuth Gas Diffusion Electrodes, *ChemSusChem* **2025**, e202501583.

[189] Creative Commons, "CC BY 4.0 Deed, Attribution 4.0 International", can be found under https : / / creativecommons . org / licenses / by / 4 . 0/, (accessed: 08.10.2025).

[190] R. Hegner, K. Neubert, C. Kroner, D. Holtmann, F. Harnisch, Coupled Electrochemical and Microbial Catalysis for the Production of Polymer Bricks, *ChemSusChem* **2020**, *13*, 5295–5300.

[191] Z. Jiang, S. Ren, X. Cao, Q. Fan, R. Yu, J. Yang, J. Mao, pH-Universal Electrocatalytic CO_2 Reduction with Ampere-Level Current Density on Doping-Engineered Bismuth Sulfide, *Angew. Chem. Int. Ed.* **2024**, *63*, e202408412.

[192] Q. Huang, Z. Qian, N. Ye, Y. Tan, M. Li, M. Luo, S. Guo, In Situ Reconstructed Hydroxyl-Rich Atomic-Thin $Bi_2O_2CO_3$ Enables Ampere-Scale Synthesis of Formate from CO_2 with Activated Water Dissociation, *Adv. Mater.* **2025**, *37*, 2415639.

[193] S. He, F. Ni, Y. Ji, L. Wang, Y. Wen, H. Bai, G. Liu, Y. Zhang, Y. Li, B. Zhang, H. Peng, The p-Orbital Delocalization of Main-Group Metals to Boost CO_2 Electroreduction, *Angew. Chem. Int. Ed.* **2018**, *57*, 16114–16119.

[194] T. Fan, W. Ma, M. Xie, H. Liu, J. Zhang, S. Yang, P. Huang, Y. Dong, Z. Chen, X. Yi, Achieving high current density for electrocatalytic reduction of CO_2 to formate on bismuth-based catalysts, *Cell Rep. Phys. Sci.* **2021**, *2*, 100353.

[195] E. Vlaeminck, K. Quataert, E. Uitterhaegen, K. De Winter, W. K. Soetaert, Advanced PHB fermentation strategies with CO_2-derived organic acids, *J. Biotechnol.* **2022**, *343*, 102–109.

[196] Federal Statistical Office of Germany, "Electricity prices for non-household customers: Germany, half-years, annual consumption classes, price types", can be found under https://www-genesis.destatis.de/datenbank/beta/statistic/61243/table/61243-0005, **2023** (accessed: 11.10.2023).

[197] S. Schneider, M. Stöckl, General Route to Indirect and On-Demand Electrosynthesis of (Various) Peroxy Acids via *In Situ* Generated Hydrogen Peroxide on a Gas Diffusion Electrode, *ACS Sustainable Chem. Eng.* **2024**, *12*, 5160–5168.

[198] H. Heinonen-Tanski, H. Miettinen, Performic Acid as a potential Disinfectant at low Temperature, *J. Food Process Eng.* **2010**, *33*, 1159–1172.

[199] M. Mora, A.-M. Veijalainen, H. Heinonen-Tanski, Performic Acid Controls Better Clostridium tyrobutyricum Related Bacteria than Peracetic Acid, *Sustainability* **2018**, *10*, 4116.

[200] P. Ragazzo, N. Chiucchini, V. Piccolo, M. Spadolini, S. Carrer, F. Zanon, R. Gehr, Wastewater disinfection: long-term laboratory and full-scale studies on performic acid in comparison with peracetic acid and chlorine, *Water Res.* **2020**, *184*, 116169.

[201] T. Karpova, P. Pekonen, R. Gramstad, U. Öjstedt, S. Laborda, H. Heinonen-Tanski, A. Chávez, B. Jiménez, Performic acid for advanced wastewater disinfection, *Water Sci. Technol.* **2013**, *68*, 2090–2096.

[202] J. R. Van Wazer, C. F. Callis, Metal Complexing By Phosphates, *Chem. Rev.* **1958**, *58*, 1011–1046.

[203] Federal Statistical Office of Germany, "Electricity Prices for Non-Household Customers: Germany, Half-Years, Annual Consumption Classes, Price Types", can be found under https://www-genesis.destatis.de/datenbank/online/statistic/61243/table/61243-0005, **2024** (accessed: 02.12.2024).

7 Publications, Conferences and Supervision

7.1 Publications

1. Ida Dinges, Siegfried R. Waldvogel, Markus Stöckl, CO_2 Reduction to Formic Acid/Formate by Intermittent Electricity at Bismuth Gas Diffusion Electrodes, *ChemSusChem* **2025**, e202501583, DOI: 10.1002/cssc.202501583
2. Ida Dinges, Ina Depentori, Lisa Gans, Dirk Holtmann, Siegfried R. Waldvogel, Markus Stöckl, Coupling of CO_2 Electrolysis with Parallel and Semi-Automated Biopolymer Synthesis – Ex-Cell and without Downstream Processing, *ChemSusChem* **2024**, *17*, e202301721, DOI: 10.1002/cssc.202301721
3. Ida Dinges, Markus Pyschik, Julian Schütz, Selina Schneider, Elias Klemm, Siegfried R. Waldvogel, Markus Stöckl, All Electrochemical Synthesis of Performic Acid Starting from CO_2, O_2, and H_2O, *ChemSusChem* **2025**,*18*, e202500180, DOI: 10.1002/cssc.202500180

7.2 Contribution to Conferences

2022 ACHEMA (Frankfurt / Germany)
Oral contribution: *GAMES – Gas diffusion electrodes for coupled microbial-electrochemical syntheses from CO_2*

2022 Electrochemistry (Berlin / Germany)
Poster contribution: *CO_2 reduction at gas diffusion electrodes coupled with microbial conversion*

2023 General Assembly of the GDCh Division Chemistry & Energy (Pfinztal / Germany)
Poster contribution: *Increasing energy efficiency and integrating CO_2 utilisation at municipal waste water treatment plants*

2024 Electrochemistry (Brunswick / Germany)
Oral contribution: *Coupling of CO_2 Electrolysis with Parallel and Semi-Automated Biopolymer Synthesis without Intermediate Downstream Processing*

2025 76^{th} Meeting of the International Society of Electrochemistry (Mainz / Germany)
Oral contribution: *Complete Electrosynthesis of Performic Acid from CO_2, O_2, and H_2O*

7.3 Supervised Students

2022 [redacted] (Research Internship, Goethe University Frankfurt)
„*Erste Untersuchungen zur Entwicklung eines elektrochemischen Formiat-Sensors*“ (*Initial Examination for the Development of an Electrochemical Sensor for Formate*)

2023 [redacted] (Bachelor Thesis, Technical University of Central Hesse)
„*Scale-up der Drop-In-Elektrolyse – PHB-Synthese mit Cupriavidus necator auf eFormiat*“ (*Scale-up of the Drop-in Electrolysis - PHB Synthesis with Cupriavidus necator on eFormate*)

2024 [redacted] (Bachelor Thesis, Technical University of Central Hesse)
„*Untersuchungen zur Entwicklung eines elektrochemischen, biokompatiblen Formiat-Sensors*“ (*Examinations for the Development of an Electrochemical, Biocompatible Sensor for Formate*)

Acknowledgements

Not included in the electronic version for data protection reasons.

Appendix

The sections (B), (C) and (D) have been reprinted according to the CC BY 4.0 license.[189]

Supporting Information

- Unpublished Results -

Development of Gas Diffusion Electrodes – Unpublished Stages

Ida Dinges, Siegfried R. Waldvogel, Markus Stöckl

Outline

S. R. Waldvogel, M. Stöckl, H. J. Kohnke and I. Dinges conceptualised the development of GDE. The development was carried out in cooperation with H. J. Kohnke from Gaskatel (Kassel / Germany), a commercial fabricator of GDEs. All experimental work, including fabrication of GDE, electrosynthesis of formate and analysis of the data, was carried out by I. Dinges if not stated otherwise. This section was written by I. Dinges.

1. General information

1.1 Chemical compounds

All chemical compounds were used in analytical grades and were obtained from common commercial sources. They were used without further purification and all solutions were prepared using high purity H_2O (0.055 µS cm^{-1}, 25 °C).

1.2 Materials for fabrication of GDEs

Materials used for fabrication of gas diffusion electrodes (GDEs) are summarised in Table S1.

Table S1: Overview of materials used for fabrication of GDEs.

Catalyst / Material	Specification	Supplier
Sn (powder)	Purity 99.9%, particle size ≤20 µm	Metallpulver24, Sankt Augustin / Germany
Bi (powder)	Purity 99.9%, particle size ≤40 µm	Metallpulver24, Sankt Augustin / Germany
PTFE (powder)	Dyneon™ PTFE TF 2072Z	3M, Saint Paul / USA
C65	C-NERGY™ SUPER C65 (Conductive carbon black)	Imerys, Paris / France
Ni mesh	Material 1.4301, mesh size = 0.5 cm, *d* = 240 µm	Haver & Boecker, Oelde / Germany
Ni foam	Ni-5763, density 420 - 450 g m^{-2}	Recemat BV, Dodewaard / Netherlands

1.3 Fabrication of GDE

The gas diffusion electrodes (GDE) were fabricated by pressing catalyst mixture onto support material with either a calender or a heat press. Each catalyst mixture was homogenised in a knife mill (A 10 basic, IKA, Staufen / Germany). The mixing (30 s, 25000 rpm) lead to a temperature increase of the mixture (T > 35 °C).

For fabrication with the calender (LaboWalz W80T, Vogt Labormaschinen, Berlin / Germany equipped with thermostat TT188, Tool-Temp, Sulgen / Switzerland), a two-step process was used (cf. Figure S1). Firstly, the catalyst mixture was distributed onto the rollers (T = 60-65 °C, gap width = 150 µm, roller velocity = 0.6 rpm) with a dispensing device and pressed vertically into a sheet of catalyst mixture (≙ GDE felt). Afterwards, the sheet of catalyst mixture was pressed onto Ni mesh as support material with the rollers (T = 60-65 °C, gap width = 350 µm, roller velocity = 0.6 rpm). Thereby, GDEs with a size >100 cm^2 could be fabricated. For evaluation by electrolysis, large GDEs was cut into smaller GDEs suitable for the screening set-up (3.5 cm x 4.0 cm ≙ 14 cm^2).

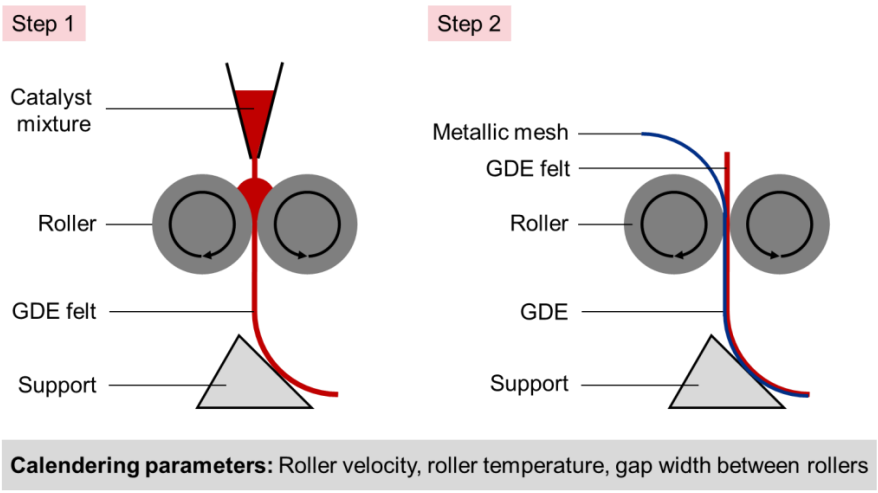

Figure S1: Schematic illustration of the two-step calendering process for fabrication of GDEs (the GDE blank is pressed in vertical orientation).

For fabrication with the heat press (cf. Figure S2), the catalyst mixture was equally distributed onto support material (3.5 cm x 4.0 cm ≙ 14 cm^2) with a sieve (stainless-steel wire mesh, mesh size = 500 µm, ISO 3310-1, Retsch / Verder Scientific, Haan / Germany) and a stencil (Cut-out 3.5 cm x 4.0 cm). Afterwards, the GDE blank was placed in between two pieces of ordinary baking sheet in the heat press (LaboPress P200S, Vogt Labormaschinen, Berlin / Germany) and compressed (plate temperature 120 °C, pressure 10 bar, 60 s). After compressing, excess material at the GDE edges was removed. The GDE's final catalyst loading *b* was determined by differential weighing (Sartorius 1712004, Sartorius Lab Instruments, Göttingen / Germany) and its thickness *d* was measured at the centre point (Micromar 40 ER, Mahr, Göttingen / Germany). The results have been provided if available (cf. Table S2).

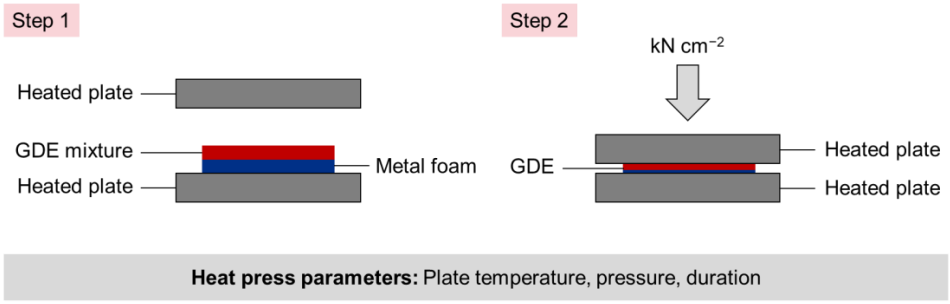

Figure S2: Schematic illustration of the heat press process for fabrication of GDEs (the GDE blank is pressed in a horizontal orientation).

If not stated otherwise, all GDEs were self-fabricated as described either with the calender or the heat press.

Table S2: Overview of electrocatalyst composition, catalyst mixture loading *b* and thickness *d* of the fabricated GDEs by heat pressing if available.

GDE	Composition	Support	*b* (catalyst mixture) / mg cm^{-2}	*d* (GDE, centre point) / µm
(D1)	85 wt% Sn, 10 wt% PTFE, 5 wt% C65	Ni foam	71.12	522
(D2)	85 wt% Sn, 10 wt% PTFE, 5 wt% C65	Ni foam	67.89	473
(D3)	85 wt% Sn, 10 wt% PTFE, 5 wt% C65	Ni foam	97.34	627
(E1)	85 wt% Sn, 10 wt% PTFE, 5 wt% C65	Ni mesh	-	501
(E2)	87.5 wt% Sn, 12.5 wt% PTFE	Ni mesh	117.82	393
(G1)	87.5 wt% Sn, 12.5 wt% PTFE	Ni foam	96.20	511
(G2)	87.5 wt% Sn, 12.5 wt% PTFE	Ni foam	110.67	553
(H1)	87.5 wt% Sn, 12.5 wt% PTFE	Ni foam	-	532
(I1)	87.5 wt% Bi, 12.5 wt% PTFE	Ni foam	105.01	503

1.4 Electrosynthesis of formate

Detailed descriptions of the electrochemical flow reactor and the electrolysis set-up have been published (DOI: 10.1002/cssc.202301721). The same electrochemical flow reactor and electrolysis set-up have been employed for the electrosynthesis of formate in this supporting information. Some electrolyses were carried out using a slightly modified set-up with additional integrated sensors, which has also been published (DOI: 10.1002/cssc.202500180). Operational conditions are specified in the respective section of the results (cf. chapter 2).

1.5 High performance liquid chromatography (HPLC)

The quantification of formate was carried out via HPLC (cf. Table S3), the system was operated with the software *LabSolutions* (Version 5.93).

Table S3: HPLC measurement conditions for formate and PHB analysis performed on an HPLC unit (LC-20AD, SIL-20AC HT, CBM-20A, CTO-20AC, SPD-M20A - Shimadzu, Kyoto / Japan).

Conditions	Formate
Eluent	5 mmol L^{-1} H_2SO_4
Flow rate	0.6 mL min^{-1}
Pressure	30 ± 1
Column oven	35 °C
Column	Rezex ROA- Organic Acid (8%), 300 mm × 7.8 mm, Phenomenex, Torrance / USA
Injection volume	10 µL
Detector	Photodiode array (PDA)
Wavelength λ	194 nm
Retention time	15.3 min
Duration	25 min

Formate standards were prepared from a stock solution by a dilution series with the dilution factor 2. The stock solution was prepared with HCOONa (3.482 g, 51.2 mmol) in a volumetric flask (100 mL, ISO 1042).

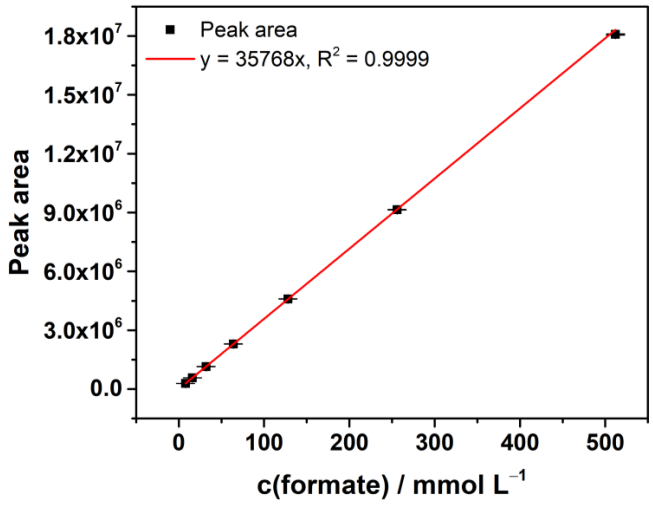

Figure S3: Calibration for formate quantification via HPLC measurement**.** Plot of formate concentration (8, 16, 32, 64, 128, 256, 512 mmol L^{-1}) against the peak area of the measured signal (n = 3) with a linear fit forced through zero.

1.6 Calculations

The FE for formate was calculated based on the determined amount of electrosynthesised formate using equation (1).

$$FE = \frac{F \cdot z \cdot n}{I \cdot t} \cdot 100\% \quad (1)$$

With FE = Faradaic efficiency / %, F = Faraday constant / A s mol^{-1}, z = Number of transferred electrons (z = 2), n = Amount of synthesised formate / mol, I = Current / A, t = Electrolysis runtime / s.

The electric energy consumption (EEC) was either given in total for an electrolysis or calculated for formate based on the determined amount of electrosynthesised formate using equation (2).

$$EEC = \frac{F \cdot z \cdot U}{FE \cdot M} \cdot (2.778 \cdot 10^{-7}) \quad (2)$$

With EEC = Electric energy consumption / kWh kg^{-1}, F = Faraday constant / A s mol^{-1}, z = Number of transferred electrons per molecule (z = 2), U = Averaged cell voltage / V, FE = Faradaic efficiency / %, M = Molar mass of formate / kg mol^{-1}.

2. Results

2.1 Second stage (II) of GDE development

In total, electrosynthesis of formate was carried out six times with the second stage (II) of GDE development (85 wt% Sn, 10 wt% PTFE, 5 wt% C65 on Ni mesh, fabricated with calender). The results have been summarised in Figure S3 and Table S4.

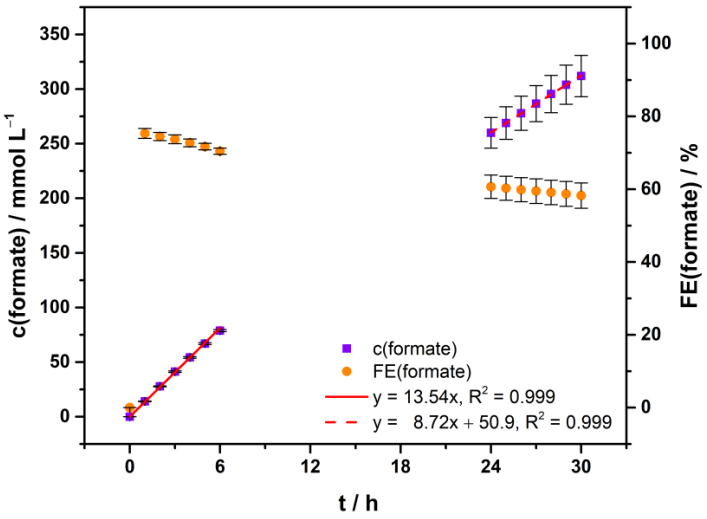

Figure S4: Concentration and Faradaic efficiency (FE) course of formate during formate electrosynthesis (n = 6, A1 - A6). The formate concentration course was fitted linearly in two intervals: t = 0 - 6 h (red, solid line) and t = 24 - 30 h (red, dashed line). Electrolysis parameters: Constant current density j = 100 mA cm^{-2}, runtime = 30 h, electrolyte = 0.2 mol L^{-1} KH_2PO_4 / K_2HPO_4, initial V(catholyte, anolyte) = 500 mL each, cathode (GDE, 5 cm^2 geometrical area) = 85 wt% Sn, 10 wt% PTFE, 5 wt% C65 on Ni mesh (fabricated with calender), reference electrode = reversible hydrogen electrode (RHE), anode = Pt on a Ti-grid (Platinode EP, Umicore).

Table S4: Overview of volume, formate concentration, formate FE and pH after 30 h electrolysis in the catholyte of formate electrosynthesis with 0.2 mol L^{-1} KH_2PO_4 / K_2HPO_4 as starting electrolyte. Accompanied by average and standard deviation of cell voltage during runtime and absolute electric energy consumption (EEC).

Electrolysis	V / mL	c(formate) / mmol L^{-1}	FE(formate) / %	pH	U / V	EEC / Wh
(A1)	520	341.7	63.5	5.68	5.8 ± 0.2	87.2
(A2)	520	288.6	53.6	6.42	6.3 ± 0.3	94.5
(A3)	525	310.1	58.2	6.18	6.3 ± 0.3	94.8
(A4)	525	295.7	55.5	6.30	6.4 ± 0.3	96.7
(A5)	520	314.8	58.5	6.15	6.1 ± 0.3	91.9
(A6)	525	321.1	60.2	6.03	6.4 ± 0.4	95.9

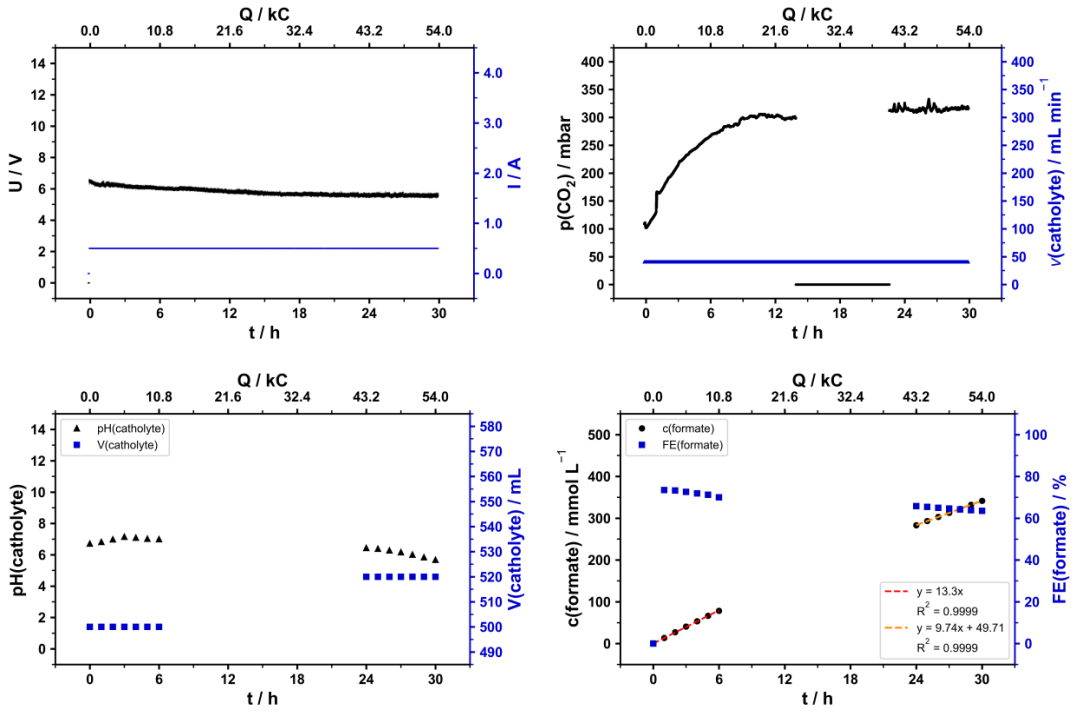

Figure S5: Data for electrolysis (A1), experimental details are provided above (cf. Figure S4 and Table S4).

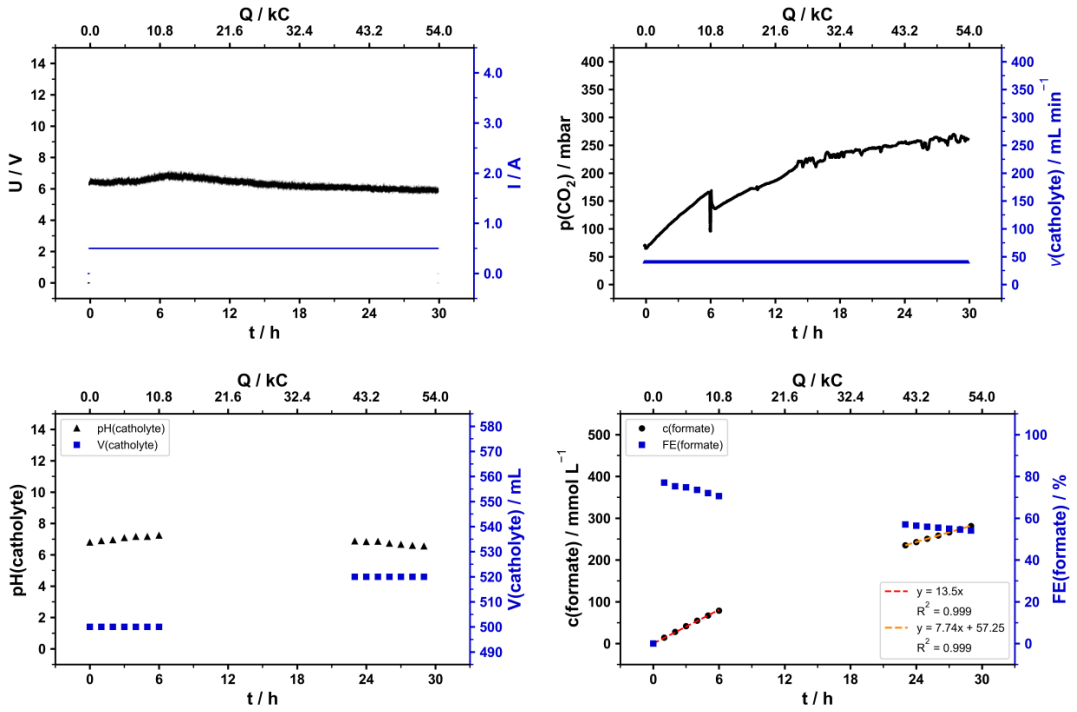

Figure S6: Data for electrolysis (A2), experimental details are provided above (cf. Figure S4 and Table S4).

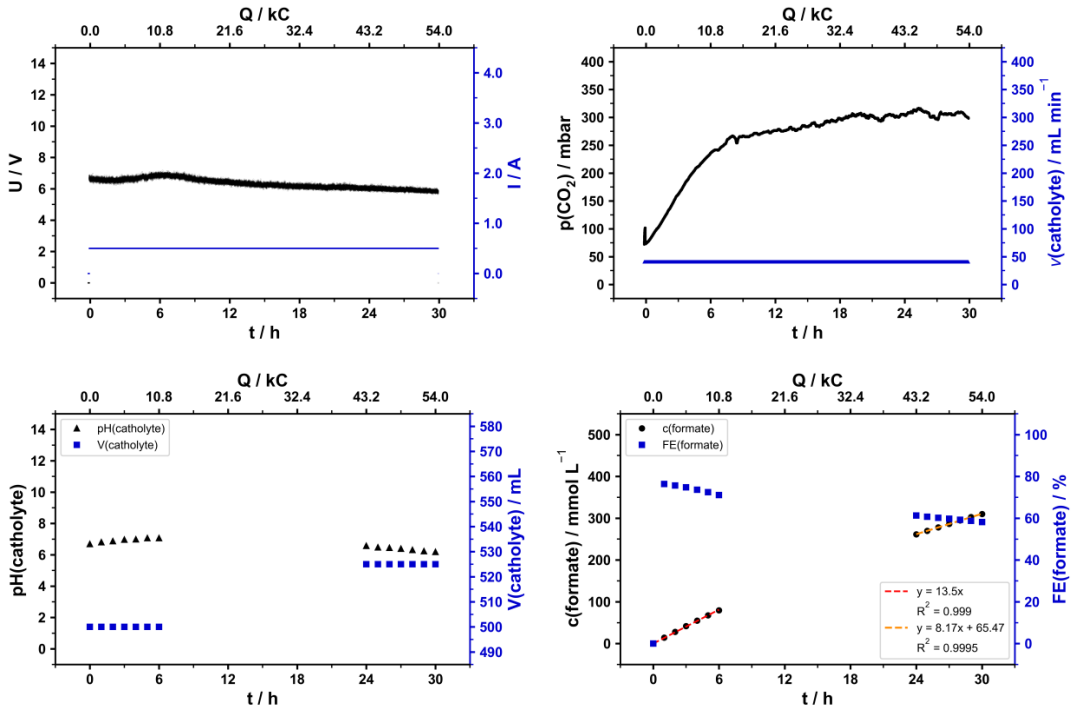

Figure S7: Data for electrolysis (A3), experimental details are provided above (cf. Figure S4 and Table S4).

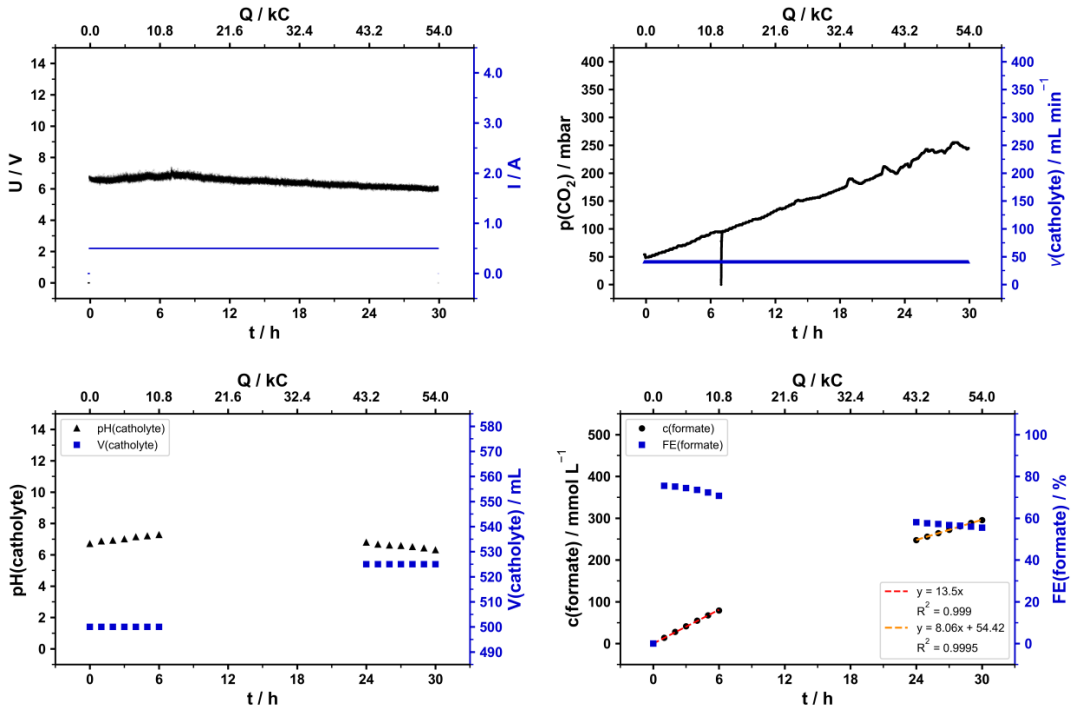

Figure S8: Data for electrolysis (A4), experimental details are provided above (cf. Figure S4 and Table S4).

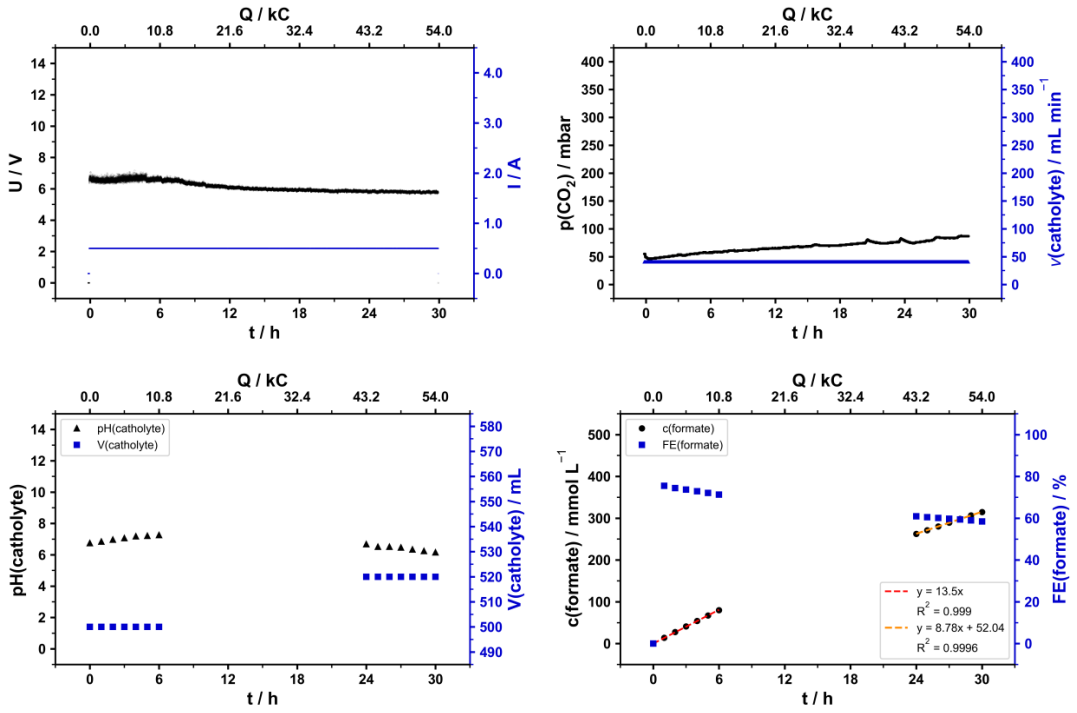

Figure S9: Data for electrolysis (A5), experimental details are provided above (cf. Figure S4 and Table S4).

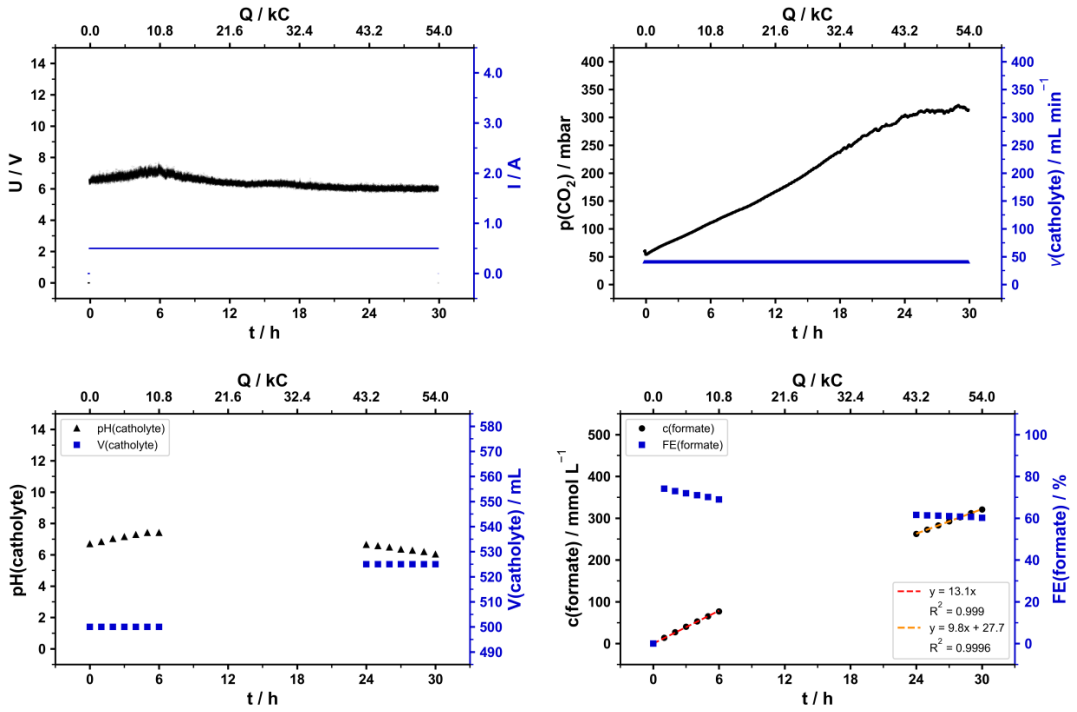

Figure S10: Data for electrolysis (A6), experimental details are provided above (cf. Figure S4 and Table S4).

2.2 Operation at intervals with and without current

Electrosynthesis of formate was exemplarily carried out at intermittent current to examine formate mass transport within the GDE. For this purpose, the electrolysis was repeatedly alternated between intervals with current (60 min) and cleaning intervals to rinse formate out of the GDE / reactor (30 min). The catholyte was passed through the reactor only once and then collected at defined intervals. It was found most of the formate was rinsed out of the GDE after 30 min. However, formate concentration increased slightly during the entire experiment in every last part of the rinsing interval. From this it was concluded the porosity of the GDEs should be increased to improve mass transport of formate during electrolysis. The results are summarised in Table S5 and Figure S11.

Table S5: Overview of intervals, current density as well as volume, concentration and FE of formate for formate electrosynthesis at intermittent current (B1). Electrolysis parameters: Runtime = 4.5 h, electrolyte = 0.2 mol L^{-1} KH_2PO_4 / K_2HPO_4, v(catholyte) = 2.7 mL min^{-1}, v(anolyte) = 9 mL min^{-1} (single pass through reactor each), $v(CO_2)$ = 3 mL min^{-1}, cathode (GDE, 5 cm^2 geometrical area) = 90 wt% Sn, 8 wt% PTFE, 2 wt% graphite on Ni mesh (fabricated with calender by Gaskatel), reference electrode = reversible hydrogen electrode (RHE), anode = Pt on a Ti-grid (Platinode EP, Umicore).

Interval / min	j / mA cm^{-2}	V(catholyte) / mL	c(formate) / mmol L^{-1}	FE(formate) / %	Cor.[a] FE(formate) / %
0 - 60	100	165	41.9	74.1	79.0
60 - 70	0	27	16.0	-	-
70 - 80	0	27	0.6	-	-
80 - 90	0	27	0.2	-	-
90 - 150	100	165	41.7	73.8	79.6
150 - 160	0	27	18.6	-	-
160 - 170	0	27	1.2	-	-
170 - 180	0	27	0.5	-	-
180 - 240	100	165	39.7	70.2	75.6
240 - 250	0	27	16.3	-	-
250 - 260	0	27	1.6	-	-
260 - 270	0	27	0.7	-	-

[a] Cor. FE(formate) includes the molar amounts of formate collected in the three respective cleaning intervals without current.

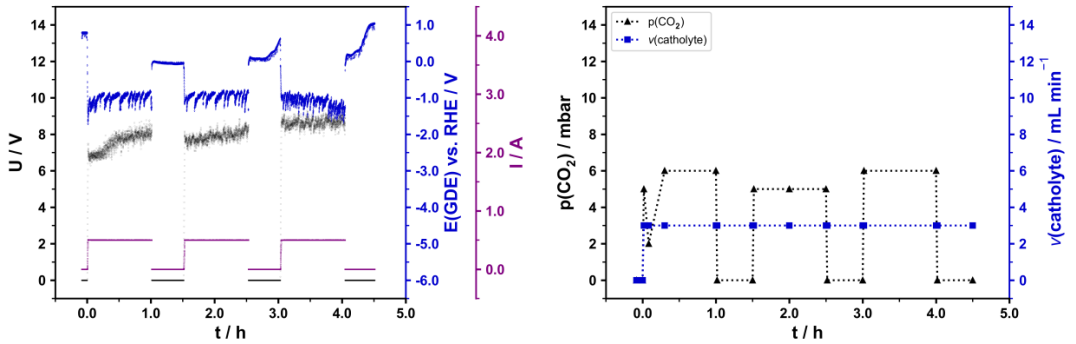

Figure S11: Data for electrolysis (B1), experimental details are provided above (cf. Table S5).

2.3 Influence of pore forming agents

The influence of GDEs with and without pore forming agent was examined exemplarily. On the one hand, NH_4HCO_3 was chosen as it could decompose during fabrication due to heat or dissolve into the catholyte during electrolysis. On the other hand, KH_2PO_4 and K_2HPO_4 were chosen as they already serve as supporting electrolyte and should dissolve into the catholyte during electrolysis. The GDEs were self-fabricated with the calender. The comparison is summarised in Table S6, all individual electrolyses are shown in the following.

Table S6: Comparison of the highest hourly (Peak FE h^{-1}) and overall FE (6 h) for formate achieved with GDEs containing either no or exemplary pore forming agents. Electrolysis conditions: Constant current density j = 100 mA cm^{-2}, runtime = 6 h, electrolyte = 0.2 M KH_2PO_4/K_2HPO_4 (equimolar), V(catholyte, anolyte) = 200 mL each, cathode (GDE, 5 cm^2 geometrical area) on Ni mesh (fabricated with calender), anode = Pt on a Ti-grid (Platinode EP, Umicore).

Electrolysis	Catalyst[a] (+ pore forming agent)	Peak FE h^{-1} / %	FE (6 h) / %	ΔFE (Peak vs. 6 h) / %
(C1)	85 wt% Sn	78.5	72.5	6.0
(C2)	85 wt% Sn	77.6	70.9	6.7
(C3)	84 wt% Sn (1 wt% NH_4HCO_3)	77.0	69.9	7.1
(C4)	84 wt% Sn (1 wt% NH_4HCO_3)	76.1	71.0	5.1
(C5)	83 wt% Sn (1 wt% KH_2PO_4, 1 wt% K_2HPO_4)	77.6	70.8	6.8
(C6)	83 wt% Sn (1 wt% KH_2PO_4, 1 wt% K_2HPO_4)	78.8	72.9	5.9

[a] Catalyst mixture also included 10 wt% PTFE and 5 wt% C65 each.

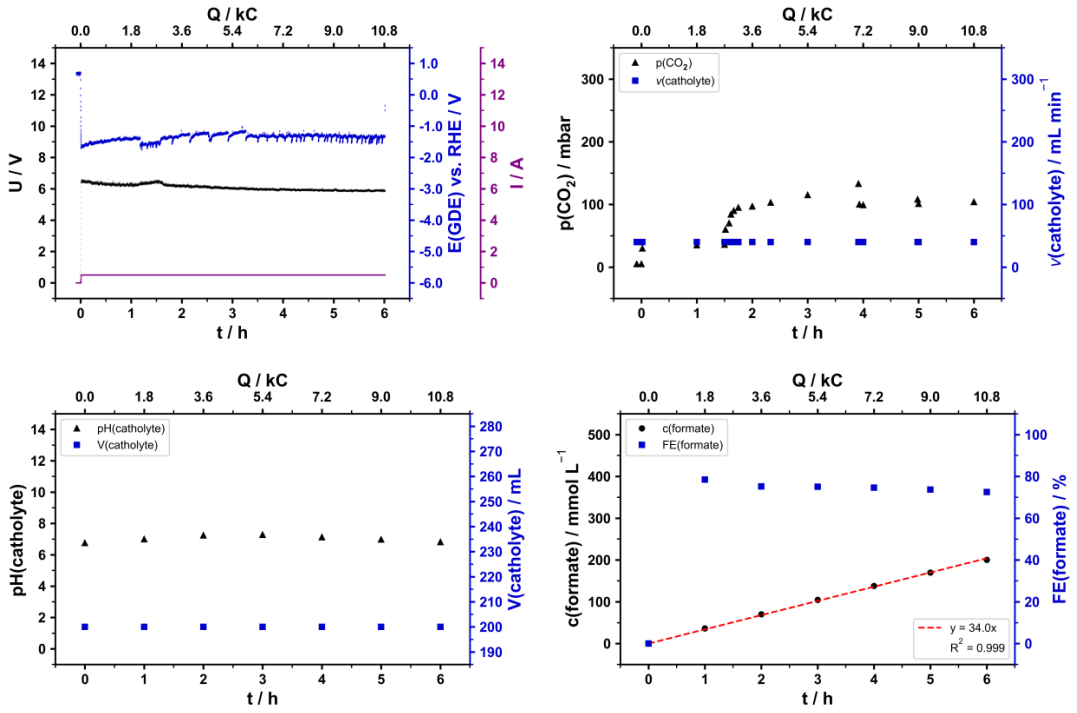

Figure S12: Data for electrolysis (C1), experimental details are provided above (cf. Table S6).

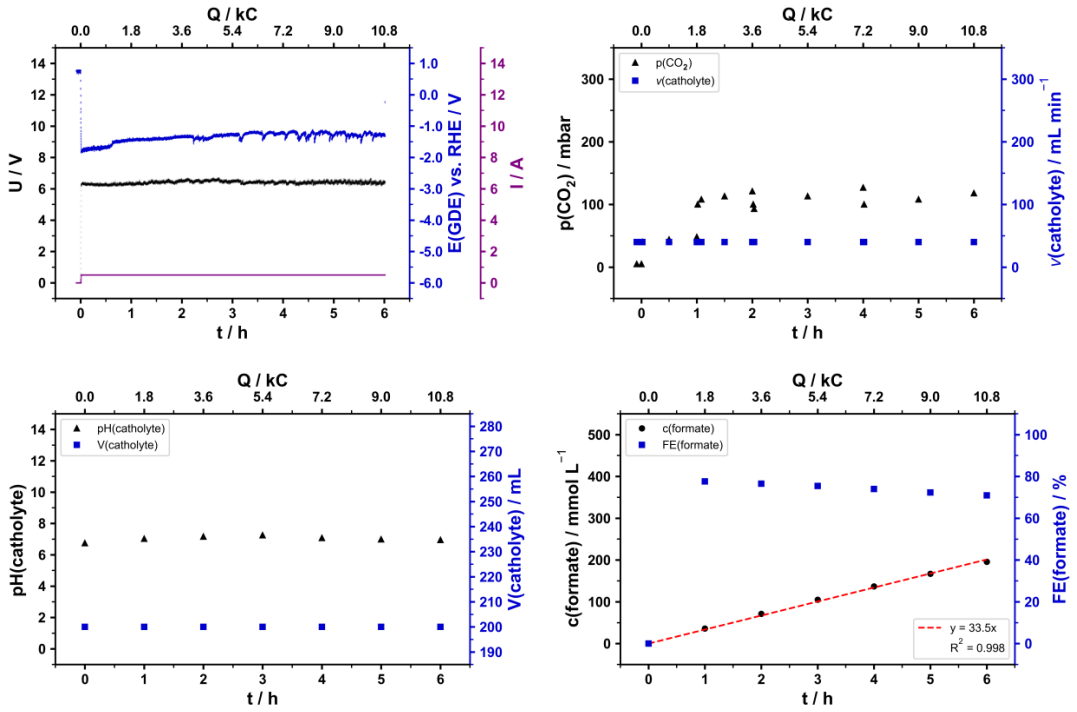

Figure S13: Data for electrolysis (C2), experimental details are provided above (cf. Table S6).

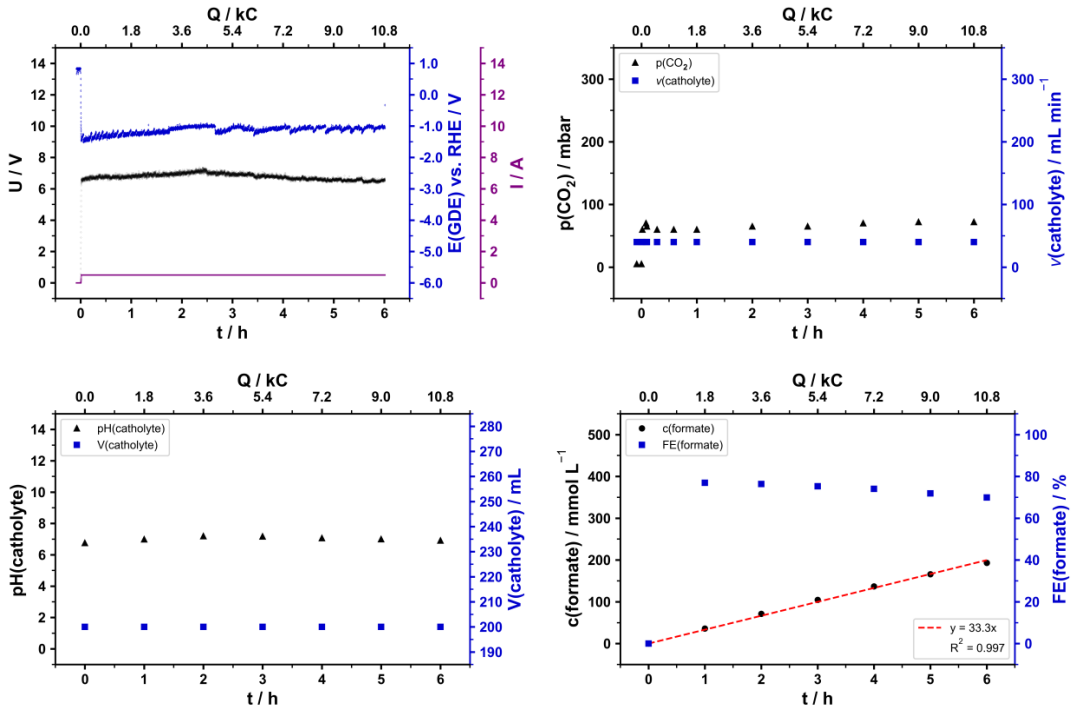

Figure S14: Data for electrolysis (C3), experimental details are provided above (cf. Table S6).

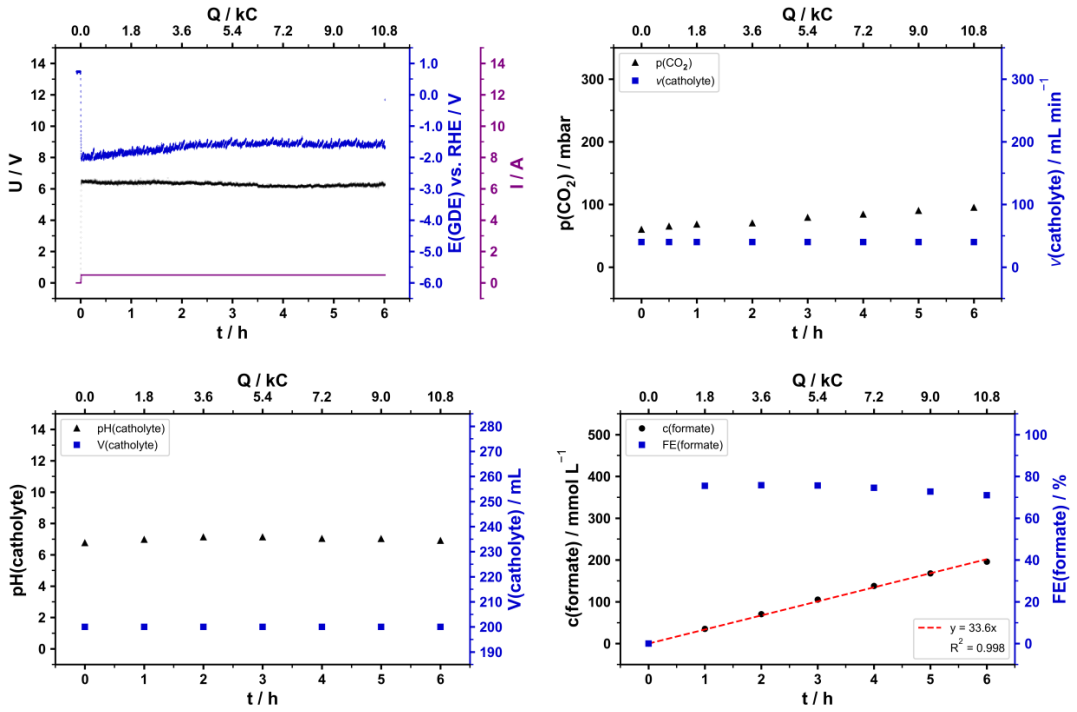

Figure S15: Data for electrolysis (C4), experimental details are provided above (cf. Table S6).

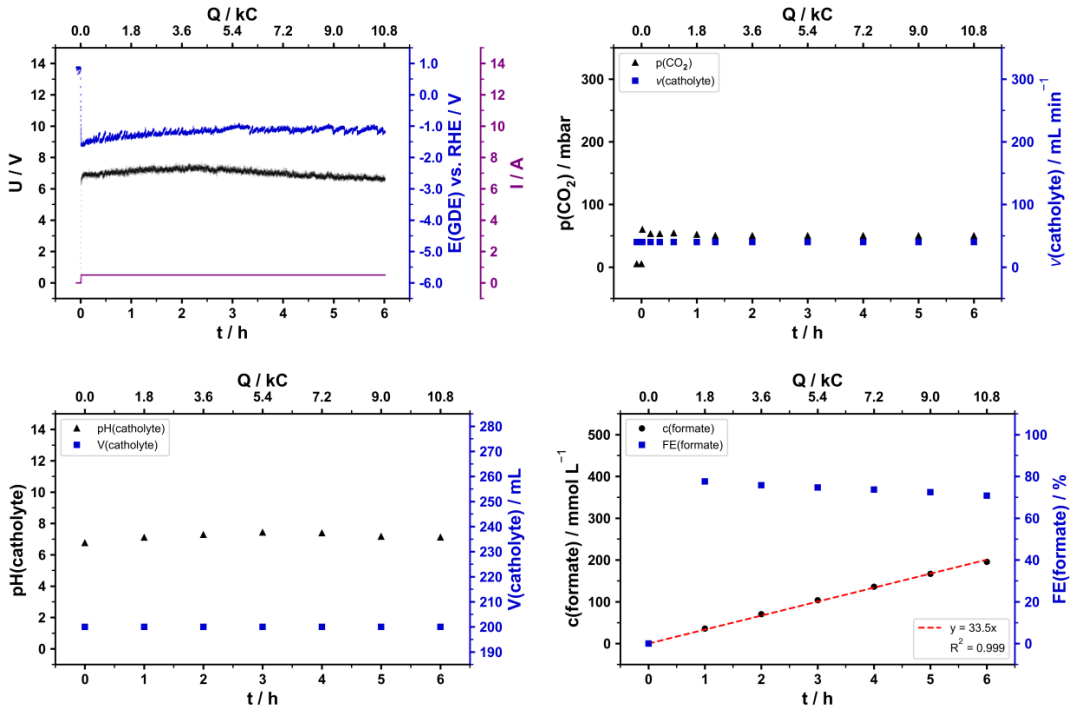

Figure S16: Data for electrolysis (C5), experimental details are provided above (cf. Table S6).

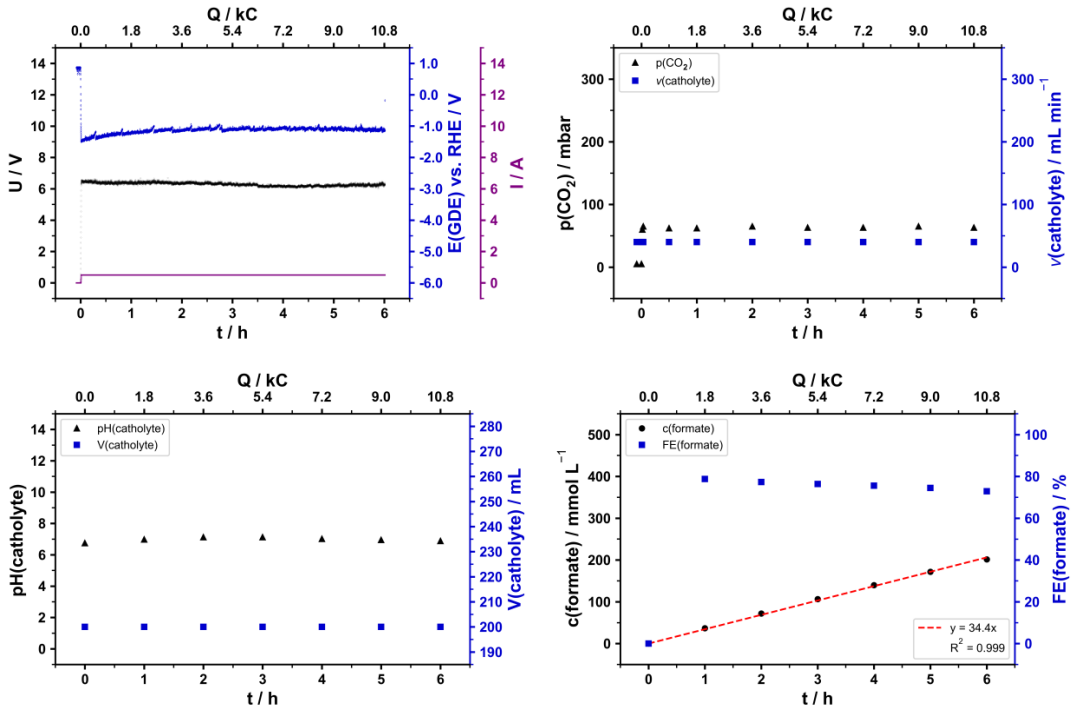

Figure S17: Data for electrolysis (C6), experimental details are provided above (cf. Table S6).

2.4 Influence of Ni foam as porous support material

The influence of GDEs with Ni foam as pore forming agent was examined with the catalyst composition of the second stage of development (cf. section 2.1). The GDEs were self-fabricated with the heat press, as incorporation of Ni foam as support material was not possible with the available vertical calender set-up (cf. Figure S1). The results are summarised in Figure S18 and Table S7. In comparison to the second stage of development (cf. section 2.1, Figure S4), the decrease of FE and synthesis rate of formate during runtime was significantly lower with Ni foam as support material.

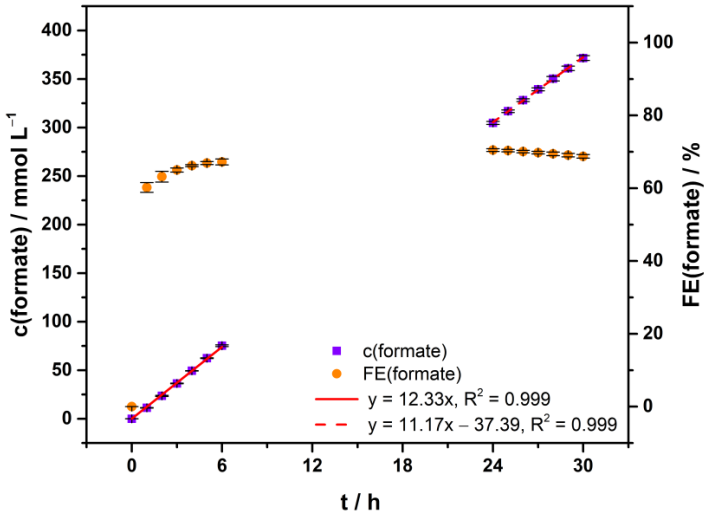

Figure S18: Concentration and Faradaic efficiency (FE) course of formate for formate electrosynthesis (n = 3, D1 - D3). The formate concentration course was fitted linearly in two intervals: t = 0 - 6 h (red, solid line) and t = 24 - 30 h (red, dashed line). Electrolysis parameters: Constant current density j = 100 mA cm^{-2}, runtime = 30 h, electrolyte = 0.2 mol L^{-1} KH_2PO_4 / K_2HPO_4, initial V(catholyte, anolyte) = 500 mL each, cathode (GDE, 5 cm^2 geometrical area) = 85 wt% Sn, 10 wt% PTFE, 5 wt% C65 on Ni foam (fabricated with heat press), reference electrode = reversible hydrogen electrode (RHE), anode = Pt on a Ti-grid (Platinode EP, Umicore).

Table S7: Overview of volume, formate concentration, formate FE and pH after 30 h electrolysis in the catholyte of formate electrosynthesis with 0.2 mol L^{-1} KH_2PO_4 / K_2HPO_4 as starting electrolyte. Accompanied by average and standard deviation of cell voltage during runtime and absolute electric energy consumption (EEC).

Electrolysis	V / mL	c(formate) / mmol L^{-1}	FE(formate) / %	pH	U / V	EEC / Wh
(D1)	518	372.0	68.9	5.09	5.7 ± 0.4	85.2
(D2)	518	373.9	69.2	5.22	5.8 ± 0.5	86.8
(D3)	517	369.0	68.2	5.19	5.8 ± 0.5	87.0

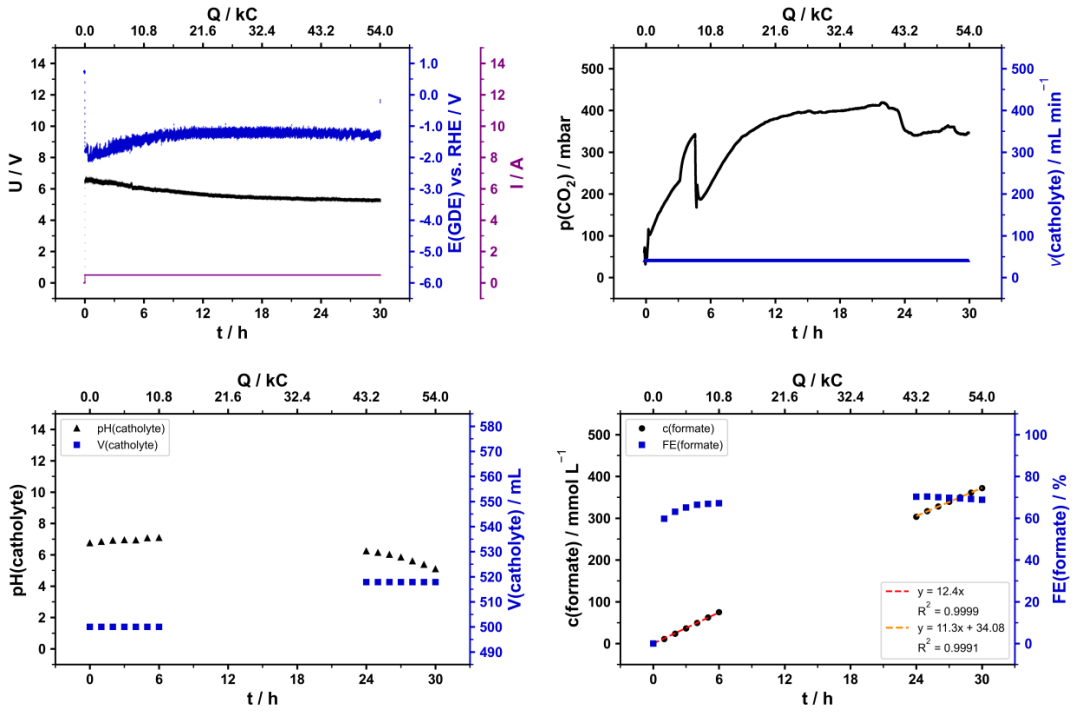

Figure S19: Data for electrolysis (D1), experimental details are provided above (cf. Figure S18).

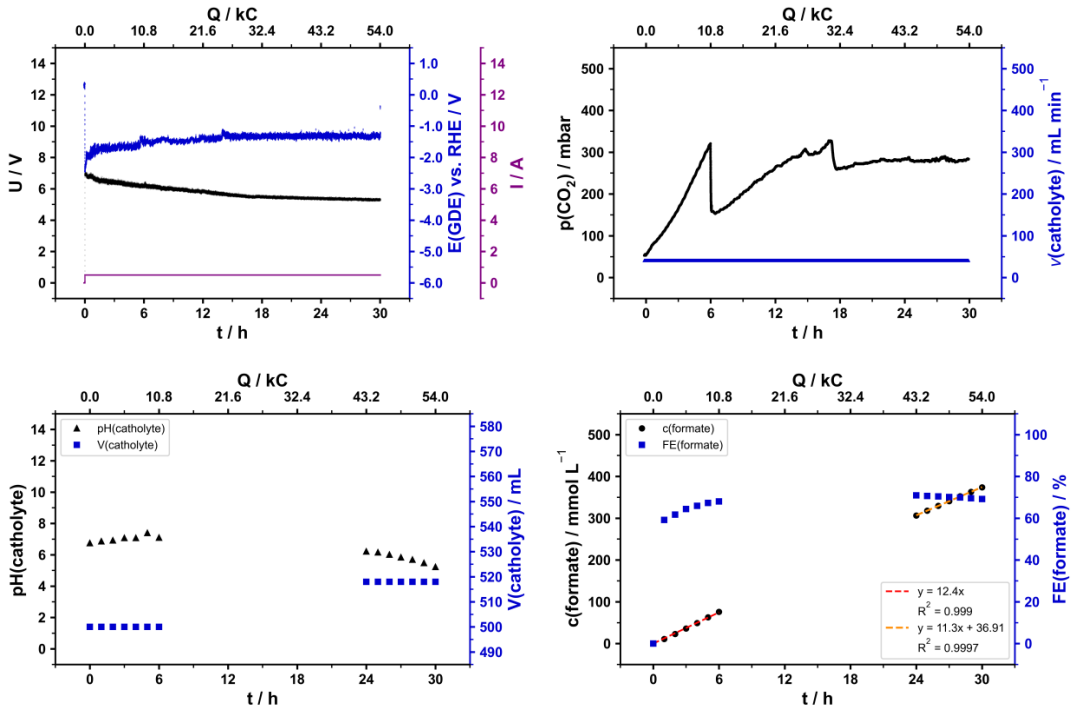

Figure S20: Data for electrolysis (D2), experimental details are provided above (cf. Figure S18).

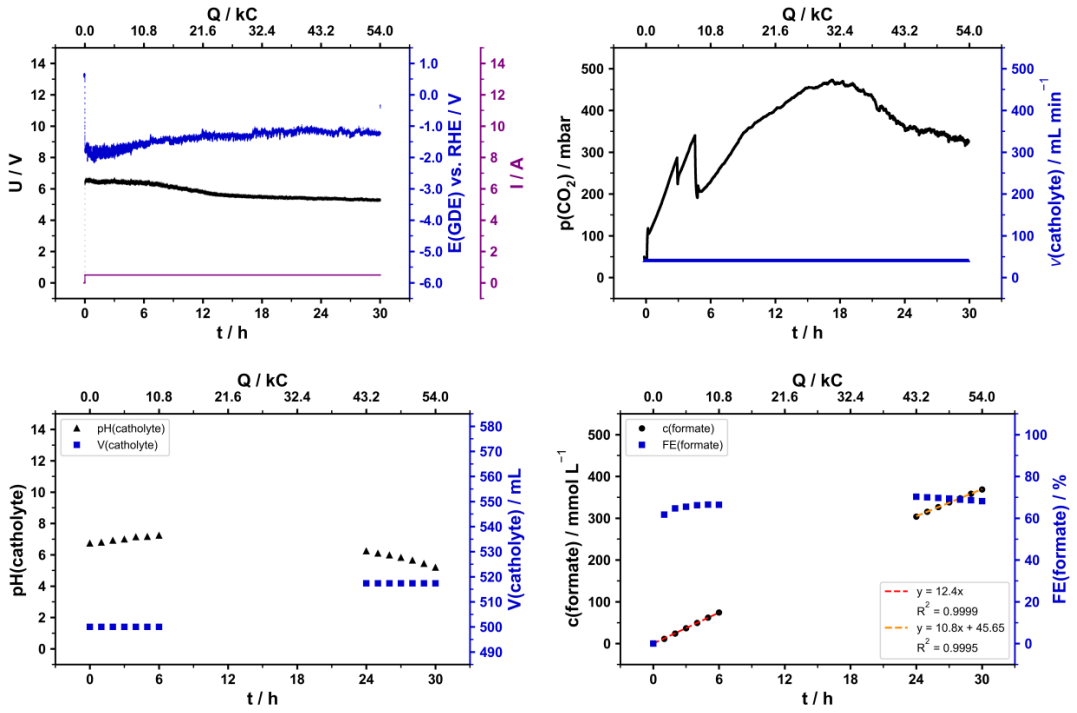

Figure S21: Data for electrolysis (D3), experimental details are provided above (cf. Figure S18).

2.5 Influence of fabrication method (calender vs. heat press) and Ni foam

Two different results of the electrosynthesis of formate are included here to demonstrate changing from calender to heat press did not influence the performance of GDEs. Thereby, they showed Ni foam (incorporation as support material only possible with heat press due to vertical calender set-up, cf. Figure S1) was responsible for an improved FE of formate.

The first results (Table S8, Figure S22) were obtained with a GDE of the same catalyst composition as the second stage (II) of development (85 wt% Sn, 10 wt% PTFE, 5 wt% C65). Ni mesh also served as support material. However, it was fabricated with the heat press instead of the calender. Consequently, the only difference between the second stage (cf. section 2.1) and electrolysis (E1) was the fabrication method. The comparison revealed their performances were similar. Hence, both fabrication methods yield comparable GDEs and switching between them had no significant influence on the results.

The second results (Table S8, Figure S23) were obtained with a GDE of the same catalyst composition as the third stage (III) of development (87.5 wt% Sn, 12.5 wt% PTFE, cf. 2.7). It was also fabricated with the heat press. However, Ni mesh served as support material instead of Ni foam. Consequently, the only difference between the third stage (cf. section 2.7) and electrolysis (E2) was the support material. The comparison of (E2) and (G1, G2) revealed Ni foam definitely improved the FE of formate.

Table S8: Overview of volume, formate concentration, formate FE and pH after 30 h electrolysis in the catholyte of formate electrosynthesis with 0.2 mol L^{-1} KH_2PO_4 / K_2HPO_4 as starting electrolyte. Accompanied by average and standard deviation of cell voltage during runtime and absolute electric energy consumption (EEC).

Electrolysis	V / mL	c(formate) / mmol L^{-1}	FE(formate) / %	pH	U / V	EEC / Wh
(E1)	510	335.3	61.9	5.96 ± 0.05	6.5 ± 0.3	97.2
(E2)	514.8 ± 3.3	325.7	59.9	5.89 ± 0.05	6.1 ± 0.5	91.1

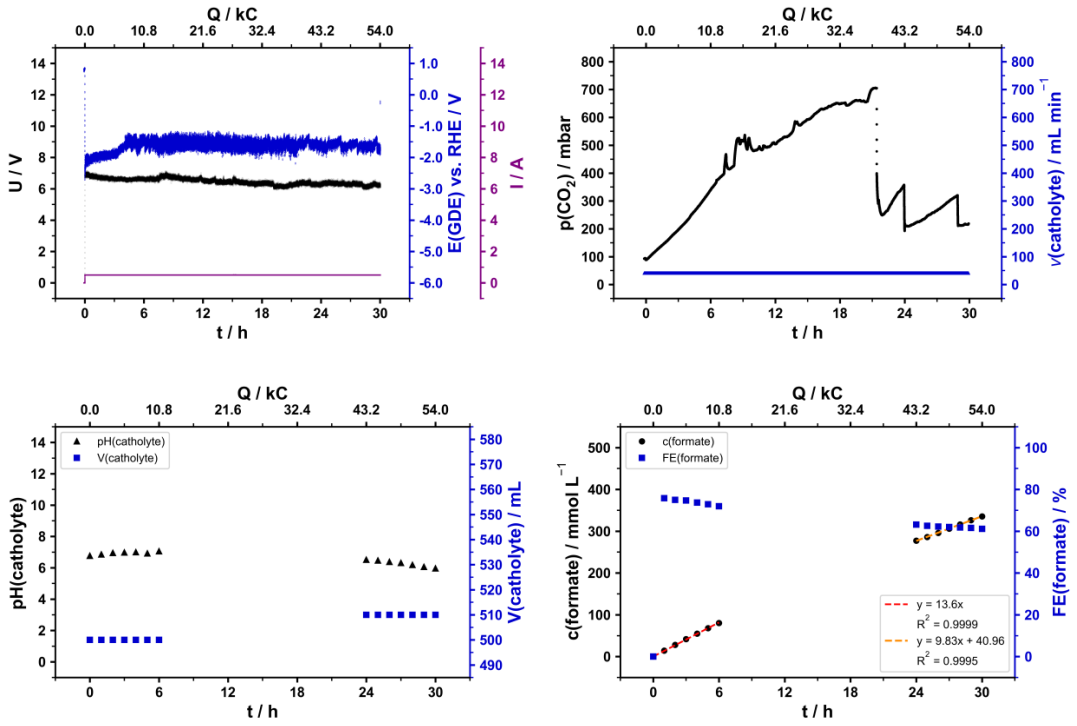

Figure S22: Data for the electrosynthesis of formate (E1) with Sn based GDE. Electrolysis parameters: Constant current density j = 100 mA cm^{-2}, runtime = 30 h, electrolyte = 0.2 mol L^{-1} KH_2PO_4 / K_2HPO_4, initial V(catholyte, anolyte) = 500 mL each, cathode (GDE, 5 cm^2 geometrical area) = 85 wt% Sn, 10 wt% PTFE, 5 wt% C65 on Ni mesh (fabricated with heat press), reference electrode = reversible hydrogen electrode (RHE), anode = Pt on a Ti-grid (Platinode EP, Umicore).

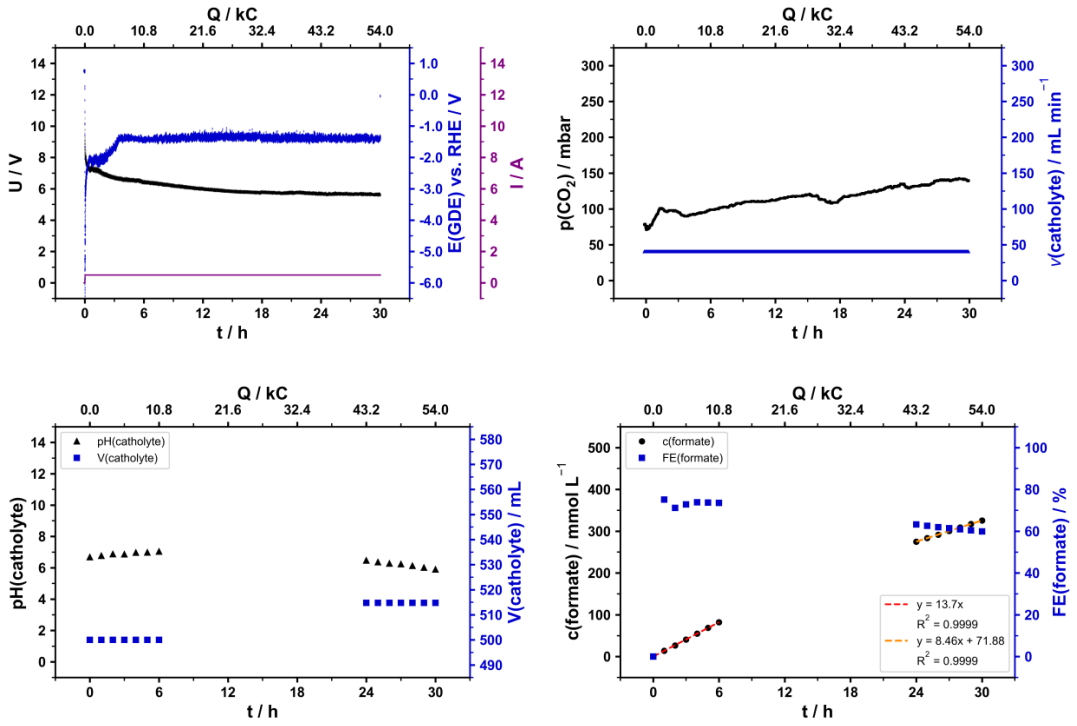

Figure S23: Data for the electrosynthesis of formate (E2) with the Sn based GDE. Electrolysis parameters: Constant current density j = 100 mA cm^{-2}, runtime = 30 h, electrolyte = 0.2 mol L^{-1} KH_2PO_4 / K_2HPO_4, initial V(catholyte, anolyte) = 500 mL each, cathode (GDE, 5 cm^2 geometrical area) = 87.5 wt% Sn, 12.5 wt% PTFE on Ni mesh (fabricated with heat press), reference electrode = reversible hydrogen electrode (RHE), anode = Pt on a Ti-grid (Platinode EP, Umicore).

2.6 Calendering of Ni foam

The commercial fabricator of GDEs Gaskatel (Kassel / Germany) has a calender set-up, which allows the pressing of GDE blanks in horizontal orientation. Thereby, calendering of Ni foam as porous support material is possible. Exemplary results are provided in the following (cf. Table S9, Figure S24).

Table S9: Overview of volume, formate concentration, formate FE and pH after 30 h electrolysis in the catholyte of formate electrosynthesis with 0.2 mol L^{-1} KH_2PO_4 / K_2HPO_4 as starting electrolyte. Accompanied by average and standard deviation of cell voltage during runtime and absolute electric energy consumption (EEC).

Electrolysis	V / mL	c(formate) / mmol L^{-1}	FE(formate) / %	pH	U / V	EEC / Wh
(F1)	510	396.2	72.2	4.67 ± 0.05	6.5 ± 0.5	97.2

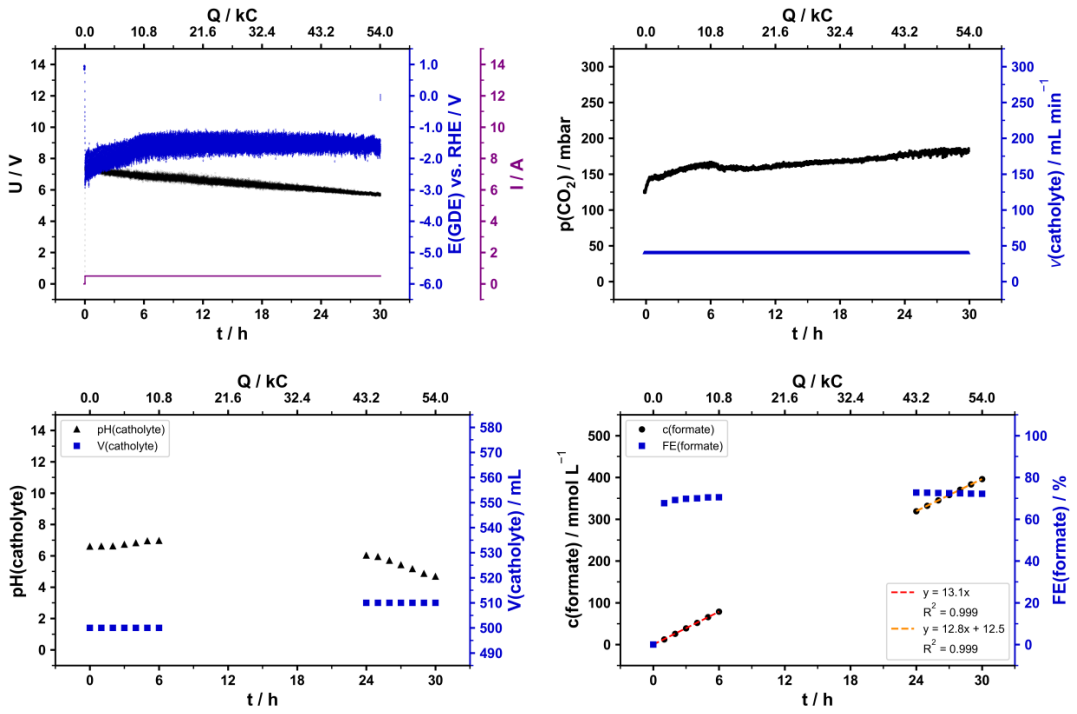

Figure S24: Data for the electrosynthesis of formate (F1) with the Sn based GDE. Electrolysis parameters: Constant current density j = 100 mA cm^{-2}, runtime = 30 h, electrolyte = 0.2 mol L^{-1} KH_2PO_4 / K_2HPO_4, initial V(catholyte, anolyte) = 500 mL each, cathode (GDE, 5 cm^2 geometrical area) = 90 wt% Sn, 7 wt% PTFE, 3 wt% activated carbon on Ni foam (fabricated with calender by Gaskatel), reference electrode = reversible hydrogen electrode (RHE), anode = Pt on a Ti-grid (Platinode EP, Umicore).

2.7 Third stage (III) of development – Operation at 100 mA cm^{-2}

The results of electrosynthesis of formate with the third stage (III) of GDE development (87.5 wt% Sn, 12.5 wt% PTFE on Ni foam) at a constant current density of 150 mA cm^{-2} have been published in a manuscript (DOI: 10.1002/cssc.202301721). In the following, its operation at 100 mA cm^{-2} is presented. The GDEs were fabricated by heat pressing with Ni foam as support material.

Table S10: Overview of volume, formate concentration, formate FE and pH after 30 h electrolysis in the catholyte of formate electrosynthesis with 0.2 mol L^{-1} KH_2PO_4 / K_2HPO_4 as starting electrolyte. Accompanied by average and standard deviation of cell voltage during runtime and absolute electric energy consumption (EEC).

Electrolysis	V / mL	c(formate) / mmol L^{-1}	FE(formate) / %	pH	U / V	EEC / Wh
(G1)	516.8 ± 1.7	419.3	77.4	4.40 ± 0.05	6.4 ± 0.6	96.8
(G2)	516.3 ± 1.5	411.6	75.9	4.52 ± 0.05	6.0 ± 0.6	90.7

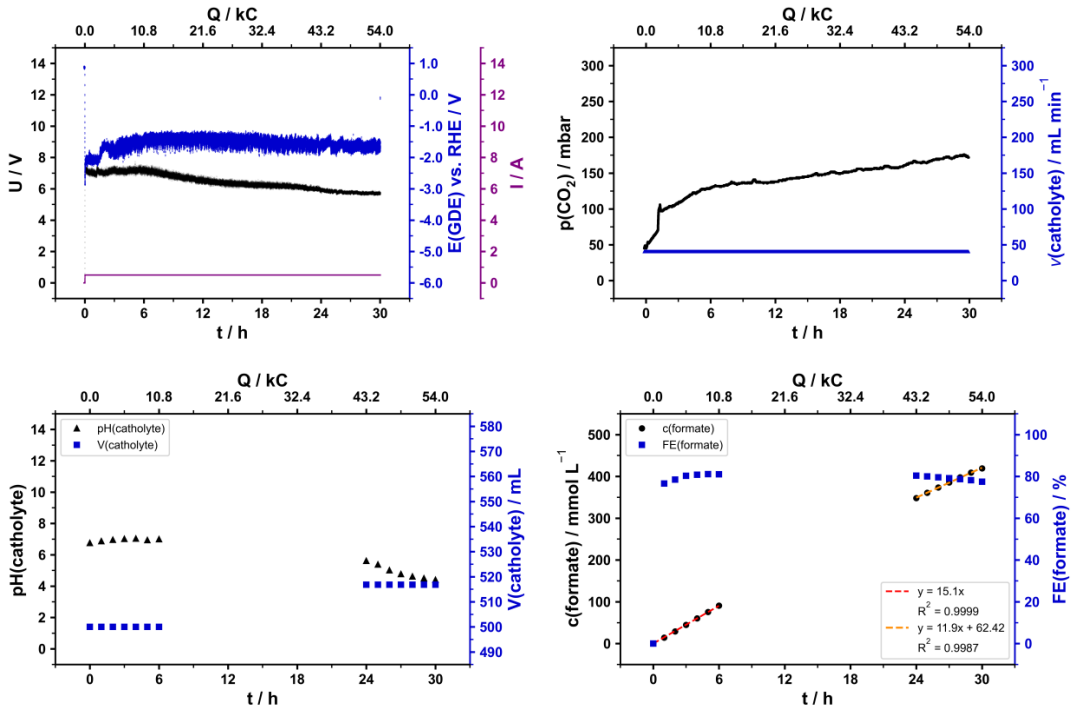

Figure S25: Data for the electrosynthesis of formate (G1) with the Sn based GDE (stage III). Electrolysis parameters: Constant current density j = 100 mA cm^{-2}, runtime = 30 h, electrolyte = 0.2 mol L^{-1} KH_2PO_4 / K_2HPO_4, initial V(catholyte, anolyte) = 500 mL each, cathode (GDE, 5 cm^2 geometrical area) = 87.5 wt% Sn, 12.5 wt% PTFE on Ni foam (fabricated with heat press), reference electrode = reversible hydrogen electrode (RHE), anode = Pt on a Ti-grid (Platinode EP, Umicore).

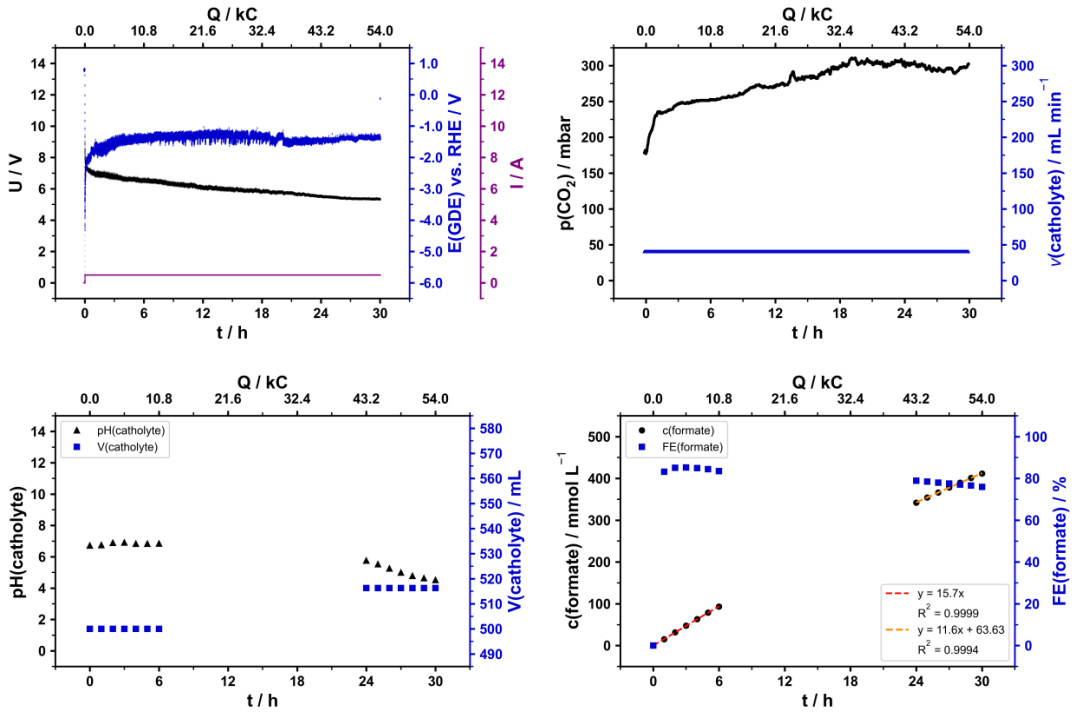

Figure S26: Data for the electrosynthesis of formate (G2) with the Sn based GDE (stage IV). Electrolysis parameters: Constant current density j = 100 mA cm^{-2}, runtime = 30 h, electrolyte = 0.2 mol L^{-1} KH_2PO_4 / K_2HPO_4, initial V(catholyte, anolyte) = 500 mL each, cathode (GDE, 5 cm^2 geometrical area) = 87.5 wt% Sn, 12.5 wt% PTFE on Ni foam (fabricated with heat press), reference electrode = reversible hydrogen electrode (RHE), anode = Pt on a Ti-grid (Platinode EP, Umicore).

2.8 Third stage (III) of development – Operation at 150 mA cm^{-2} for 30 h

The results of electrosynthesis of formate with the third stage (III) of GDE development (87.5 wt% Sn, 12.5 wt% PTFE on Ni foam) at constant current density of 150 mA cm^{-2} with 22 h runtime have been published in a manuscript (DOI: 10.1002/cssc.202301721). In the following, its operation for a runtime of 31 h is presented (1 h ramp, 30 h at constant current density of 150 mA cm^{-2}). The GDEs were fabricated by heat pressing with Ni foam as support material.

Table S11: Overview of volume, formate concentration, formate FE and pH after 30 h electrolysis in the catholyte of formate electrosynthesis with 0.2 mol L^{-1} KH_2PO_4 / K_2HPO_4 as starting electrolyte. Accompanied by average and standard deviation of cell voltage during runtime and absolute electric energy consumption (EEC).

Electrolysis	V / mL	c(formate) / mmol L^{-1}	FE(formate) / %	pH	U / V	EEC / Wh
(H1)	529.1 ± 0.6	543.5	67.4	3.83 ± 0.05	7.0 ± 0.7	161.5

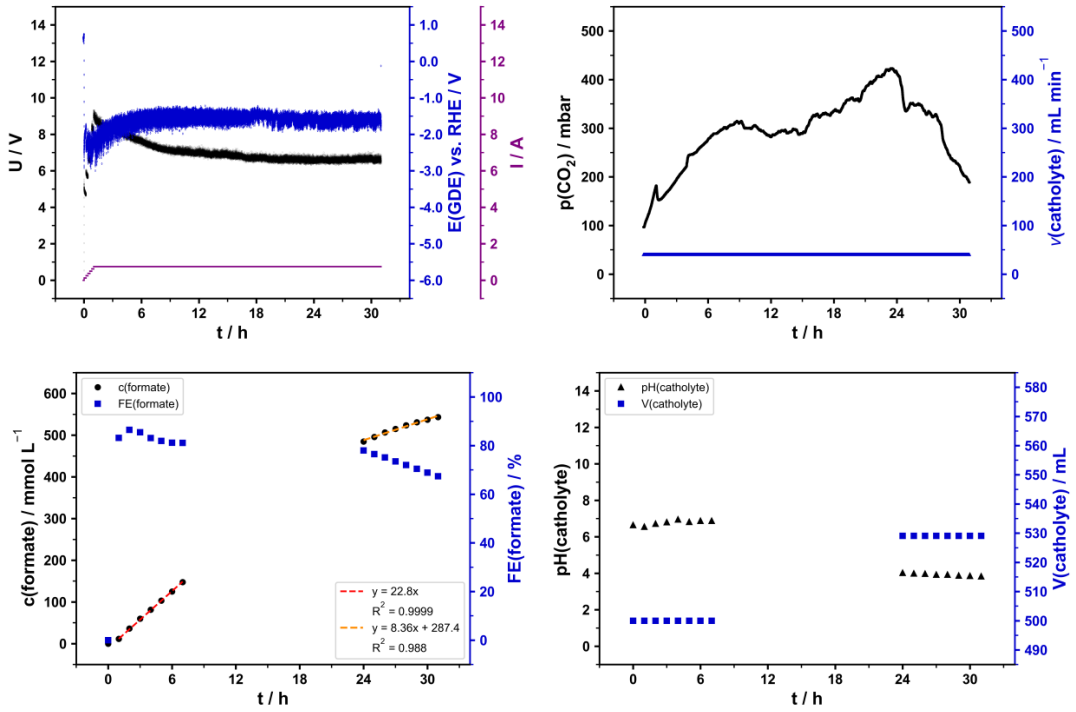

Figure S27: Data for the electrosynthesis of formate (H1) with the Sn based GDE (stage III). Electrolysis parameters: Initial ramp (12.5 mA cm^{-2} increase every 5 min), constant current density j = 150 mA cm^{-2} , runtime = 31 h, electrolyte = 0.2 mol L^{-1} KH_2PO_4 / K_2HPO_4, initial V(catholyte, anolyte) = 500 mL each, cathode (GDE, 5 cm^2 geometrical area) = 87.5 wt% Sn, 12.5 wt% PTFE on Ni foam (fabricated with heat press), reference electrode = reversible hydrogen electrode (RHE), anode = Pt on a Ti-grid (Platinode EP, Umicore).

2.9 Fourth stage (IV) of development

Key results of the electrosynthesis of formate with the fourth stage (IV) of GDE development (87.5 wt% Bi, 12.5 wt% PTFE on Ni foam) are summarised in Table S12, all data collected throughout electrolysis is presented in Figure S28. The GDE was fabricated with the heat press.

Table S12: Overview of volume, formate concentration, formate FE and pH (determined n = 3) after 22 h electrolysis in the catholyte of formate electrosynthesis with 0.2 mol L^{-1} KH_2PO_4 / K_2HPO_4 as starting electrolyte. Accompanied by average and standard deviation of cell voltage during runtime and absolute electric energy consumption (EEC).

Electrolysis	V / mL	c(formate) / mmol L^{-1}	FE(formate) / %	pH	U / V	EEC / Wh
(I1)	525.4 ± 0.8	505.4 ± 0.1	86.25 ± 0.14	4.13 ± 0.05	6.3 ± 0.5	104.9

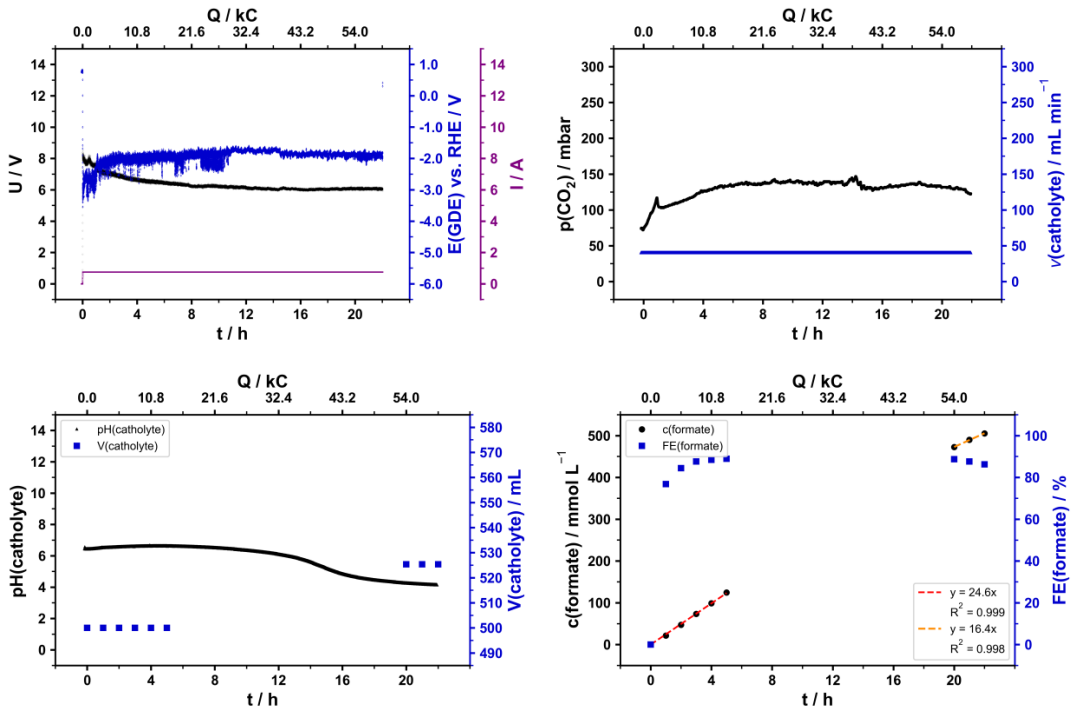

Figure S28: Data for the electrosynthesis of formate (I1) with the Bi based GDE (stage IV). Electrolysis parameters: Constant current density j = 150 mA cm^{-2}, runtime = 22 h, electrolyte = 0.2 mol L^{-1} KH_2PO_4 / K_2HPO_4, initial V(catholyte, anolyte) = 500 mL each, cathode (GDE, 5 cm^2 geometrical area) = 87.5 wt% Bi, 12.5 wt% PTFE on Ni foam (fabricated with heat press), reference electrode = reversible hydrogen electrode (RHE), anode = mixed Ir oxide on a Ti-grid (Platinode EP, Type 117, Umicore).

Supporting Information

CO_2 Reduction to Formic acid/Formate by Intermittent Electricity at Bismuth Gas Diffusion Electrodes

Ida Dinges, Siegfried R. Waldvogel, Markus Stöckl*

Outline

1 Experimental protocols and analytical methods

1.1 General Information

Selected chemical compounds and details on employed equipment are listed in this section (cf. Table S1, Table S2). All chemicals were used without further purification and all solutions were prepared using high purity H_2O (0.055 µS cm^{-1}, 25 °C, PURELAB Ultra).

Table S1: Selected chemical compounds (Purity grade, supplier, charge number).

Compound	Purity grade	Supplier	Charge
KH_2PO_4	>99% (p.a.)	Carl Roth, Karlsruhe / Germany	453340544
K_2HPO_4	>99% (p.a.)	Carl Roth, Karlsruhe / Germany	024350089
HCOOK	99% (p.a.)	Alfa Aesar, Haverhill / USA	10183323
HCOONa	≥99% (p.a.), ACS	Merck, Darmstadt / Germany	A0703243 608
H_2SO_4	75%, pure	Carl Roth, Karlsruhe / Germany	262322778
HNO_3	69%, ROTIPURAN Supra	Carl Roth, Karlsruhe / Germany	1121091
HCOOH	≥98%, for synthesis	Carl Roth, Karlsruhe / Germany	083329609

Table S2: Equipment / device, function and manufacturer.

Equipment / device	Function / use	Manufacturer
PURELAB Ultra	High purity H_2O	ELGA LabWater, High Wycombe / United Kingdom
A 10 basic	Knife mill	IKA, Staufen / Germany
LaboPress P200S	Heat press	Vogt Labormaschinen, Berlin / Germany
Micromar 40 ER	Thickness measurement	Mahr, Göttingen / Germany
Sartorius 1712004	Analytical scale (0.00000 g)	Sartorius Lab Instruments, Göttingen / Germany
Entris 3202I-1S	Scale (0.00 g)	Sartorius Lab Instruments, Göttingen / Germany
NGP804	Power supply	Rohde & Schwarz, Munich / Germany
CEBO-LC (CESYS C028152)	Analog data logging	CESYS, Herzogenaurach / Germany
GMH 3151	Pressure meter	GHM Messtechnik, Regenstauf / Germany
GMSD 2 BR - K31	Differential pressure sensor	GHM Messtechnik, Regenstauf / Germany
Transferpette® S	Pipetting, sampling (100-1000 µL, 500-5000 µL, 1000-10000 µL)	Brand, Wertheim / Germany
ECOLINE VC–MS/CA8-6	Peristaltic pump	ISMATEC Laboratoriums-technik, Wertheim / Germany

1.2 Fabrication of GDE

The gas diffusion electrodes (GDE) were fabricated by pressing catalyst mixture onto Ni foam as support material and current collector with a heat press. Each catalyst mixture (30.00 g) had the same electrocatalyst to binder ratio (87.5:12.5). As electrocatalysts, Bi (Purity 99.9, particle size <40 µm, Metallpulver24, Sankt Augustin / Germany) and / or Bi_2O_3 (Purity 99.9%, particle size approx. 80 nm, US Research Nanomaterials, Houston / USA) were used. Polytetrafluoroethylene (PTFE) powder (Dyneon™ PTFE TF 2072Z, 3M, Saint Paul / USA) served as hydrophobic binder. The different compositions are summarized in Table S3**.**

Table S3: Overview of the catalyst mixtures' composition of the fabricated GDEs.

GDE	*m* (Bi) / g	*m* (Bi_2O_3) / g	*m* (PTFE) / g
(A)	26.25	0	3.75
(B)	21.00	5.25	3.75
(C)	15.75	10.50	3.75
(D)	10.50	15.75	3.75
(E)	5.25	21.00	3.75
(F)	0	26.25	3.75

Each catalyst mixture was homogenized in a knife mill (A 10 basic). The mixing (30 s, 25000 rpm) was carried out twice and lead to a temperature increase of the mixture (T > 35 °C). After cooling to room temperature, the catalyst mixture was equally distributed onto Ni foam (d = 1.4 cm, 3.5 cm x 4.0 cm ≙ 14 cm^2, Ni-5763, density 420 - 450 g m^{-2}, Recemat BV, Dodewaard / Netherlands) with a sieve (stainless-steel wire mesh, mesh size = 500 µm, ISO 3310-1, Retsch / Verder Scientific, Haan / Germany) and a stencil (Cut-out 3.5 cm x 4.0 cm). The loading of the GDE with catalyst mixture was adjusted by differential weighting (Entris 3202I-1S) of the Ni foam. Afterwards, the GDE blank was placed in between two pieces of ordinary baking sheet in the heat press (LaboPress P200S) and compressed (plate temperature 120 °C, pressure 10 bar, 60 s). After compressing, excess material at the GDE edges was removed. The GDE's final catalyst loading *b* was determined by differential weighing (Sartorius 1712004) and its thickness *d* was measured at the center point/geometrical middle of the 14 cm^2 GDE area (Micromar 40 ER). A summary of all fabricated GDEs is provided in Table S4.

Table S4: Overview of electrocatalyst composition, catalyst mixture loading *b* and thickness *d* of the fabricated GDEs.

GDE	Composition	*b* (catalyst mixture) / mg cm^{-2}	*d* (GDE, center point) / µm
(A1)	Bi	78.21	461
(A2)	Bi	78.30	468
(A3)	Bi	78.52	486
(B1)	Bi / Bi_2O_3 (80:20)	80.19	475
(B2)	Bi / Bi_2O_3 (80:20)	79.66	498
(B3)	Bi / Bi_2O_3 (80:20)	78.10	493
(B4)	Bi / Bi_2O_3 (80:20)	80.29	496
(B5)	Bi / Bi_2O_3 (80:20)	78.24	491
(B6)	Bi / Bi_2O_3 (80:20)	79.54	498
(B7)	Bi / Bi_2O_3 (80:20)	80.48	487
(B8)	Bi / Bi_2O_3 (80:20)	78.52	491
(B9)	Bi / Bi_2O_3 (80:20)	79.92	486
(B10)	Bi / Bi_2O_3 (80:20)	80.81	494
(B11)	Bi / Bi_2O_3 (80:20)	78.34	494
(B12)	Bi / Bi_2O_3 (80:20)	78.99	496
(C1)	Bi / Bi_2O_3 (60:40)	77.12	500
(C2)	Bi / Bi_2O_3 (60:40)	80.24	520
(C3)	Bi / Bi_2O_3 (60:40)	81.48	511
(D1)	Bi / Bi_2O_3 (40:60)	77.67	516
(D2)	Bi / Bi_2O_3 (40:60)	76.55	514
(D3)	Bi / Bi_2O_3 (40:60)	75.95	516
(E1)	Bi / Bi_2O_3 (20:80)	73.47	515
(E2)	Bi / Bi_2O_3 (20:80)	71.09	508
(E3)	Bi / Bi_2O_3 (20:80)	72.57	521
(F1)	Bi_2O_3	74.33	521
(F2)	Bi_2O_3	74.77	544
(F3)	Bi_2O_3	74.68	558

1.3 Electrochemical flow reactor and electrolysis set-up

Detailed descriptions of the electrochemical flow reactor and the electrolysis set-up have already been provided in a previous publication (https://doi.org/10.1002/cssc.202301721). The same electrochemical flow reactor and electrolysis set-up have been employed for the electrosynthesis of formate herein. However, Nafion 424 (The Chemours Company, Wilmington, USA) was used as cation exchange membrane instead of Nafion 117. Nafion 424 is a reinforced and more stable membrane, which will be necessary for an upscaled reactor in the future. It has already been used here to enable a better comparison.

1.4 Electrosynthesis of formate

Electrosynthesis of formate using CO_2 was carried out with self-fabricated Bi / Bi_2O_3 based GDEs (cf. section 1.2) in a flow reactor (cf. section 1.3), whereby each GDE was only used once per experiment.

All electrosyntheses were run with a power supply unit (NGP804), which recorded terminal voltage (*U*), current (*I*) and power (*P*). The power supply unit was operated by analog input (NGP-K107) using *ProfiLab-Expert* (Version 4.0). Furthermore, the electrode potential of the GDE was referenced to a RHE (CEBO-LC). The electrosynthesis at constant current density started with a current ramp (60 s), in which the current density (*j*) reached 150 mA cm^{-2} (750 mA in total), which was maintained for 21 h runtime. The start-up procedure of the electrosynthesis at variable current density was identical, but the current density was adjusted during runtime with current ramps (60 s). The respective courses of current density are provided in section 3.2.

CO_2 (N4.5) was supplied to the GDE at a flow rate of 10 - 15 mL min^{-1} (Float-type flow meter, Wagner Mess- und Regeltechnik, Offenbach / Germany) and an initial overpressure in range of 50 - 200 mbar relative to ambient pressure. The pressure was recorded (every 2 s) during the running electrolysis (CEBO-LC).

Phosphate based buffer (0.2 mol L^{-1} KH_2PO_4 / K_2HPO_4, equimolar) served as electrolyte for all electrolyses. For each electrolysis, anolyte and catholyte had a starting volume of 500 mL (Volumetric flask, ISO 1042). Anolyte and catholyte were both circulated continuously at a flow rate of approx. 40 mL min^{-1} between flow reactor compartment and reservoir. Moreover, the catholyte reservoir was equipped with a pH electrode (EGA142, Xylem Analytics Germany Sales, Weilheim / Germany). The pH of the catholyte was recorded (every 2 s) during electrolysis (CEBO-LC). Catholyte samples were taken either hourly (1 mL, Transferpette® S) or every 15 min (200 µL, Transferpette® S) in certain intervals to monitor formate concentration and calculate the corresponding Faradaic efficiency (FE). After electrolysis, the catholyte volume was determined by its weight (Entris 3202I-1S) and density. The density was calculated

by taking samples (1 mL, *n* = 3, Transferpette® S) and weighing them (Sartorius 1712004). The GDE was rinsed with H_2O and dried at room temperature.

Details on the experimental parameters and results for all individual electrolyses generating formate are provided in section 3.1.

1.5 Determination of density

The densities of GDE were determined with the gas pycnometer BELPYCNO L (cf. Table S5), which was operated via *BELPycno-L* (Version 3.1.4).

Table S5: Volume / density measurement conditions performed on BELPYCNO L (Microtrac Retsch, Haan / Germany).

Conditions		Conditions	
Carrier gas	Helium	Restriction delta pressure	2.00000 bar
Temperature	20.00 °C	Equilibrium delta pressure	0.00020 bar
Reference volume	I	Equilibrium delta time	15 s
Flow cleaning time	0 s	Standard deviation (max.)	10%
Number of cleaning cycles	10	Nr. of good measurements	10
Sample cleaning time	5 s	Nr. of max. measurements	10
Atm. stabilization time	15 s	High precision mode	Disabled

The reference volume chamber I was calibrated with steel calibration sphere S using the instrument's standard protocol. All samples were measured (*n* = 3) in sample chamber S (20 cm^3) using glass beads (⌀ = 2.85 - 3.45 mm, charge 381176662, Carl Roth, Karlsruhe / Germany) as filler volume (approx. 50%). The sample weights (Sartorius 1712004) were used to calculate the densities from the measured volumes. GDE samples before electrolysis remained as fabricated (14 cm^2). To measure the GDE after electrolysis, the area exposed in the reactor during electrolysis was cut out (5 cm^2). As the sample volumes were relatively small compared to the sample chamber despite the filler, GDEs of the same composition were measured together (if available) in order to minimize relative errors. The results are summarized in Table S6.

Table S6: Volume and density results for Bi and / or Bi_2O_3 GDEs before and after electrolysis.

GDE composition	Electrolysis	Volume / cm^3	Density / g cm^{-3}
Bi	-	0.227 ± 0.003	7.37 ± 0.02
Bi	(A1), (A2)	0.190 ± 0.007	7.31 ± 0.09
Bi / Bi_2O_3 (80:20)	-	0.224 ± 0.004	7.46 ± 0.08
Bi / Bi_2O_3 (80:20)	(B1)	0.101 ± 0.002	7.2 ± 0.1
Bi / Bi_2O_3 (60:40)	-	0.223 ± 0.001	7.36 ± 0.04
Bi / Bi_2O_3 (60:40)	(C1)	0.108 ± 0.001	7.18 ± 0.04
Bi / Bi_2O_3 (40:60)	-	0.219 ± 0.004	7.47 ± 0.08
Bi / Bi_2O_3 (40:60)	(D1), (D2)	0.205 ± 0.001	7.11 ± 0.08
Bi / Bi_2O_3 (20:80)	-	0.168 ± 0.003	7.2 ± 0.2
Bi / Bi_2O_3 (20:80)	(E1), (E2)	0.173 ± 0.002	7.06 ± 0.09
Bi_2O_3	-	0.228 ± 0.001	7.13 ± 0.03
Bi_2O_3	(F1), (F2)	0.187 ± 0.001	6.97 ± 0.04

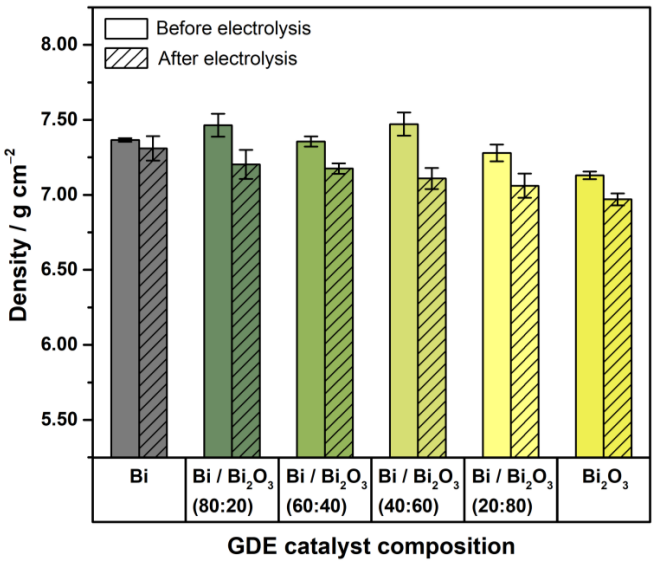

Figure S1: Density results of Bi / Bi_2O_3 GDEs before and after electrolysis (cf. Table S6).

1.6 Cross sections of GDE

Cross sections of GDEs were prepared before and after electrolysis. GDEs after electrolysis were dabbed dry with a paper towel without any prior rinsing. For preparation, each GDE was cut in half vertically with a scissor. Afterwards, one half was placed inside resin (transparent epoxy, Specifix-40, Struers, Ballerup / Denmark) with the cut edge facing upwards. All samples were vacuum impregnated using the CitoVac (Struers, Ballerup / Denmark). The cured, enclosed cross section was sanded with SiC paper (FEPA P320, P500, P1000, P2400 - Struers, Ballerup / Denmark) using water as coolant. Lastly, cross sections were polished with diamond paste (3 µm, 1 µm - Struers, Ballerup / Denmark). Sanding and polishing were both carried out with the Saphir 550 (ATM Qness, Mammelzen / Germany).

Pictures of the cross sections were taken with the bright-field microscope DM6000 M (Leica Microsystems, Wetzlar / Germany). Exemplary pictures are provided in section 3.3.

1.7 Inductively coupled plasma optical emission spectroscopy (ICP-OES)

ICP-OES measurements were performed on Agilent 5800 ICP-OES equipped with an SPS 4 Autosampler, a borosilicate double-pass spray chamber and a Seaspray concentric glass nebulizer (cf. Table S7). The system was operated via *ICP Expert* (Version 7.6.3.12735).

Table S7: ICP-OES measurement conditions performed on Agilent 5800 ICP-OES (Agilent Technologies, Santa Clara / USA).

Conditions		Conditions	
Replicate count	10	Viewing mode	Axial
Pump speed	12 rpm	Viewing height	-
Sample uptake time	25 s	Nebulizer flow	0.7 mL min^{-1}
Stabilization time	15 s	Plasma flow	12 mL min^{-1}
Read time	5 s	Aux Flow	1 mL min^{-1}
Rinse time	30 s	Oxygen content	0%
RF power	1.2 kW	IntelliQuant	Enabled

In between samples, autosampler and measurement system were rinsed with 2 wt% HNO_3 (prepared from 69 wt% HNO_3, Supra Quality, cf. Table S1).

All samples were measured without dilution except for acidification to 2 wt% HNO_3 (using 69 wt% HNO_3). In initial qualitative tests using an IntelliQuant screening, no elements of interest were detected in the anolyte samples. Consequently, only catholyte samples were examined further.

Standards to determine the concentrations of Bi^{3+} (λ = 306.771 nm) and Ni^{2+} (λ = 231.604 nm) were prepared from a stock solution (100 mg L^{-1}). The stock solution was prepared by combining the respective standards (10 mL each, cf. Table S8) in a volumetric flask (100 mL, ISO 1042) using 2 wt% HNO_3 for dilution. Afterwards, the solution was diluted further with 2 wt% HNO_3 to either 6 or 8 mg L^{-1} in a volumetric flask (100 mL, ISO 1042). This was followed by a dilution series by factor 2, respectively. Finally, both sets of standards (0.25, 0.5, 1, 2, 4, 8 mg L^{-1} and 0.1875, 0.375, 0.75, 1.5, 3, 6 mg L^{-1}) were diluted again by factor 2 with a matrix solution (0.4 mol L^{-1} KH_2PO_4 / K_2HPO_4, 0.5 mol L^{-1} HCOOH, 0.5 mol L^{-1} HCOOK in 2 wt% HNO_3). Thereby, a set of standards with a matrix based on the catholyte's composition was obtained. Furthermore, two additional standards (5 and 6 mg L^{-1}) were prepared from the initial stock solution (100 mg L^{-1}) by dilution to 10 and 12 mg L^{-1} with 2 wt% HNO_3, which were diluted again by factor 2 with matrix solution. In the following, the calibrations for each targeted analyte with either catholyte matrix or 2 wt% HNO_3 matrix are presented. The calibration with catholyte matrix was used to calculate the results for the catholyte samples.

Table S8: Single Element ICP-Standard-Solutions used for analyte quantification (Element, Concentration, Supplier, Lot. No.).

Element	Concentration	Supplier	Lot. No.
Bi	1000 mg L^{-1}	Carl Roth, Karlsruhe / Germany	794591
Ni	1000 mg L^{-1}	Carl Roth, Karlsruhe / Germany	974203

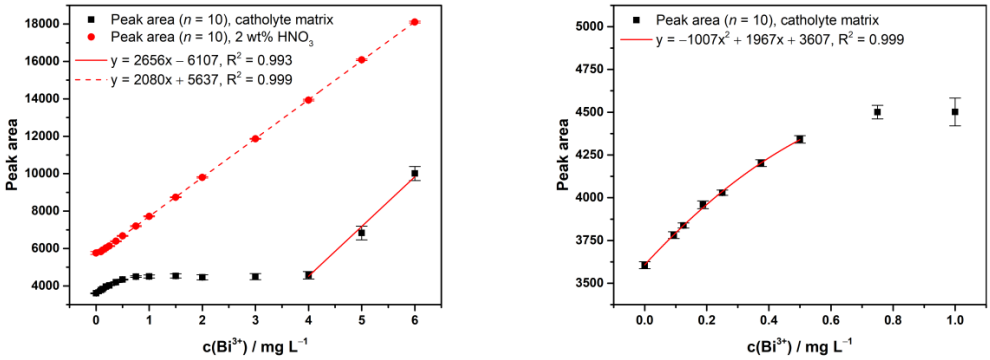

Figure S2: Calibration for Bi^{3+} (λ = 306.771 nm) via ICP-OES measurement with catholyte and 2% HNO_3 matrix**.** Plot of Bi^{3+} concentration (0, 0.09375, 0.125, 0.1875, 0.25, 0.375, 0.5, 1, 1.5, 2, 4, 5, 6 mg L^{-1}) against the peak area of the measured signal (*n* = 10) with a linear or quadratic fit.

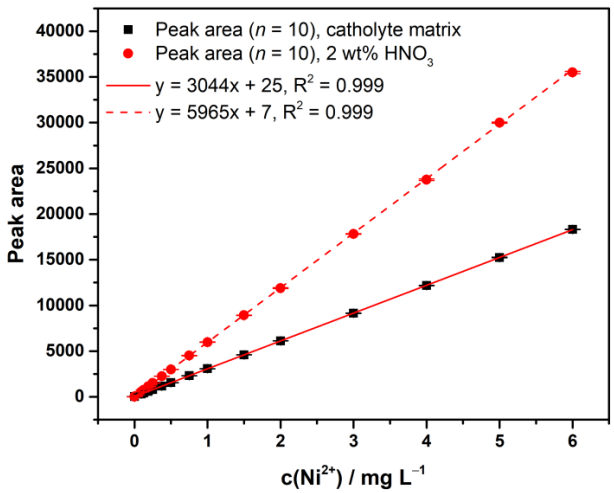

Figure S3: Calibration for Ni^{2+} (λ = 231.604 nm) via ICP-OES measurement with catholyte and 2% HNO_3 matrix**.** Plot of Ni^{2+} concentration (0, 0.09375, 0.125, 0.1875, 0.25, 0.375, 0.5, 1, 1.5, 2, 4, 5, 6 mg L^{-1}) against the peak area of the measured signal (*n* = 10) with a linear fit forced through zero, respectively.

Table S9: ICP-OES results for Bi^{3+} and Ni^{2+} concentrations in the catholyte samples.

Electrolysis	GDE catalyst composition	c(Bi^{3+}) / µg L^{-1}	c(Ni^{2+}) / µg L^{-1}
(P)[a]	-	0	0
(A1)	Bi	4099 ± 20	27.7 ± 1.6
(A2)	Bi	492 ± 35	28.7 ± 1.9
(A3)	Bi	192 ± 16	18.2 ± 2.0
(B1)	Bi / Bi_2O_3 (80:20)	4053 ± 10	22.4 ± 2.2
(B2)	Bi / Bi_2O_3 (80:20)	131 ± 11	21.9 ± 2.0
(B3)	Bi / Bi_2O_3 (80:20)	87 ± 6	17.2 ± 1.5
(B4)	Bi / Bi_2O_3 (80:20)	151 ± 7	23.9 ± 1.3
(B5)	Bi / Bi_2O_3 (80:20)	210 ± 9	24.9 ± 1.8
(B6)	Bi / Bi_2O_3 (80:20)	144 ± 10	31.9 ± 2.8
(B7)	Bi / Bi_2O_3 (80:20)	4489 ± 16	421 ± 4
(B8)	Bi / Bi_2O_3 (80:20)	4306 ± 13	308 ± 2
(B9)	Bi / Bi_2O_3 (80:20)	4452 ± 14	501 ± 4
(B10)	Bi / Bi_2O_3 (80:20)	117 ± 7	123.8 ± 2.4
(B11)	Bi / Bi_2O_3 (80:20)	137 ± 9	213.9 ± 3.3
(B12)	Bi / Bi_2O_3 (80:20)	150 ± 11	92.8 ± 0.9
(C1)	Bi / Bi_2O_3 (60:40)	110 ± 8	62.7 ± 2.1
(C2)	Bi / Bi_2O_3 (60:40)	95 ± 10	51.6 ± 1.8
(C3)	Bi / Bi_2O_3 (60:40)	99 ± 11	49.9 ± 1.0
(D1)	Bi / Bi_2O_3 (40:60)	126 ± 10	56.4 ± 2.6
(D2)	Bi / Bi_2O_3 (40:60)	122 ± 10	77.7 ± 2.2
(D3)	Bi / Bi_2O_3 (40:60)	102 ± 7	47.2 ± 1.5
(E1)	Bi / Bi_2O_3 (20:80)	79 ± 10	79.9 ± 2.7
(E2)	Bi / Bi_2O_3 (20:80)	83 ± 12	112.3 ± 2.3
(E3)	Bi / Bi_2O_3 (20:80)	95 ± 11	76.0 ± 1.5
(F1)	Bi_2O_3	97 ± 7	47.6 ± 1.6
(F2)	Bi_2O_3	113 ± 10	56.2 ± 2.1
(F3)	Bi_2O_3	124 ± 12	53.7 ± 1.1

[a] The phosphate buffer (0.2 mol L^{-1} KH_2PO_4 / K_2HPO_4) serving as supporting electrolyte for formate electrosynthesis was measured prior to electrolysis for comparison.

1.8 High-performance liquid chromatography (HPLC)

The quantification of formate was carried out via HPLC (cf. Table S10), the system was operated with the software *LabSolutions* (Version 5.93).

Table S10: HPLC measurement conditions for formate and PHB analysis performed on an HPLC unit (LC-20AD, SIL-20AC HT, CBM-20A, CTO-20AC, SPD-M20A - Shimadzu, Kyoto / Japan).

Conditions	Formate
Eluent	5 mmol L^{-1} H_2SO_4
Flow rate	0.6 mL min^{-1}
Pressure	30 ± 1
Column oven	35 °C
Column	Rezex ROA- Organic Acid (8%), 300 mm × 7.8 mm, Phenomenex, Torrance / USA
Injection volume	10 µL
Detector	Photodiode array (PDA)
Wavelength λ	194 nm
Retention time	14.9 min
Duration	25 min

Formate standards were prepared from a stock solution by a dilution series with the dilution factor 2. The stock solution was prepared with HCOONa (3.482 g, 51.2 mmol) in a volumetric flask (100 mL, ISO 1042).

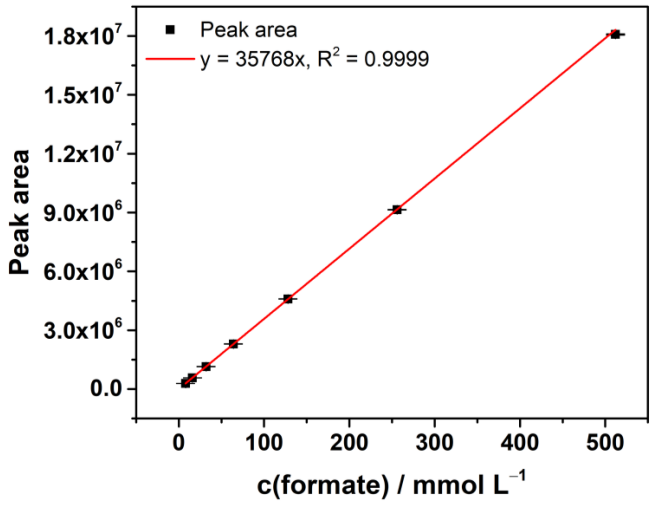

Figure S4: Calibration for formate quantification via HPLC measurement**.** Plot of formate concentration (8, 16, 32, 64, 128, 256, 512 mmol L^{-1}) against the peak area of the measured signal (n = 3) with a linear fit forced through zero.

2 Calculations

2.1 Faradaic efficiency (FE)

The FE for formate was calculated based on the determined amount of electrosynthesized formate using equation (1).

$$FE = \frac{F \cdot z \cdot n}{I \cdot t} \cdot 100\% \quad (1)$$

With FE = Faradaic efficiency / %, F = Faraday constant / A s mol^{-1}, z = Number of transferred electrons (z = 2), n = Amount of synthesised formate / mol, I = Current / A, t = Electrolysis runtime / s.

The results for the different catholytes were averaged and their standard deviation was provided as uncertainty.

2.2 Electric energy consumption (EEC)

The EEC for formate was calculated based on the determined amount of electrosynthesized formate using equation (2).

$$EEC = \frac{F \cdot z \cdot U}{FE \cdot M} \cdot (2.778 \cdot 10^{-7}) \quad (2)$$

With EEC = Electric energy consumption / kWh kg^{-1}, F = Faraday constant / A s mol^{-1}, z = Number of transferred electrons per molecule (z = 2), U = Averaged cell voltage / V, FE = Faradaic efficiency / %, M = Molar mass of formate / kg mol^{-1}.

The results for the different catholytes were averaged and their standard deviation was provided as uncertainty.

3 Results

This chapter contains detailed data for all electrolyses carried out at constant current density (cf. section 3.1) and variable current density (cf. section 3.2). Furthermore, pictures of the self-fabricated GDEs and their cross sections before and after electrolysis are provided (cf. section 3.3).

3.1 Electrosynthesis of formate at constant current density

A comparative overview of the results is presented in Table S11, operational electrolysis parameters have been summarized in Table S12, further electrolysis results have been collected in Table S13. Moreover, detailed courses of each individual electrolysis are provided.

Discussion of cell voltage and potential of GDE

Electrolyses were run with an average cell voltage of 6.46 ± 0.12 V for all different compositions of catalyst (n = 18). The generally relatively high cell voltage was mainly caused by ohmic losses in the anode chamber, as a non-zero gap anode was used for the oxygen evolution reaction (OER) as counter reaction of CO_2 reduction to formate. Accordingly, the average potential of GDEs was only −1.57 ± 0.14 V vs. RHE for all different compositions of catalyst (n = 18). As expected, the average potential of Bi GDE (−1.7 ± 0.1 V) was higher than that of Bi_2O_3 GDE (−1.52 ± 0.13 V). Despite that, there was no clear trend in between. Starting from Bi GDE, the average potential of GDE decreased with addition of Bi_2O_3 until Bi/Bi_2O_3 (60:40) GDE (−1.5 ± 0.1 V), as expected. However, the following Bi/Bi_2O_3 (40:60) GDE (−1.7 ± 0.3 V) and Bi/Bi_2O_3 (20:80) GDE (−1.37 ± 0.14 V) deviated from the preliminary trend, whereby Bi/Bi_2O_3 (20:80) had the overall lowest average potential. Consequently, stepwise addition of Bi_2O_3 as a reductive binder did not lead to the presumed stepwise lowering of GDE potential / increase in conductivity of the GDE. Besides, the average cell voltage of the different compositions showed the same relative correlations as the average potential of GDE, except for Bi/Bi_2O_3 (40:60). Thereby, Bi GDE required the highest average cell voltage (6.63 ± 0.06 V) whereas Bi/Bi_2O_3 (20:80) GDE required the lowest (6.3 ± 0.2 V).

Table S11: Comparative overview of results (expansion of Table 2 in the main text) for electrosynthesis of formate at constant current density (150 mA cm^{-2}, 21 h) with GDEs of variable catalyst composition (n = 3, respectively).

Catalyst composition of GDE	GDE catalyst[a] cost [€ m^{-2}]	GDE material[b] cost [€ m^{-2}]	c(formate) [mmol L^{-1}]	FE [%]	U[c] [V]	E(GDE)[c] [V]	EEC [kWh kg^{-1}]	c(formate) rate r_1[d] [mmol L^{-1} h^{-1}]	c(formate) rate r_2[e] [mmol L^{-1} h^{-1}]	pH[f]
Bi	34.3 ± 0.1	376.9 ± 0.1	488 ± 3	87.5 ± 1.1	6.63 ± 0.06	−1.7 ± 0.1	8.84 ± 0.05	24.71 ± 0.09	17.45 ± 0.14	4.20 ± 0.01
Bi / Bi_2O_3 (80:20)	55.5 ± 0.1	398.3 ± 0.1	501 ± 5	90.3 ± 1.2	6.48 ± 0.06	−1.6 ± 0.1	8.37 ± 0.13	25.62 ± 0.12	20.16 ± 0.14	4.13 ± 0.03
Bi / Bi_2O_3 (60:40)	76.6 ± 2.2	419 ± 3	485 ± 15	87 ± 3	6.47 ± 0.01	−1.5 ± 0.1	8.6 ± 0.3	25.04 ± 0.11	16.8 ± 0.5	4.19 ± 0.03
Bi / Bi_2O_3 (40:60)	94.0 ± 1.1	436.6 ± 1.2	483 ± 5	87.0 ± 0.9	6.44 ± 0.08	−1.7 ± 0.3	8.63 ± 0.15	25.16 ± 0.13	15.4 ± 0.3	4.22 ± 0.01
Bi / Bi_2O_3 (20:80)	107.7 ± 1.8	450.0 ± 1.9	462 ± 18	83 ± 3	6.3 ± 0.2	−1.37 ± 0.14	8.79 ± 0.34	25.41 ± 0.17	12.9 ± 0.3	4.31 ± 0.08
Bi_2O_3	130.5 ± 0.5	473.0 ± 0.5	488 ± 6	88.0 ± 1.2	6.4 ± 0.3	−1.52 ± 0.13	8.55 ± 1.5	25.3 ± 0.2	19.0 ± 0.3	4.19 ± 0.02

[a] Bi and/or Bi_2O_3; [b] Including electrocatalyst (Bi and/or Bi_2O_3), PTFE and Ni foam; [c] Average of 21 h runtime, without compensation for *iR* losses; [d] t = 4 - 5 h; [e] t = 20 - 21 h; [f] After electrolysis (t = 21 h).

Table S12: Overview of operational electrolysis parameters for electrosynthesis of formate using 0.2 mol L^{-1} KH_2PO_4 / K_2HPO_4 as electrolyte. All values are given as average with standard deviation for the 21 h electrolysis duration, excluding the absolute electric energy consumption (EEC).

Electrolysis	OCP vs. RHE / V[a]	E(GDE) vs. RHE / V	U / V	EEC / Wh	$p(CO_2)$ / mbar
(A1)	0.950 ± 0.002	−1.63 ± 0.13	6.6 ± 0.7	103.6	98 ± 5
(A2)	0.966 ± 0.001	−1.82 ± 0.11	6.7 ± 0.7	105.1	252 ± 10
(A3)	0.901 ± 0.001	−1.74 ± 0.11	6.7 ± 0.6	105.1	78 ± 5
(B1)	0.817 ± 0.002	−1.47 ± 0.16	6.5 ± 0.8	102.3	116 ± 19
(B2)	0.965 ± 0.001	−1.67 ± 0.14	6.4 ± 0.7	101.3	174 ± 22
(B3)	0.991 ± 0.001	−1.56 ± 0.14	6.5 ± 0.7	102.9	147 ± 10
(C1)	0.543 ± 0.001	−1.46 ± 0.17	6.5 ± 0.7	102.0	141 ± 42
(C2)	0.586 ± 0.002	−1.63 ± 0.15	6.5 ± 0.6	101.9	179 ± 17
(C3)	0.510 ± 0.003	−1.53 ± 0.16	6.5 ± 0.6	101.8	114 ± 7
(D1)	0.503 ± 0.001	−2.0 ± 0.2	6.5 ± 0.7	102.6	230 ± 18
(D2)	0.506 ± 0.001	−1.67 ± 0.10	6.4 ± 0.6	101.7	208 ± 21
(D3)	0.836 ± 0.001	−1.52 ± 0.11	6.4 ± 0.6	100.4	147 ± 20
(E1)	0.296 ± 0.003	−1.21 ± 0.14	6.1 ± 0.6	96.7	191 ± 27
(E2)	0.512 ± 0.001	−1.43 ± 0.15	6.4 ± 0.6	101.7	148 ± 17
(E3)	0.41 ± 0.02	−1.47 ± 0.16	6.2 ± 0.6	98.4	218 ± 19
(F1)	0.262 ± 0.001	−1.51 ± 0.13	6.3 ± 0.7	99.9	260 ± 18
(F2)	1.13 ± 0.04	−1.40 ± 0.11	6.3 ± 0.7	99.7	182 ± 11
(F3)	1.15 ± 0.04	−1.65 ± 0.14	6.7 ± 0.8	105.6	227 ± 12

[a] Average with standard deviation measured for 5 min prior to electrolysis.

Table S13: Overview of volume, formate concentration, formate FE and pH determined *n* = 3 after 21 h electrolysis in the catholyte of formate electrosynthesis with 0.2 mol L^{-1} KH_2PO_4 / K_2HPO_4 as starting electrolyte.

Electrolysis	V / mL	c(formate) / mmol L^{-1}	FE(formate) / %	pH
(A1)	522.9 ± 0.2	485.0 ± 0.3	86.32 ± 0.04	4.20 ± 0.05
(A2)	528.6 ± 0.4	488.0 ± 0.4	86.79 ± 0.04	4.21 ± 0.05
(A3)	529.9 ± 0.3	490.2 ± 0.2	88.41 ± 0.03	4.19 ± 0.05
(B1)	527.1 ± 0.4	496.2 ± 0.3	89.01 ± 0.06	4.10 ± 0.05
(B2)	530.4 ± 0.6	503.4 ± 0.2	90.87 ± 0.08	4.14 ± 0.05
(B3)	530.2 ± 0.3	504.1 ± 0.2	90.97 ± 0.07	4.14 ± 0.05
(C1)	527.2 ± 0.1	469.8 ± 0.2	84.29 ± 0.03	4.21 ± 0.05
(C2)	531.4 ± 0.4	484.8 ± 0.1	87.67 ± 0.07	4.20 ± 0.05
(C3)	530.0 ± 0.2	499.5 ± 0.2	90.11 ± 0.05	4.16 ± 0.05
(D1)	529.3 ± 0.3	484.1 ± 0.2	87.21 ± 0.06	4.21 ± 0.05
(D2)	528.9 ± 0.4	478.3 ± 0.3	86.09 ± 0.05	4.23 ± 0.05
(D3)	529.5 ± 0.3	486.4 ± 0.1	87.65 ± 0.06	4.12 ± 0.05
(E1)	530.1 ± 0.6	446.3 ± 0.2	80.5 ± 0.1	4.38 ± 0.05
(E2)	531.0 ± 0.3	458.6 ± 0.2	82.86 ± 0.08	4.32 ± 0.05
(E3)	528.5 ± 0.5	480.2 ± 0.3	86.38 ± 0.06	4.23 ± 0.05
(F1)	529.6 ± 0.5	491.2 ± 0.5	88.53 ± 0.05	4.19 ± 0.05
(F2)	529.2 ± 0.5	481.0 ± 0.1	86.64 ± 0.07	4.21 ± 0.05
(F3)	531.2 ± 0.4	490.8 ± 0.2	88.73 ± 0.04	4.18 ± 0.05

3.1.1 Bi GDEs

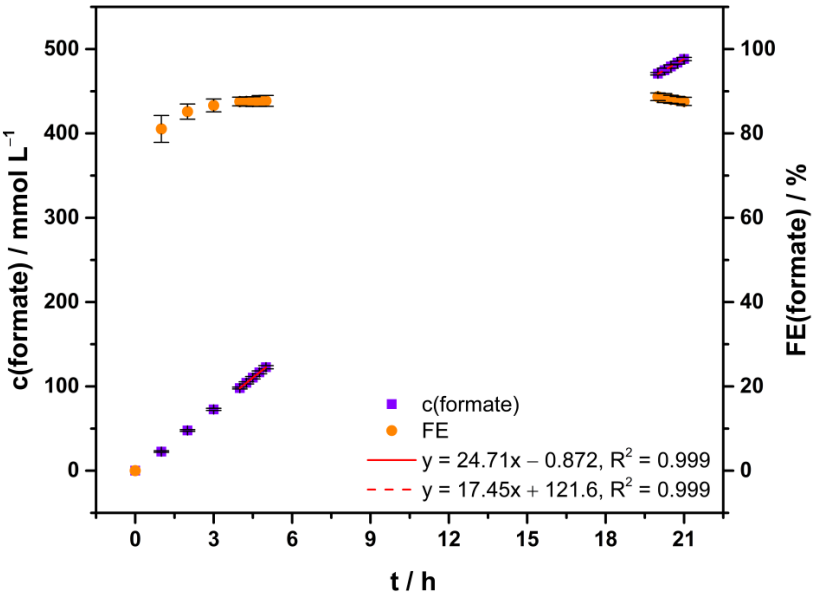

Figure S5: Data for electrolysis (A1, A2, A3), experimental details are provided in section 1.4 and results in Table S11, Table S12 and Table S13.

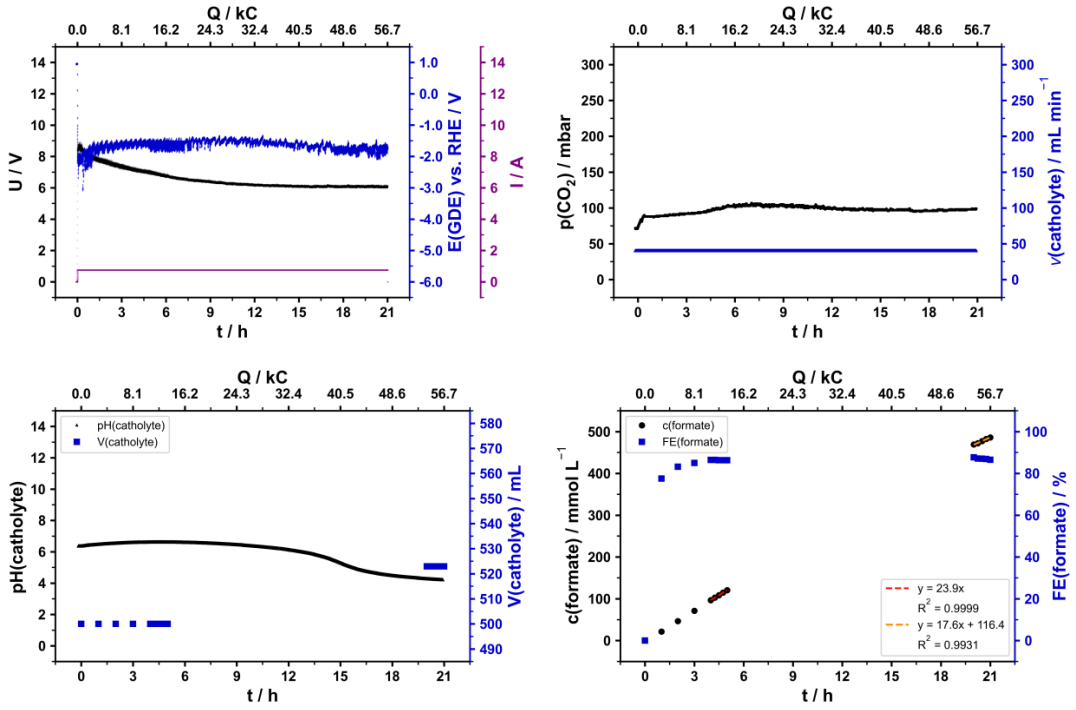

Figure S6: Data for electrolysis (A1), experimental details are provided in section 1.4 and results in Table S12 and Table S13.

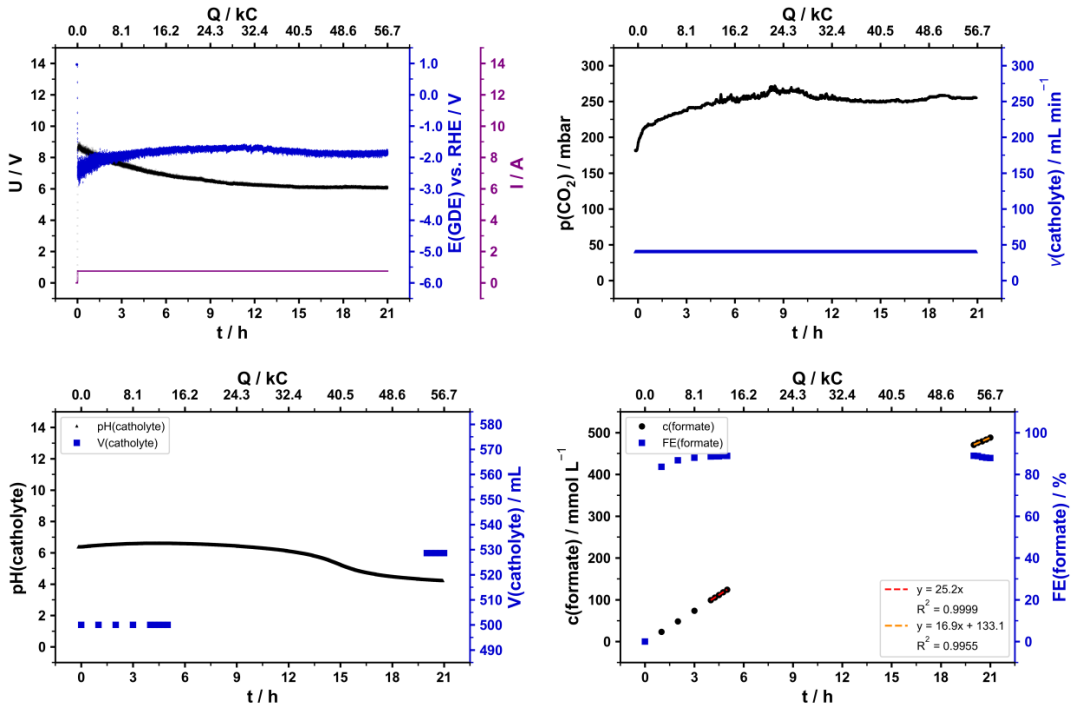

Figure S7: Data for electrolysis (A2), experimental details are provided in section 1.4 and results in Table S12 and Table S13.

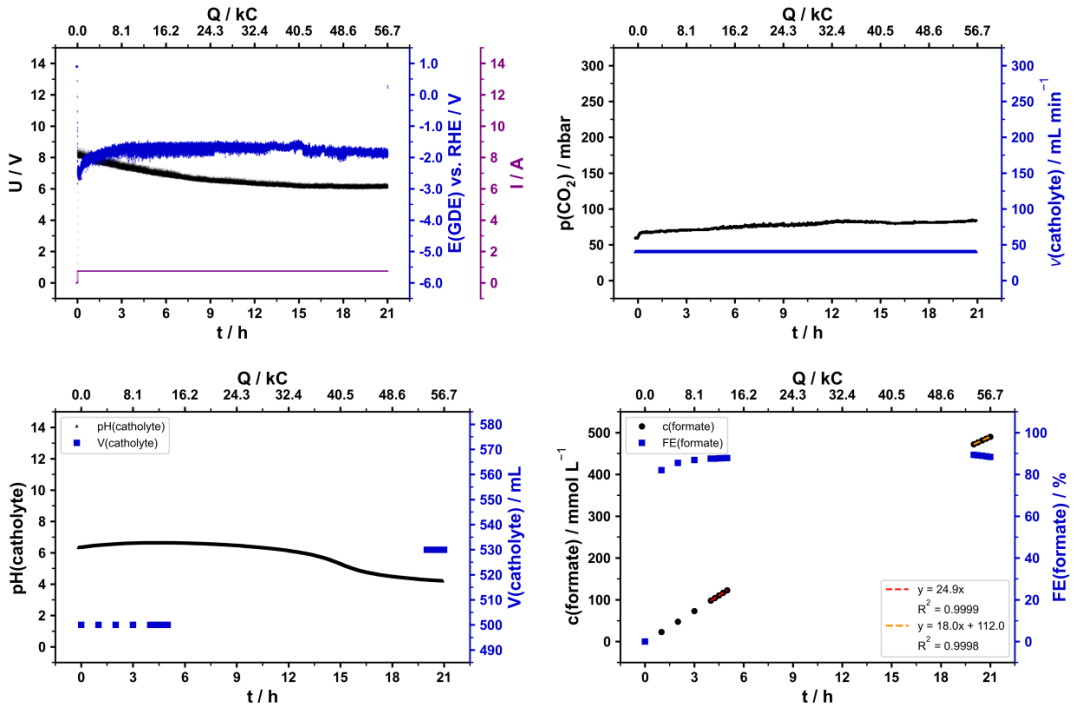

Figure S8: Data for electrolysis (A3), experimental details are provided in section 1.4 and results in Table S12 and Table S13.

3.1.2 Bi / Bi_2O_3 (80:20) GDEs

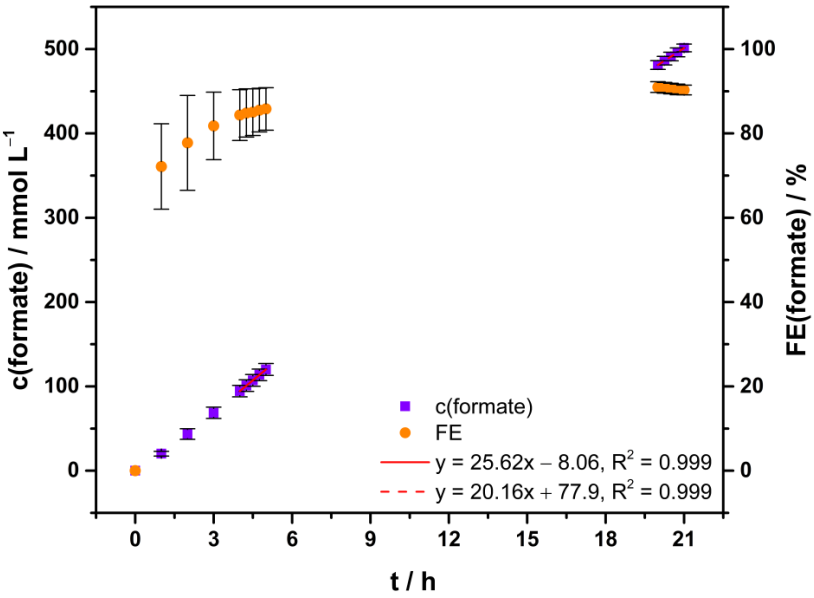

Figure S9: Data for electrolysis (B1, B2, B3), experimental details are provided in section 1.4 and results in Table S11, Table S12 and Table S13.

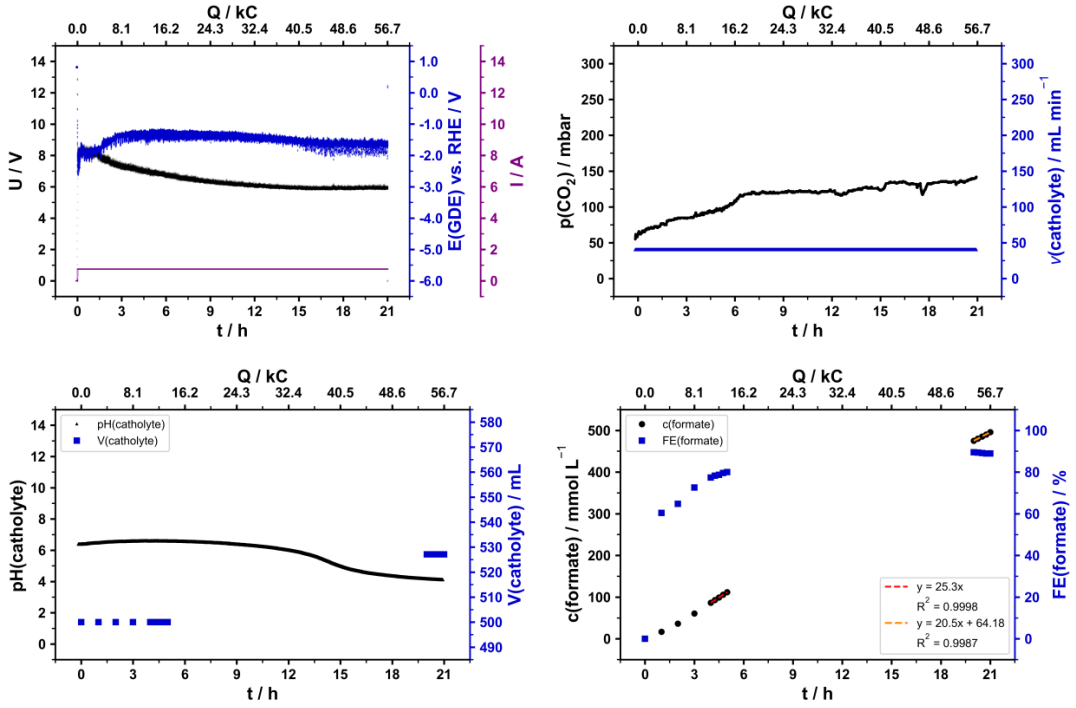

Figure S10: Data for electrolysis (B1), experimental details are provided in section 1.4 and results in Table S12 and Table S13.

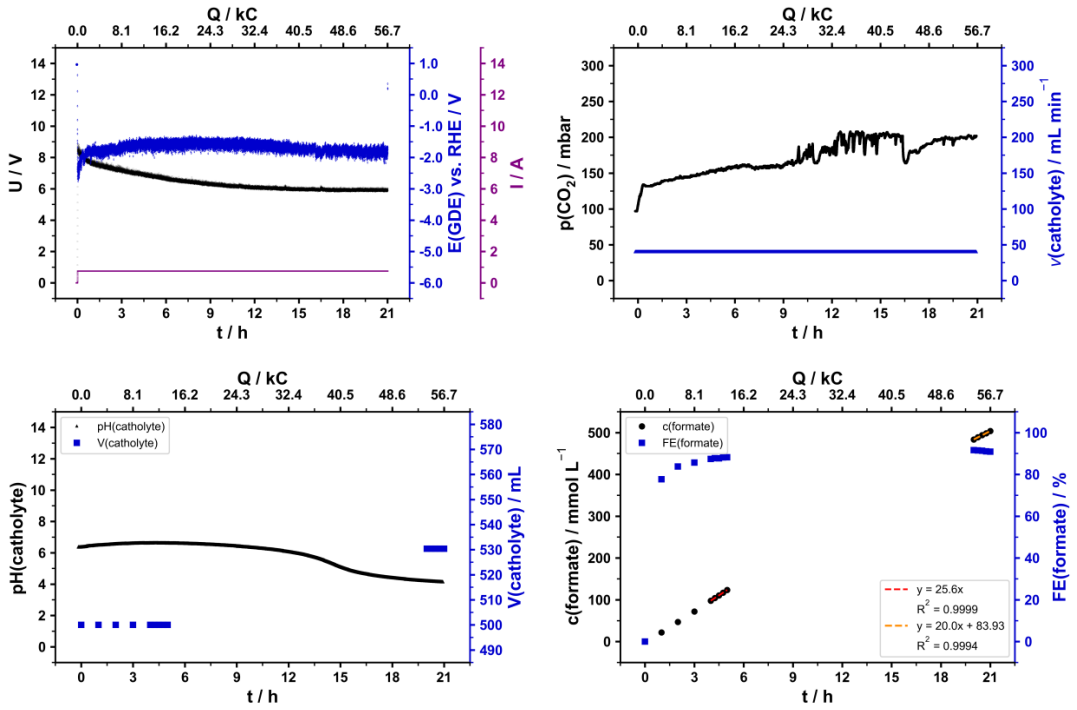

Figure S11: Data for electrolysis (B2), experimental details are provided in section 1.4 and results in Table S12 and Table S13.

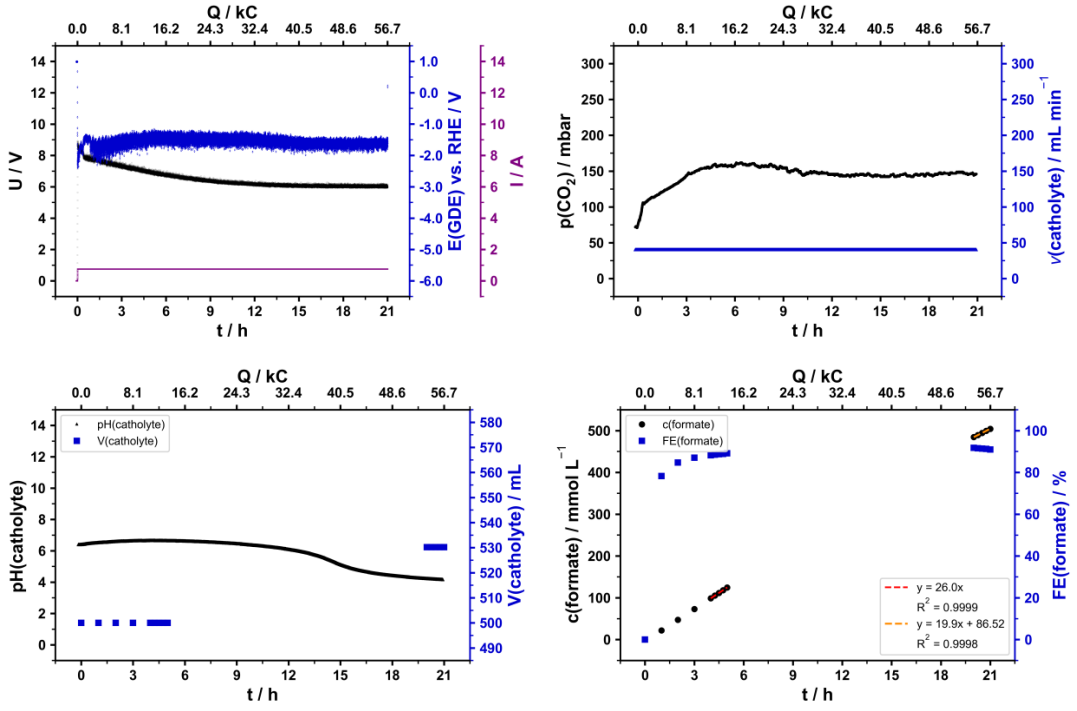

Figure S12: Data for electrolysis (B3), experimental details are provided in section 1.4 and results in Table S12 and Table S13.

3.1.3 Bi / Bi_2O_3 (60:40) GDEs

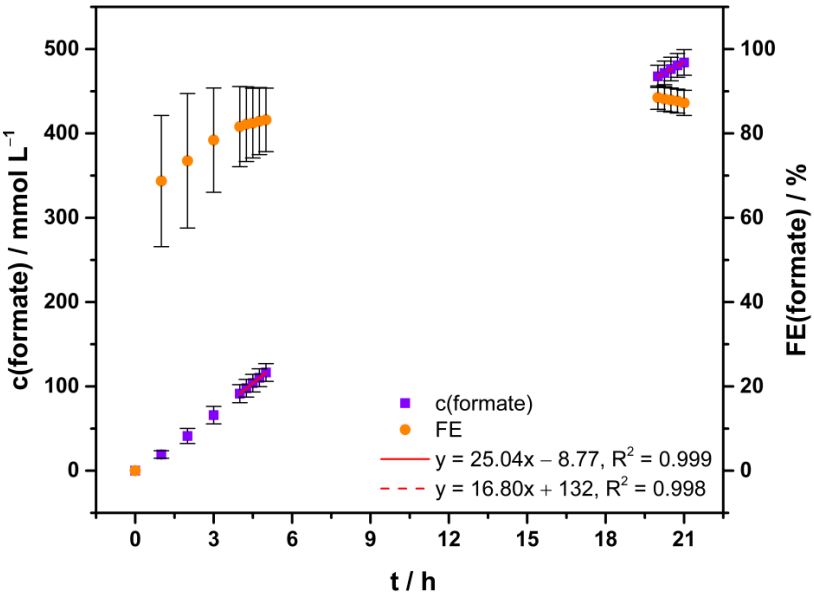

Figure S13: Data for electrolysis (C1, C2, C3), experimental details are provided in section 1.4 and results in Table S11, Table S12 and Table S13.

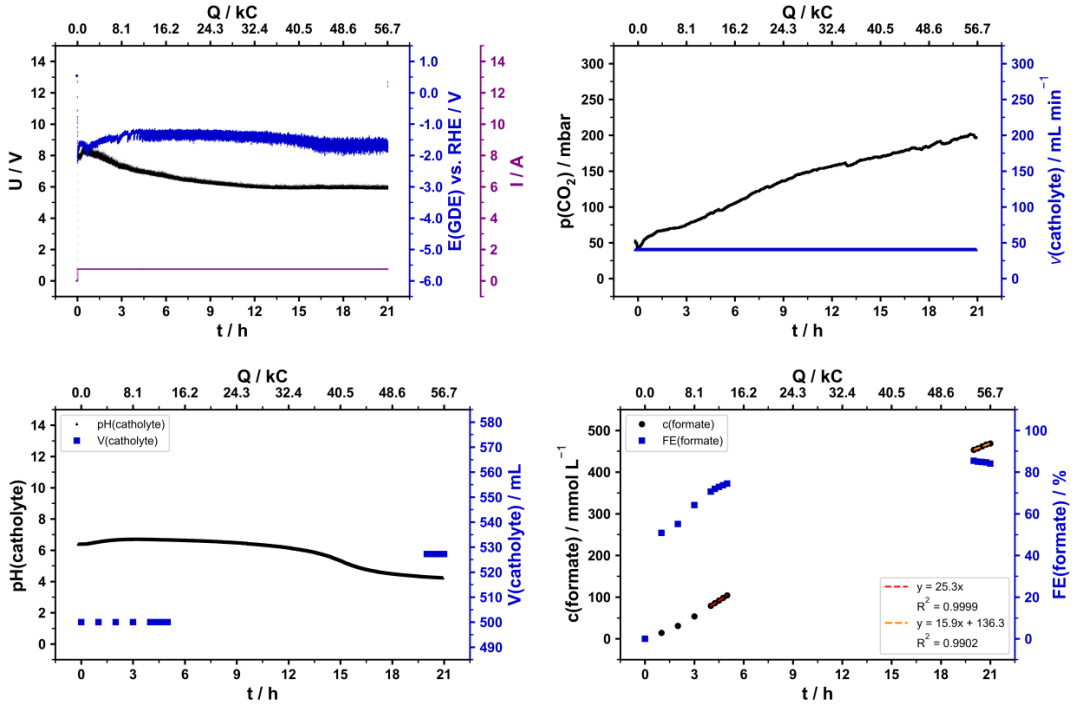

Figure S14: Data for electrolysis (C1), experimental details are provided in section 1.4 and results in Table S12 and Table S13.

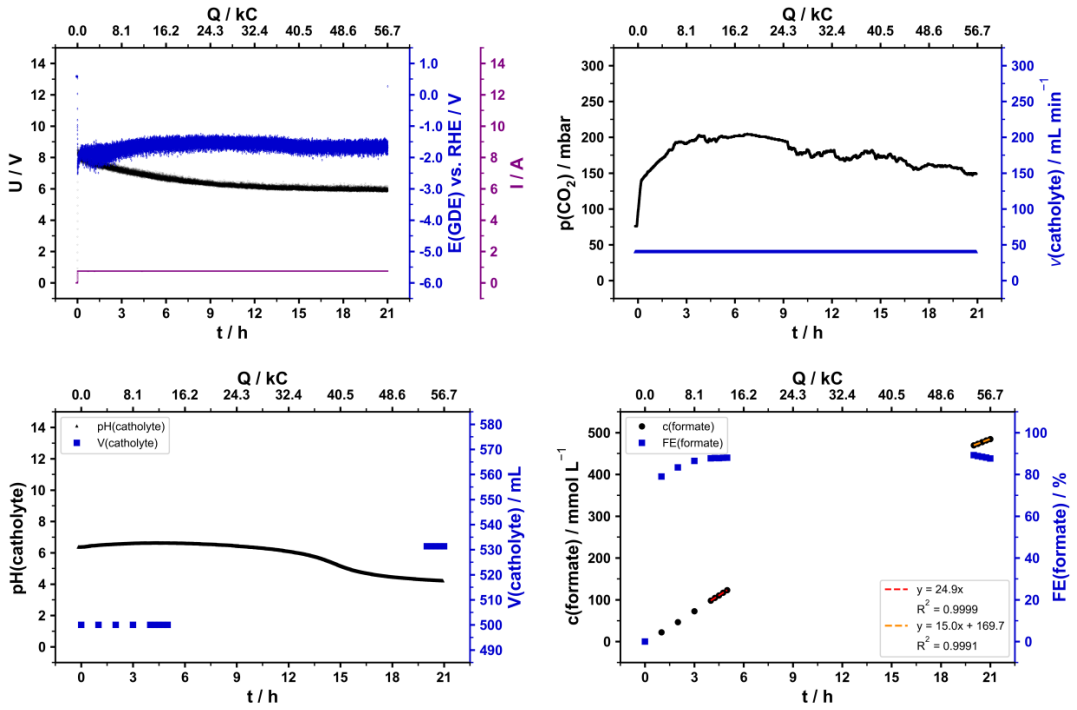

Figure S15: Data for electrolysis (C2), experimental details are provided in section 1.4 and results in Table S12 and Table S13.

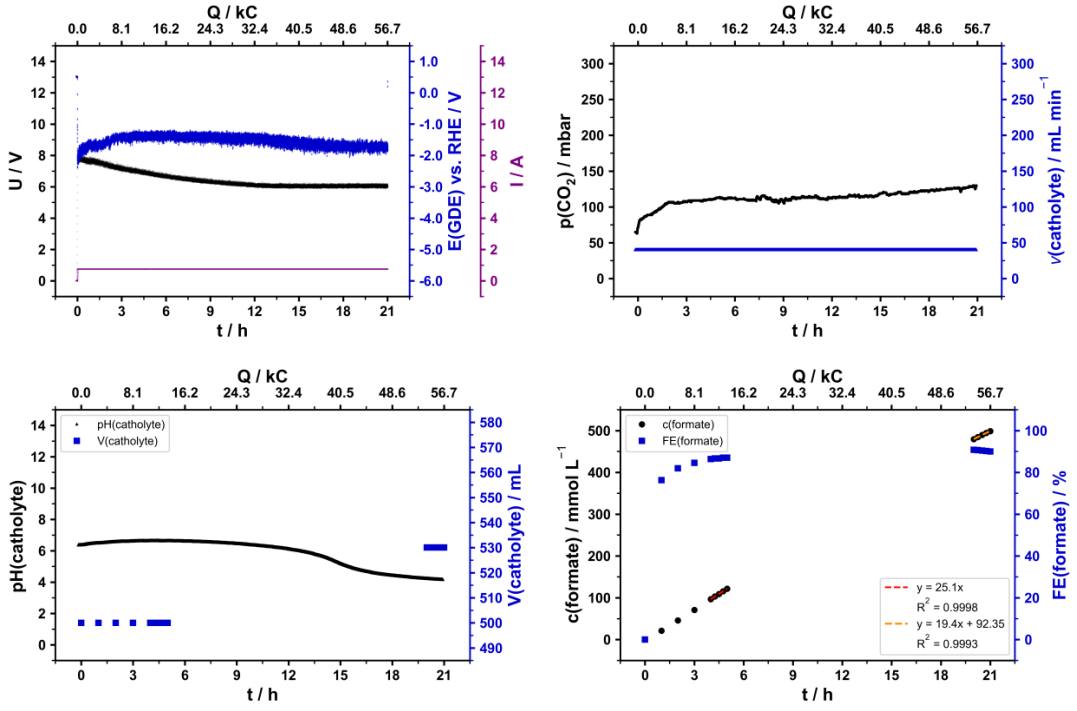

Figure S16: Data for electrolysis (C3), experimental details are provided in section 1.4 and results in Table S12 and Table S13.

3.1.4 Bi / Bi_2O_3 (40:60) GDEs

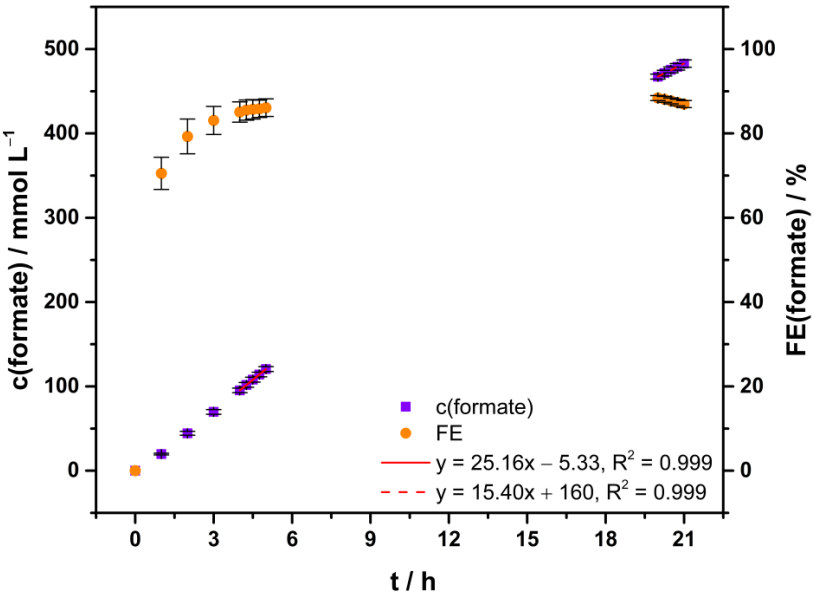

Figure S17: Data for electrolysis (D1, D2, D3), experimental details are provided in section 1.4 and results in Table S11, Table S12 and Table S13.

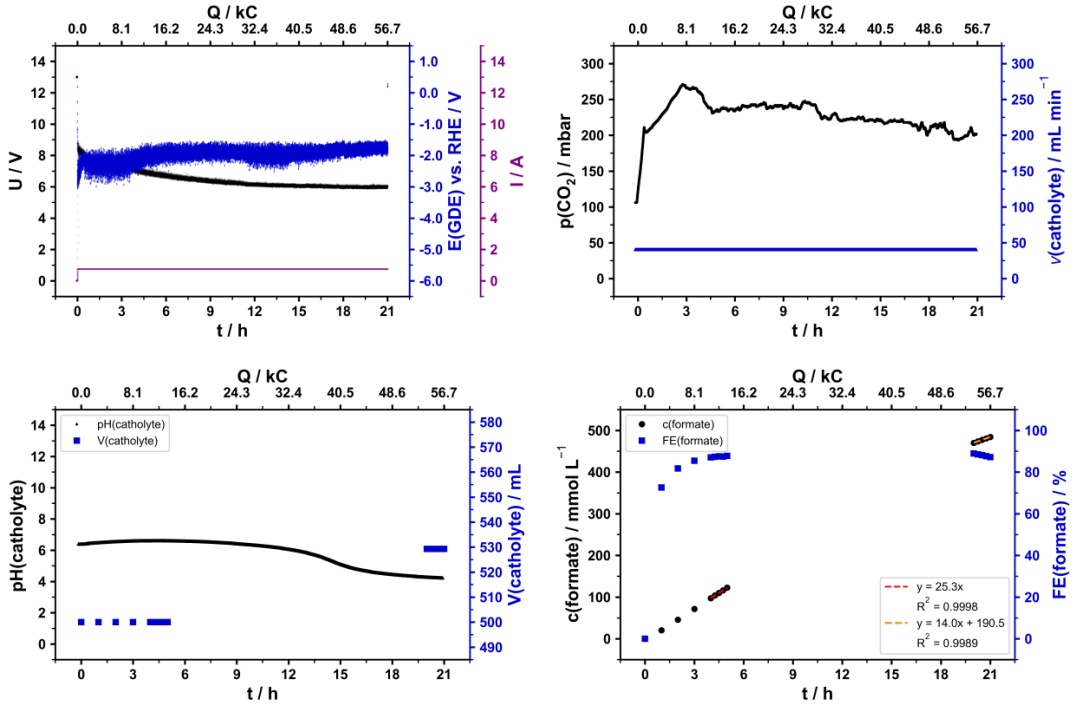

Figure S18: Data for electrolysis (D1), experimental details are provided in section 1.4 and results in Table S12 and Table S13.

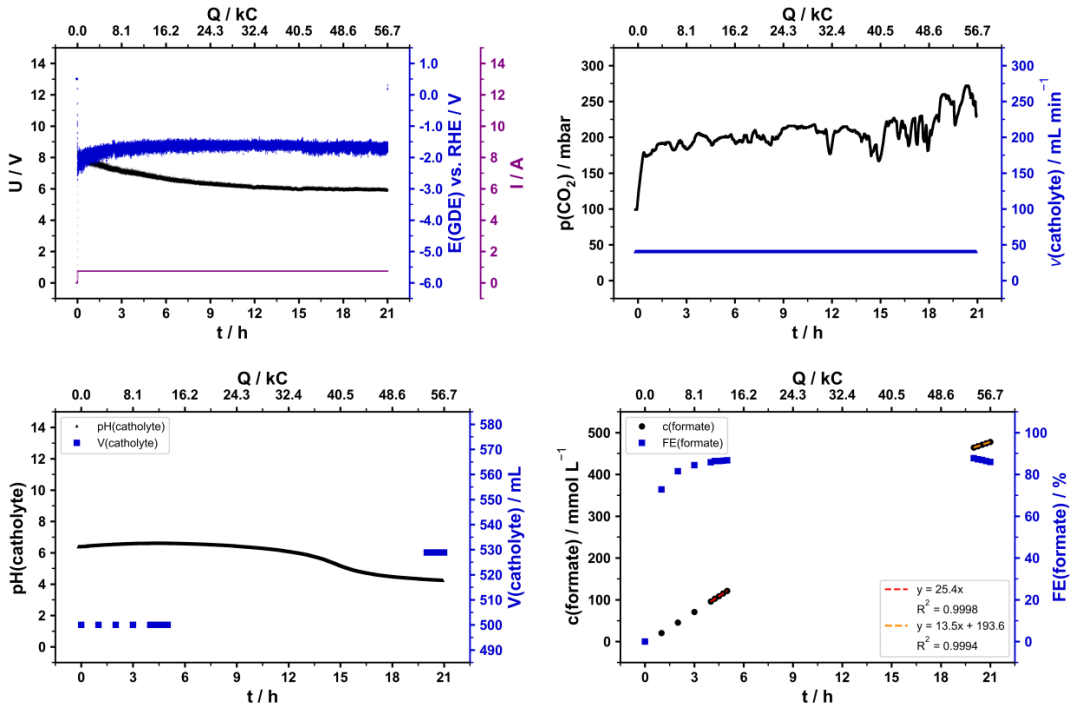

Figure S19: Data for electrolysis (D2), experimental details are provided in section 1.4 and results in Table S12 and Table S13.

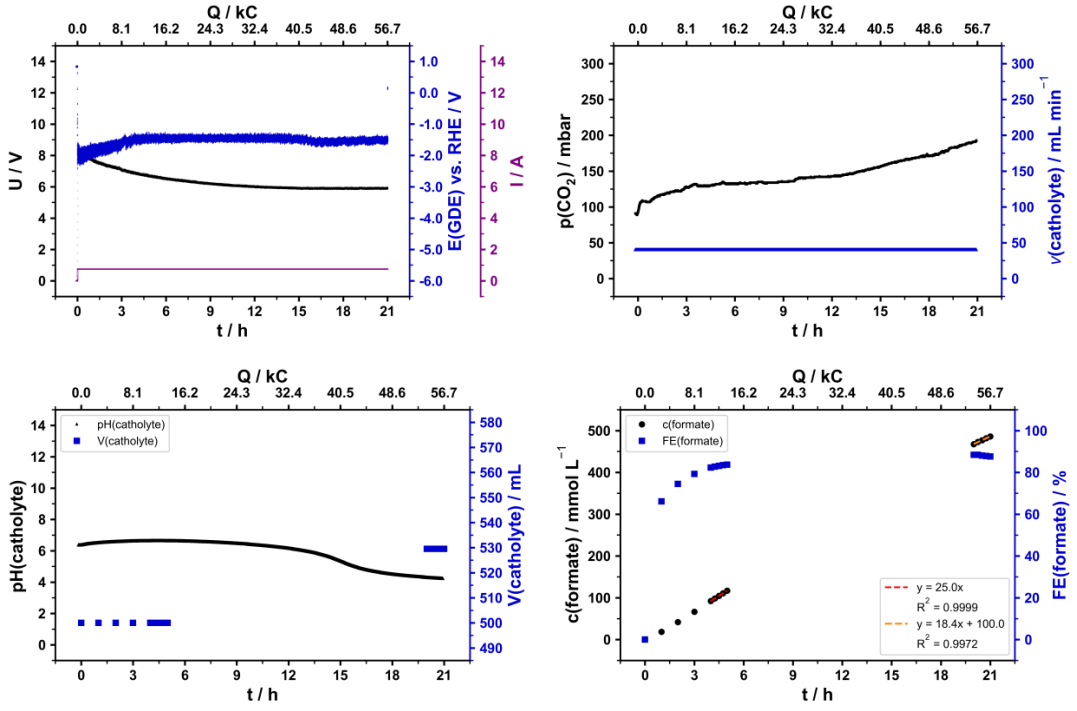

Figure S20: Data for electrolysis (D3), experimental details are provided in section 1.4 and results in Table S12 and Table S13.

3.1.5 Bi / Bi_2O_3 (20:80) GDEs

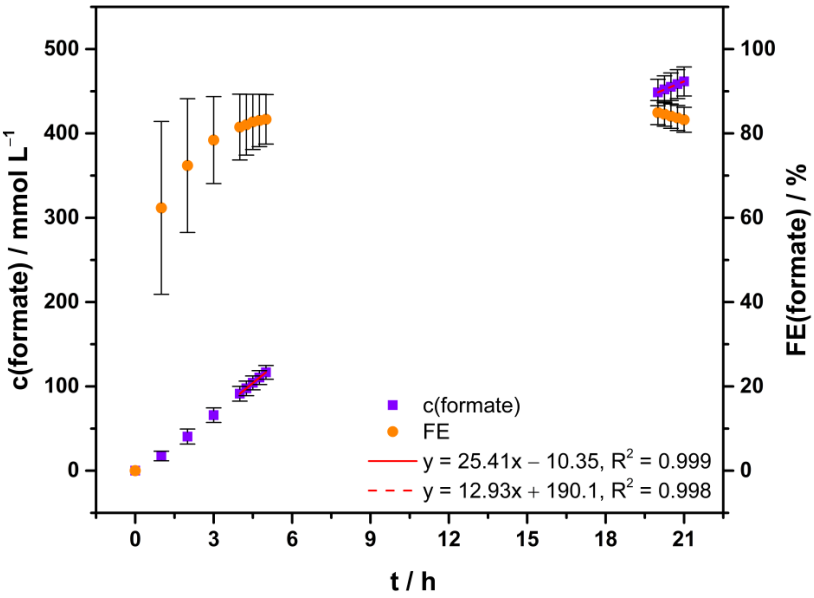

Figure S21: Data for electrolysis (E1, E2, E3), experimental details are provided in section 1.4 and results in Table S11, Table S12 and Table S13.

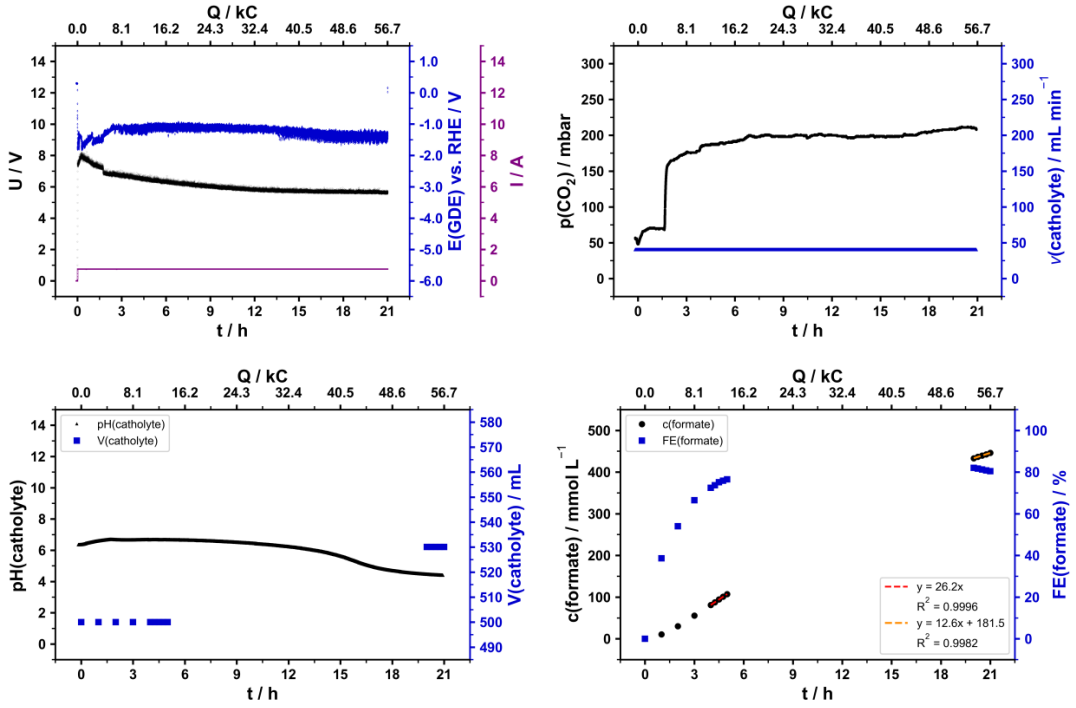

Figure S22: Data for electrolysis (E1), experimental details are provided in section 1.4 and results in Table S12 and Table S13.

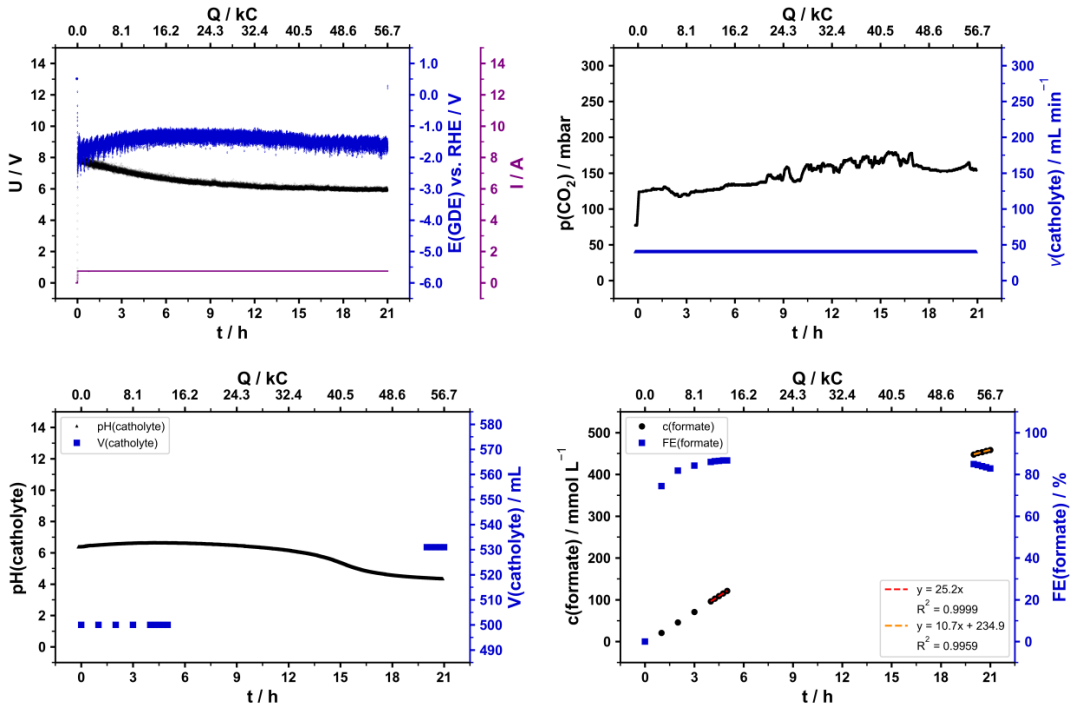

Figure S23: Data for electrolysis (E2), experimental details are provided in section 1.4 and results in Table S12 and Table S13.

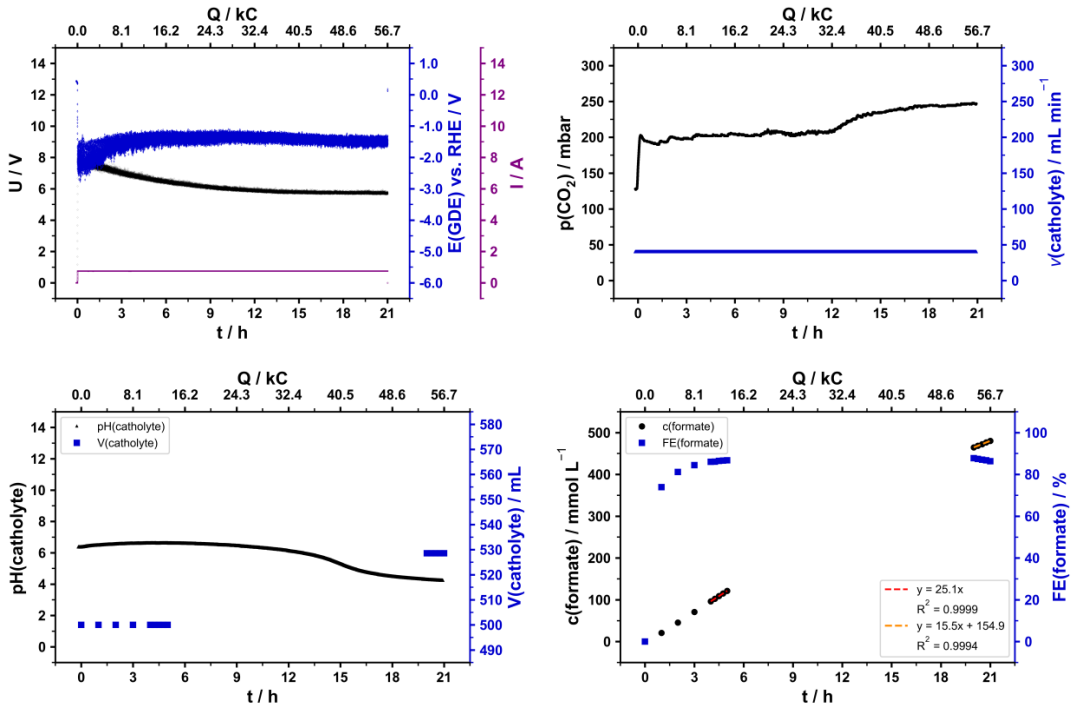

Figure S24: Data for electrolysis (E3), experimental details are provided in section 1.4 and results in Table S12 and Table S13.

3.1.6 Bi_2O_3 GDEs

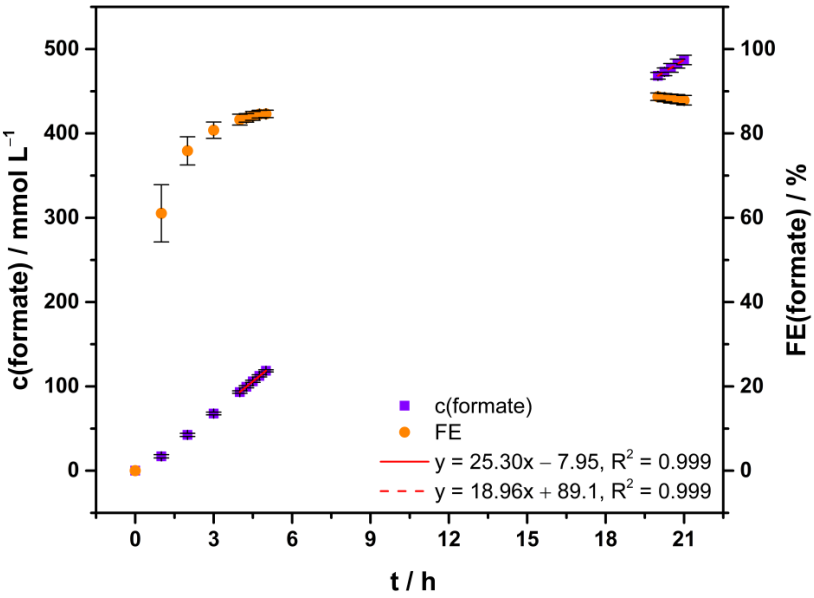

Figure S25: Data for electrolysis (F1, F2, F3), experimental details are provided in section 1.4 and results in Table S11, Table S12 and Table S13.

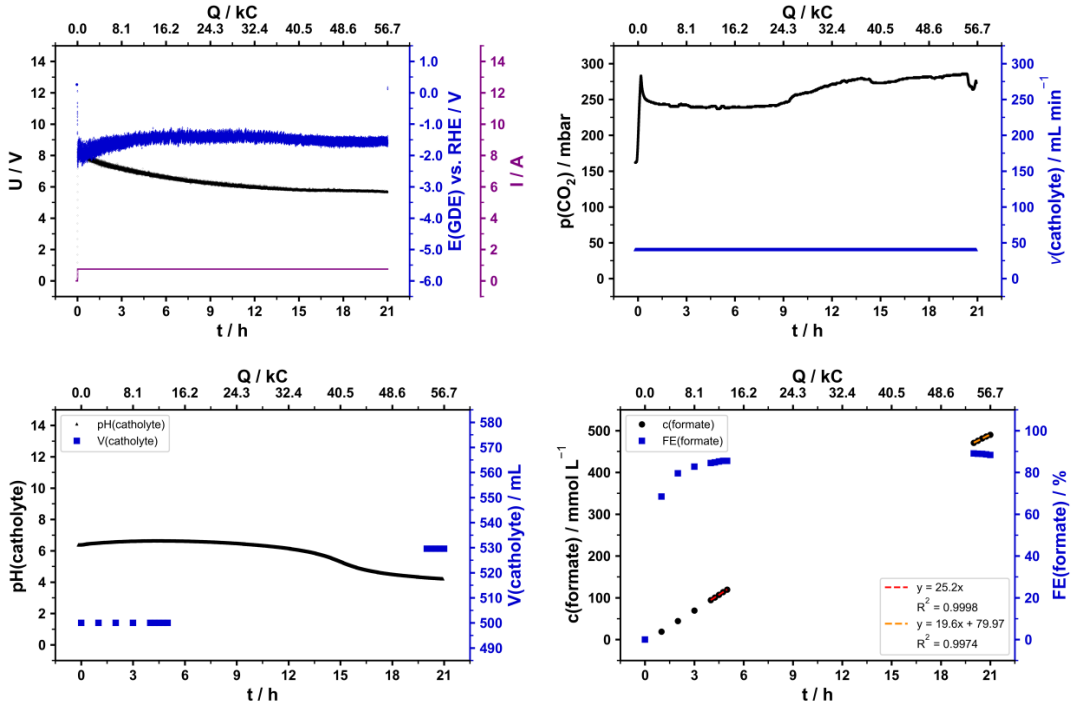

Figure S26: Data for electrolysis (F1), experimental details are provided in section 1.4 and results in Table S12 and Table S13.

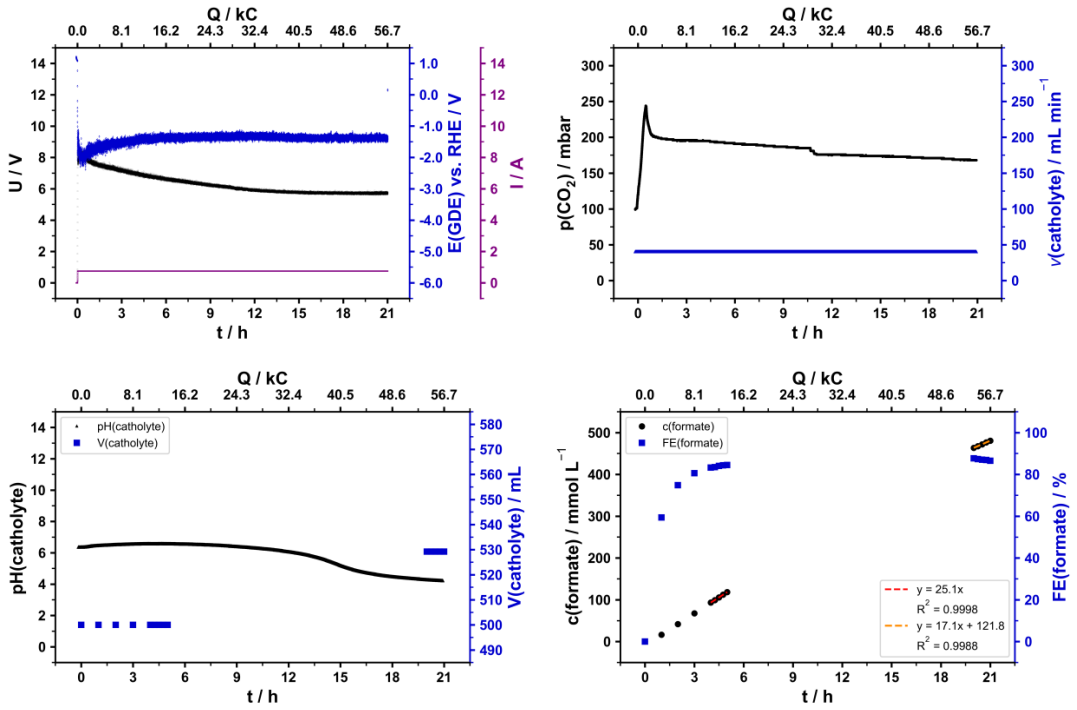

Figure S27: Data for electrolysis (F2), experimental details are provided in section 1.4 and results in Table S12 and Table S13.

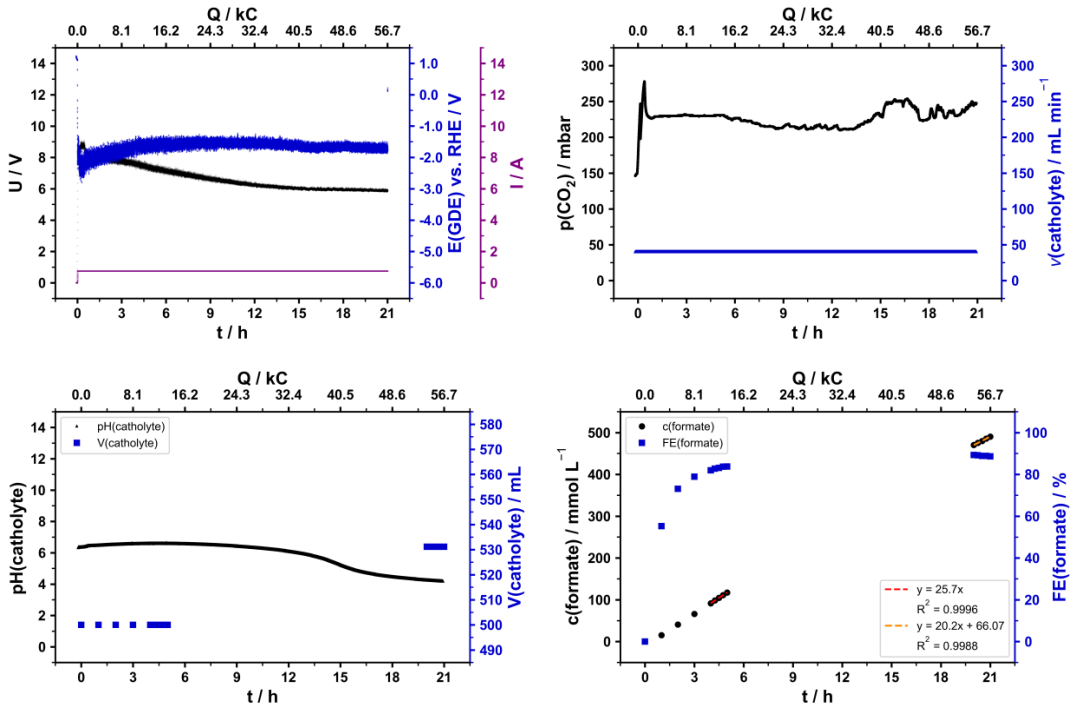

Figure S28: Data for electrolysis (F3), experimental details are provided in section 1.4 and results in Table S12 and Table S13.

3.2 Electrosynthesis of formate at variable current density

Electrolysis results have been summarized in Table S14. Moreover, detailed courses of each individual electrolysis are provided.

Table S14: Overview of volume, formate concentration, formate FE and pH determined *n* = 3 after electrolysis at variable current densities in the catholyte of formate electrosynthesis with 0.2 mol L^{-1} KH_2PO_4 / K_2HPO_4 as starting electrolyte.

Electrolysis	V / mL	c(formate) / mmol L^{-1}	FE(formate) / %	pH
(B4)	507.1 ± 0.4	238.9 ± 0.3	91.44 ± 0.07	6.41 ± 0.05
(B5)	508.7 ± 0.8	236.1 ± 0.4	90.6 ± 0.3	6.42 ± 0.05
(B6)	509.3 ± 1.0	236.9 ± 0.1	91.3 ± 0.2	6.43 ± 0.05
(B7)	527.1 ± 0.4	198.4 ± 0.3	90.8 ± 0.2	6.47 ± 0.05
(B8)	530.4 ± 0.4	199.6 ± 0.4	91.87 ± 0.09	6.47 ± 0.05
(B9)	530.2 ± 0.5	196.4 ± 0.3	90.43 ± 0.04	6.52 ± 0.05
(B10)	518.3 ± 1.3	362.1 ± 0.2	87.3 ± 0.3	5.47 ± 0.05
(B11)	518.4 ± 1.1	354.5 ± 0.2	86.9 ± 0.3	5.57 ± 0.05
(B12)	516.9 ± 0.7	347.2 ± 0.5	83.5 ± 0.3	5.72 ± 0.05

3.2.1 Operation alternating between full and half load

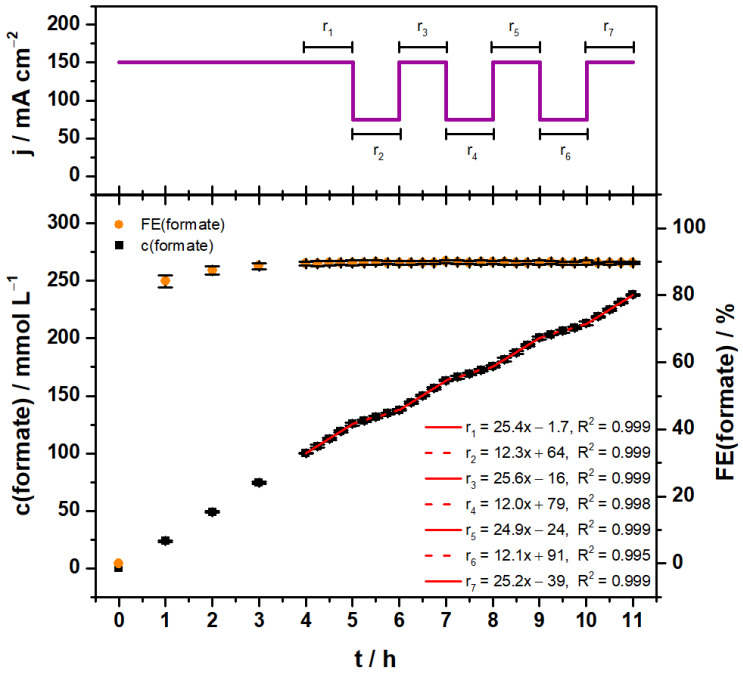

Figure S29: Data for electrolysis (B4, B5, B6), experimental details are provided in section 1.4 and results in Table S14.

Table S15: Synthesis rates of formate for different time intervals at different current densities as shown in Figure S29.

Rate	Interval	Current density / mA cm^{-2}	c(formate) rate / mmol L^{-1} h^{-1}
r_1	4 - 5 h	150	25.43 ± 0.08
r_2	5 - 6 h	75	12.28 ± 0.12
r_3	6 - 7 h	150	25.6 ± 0.3
r_4	7 - 8 h	75	12.0 ± 0.3
r_5	8 - 9 h	150	24.95 ± 0.06
r_6	9 - 10 h	75	12.1 ± 0.5
r_7	10 - 11 h	150	25.2 ± 0.4

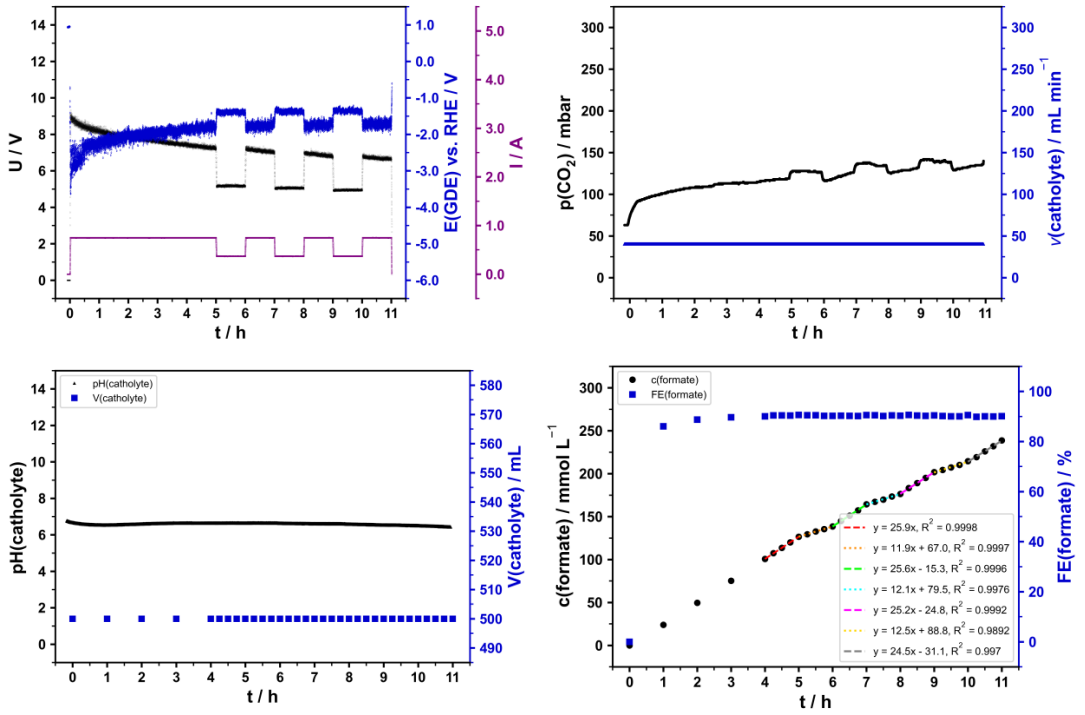

Figure S30: Data for electrolysis (B4), experimental details are provided in section 1.4 and results in Table S14.

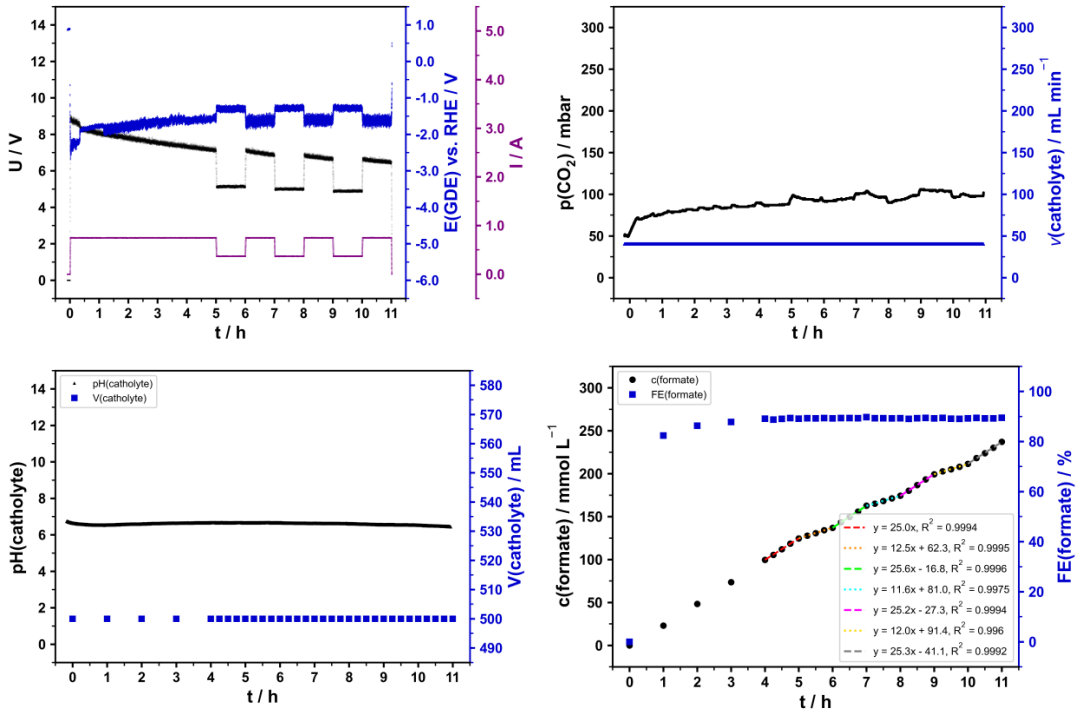

Figure S31: Data for electrolysis (B5), experimental details are provided in section 1.4 and results in Table S14.

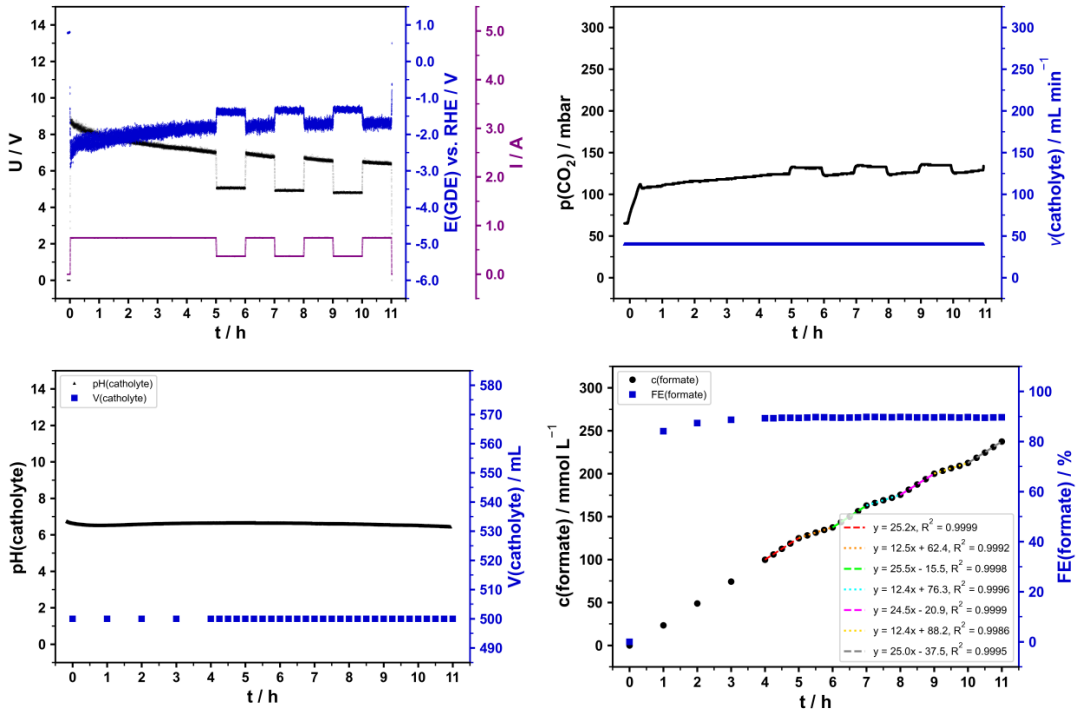

Figure S32: Data for electrolysis (B6), experimental details are provided in section 1.4 and results in Table S14.

3.2.2 Operation alternating between full and zero load

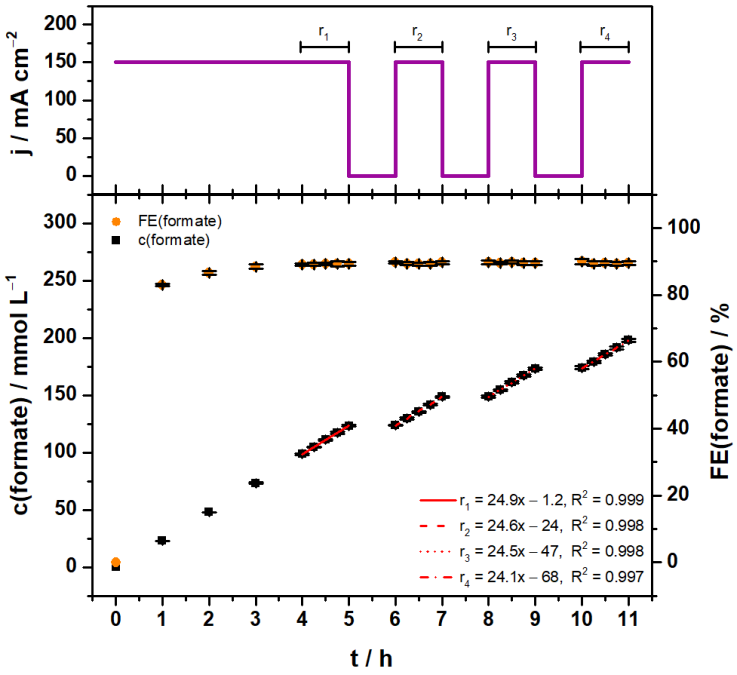

Figure S33: Data for electrolysis (B7, B8, B9), experimental details are provided in section 1.4 and results in Table S14.

Table S16: Synthesis rates of formate for different time intervals at different current densities as shown in Figure S33.

Rate	Interval	Current density / mA cm^{-2}	c(formate) rate / mmol L^{-1} h^{-1}
r_1	4 - 5 h	150	24.93 ± 0.07
r_2	6 - 7 h	150	24.6 ± 0.5
r_3	8 - 9 h	150	24.5 ± 0.4
r_4	10 - 11 h	150	24.1 ± 0.7

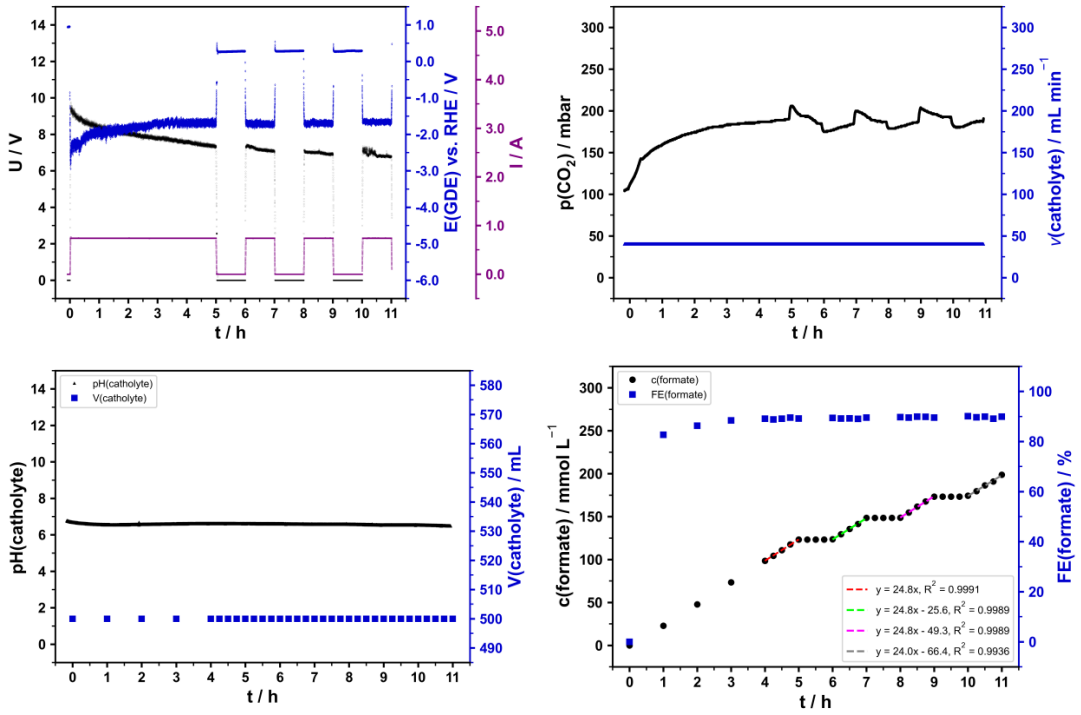

Figure S34: Data for electrolysis (B7), experimental details are provided in section 1.4 and results in Table S14.

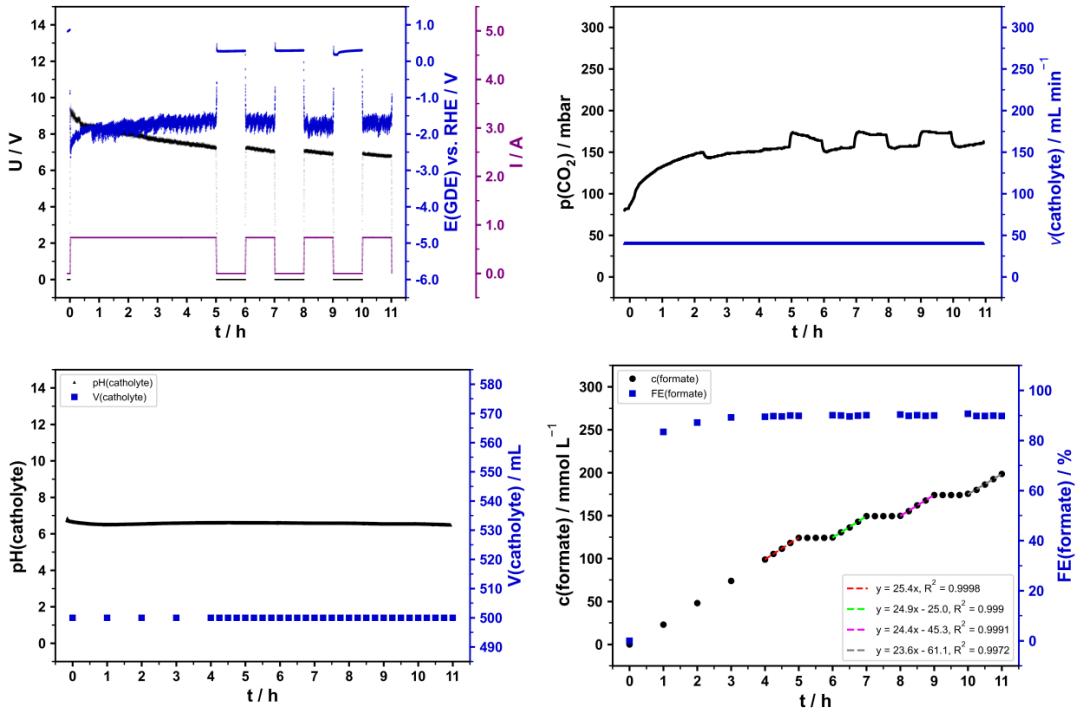

Figure S35: Data for electrolysis (B8), experimental details are provided in section 1.4 and results in Table S14.

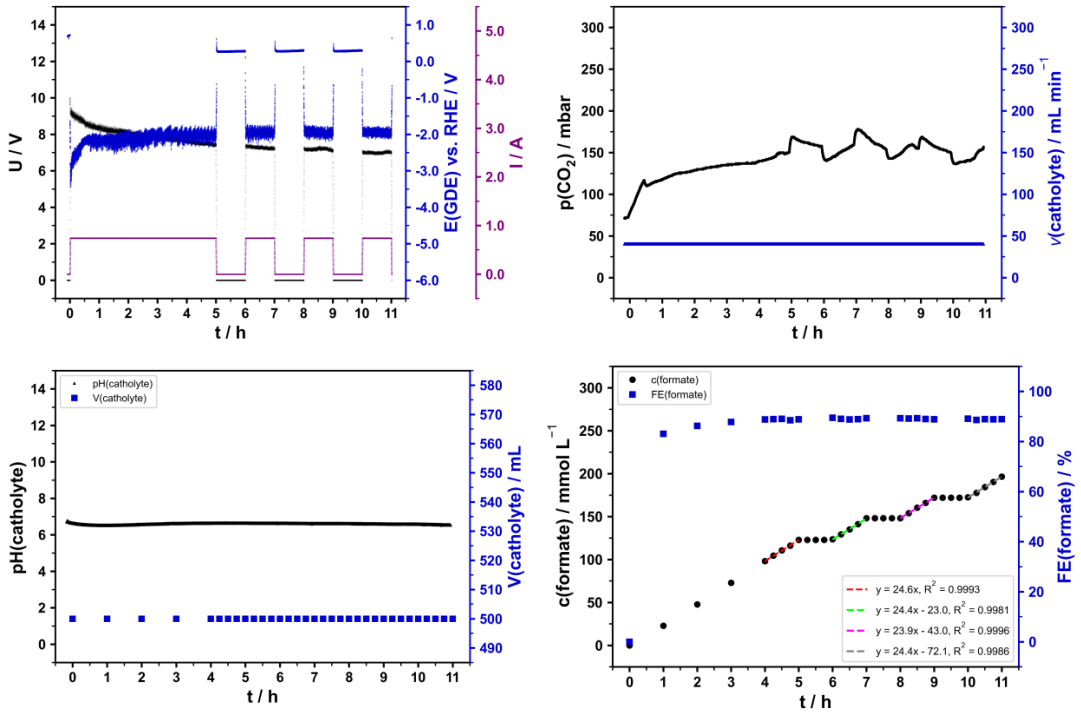

Figure S36: Data for electrolysis (B9), experimental details are provided in section 1.4 and results in Table S14.

3.2.3 Day-night cycle

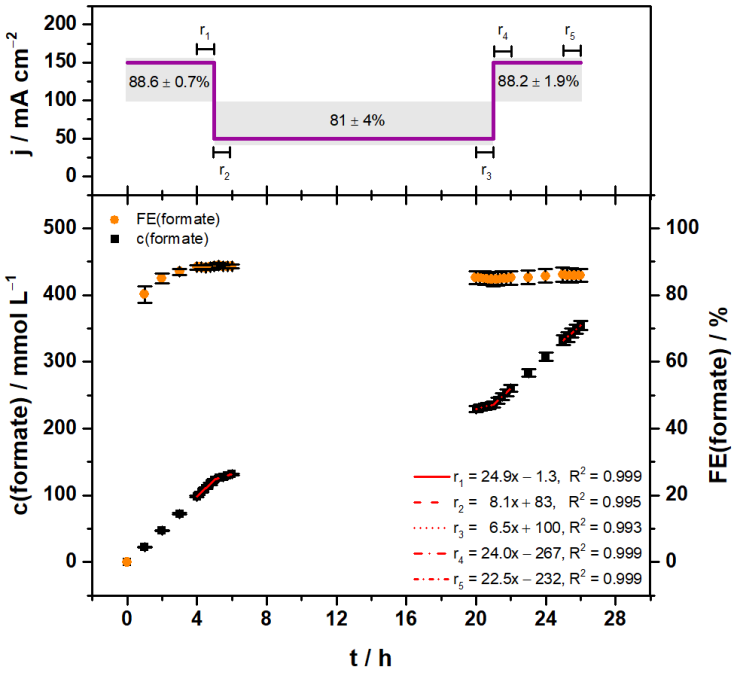

Figure S37: Data for electrolysis (B10, B11, B12), experimental details are provided in section 1.4 and results in Table S14.

Table S17: Synthesis rates of formate for different time intervals at different current densities as shown in Figure S37.

Rate	Interval	Current density / mA cm^{-2}	c(formate) rate / mmol L^{-1} h^{-1}
r_1	4 - 5 h	150	24.93 ± 0.16
r_2	5 - 6 h	50	8.1 ± 0.3
r_3	20 - 21 h	50	6.5 ± 0.3
r_4	21 - 22 h	150	23.97 ± 0.07
r_5	25 - 26 h	150	22.5 ± 0.3

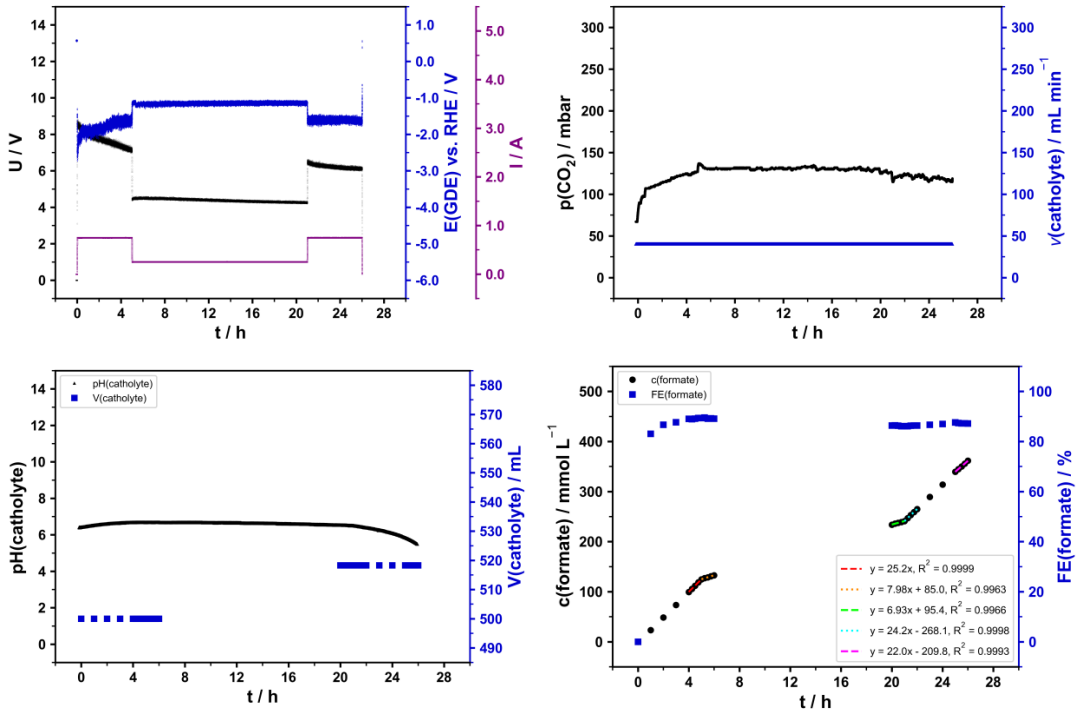

Figure S38: Data for electrolysis (B10), experimental details are provided in section 1.4 and results in Table S14.

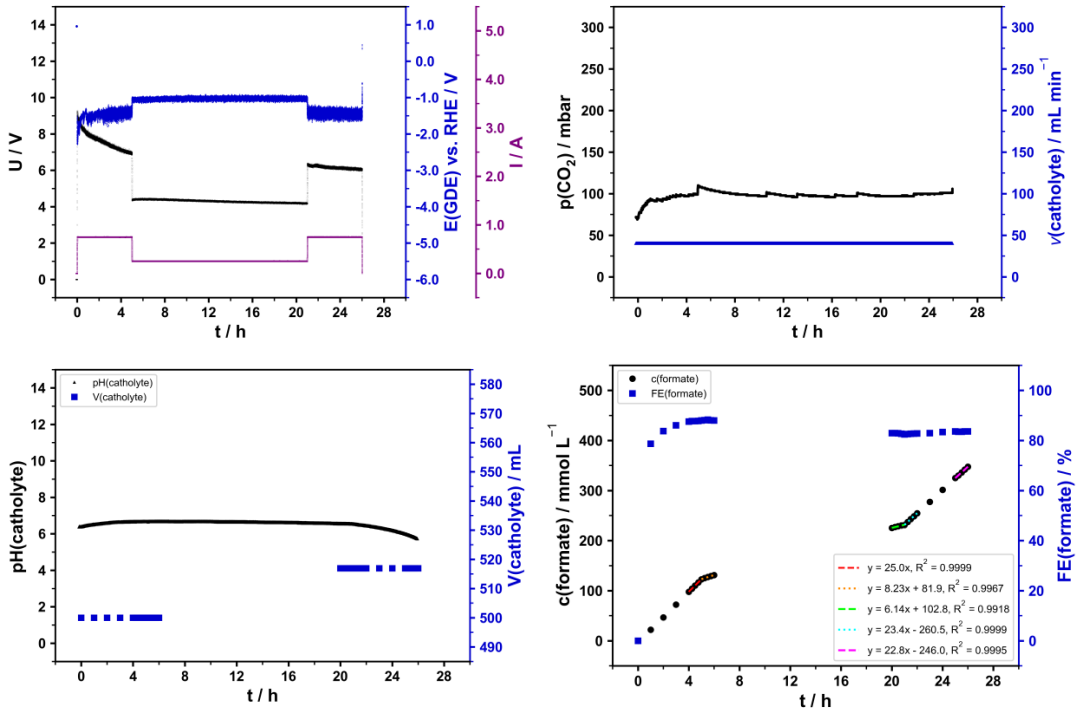

Figure S39: Data for electrolysis (B11), experimental details are provided in section 1.4 and results in Table S14.

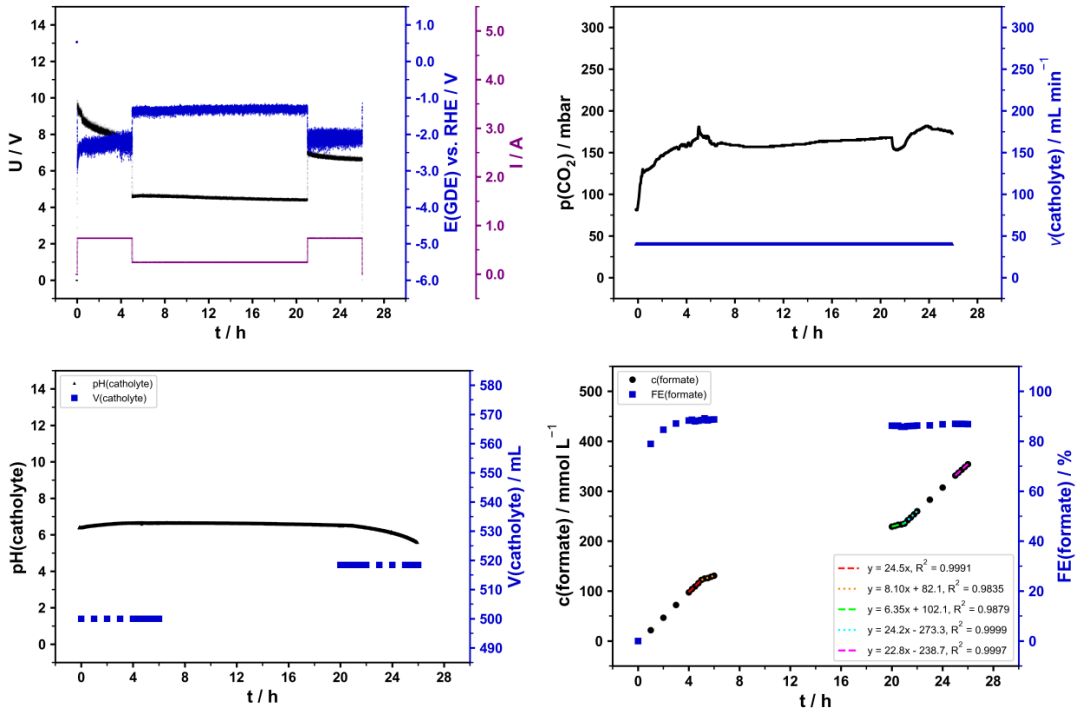

Figure S40: Data for electrolysis (B12), experimental details are provided in section 1.4 and results in Table S14.

3.3 Pictures and cross sections of GDE before and after electrolysis

3.3.1 Bi GDEs

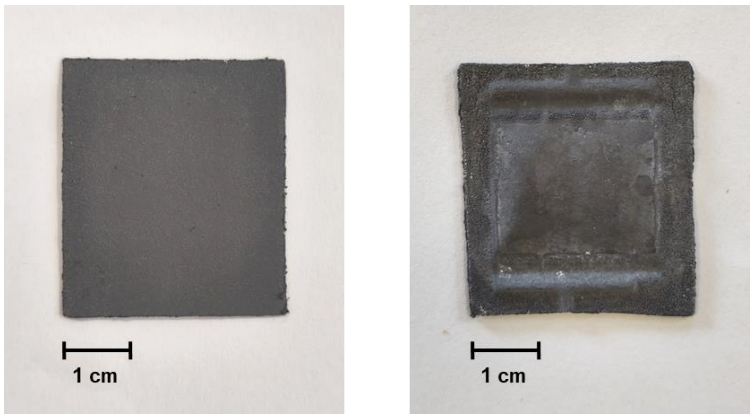

Figure S41: Exemplary pictures of a self-fabricated Bi based GDE (A, cf. Table S3) before (left) and after (right) electrolysis. Details of the fabrication process are provided in section 1.2, details on the electrolysis conditions in section 1.4.

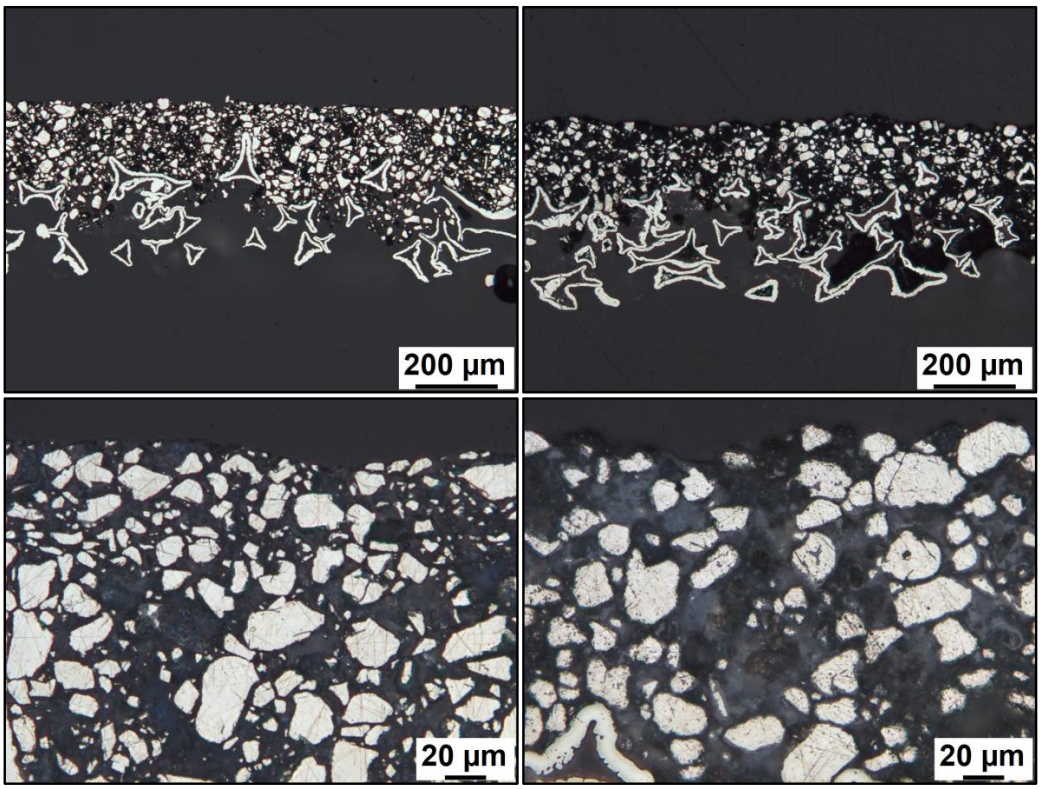

Figure S42: Exemplary cross section of a self-fabricated Bi based GDE (A, cf. Table S3) before (left) and after (right) electrolysis. Details of the fabrication process are provided in section 1.2, details on the electrolysis conditions in section 1.4.

3.3.2 Bi / Bi_2O_3 (80:20) GDEs

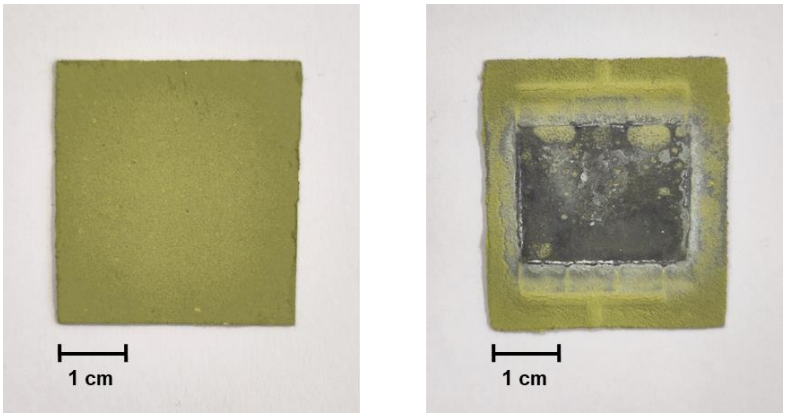

Figure S43: Exemplary pictures of a self-fabricated Bi / Bi_2O_3 (80:20) based GDE (B, cf. Table S3) before (left) and after (right) electrolysis. Details of the fabrication process are provided in section 1.2, details on the electrolysis conditions in section 1.4.

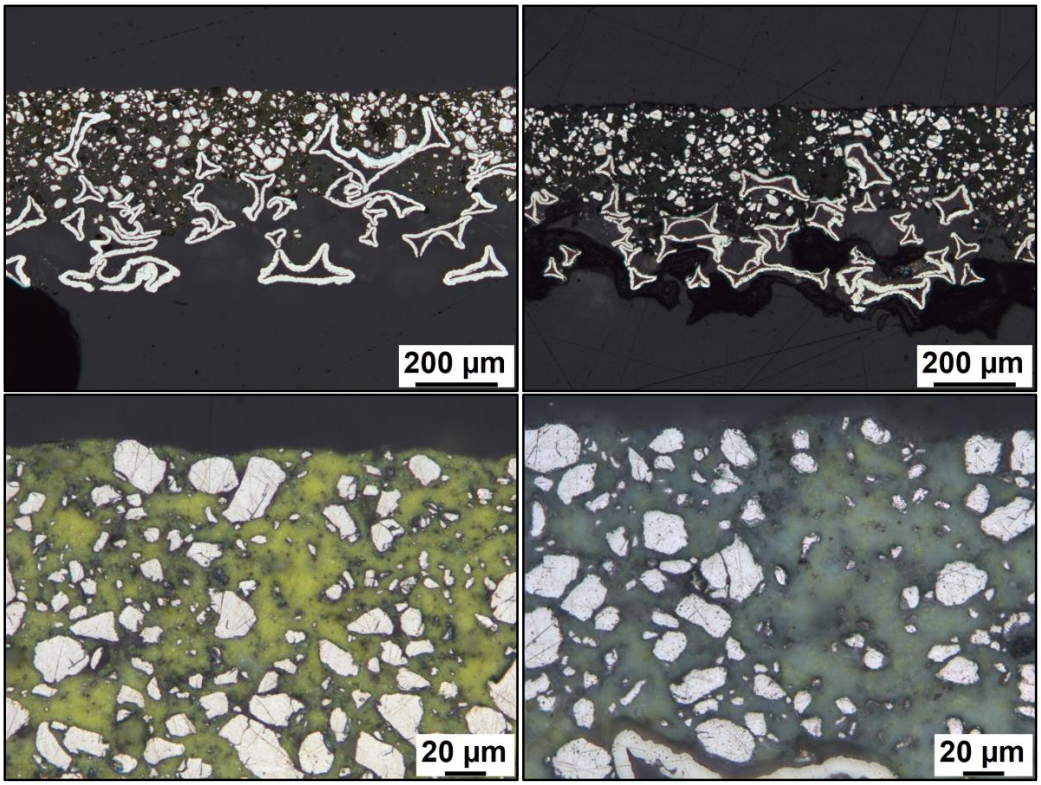

Figure S44: Exemplary cross section of a self-fabricated Bi / Bi_2O_3 (80:20) based GDE (B, cf. Table S3) before (left) and after (right) electrolysis. Details of the fabrication process are provided in section 1.2, details on the electrolysis conditions in section 1.4.

3.3.3 Bi / Bi_2O_3 (60:40) GDEs

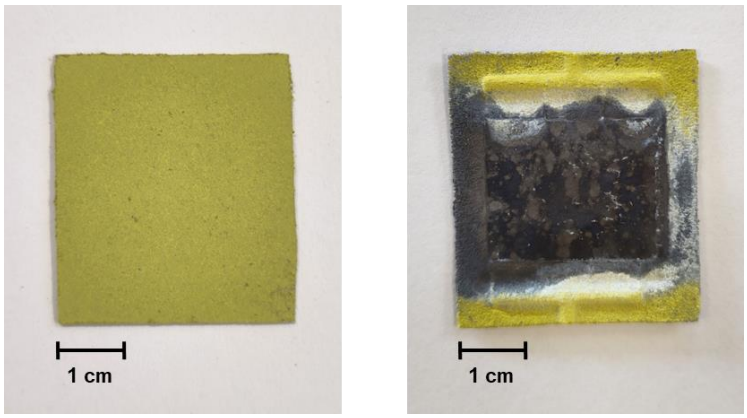

Figure S45: Exemplary pictures of a self-fabricated Bi / Bi_2O_3 (60:40) based GDE (C, cf. Table S3) before (left) and after (right) electrolysis. Details of the fabrication process are provided in section 1.2, details on the electrolysis conditions in section 1.4.

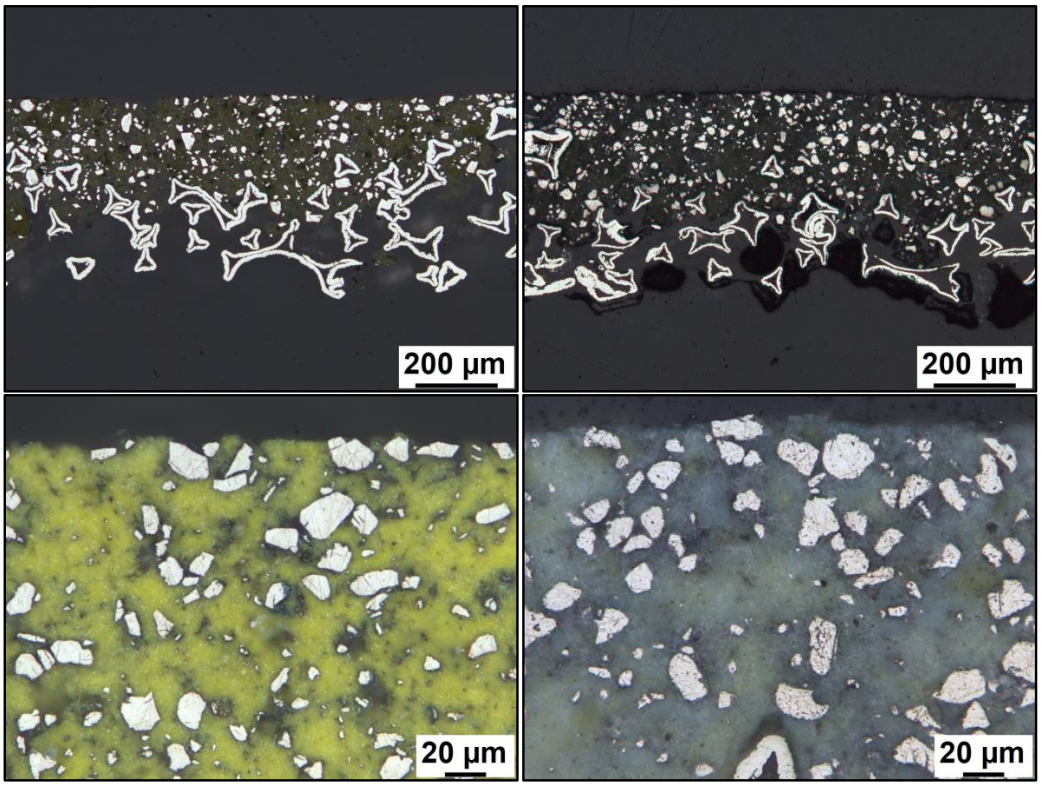

Figure S46: Exemplary cross section of a self-fabricated Bi / Bi_2O_3 (60:40) based GDE (C, cf. Table S3) before (left) and after (right) electrolysis. Details of the fabrication process are provided in section 1.2, details on the electrolysis conditions in section 1.4.

3.3.4 Bi / Bi_2O_3 (40:60) GDEs

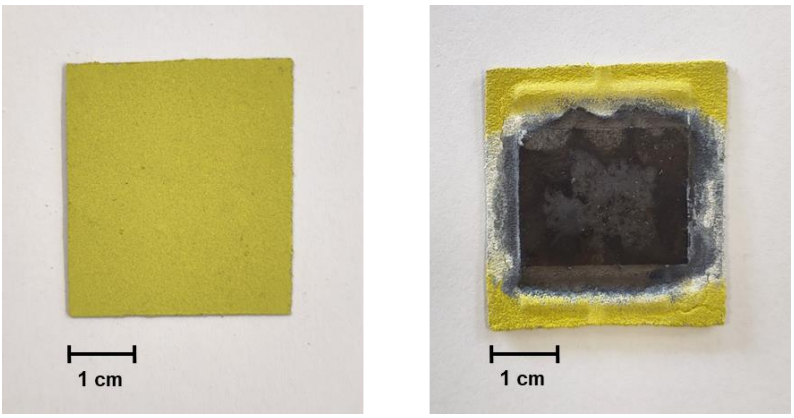

Figure S47: Exemplary pictures of a self-fabricated Bi / Bi_2O_3 (40:60) based GDE (D, cf. Table S3) before (left) and after (right) electrolysis. Details of the fabrication process are provided in section 1.2, details on the electrolysis conditions in section 1.4.

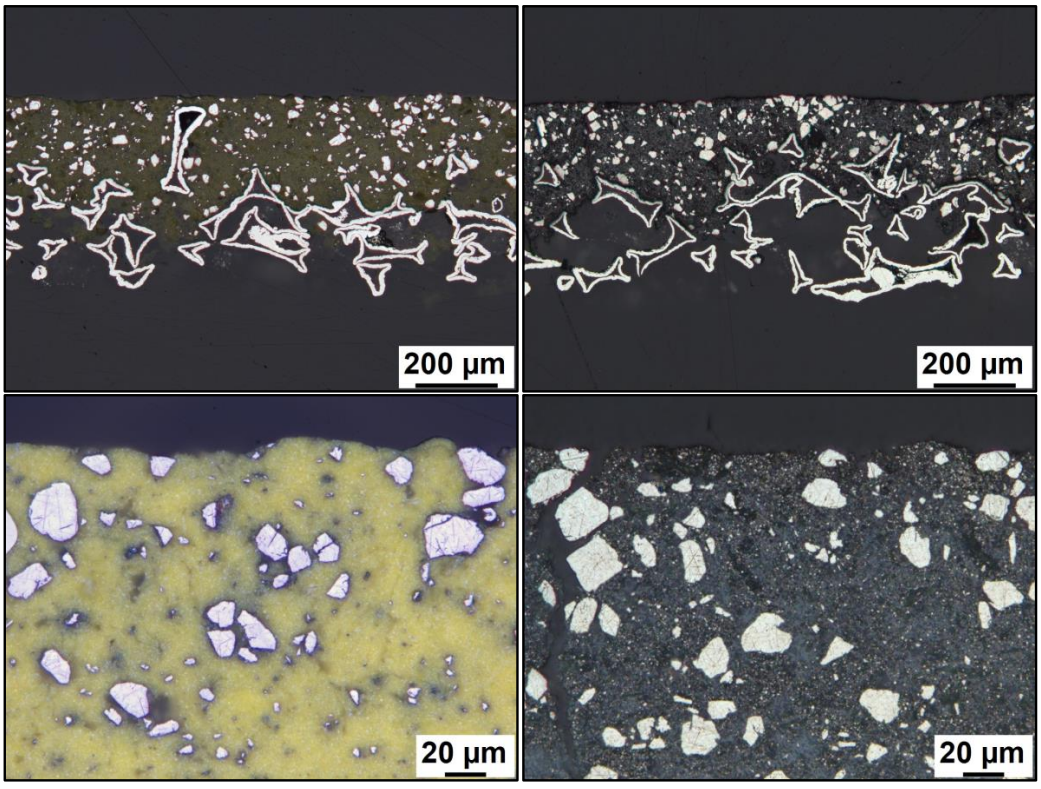

Figure S48: Exemplary cross section of a self-fabricated Bi / Bi_2O_3 (40:60) based GDE (D, cf. Table S3) before (left) and after (right) electrolysis. Details of the fabrication process are provided in section 1.2, details on the electrolysis conditions in section 1.4.

3.3.5 Bi / Bi_2O_3 (20:80) GDEs

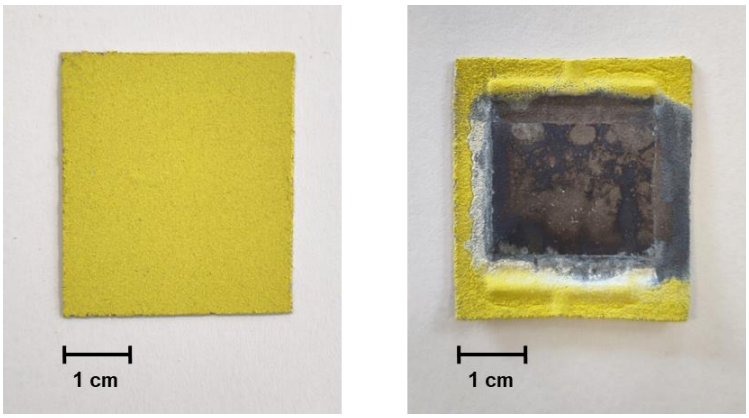

Figure S49: Exemplary pictures of a self-fabricated Bi / Bi_2O_3 (20:80) based GDE (E, cf. Table S3) before (left) and after (right) electrolysis. Details of the fabrication process are provided in section 1.2, details on the electrolysis conditions in section 1.4.

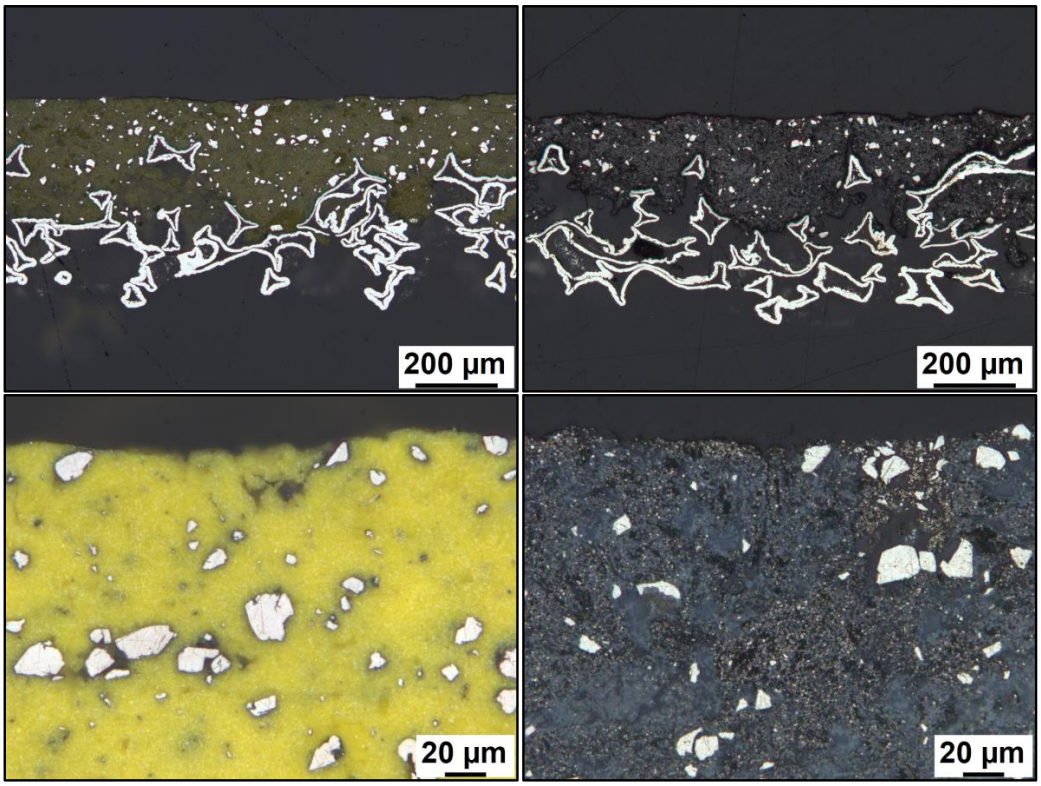

Figure S50: Exemplary cross section of a self-fabricated Bi / Bi_2O_3 (20:80) based GDE (E, cf. Table S3) before (left) and after (right) electrolysis. Details of the fabrication process are provided in section 1.2, details on the electrolysis conditions in section 1.4.

3.3.6 Bi_2O_3 GDEs

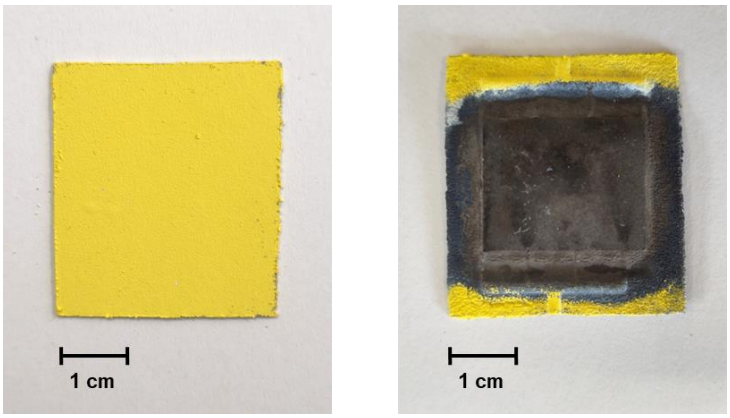

Figure S51: Exemplary pictures of a self-fabricated Bi_2O_3 based GDE (F, cf. Table S3) before (left) and after (right) electrolysis. Details of the fabrication process are provided in section 1.2, details on the electrolysis conditions in section 1.4.

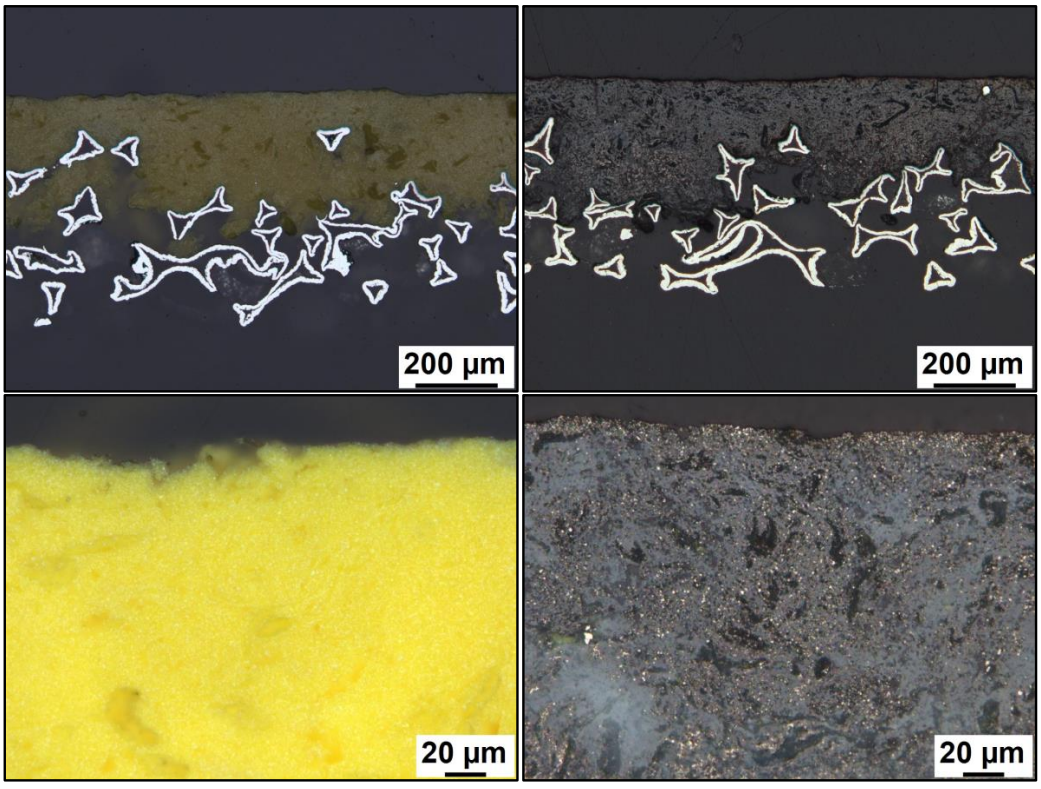

Figure S52: Exemplary cross section of a self-fabricated Bi_2O_3 based GDE (F, cf. Table S3) before (left) and after (right) electrolysis. Details of the fabrication process are provided in section 1.2, details on the electrolysis conditions in section 1.4.

Supporting Information

Coupling of CO_2 Electrolysis with Parallel and Semi-Automated Biopolymer Synthesis – Ex-Cell and without Downstream Processing

I. Dinges, I. Depentori, L. Gans, D. Holtmann, S. R. Waldvogel, M. Stöckl*

Content

1 Experimental procedures and analytical methods

1.1 General Information

Selected chemical compounds and details on employed equipment are listed in this section (cf. Table S1, Table S2). All solutions were prepared using high-purity H_2O (0.055 µS cm^{-1}, 25 °C, PURELAB Ultra).

Table S1: Selected chemical compounds (Purity grade, Supplier, Charge number).

Compound	Purity grade	Supplier	Charge number
KH_2PO_4	> 99 % (p.a.)	Carl Roth GmbH + Co. KG	312327156
K_2HPO_4	> 99 % (p.a.)	Carl Roth GmbH + Co. KG	252322868
$NaH_2PO_4 \cdot 2\ H_2O$	> 99 % (p.a.)	Carl Roth GmbH + Co. KG	053330675
$Na_2HPO_4 \cdot 2\ H_2O$	> 99 % (p.a.)	Carl Roth GmbH + Co. KG	143333521
HCOOK	99 % (p.a.)	Sigma Aldrich	BCBX1022
HCOONa	≥ 99 % (p.a.), ACS	Merck KGaA	A0703243 608
NaCl	≥ 99.5 % (p.a.), ACS, ISO	Carl Roth GmbH + Co. KG	238269100
KCl	≥ 99.5 % (p.a.), ACS, ISO	Carl Roth GmbH + Co. KG	392328190
H_2SO_4	75%, pure	Carl Roth GmbH + Co. KG	262322778
HNO_3	69%, ROTIPURAN Supra	Carl Roth GmbH + Co. KG	1121091
Polyhydroxybutyrate (PHB)	-	Sigma Aldrich	BCBV5095

Table S2: Equipment / device, function and manufacturer.

Equipment / device	Function / use	Manufacturer
PURELAB Ultra	High-purity H_2O	ELGA LabWater, High Wycombe, United Kingdom
A 10 basic	Knife mill	IKA, Staufen, Germany
LaboPress P200S	Heating press	VOGT Labormaschinen GmbH, Berlin, Germany
MicroMahr E 40	Thickness measurement	Mahr GmbH, Göttingen, Germany
Sartorius 1712004	Analytical scale (0.00000 g)	Sartorius Lab Instruments GmbH & Co KG, Göttingen, Germany
Entris 3202I-1S	Scale (0.00 g)	Sartorius Lab Instruments GmbH & Co KG, Göttingen, Germany
NGP804	Power supply	Rohde & Schwarz GmbH & Co. KG, Munich, Germany
CEBO-LC (CESYS C028152)	Analog data logging	CESYS Gesellschaft für angewandte Mikroelektronik mbH, Herzogenaurach, Germany
GMH 3151	Pressure meter	GHM Messtechnik GmbH, Regenstauf, Germany
GMSD 2 BR - K31	Differential pressure sensor	GHM Messtechnik GmbH, Regenstauf, Germany
Transferpette® S	Pipetting, sampling (100-1000 µL, 500-5000 µL, 1000-10000 µL)	BRAND GmbH, Wertheim, Germany
InLab micro	pH electrode coupled with SevenCompact pH/Cond S213	Mettler Toledo, Columbus, USA
SevenCompact pH/Cond S213	pH meter	Mettler Toledo, Columbus, USA
LF 197-S	Conductivity measurement	WTW, Xylem Analytics Germany Sales GmbH & Co. KG, Weilheim, Germany
Sorvall Lynx 6000	Fixed-angle centrifuge, volumes up to 1000 mL	Thermo Fisher Scientific, Waltham, MA USA
MiniSpin plus	Table-top centrifuge, volumes up to 2 mL	Eppendorf SE, Hamburg, Germany
T 6060	Oven	Heraeus Instruments, Hanau, Germany
Thermomixer comfort	Incubator for 1.5 mL and 2.0 mL centrifuge tubes	Eppendorf SE, Hamburg, Germany
Ecotron	Incubation shaker	INFORS HT, Bottmingen, Switzerland

1.2 GDE fabrication

The gas diffusion electrodes (GDE) were fabricated by pressing a Sn-based catalyst mixture onto Ni foam as support material and current collector with a heating press. The catalyst mixture (30.00 g) consisted of Sn (87.5 wt%, 26.25 g, Particle size ≤ 20 µm, Metallpulver24, Sankt Augustin, Germany) and polytetrafluoroethylene (PTFE) powder (12.5 wt%, 3.75 g, Dyneon^{TM} PTFE TF 2072Z, 3M, Saint Paul, USA). The catalyst mixture was homogenised in a knife mill (A 10 basic). The mixing (30s, 25000 rpm) lead to a temperature increase of the mixture (T > 35 °C). After cooling to room temperature, the catalyst mixture (4.00 g) was equally distributed onto Ni foam (d = 1.4 cm, 3.5 cm x 4.0 cm ≙ 14 cm^2, Ni-5763, density 420-450 g m^{-2}, Recemat BV, Dodewaard, Netherlands) with a sieve (Stainless-steel wire mesh, mesh size = 500 µm, ISO 3310-1, Retsch / Verder Scientific, Haan, Germany) and a stencil (Cut-out 3.5 cm x 4.0 cm). The GDE blank was placed in between two pieces of ordinary baking sheet in the heating press (LaboPress P200S) and compressed (plate temperature 120 °C, pressure 10 bar, 60 s). After compressing excess material at the GDE edges was removed with a scalpel. The GDE's catalyst loading *b* was determined by differential weighing (Sartorius 1712004) and its thickness was measured at the centre point (Micromar 40 ER). In total, twelve GDEs were fabricated with a catalyst loading of $b = 103 \pm 5$ mg cm^{-2} and $d = 558 \pm 15$ µm ($n = 12$) for the electrolyses within this study (cf. Table S3).

Table S3: Overview of catalyst mixture loading, Sn loading and thickness of the fabricated GDEs.

GDE	*b* (catalyst mixture) / mg cm^{-2}	*b* (Sn, wt%) / mg cm^{-2}	*d* (GDE, centre point) / µm
(A1)	99	87	532
(A2)	104	91	561
(A3)	101	88	567
(B1)	101	89	557
(B2)	98	85	564
(B3)	103	90	579
(B4)	105	92	568
(B5)	97	85	561
(B6)	111	97	565
(C1)	98	86	528
(C2)	104	91	548
(C3)	110	96	563

1.3 Electrochemical flow reactor and electrolysis set-up

The electrochemical reduction of CO_2 to formate was performed in a custom designed, gas-fed flow reactor (cf. Figure S1). It consisted of three different compartments made from PEEK (polyetheretherketone), one for gaseous CO_2, followed by a catholyte and an anolyte compartment, respectively. The CO_2 compartment (2.0 cm x 2.5 cm x 1 mm, flow field) was separated from the catholyte compartment by the GDE (3.5 cm x 4.0 cm, accessible geometrical surface area 2.0 cm x 2.5 cm ≙ 5 cm^2). Furthermore, it incorporated a flow field for mechanical support of the GDE (cf. Figure S3). The GDE was placed in between two silicone gaskets (thickness 0.5 cm) to prevent fluid leakage and enable application of CO_2 overpressure. The following catholyte compartment frame (thickness 3 mm) had spatial cut-outs to allow equal distribution of catholyte flow and a port to incorporate a reversible hydrogen electrode (RHE, Mini HydroFlex, Gaskatel GmbH, Kassel, Germany) as reference electrode. Catholyte and anolyte compartment were separated by a proton exchange membrane (2.5 cm x 3.0 cm, Nafion™, PFSA 117, DuPont, Wilmington, USA) sealed in between two silicone gaskets (thickness 0.5 cm). The anolyte compartment (2.0 cm x 2.5 cm x 2.0 mm) had spatial cut-outs like the catholyte compartment and contained a titanium mesh coated with Ir mixed oxide as an anode (PLATINODE® EP, 2.0 cm x 2.5 cm, mesh type F, anode type 177, Umicore, Brussels, Belgium). The anode was contacted by titanium wire (⌀ = 0.5 mm, purity ≥ 99.6%, CHEMPUR Feinchemikalien und Forschungsbedarf GmbH, Karlsruhe, Germany) that was welded onto it. The wire was accessible from outside the reactor through a drilling hole in the anolyte compartment frame sealed by silicone (picodent twinsil® A and B, Dental-Produktions- und Vertriebs-GmbH, Wipperfürth, Germany). All three compartments had an in- and outlet each, located on the top and bottom of the compartment frames. The in- and outlets were equipped with PVDF (Polyvinylidene fluoride) adapters (hose nozzle, ⌀ = 4 mm, SERTO AG, Frauenfeld, Switzerland) connecting to the CO_2 supply, as well as the catholyte and anolyte reservoir by tubing (ROTILABO®, Polyvinyl chloride, ⌀ = 2 mm / 4 mm, Carl Roth GmbH + Co. KG). The assembled reactor was enclosed in between two stainless-steel plates (*d* = 8 mm) to ensure an equal distribution of compacting pressure.

The CO_2 was fed into the reactor through a water-filled bubble counter to saturate the CO_2 with water at room temperature (RT). It flowed top-down through the gas compartment to prevent fluid accumulation within. The CO_2 outlet of the reactor's gas compartment was followed by a collecting vessel (500 mL) to catch any electrolyte potentially breaking through the GDE. The CO_2 overpressure was adjusted at the end of the CO_2 line with a regulating valve (SO NV 32A21-6, ⌀ = 6 mm, SERTO AG, Frauenfeld, Switzerland) as well a differential pressure sensor (GMSD 2 BR - K31) combined with a pressure meter (GMH 3151).

Catholyte and anolyte were circulated between the respective reactor compartment and reservoir with a peristaltic pump (ECOLINE VC–MS/CA8-6, ISMATEC, Wertheim, Germany). To prevent gas entrapment and maintain fluid coverage of the electrodes both anolyte and catholyte were passed through the reactor bottom-up.

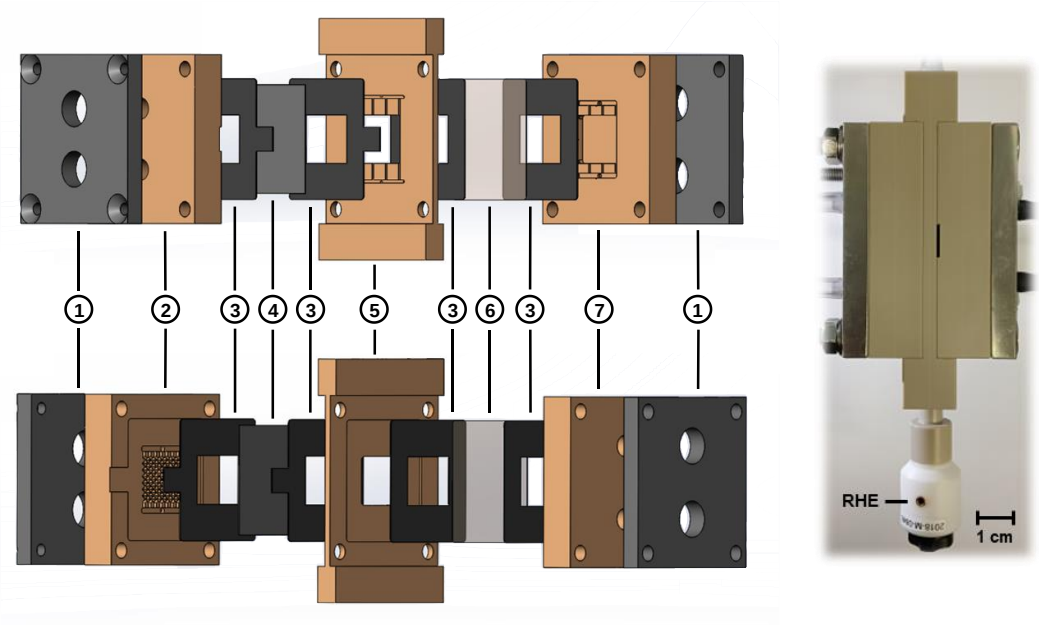

Figure S1: Schematic illustration (left) of the custom designed, gas-fed flow reactor fabricated by the DECHEMA workshop composed of: (1) Stainless-steel plate, (2) CO_2 compartment with flow-field, (3) silicone gasket, (4) GDE (geo. 5 cm^2), (5) catholyte compartment with an RHE port, (6) cation exchange membrane, (7) anolyte compartment (incorporating the anode). Photograph of the assembled flow reactor from the side (right).

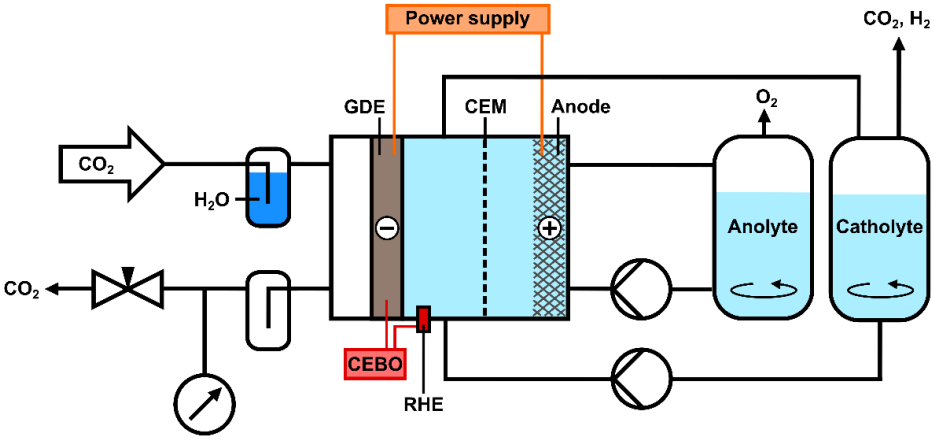

Figure S2: Schematic set-up for the operation of the electrolysis flow reactor (cf. Figure S1) for the electrosynthesis of formate with gaseous CO_2 as starting material. Abbreviations: GDE = Gas diffusion electrode, CEM = Cation exchange membrane and RHE = Reversible hydrogen electrode, CEBO = Data logger.

Figure S3: Photograph of the CO_2 compartment in the electrolysis reactor with an integrated flow-field for mechanical GDE support (cf. Figure S1).

1.4 Formate electrosynthesis

The electrosynthesis of formate using CO_2 was carried out with self-fabricated Sn-based GDEs (cf. section 1.2) in a flow reactor (cf. section 1.3).

All electrosyntheses were performed for 22 h. A power supply unit (NGP804) was employed to run the electrolysis, it recorded terminal voltage (*U*), current (*I*) and power (*P*). Furthermore, the electrode potential of the GDE was referenced to RHE (CEBO-LC). The electrosynthesis started with a current ramp in the first hour, in which the current density (*j*) was increased in steps of 12.5 mA cm^{-2} every 5 min until it reached 150 mA cm^{-2}, which was maintained for the remaining 21 h runtime.

CO_2 (N4.5) was supplied to the GDE at a flow rate of 15 - 20 mL min^{-1} (Float-type flow meter, Wagner Mess- und Regeltechnik GmbH, Offenbach, Germany) and an initial overpressure of approx. 100 mbar relative to ambient pressure. The pressure was recorded continuously during the running electrolysis (CEBO-LC).

Three different phosphate-based buffers were used as electrolyte: (A) 0.2 M KH_2PO_4 / K_2HPO_4 (equimolar), (B) 0.2 M NaH_2PO_4 / K_2HPO_4 (equimolar) and (C) 0.2 M NaH_2PO_4 / Na_2HPO_4 (equimolar). For each electrolysis, anolyte and catholyte had a starting volume of 500 mL (Volumetric flask, ISO 1042). Anolyte and catholyte were circulated continuously at a flow rate of 40 mL min^{-1} between flow reactor compartment and reservoir, respectively. During the electrolysis, catholyte samples (1 mL, Transferpette® S) were taken hourly in the first six (t = 0 - 6 h) and the last four (t = 19 - 22 h) hours to monitor the pH value (InLab Micro, pH-Meter), formate concentration and calculate the corresponding Faradaic efficiency (FE). After electrolysis, the respective anolyte and catholyte volume was determined by its weight (Entris 3202I-1S) and density. Therefore, the density was calculated by taking samples (1 mL, *n* = 3, Transferpette® S) and weighing them (Sartorius 1712004). Catholyte containing

electrochemically generated formate (e-formate) was stored at −20 °C until its application for microbial PHB synthesis. The GDE was rinsed with H_2O and dried at RT.

Detailed information on the experimental parameters and results for all individual formate electrosyntheses are provided in section 3.1.

1.5 Scanning electron microscopy (SEM)

SEM imaging was performed employing Flex SEM 1000 II (cf. Table S4), operated by *FlexSEM1000* (Version 2.3).

Table S4: Conditions for SEM imaging performed on Flex SEM 1000 II (Hitachi, Tokyo, Japan).

Conditions		Conditions	
Operation mode	Composition	Viewing height	6-8 mm
Pressure	High vacuum	Spot size	40
Accelerating voltage	15 kV	Cathode	Tungsten
Magnification	x2000	Detector	Back-scattering electrons (BSE)

Images of the GDEs were taken at the centre point of the geometrical GDE surface (2 cm x 2.5 cm) exposed within the reactor before and after application for formate electrosynthesis. Prior to imaging, the GDEs were cleaned (H_2O bath, 60 mL, 24 h) and dried (RT, 24 h). All SEM images are provided in section 3.3.

1.6 Inductively coupled plasma optical emission spectrometry (ICP-OES)

ICP-OES measurements were performed on Agilent 5800 ICP-OES equipped with an SPS 4 Autosampler, a borosilicate double-pass spray chamber and a Seaspray concentric glass nebulizer (cf. Table S5). The system was operated via *ICP Expert* (Version 7.6.1.12212).

Table S5: ICP-OES measurement conditions performed on Agilent 5800 ICP-OES (Agilent Technologies, Santa Clara, USA).

Conditions		Conditions	
Replicate count	10	Viewing mode	Radial
Pump speed	12 rpm	Viewing height	6 mm
Sample uptake time	25 s	Nebulizer flow	0.7 mL min^{-1}
Stabilization time	15 s	Plasma flow	12 mL min^{-1}
Read time	5 s	Aux Flow	1 mL min^{-1}
Rinse time	30 s	Oxygen content	0%
RF power	1.2 kW	IntelliQuant	Disabled

In between samples, autosampler and measurement system were rinsed with 3 wt% HNO_3 (prepared from 69 wt% HNO_3, Supra Quality, cf. Table S1).

The wavelength for Sn determination was 283.998 nm and the Ar wavelength 420.067 nm served as an internal standard, for which errors less than 5% were accepted. All electrolyte samples had to be diluted by factor 4 to meet the internal standard criterion. In initial qualitative tests, Sn was only detected in catholyte samples, but not in anolyte samples. Therefore, only the catholyte's Sn content was quantified via standard addition of a stock solution containing 1 ppm Sn. The stock solution was prepared from a Sn standard (1000 ppm, Single-Element ICP-Standard-Solution, Lot N. 83131639, Carl Roth GmbH + Co. KG) via a dilution series by factor 10 using volumetric flasks (100 mL, ISO 1042).

For each sample, four different aliquots of stock solution (0.5, 1.0, 1.5, 2 mL, Transferpette® S) were added to the undiluted sample (1 mL, Transferpette® S). The analyte spiked samples were filled up to 4 mL (Transferpette® S) with H_2O, respectively. Hence, five points were measured for each sample to determine the original Sn-content in the undiluted sample with a linear weighted fit. Linear fits with $R^2 \geq 0.995$ were accepted due to the limited available sample volumes and several signals being close to the lower limit of detection (LOD, approx. 0.2 ppm for Sn at 283.998 nm) resulting out of necessary dilution factor.

Table S6: ICP-OES results of the catholyte determined by standard addition (STAD).

Electrolysis	c(Sn) / ppm	m(Sn in catholyte) / mg	R^2 of linear fit (STAD)
(A1)	1.016	0.531	0.999
(A2)	1.212	0.631	0.997
(A3)	0.952	0.498	0.998
(A4)	0.764	0.402	0.996
(A5)	0.912	0.479	0.995
(A6)	1.312	0.684	0.999
(B1)	1.032	0.541	0.999
(B2)	1.040	0.546	0.995
(C1)	3.280	1.741	0.999
(B3)	1.625	0.855	0.996
(C2)	1.828	0.972	0.999
(C3)	2.068	1.096	0.999

1.7 Ion chromatography (IC)

IC measurements were carried out with two different IC units to determine the cation and anion concentrations in the electrolyte samples (cf. Table S7). Both units were operated with *Chromeleon* (Version 7).

Table S7: IC measurement conditions for Na^+, K^+ and PO_4^{3-} analysis performed on two different IC units (Thermo Fisher Scientific Inc., Waltham, USA).

Conditions	Na^+, K^+	PO_4^{3-}
IC Unit	Dionex™ ICS-5000$^+$ DC, ICS-5000$^+$ SP, VWD, AS-AP autosampler	Dionex™ Aquion™ system, AS-DV autosampler
Pre column	Dionex™ IonPac CG17	Dionex™ IonPac™ AS22 IC column (4 x 50 mm)
Column	Dionex™ IonPacTM CS17 (Analytical 2 x 250 mm)	Dionex™ IonPac™ AS22 IC column (4 x 250 mm)
Suppressor	CERS 500 (2 mm)	ACRS 500 Suppressor (4 mm)
Eluent	6 mmol L^{-1} CH_3SO_3H (MSA)	4.5 mmol L^{-1} Na_2CO_3 / 1.4 mmol L^{-1} $NaHCO_3$
Flow rate	0.1 mL min^{-1}	1.2 mL min^{-1}
Method	gradient 1. −5 - 0 min, 1.5 mmol L^{-1} MSA 2. 0 - 25 min, 1.5 - 2.1 mmol L^{-1} MSA 3. 25 - 40 min, 6 mmol L^{-1} MSA 4. 40 - 60 min, 1.5 mmol L^{-1} MSA	isocratic
Injection volume	10 µL	5 mL
Sample dilution factor	200 or 400	200
Detector	Conductivity cell	Conductivity cell
Retention time	Na^+ 29.063 min K^+ 35.137 min	PO_4^{3-} 8.721 min
Duration	60 min	15 min

Standards to determine the concentrations of Na^+ and K^+ were prepared by a dilution series of a stock solution. The stock solution was prepared with NaCl (3.254 g ≙ 1280 ppm Na^+) and

KCl (2.441 g ≙ 1280 ppm K^+) in a volumetric flask (1 L, ISO 1042). The stock solution was first diluted by 10, followed by a dilution series with the dilution factor 2 (cf. Figure S4).

The PO_4^{3-} standards were prepared from an anion multi-element standard (Certipur, Anion multi-element standard I, 1000 ppm F^-, PO_4^{3-}, Br^-, Merck KGaA, HC17168637) by a dilution series (cf. Figure S5).

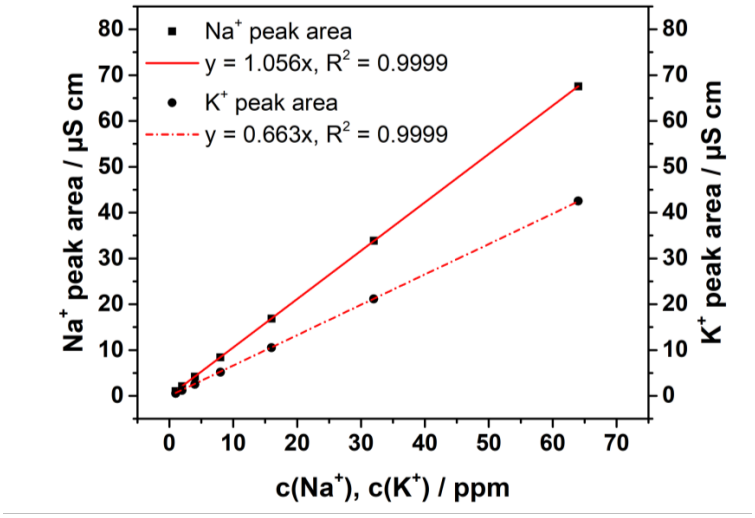

Figure S4: Calibration for Na^+ and K^+ quantification via IC measurement**.** Plot of Na^+ and K^+ concentration (1, 2, 4, 8, 16, 32, 64 ppm) against the peak area of the measured signal (n = 1) with a linear fit forced through zero, respectively.

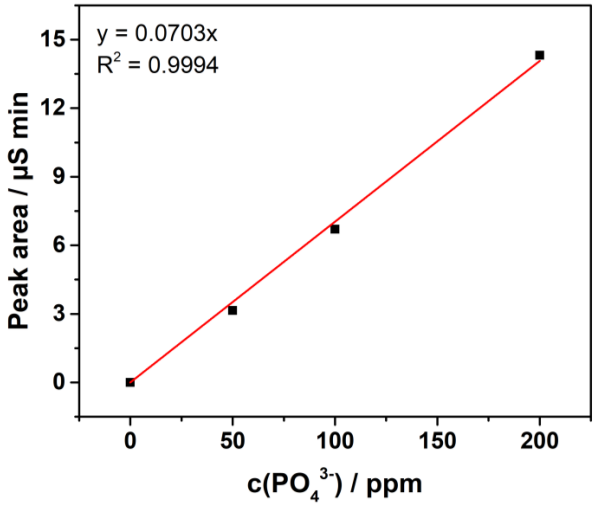

Figure S5: Calibration for PO_4^{3-} quantification via IC measurement**.** Plot of PO_4^{3-} concentration (50, 100, 200 ppm) against the peak area of the measured signal (n = 1) with a linear fit forced through zero.

Table S8: Concentrations of Na^+, K^+ and PO_4^{3-} determined by IC in catholyte and anolyte after electrolysis (22 h, 150 mA cm^{-2}) with different phosphate buffers as electrolytes: (A) 0.2 M KH_2PO_4 / K_2HPO_4, (B) 0.2 M NaH_2PO_4 / K_2HPO_4, (C) 0.2 M NaH_2PO_4 / Na_2HPO_4.

Electrolysis	c(Na^+) / mmol L^{-1}		c(K^+) / mmol L^{-1}		c(PO_4^{3-}) / mmol L^{-1}	
	Catholyte	Anolyte	Catholyte	Anolyte	Catholyte	Anolyte
(A)[a]	3.0	3.0	289.3	289.3	196.5	196.5
(A1)	5.2	0.5	533.1	4.7	183.1	208.5
(A2)	5.3	0.6	534.4	5.8	184.8	207.8
(A3)	5.9	0.6	536.6	6.0	184.9	207.8
(B)[a]	102.2	102.0	192.1	192.1	196.6	196.6
(B1)	187.5	4.8	355.9	3.8	182.9	208.8
(B2)	187.4	4.8	352.8	4.0	185.1	209.8
(B3)	188.1	5.3	359.2	4.3	183.4	207.6
(B4)	188.3	5.4	355.3	5.0	184.1	210.8
(B5)	185.5	6.5	355.3	4.2	183.1	210.6
(B6)	186.1	8.8	350.1	5.0	181.7	208.3
(C)[a]	297.2	297.2	1.4	1.4	196.0	196.0
(C1)	536.2	7.9	1.6	1.3	181.7	211.2
(C2)	538.1	8.9	2.7	1.4	183.2	210.3
(C3)	534.9	9.8	3.1	2.6	180.5	214.0

[a] The phosphate buffers serving as electrolyte were measured prior to electrolysis for comparison.

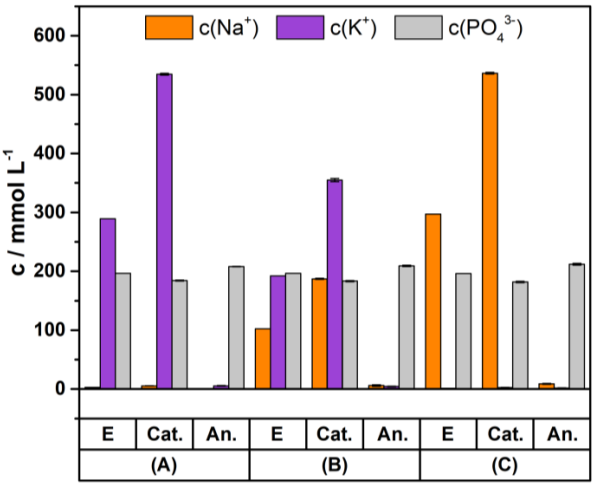

Figure S6: IC results for c(Na^+, orange), c(K^+, purple) and c(PO_4^{3-}, grey) in the electrolyte before electrolysis (E) as well as in both catholyte (Cat.) and anolyte (An.) after 22 h electrolysis with different phosphate buffers as starting electrolytes: (A) 0.2 M KH_2PO_4 / K_2HPO_4 (n = 3), (B) 0.2 M NaH_2PO_4 / K_2HPO_4 (n = 6) and (C) 0.2 M NaH_2PO_4 / Na_2HPO_4 (n = 3).

1.8 Gas chromatography (GC)

Gas analysis was performed with an Agilent 490 micro-GC (Agilent Technologies Deutschland GmbH, Waldbronn, Germany) operated with the software *Agilent OpenLab CDS* (Version A04.07). The system contained three column units to analyse different analytes (cf. Table S9).

Table S9: GC column units for gas sample analysis performed on Agilent 490 micro-GC (Agilent Technologies Deutschland GmbH, Waldbronn, Germany).

Conditions	Channel 1	Channel 2	Channel 3
Pre column	PoraPLOT U	PoraPLOT U	PoraPLOT U
Main column	Molsieve 5Å	Molsieve 5Å	PoraPLOT U
Carrier gas	Argon (N5.0)	Helium (N5.0)	Helium (N5.0)
Analyte	H_2	O_2, N_2	CO_2

All analytes were detected with a thermal conductivity detector (TCD), the sample injection temperature was 100 °C and the columns were kept at 60 °C. The sampling time was 30 s and the runtime 3 min. All column units were heated to 180 °C for at least 18 h prior to measurements to remove accumulated H_2O.

The micro-GC was calibrated for H_2 (retention time = 0.51 min) using pure H_2 (N5.0) as well as an H_2 / CO_2 mixture (80:20, 20.21 ± 0.40, relative error 2%, Air Liquide).

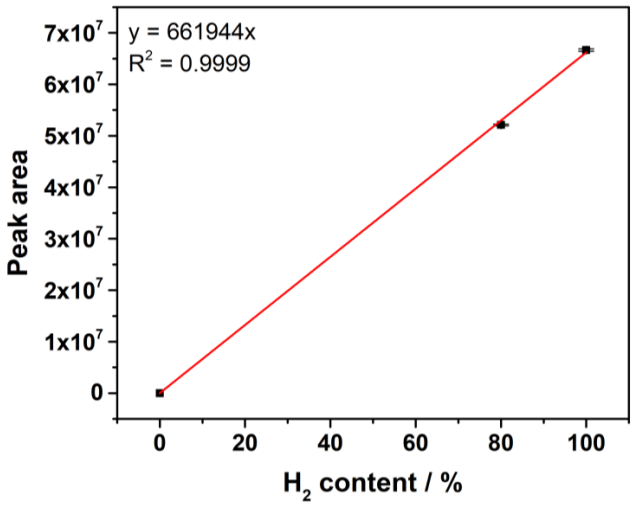

Figure S7: Calibration for H_2 quantification via GC measurement**.** Plot of H_2 content (0, 80, 100%) against the peak area of the measured signal (n = 3) with a linear fit forced through zero.

The gas samples (approx. 50 mL in 5 min) were collected in the last hour of the electrolysis (t = 21 h) to identify side products of the formate electrosynthesis at the exhaust of the catholyte reservoir (where gas mainly bubbled through, cf. Figure S2).

Table S10: GC results for H_2 quantification during formate electrosynthesis (t = 21 h).

Electrolysis	H_2 content / %
(A1)	3.67 ± 0.03
(A2)	5.65 ± 0.04
(A3)	4.76 ± 0.03
(A4)	6.06 ± 0.04
(A5)	3.96 ± 0.03
(A6)	8.23 ± 0.06
(B1)	4.74 ± 0.03
(B2)	3.70 ± 0.03
(C1)	7.63 ± 0.05
(B3)	4.52 ± 0.03
(C2)	6.81 ± 0.05
(C3)	2.95 ± 0.02

1.9 High-performance liquid chromatography (HPLC)

The quantification of formate and PHB was carried out via HPLC (cf. Table S11), the system was operated with the software *LabSolutions* (Version 5.93).

Table S11: HPLC measurement conditions for formate and PHB analysis performed on an HPLC unit (LC-20AD, SIL-20AC HT, CBM-20A, CTO-20AC, SPD-M20A - Shimadzu, Kyoto, Japan).

Conditions	Formate	PHB (Analyte: Crotonic acid)
Eluent	5 mmol L^{-1} H_2SO_4	5 mmol L^{-1} H_2SO_4
Flow rate	0.6 mL min^{-1}	0.6 mL min^{-1}
Pressure	30 ± 1	27 ± 1
Column oven	35 °C	40 °C
Column	Rezex ROA- Organic Acid (8%), 300 mm × 7.8 mm Phenomenex, California, USA	Rezex ROA- Organic Acid (8%), 300 mm × 7.8 mm Phenomenex, California, USA
Injection volume	10 µL	10 µL
Detector	Photodiode array (PDA)	Photodiode array (PDA)
Wavelength λ	194 nm	207 nm
Retention time	15.3 min	29.2 min
Duration	25 min	40 min

Formate standards were prepared by a dilution series from a stock solution. The stock solution was prepared with HCOONa (3.482 g, 51.2 mmol) in a volumetric flask (100 mL, ISO 1042).

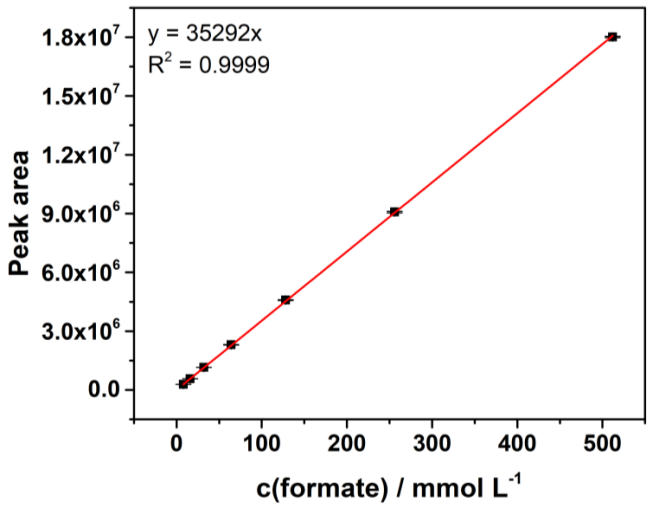

Figure S8: Calibration for formate quantification via HPLC measurement**.** Plot of formate concentration (8, 16, 32, 64, 128, 256, 512 mmol L^{-1}) against the peak area of the measured signal (n = 3) with a linear fit forced through zero.

PHB was depolymerised to its monomer unit crotonic acid for quantitative analysis. Therefore, sample preparation was conducted as follows: Samples were taken from the cultivation broth (10 or 30 mL, depending on the available volume, respectively). They were centrifuged (6000 x g, 30 min, Sorvall Lynx 6000) and the supernatant was discarded. The cell pellet was carefully resuspended in 1 mL H_2O. The resulting cell suspension was transferred completely into a 2 mL-centrifuge tube and centrifuged (14100 x g, 5 min, MiniSpin plus). The supernatant was discarded and the cell pellet was dried overnight (100 °C, T 6060). The dried cell pellet was mixed with 1 mL of concentrated H_2SO_4 and incubated (99 °C, 500 rpm, 60 min, Thermomixer comfort). The resulting solution was diluted 1:50 with H_2O and subsequently used for HPLC analysis.

PHB standards were prepared by a dilution series from a stock solution. For the preparation of the stock solution, PHB (7.45 mg) was weighed (Sartorius 1712004) in a 2 mL centrifuge tube. The PHB was depolymerised in the same manner as described for the dried cell pellets above. Hence, the PHB was mixed with 1 mL of concentrated H_2SO_4, incubated (99 °C, 500 rpm, 60 min) and afterwards diluted 1:50 with H_2O. The reliability of the obtained calibration curve was verified by preparing an independent PHB standard (5.20 mg, Sartorius 1712004), which was diluted to a calculated amount of 1000 µg. Using the calibration curve obtained from the dilution series of the stock solution, the quantification of this verification standard showed an amount of 1022.27 µg which corresponded to a deviation of 2%.

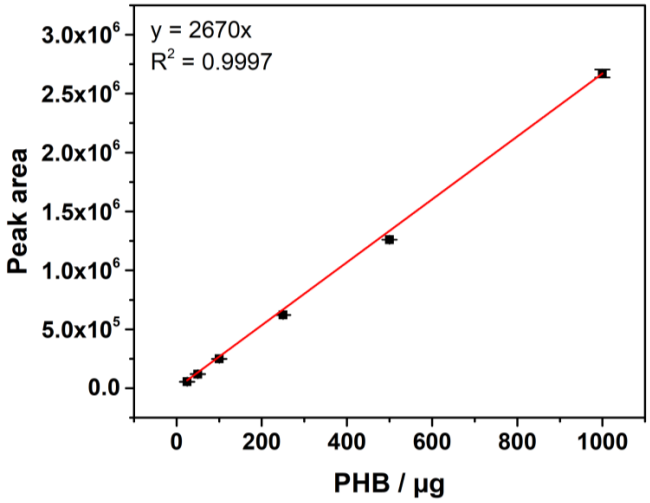

Figure S9: Calibration for PHB quantification via HPLC measurement**.** Plot of PHB content (25, 50, 100, 250, 500, 1000 µg) against the peak area of the measured signal (*n* = 3) with a linear fit forced through zero.

1.10 Microbial PHB synthesis

1.10.1 Microorganisms

The bioconversion of formate was demonstrated with *Cupriavidus necator* (*C. necator*) wildtype (DSM-428, DSMZ, Braunschweig, Germany) as model organism, which produces PHB from formate under NH_4^+ limitation.

1.10.2 Cultivation and incubation media

The cultivation and incubation of *C. necator* was carried out with the different growth media listed below.

Lysogeny broth (LB):

Yeast extract (5 g L^{-1}), tryptone (10 g L^{-1}) and NaCl (5 g L^{-1}) in H_2O, the pH value was set to 7.0 with NaOH (2 M) and HCl (2 M).

Minimal medium adapted from Sydow et al. [36] with commercially available formate:

HCOONa (6.801 g L^{-1}), Na_2HPO_4 (2.895 g L^{-1}), $NaH_2PO_4 \cdot 2\ H_2O$ (3.980 g L^{-1}), K_2SO_4 (0.171 g L^{-1}), $MgSO_4 \cdot H_2O$ (0.390 g L^{-1}), $(NH_4)_2SO_4$ (0.980 g L^{-1}), $CaSO_4 \cdot 2\ H_2O$ (0.097 g L^{-1}) and trace element solution (350 µL L^{-1}).

All media components were prepared sterile as separate stock solutions and combined prior to each experiment. The pH value was set to 7.0 with sterile H_2SO_4 (2 M) and NaOH (2 M).

Trace element solution:

$FeSO_4 \cdot 7\ H_2O$ (15.00 g L^{-1}), $MnSO_4 \cdot H_2O$ (1.46 g L^{-1}), $ZnSO_4 \cdot 7\ H_2O$ (2.40 g L^{-1}), $CuSO_4 \cdot 5\ H_2O$ (0.48 g L^{-1}), $Na_2MoO_4 \cdot 2\ H_2O$ (1.80 g L^{-1}), $NiSO_4 \cdot 6\ H_2O$ (1.50 g L^{-1}), $CoSO_4 \cdot 7\ H_2O$ (0.04 g L^{-1}) dissolved in 0.1 M HCl.

Minimal medium with electrochemically produced formate (e-formate):

The calculated volume of the catholyte (depending on the e-formate concentration) for 100 mmol L^{-1} e-formate was mixed with the ingredients of the minimal medium described above, except for HCOONa, Na_2HPO_4 and NaH_2PO_4, which were not added in this case.

Formate-containing buffer for resting cells:

The phosphate buffer was either (A) 0.2 M KH_2PO_4 / K_2HPO_4, (B) 0.2 M NaH_2PO_4 / K_2HPO_4, 0.2 M KH_2PO_4 / Na_2HPO_4 or (C) 0.2 M NaH_2PO_4 / Na_2HPO_4 depending on the incubation experiment. The different formate concentrations were adjusted with either commercially available formate (HCOONa or HCOOK) or e-formate feedstock originating from electrosynthesis.

1.10.3 Cultivation and incubation of *C. necator*

All experiments were conducted using a first preculture raised in LB and a second preculture raised in minimal medium before the main incubation in formate-containing buffer. All cultivations were carried out at 30 °C. All shake flask and test tube cultivations were shaken at 180 rpm (shaking diameter of 25 mm, Ecotron). The second precultures (in minimal medium) were conducted in shake flasks of varying sizes depending on the required volume for the main incubation with filling volumes of 25% of the nominal volume. All samples taken during the incubation were frozen at −20 °C until further analysis.

One or several *C. necator* precultures (depending on the required volume for further cultivation steps) were raised from a cryo stock in 5 mL LB in test tubes. After 22 - 24 h of cultivation, cells were harvested by centrifugation (5 min, 5000 x g, Sorvall Lynx 6000), washed with fresh minimal medium, centrifuged again (5 min, 5000 x g, Sorvall Lynx 6000), resuspended and added to the required volume of prepared minimal medium to reach a starting OD_{600} of 0.05. After 24 h the second precultures were harvested by centrifugation (7 min, 5000 x g, Sorvall Lynx 6000), washed with fresh sterilized buffer, centrifuged again (7 min, 5000 x g, Sorvall Lynx 6000) and used for inoculation of the main incubation of resting cells in formate-containing buffer.

Shake flask incubation:

Incubation of resting cells in buffer (A) 0.2 M KH_2PO_4 / K_2HPO_4, (B) 0.2 M NaH_2PO_4 / K_2HPO_4 or (C) 0.2 M NaH_2PO_4 / Na_2HPO_4 with different formate concentrations were performed in 300 mL shaking flasks with a filling volume of 75 mL. Main cultures were inoculated with the calculated cell amount for an initial OD_{600} of 0.2, whereby the actual initial OD could slightly deviate. All incubation conditions were run in triplicates.

PHB synthesis in semi-automated parallelised bioreactors:

The main PHB syntheses in semi-automated bioreactors were performed in the DASGIP® Parallel Bioreactor System (DASGIP AG, Jülich, Germany, Modules: Gas supply system = MX4/4, Temperature control system / Speed control system = TC4/SC4, Multipump module = MP8, Sensor amplifier = PH4PO4, DO-Sensor = InPro6820/12/220 from Mettler Toledo, pH electrode = 405-DPAS-SC-K8 S/225 from Mettler Toledo, PTFE air filter = Midisart® 2000 from Sartorius) in quadruplets. The initial incubation volume was 340 mL of buffer (B) 0.2 M NaH_2PO_4 / K_2HPO_4, the initial OD_{600} was 1.80. The stirring frequency was set to 800 rpm, the pH value was measured and when reaching values above 7.2 regulated by automated adding of H_2SO_4 (1 M). All bioreactors were gassed with 6 sl min^{-1} compressed air. The initial feed of the catholyte containing 441 mmol L^{-1} e-formate was regulated to 6.9 mL h^{-1}. Samples (1 mL) for formate analysis by HPLC were taken every 30 min for all bioreactors.

However, only samples of reactor 1 and 4 at 0.5 h, 1.5 h, 2.5 h, 3.5 h, 4.5 h, 5.5 h and 6.5 h of the incubation duration were analysed instantly to adjust the catholyte feed. At 0 h, 2 h, 4 h, 6 h and 7.5 h samples for PHB analysis were taken (10 mL). PHB was determined in duplicates from each sample (2 x 5 mL).

2 Calculations

2.1 Faradaic efficiency (FE)

The FE for formate was calculated based on the determined amount of electrosynthesised formate using equation (1).

$$FE = \frac{F \cdot z \cdot n}{I \cdot t} \quad (1)$$

With FE = Faradaic efficiency of formate electrosynthesis / %, F = Faraday constant / A s mol^{-1}, z = Number of transferred electrons (z = 2), n = Amount of synthesised formate / mol, I = Current / A, t = Electrolysis runtime / s.

The results for each different phosphate-based electrolyte were averaged and their standard deviation was provided as uncertainty.

2.2 PHB yield

The PHB yield was calculated based on the determined amount of PHB using equation (2), (3) and (4)[39].

$$PHB\ yield = \frac{m(PHB)}{m(PHB, theo)} \cdot 100\ \% \quad (2)$$

With $PHB\ Yield$ = Yield of the microbial PHB synthesis based on e-formate, $m(PHB)$ = Mass of synthesised PHB / mg, $m(PHB, theo)$ = Theoretical mass of PHB at quantitative conversion of the consumed formate according to *C. necator's* metabolism[39] / mg.

$$m(PHB, theo) = M(CA) \cdot \frac{n(con.\ formate)}{33} \quad (3)$$

With $m(PHB, theo)$ = Theoretical mass of PHB at quantitative conversion of the consumed formate according to *C. necator's* metabolism[39] / mg, $M(CA)$ = 86.09 g mol^{-1} (crotonic acid), $n(con.\ formate)$ = total amount of formate consumed in the bioreactor / mol.

$$33\ HCOOH + 12\ O_2 \rightarrow C_4H_6O_2 + 30\ H_2O + 29\ CO_2 \quad (4)$$

The results for each different bioreactor were averaged and their standard deviation was provided as uncertainty.

2.3 Overall process yield

The overall process yield (OPY) was calculated based on the yields of the two subprocesses using equation (5) and (6).

$$OPY = FE \cdot PHB\ Yield \cdot 100\ \% \quad (5)$$

$$\Delta(OPY) = \sqrt{(PHB\ Yield)^2 \cdot (\Delta FE)^2 + (FE)^2 \cdot (\Delta PHB\ Yield)^2} \cdot 100\% \quad (6)$$

With OPY = Overall process yield, $\Delta(OPY)$ = Uncertainty of the overall process yield, FE = Faradaic efficiency of formate electrosynthesis / %, ΔFE = Standard deviation of the formate synthesis (n = 6) / %, $PHB\ Yield$ = Yield of the microbial PHB synthesis based on e-formate / %, $\Delta PHB\ Yield$ = Standard deviation of the PHB yield (n = 4) / %. All variables in equation (5) and (6) were divided by 100% prior to implementation for OPY and $\Delta(OPY)$ calculation.

3 Supporting results

3.1 Formate electrosynthesis

The operational electrolysis parameters with the three phosphate-based electrolytes have been summarised in Table S12, further electrolysis results have been collected in Table S13. Moreover, detailed courses of each individual electrolysis are provided in section 3.1.1, 3.1.2 and 3.1.3, respectively. GDE photographs are provided in section 3.2, which is followed by SEM images of the self-fabricated GDEs before and after electrolysis in section 3.3.

Table S12: Overview of operational electrolysis parameters with different phosphate buffers as electrolytes: (A) 0.2 M KH_2PO_4 / K_2HPO_4, (B) 0.2 M NaH_2PO_4 / K_2HPO_4, (C) 0.2 M NaH_2PO_4 / Na_2HPO_4. All values are given as average with standard deviation for the 22 h electrolysis duration, excluding the absolute electric energy consumption (EEC).

Electrolysis	OCP vs. RHE / V	$E(GDE)$ vs. RHE / V	U / V	EEC / Wh	$p(CO_2)$ / mbar
(A1)	0.92 ± 0.02	−1.59 ± 0.14	6.6 ± 0.5	107.0	242 ± 63
(A2)	0.82 ± 0.04	−1.88 ± 0.17	6.3 ± 0.6	101.7	361 ± 50
(A3)	0.38 ± 0.03	−1.90 ± 0.16	6.3 ± 0.5	102.1	282 ± 44
(B1)	0.76 ± 0.02	−1.65 ± 0.17	6.6 ± 0.6	106.9	293 ± 24
(B2)	0.63 ± 0.03	−1.72 ± 0.15	6.5 ± 0.6	106.3	396 ± 24
(B3)	0.56 ± 0.02	−1.69 ± 0.21	6.8 ± 0.6	110.2	278 ± 47
(B4)	0.27 ± 0.03	−1.81 ± 0.30	6.7 ± 0.6	108.9	354 ± 54
(B5)	0.52 ± 0.02	−1.78 ± 0.18	7.3 ± 0.7	117.6	211 ± 33
(B6)	0.48 ± 0.03	−1.80 ± 0.14	6.6 ± 0.5	107.4	461 ± 75
(C1)	0.47 ± 0.02	−1.68 ± 0.22	7.7 ± 0.6	125.2	128 ± 25
(C2)	0.67 ± 0.02	−1.95 ± 0.19	7.5 ± 0.6	122.4	179 ± 18
(C3)	0.52 ± 0.03	−1.94 ± 0.23	7.4 ± 0.7	120.1	281 ± 23

Table S13: Overview of electrolyte volume, formate concentration, formate FE and pH value determined *n* = 3 after 22 h electrolysis for catholyte and anolyte with different phosphate buffers as electrolytes: (A) 0.2 M KH_2PO_4 / K_2HPO_4, (B) 0.2 M NaH_2PO_4 / K_2HPO_4, (C) 0.2 M NaH_2PO_4 / Na_2HPO_4.

	Catholyte				Anolyte			
Electrolysis	V / mL	c(formate) / mmol L^{-1}	FE(formate) / %	pH value	V / mL	c(formate) / mmol L^{-1}	FE(formate) / %	pH value
(A1)	524.2 ± 0.5	450.5 ± 0.08	78.3 ± 0.6	4.17 ± 0.05	463.0 ± 0.8	2.21 ± 0.03	0.339 ± 0.005	1.19 ± 0.05
(A2)	524.7 ± 0.5	467.2 ± 0.03	81.3 ± 0.7	4.07 ± 0.05	463.8 ± 0.2	2.39 ± 0.03	0.368 ± 0.004	1.15 ± 0.05
(A3)	525.9 ± 0.5	457.6 ± 0.1	79.8 ± 0.6	4.11 ± 0.05	463.2 ± 0.2	2.20 ± 0.02	0.337 ± 0.002	1.15 ± 0.05
(B1)	522.6 ± 1.6	449.8 ± 0.9	78.0 ± 0.4	4.16 ± 0.05	461.2 ± 0.2	2.39 ± 0.02	0.366 ± 0.002	1.20 ± 0.05
(B2)	520.4 ± 0.5	453.44 ± 0.09	78.3 ± 0.1	4.14 ± 0.05	460.9 ± 0.3	2.36 ± 0.03	0.361 ± 0.004	1.26 ± 0.05
(B3)	522.6 ± 0.9	441.4 ± 0.2	76.5 ± 0.2	4.17 ± 0.05	461.5 ± 0.3	2.21 ± 0.04	0.338 ± 0.005	1.21 ± 0.05
(B4)	525.5 ± 0.4	428.0 ± 0.1	74.64 ± 0.04	4.25 ± 0.05	461.4 ± 0.3	2.16 ± 0.02	0.331 ± 0.003	1.25 ± 0.05
(B5)	525.4 ± 0.7	441.5 ± 1.0	77.0 ± 0.2	4.15 ± 0.05	460.4 ± 0.7	2.35 ± 0.03	0.359 ± 0.003	1.23 ± 0.05
(B6)	521.4 ± 0.5	434.4 ± 0.4	75.15 ± 0.06	4.20 ± 0.05	460.9 ± 0.1	2.17 ± 0.06	0.331 ± 0.008	1.28 ± 0.05
(C1)	530.7 ± 1.0	343.1 ± 0.2	60.4 ± 0.2	5.35 ± 0.05	455.5 ± 0.4	2.34 ± 0.01	0.354 ± 0.002	1.17 ± 0.05
(C2)	531.6 ± 1.2	368.6 ± 0.2	65.0 ± 0.2	4.72 ± 0.05	457.3 ± 0.4	2.12 ± 0.02	0.322 ± 0.003	1.18 ± 0.05
(C3)	530.2 ± 0.2	362.5 ± 0.3	63.77 ± 0.04	4.84 ± 0.05	458.5 ± 0.4	2.18 ± 0.01	0.331 ± 0.001	1.17 ± 0.05

3.1.1 Electrolyte (A) 0.2 M KH_2PO_4 / K_2HPO_4

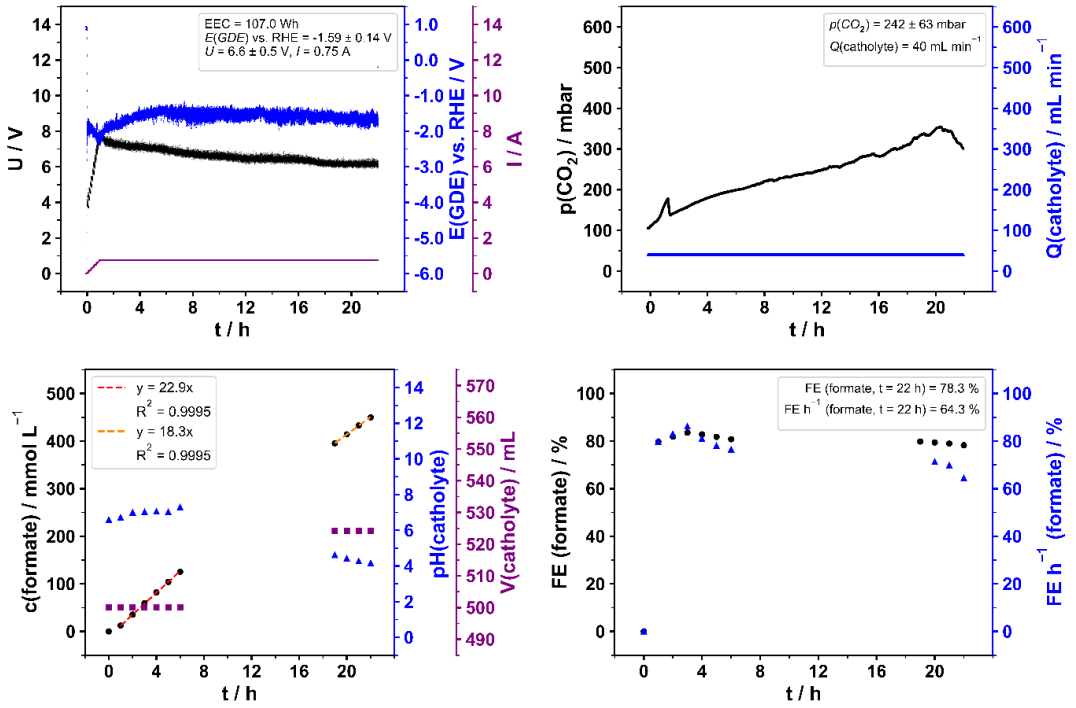

Figure S10: Supporting data for Electrolysis (A1), experimental details are provided in section 1.4 and results in Table S12 and Table S13.

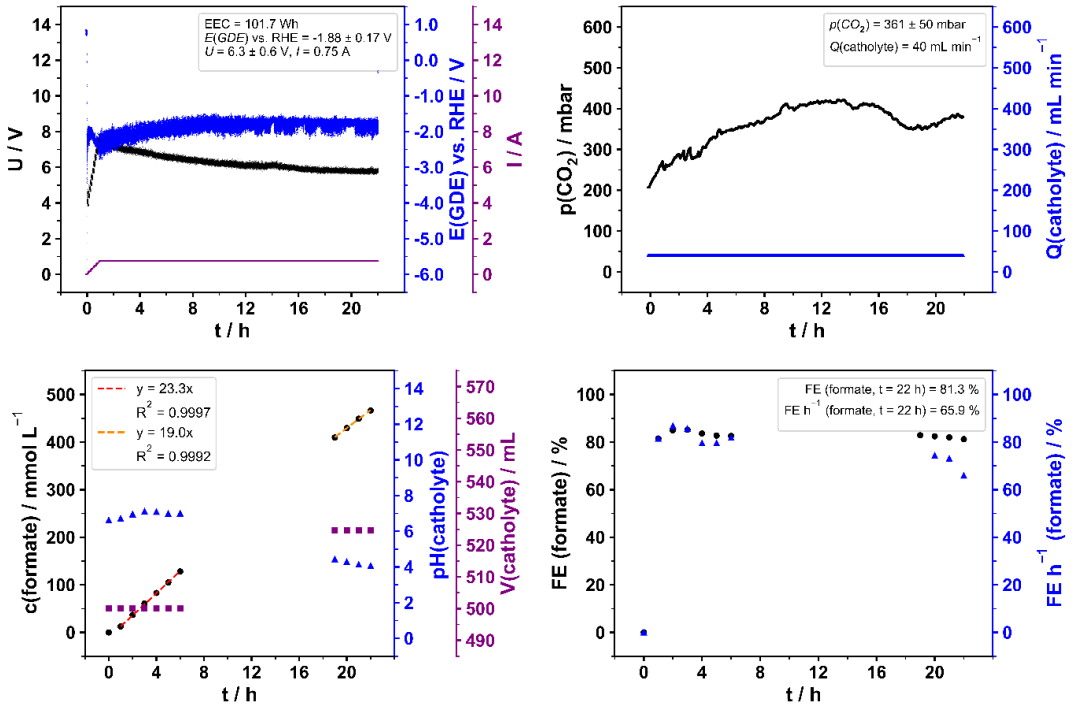

Figure S11: Supporting data for Electrolysis (A2), experimental details are provided in section 1.4 and results in Table S12 and Table S13.

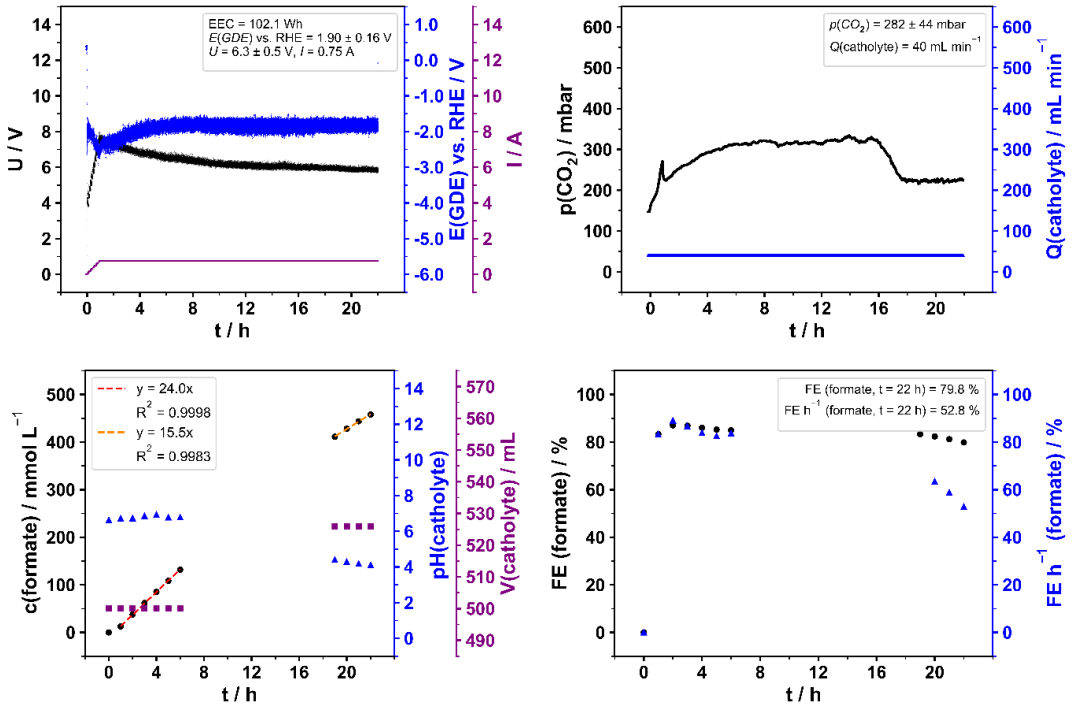

Figure S12: Supporting data for Electrolysis (A3), experimental details are provided in section 1.4 and results in Table S12 and Table S13.

3.1.2 Electrolyte (B) 0.2 M NaH_2PO_4 / K_2HPO_4

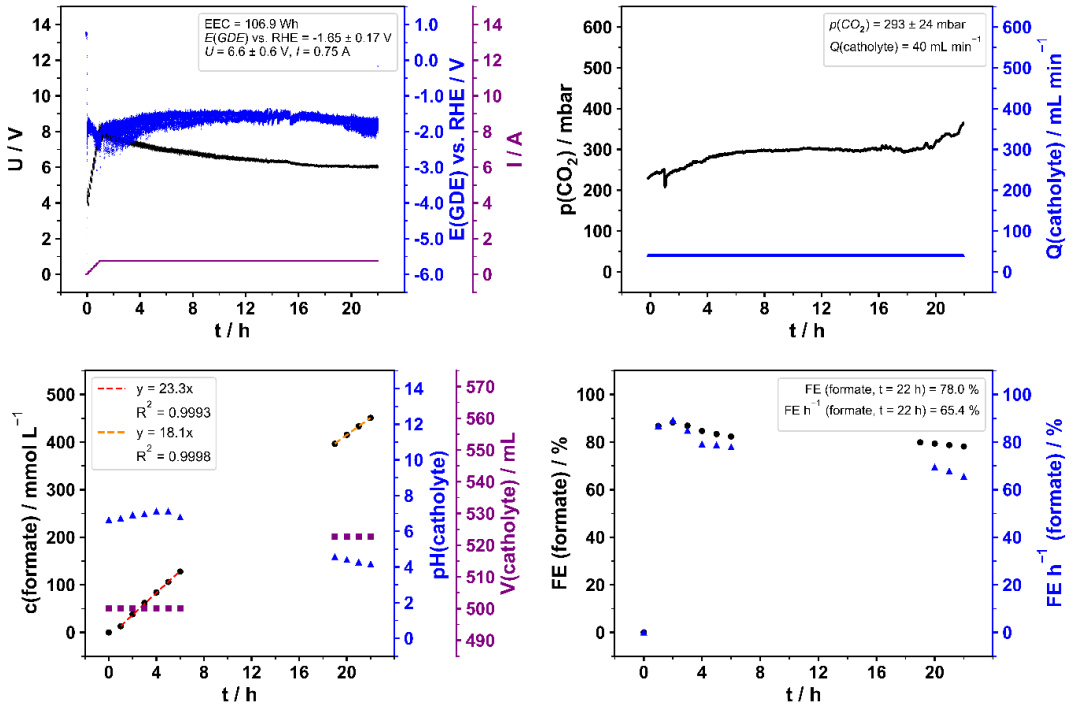

Figure S13: Supporting data for Electrolysis (B1), experimental details are provided in section 1.4 and results in Table S12 and Table S13.

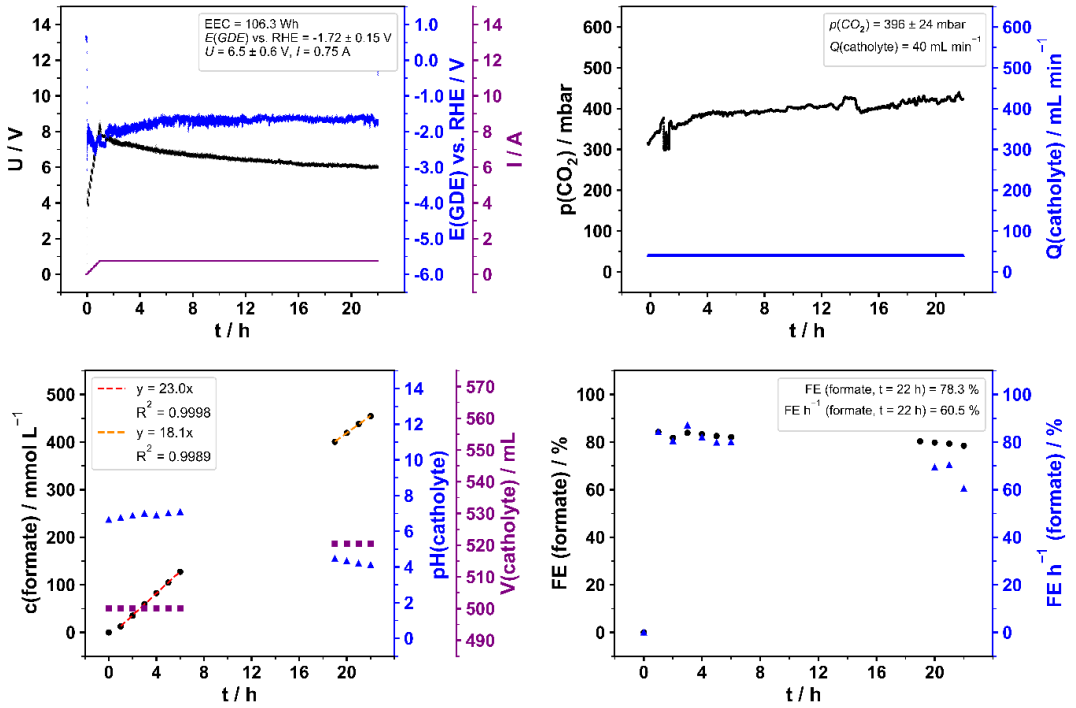

Figure S14: Supporting data for Electrolysis (B2), experimental details are provided in section 1.4 and results in Table S12 and Table S13.

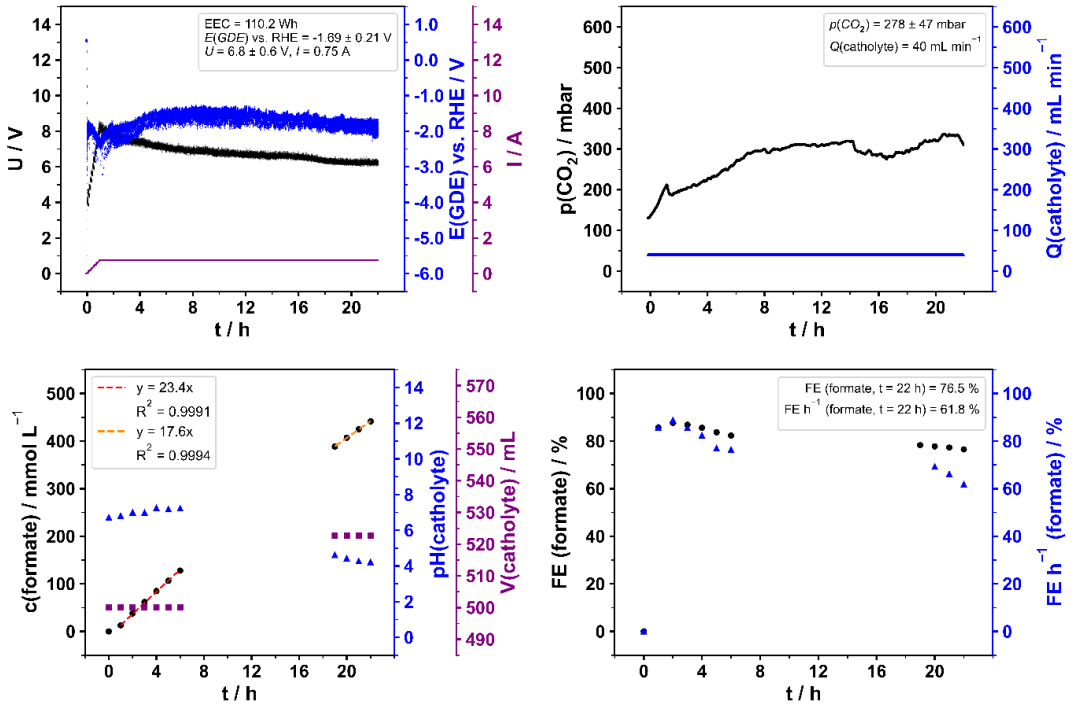

Figure S15: Supporting data for Electrolysis (B3), experimental details are provided in section 1.4 and results in Table S12 and Table S13.

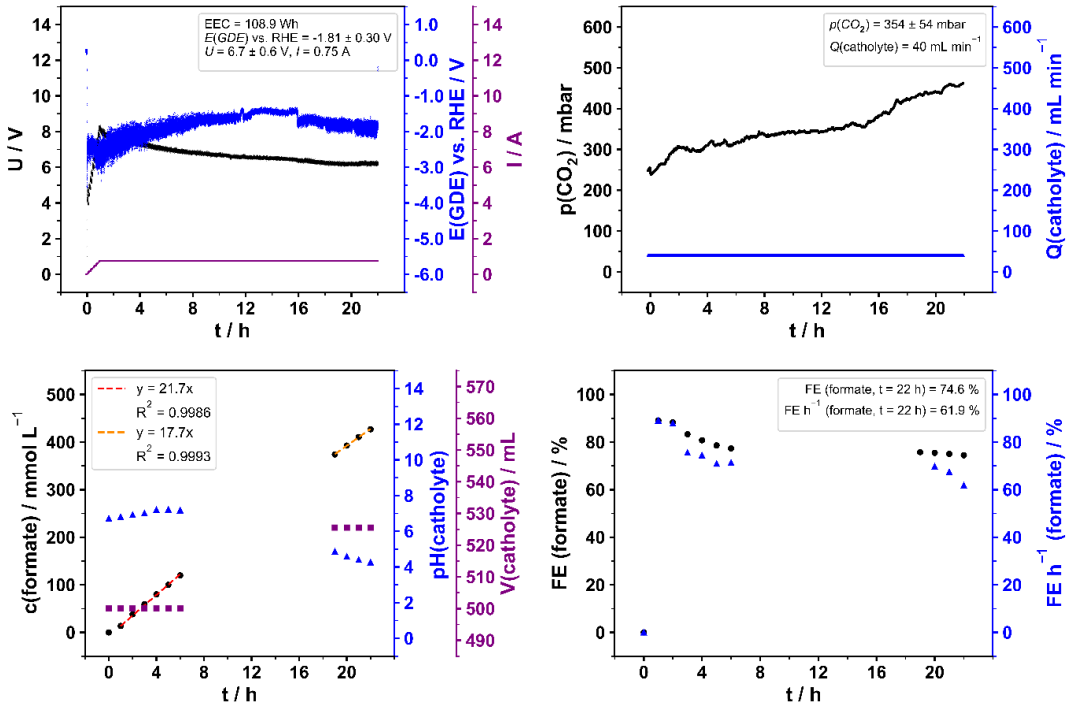

Figure S16: Supporting data for Electrolysis (B4), experimental details are provided in section 1.4 and results in Table S12 and Table S13.

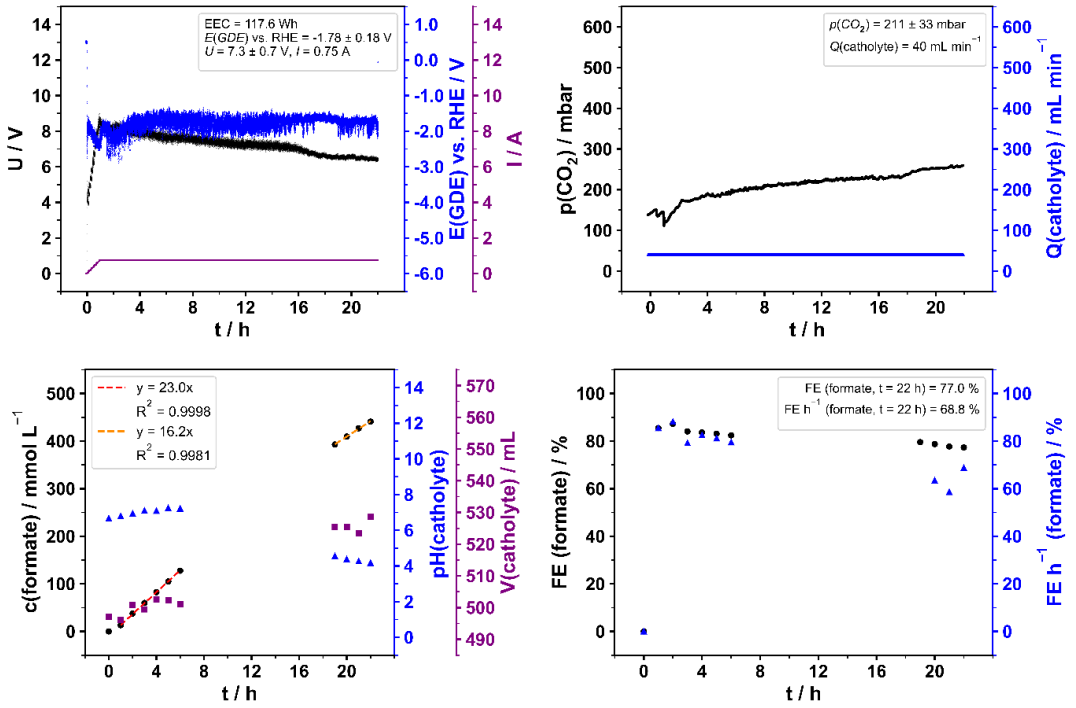

Figure S17: Supporting data for Electrolysis (B5), experimental details are provided in section 1.4 and results in Table S12 and Table S13.

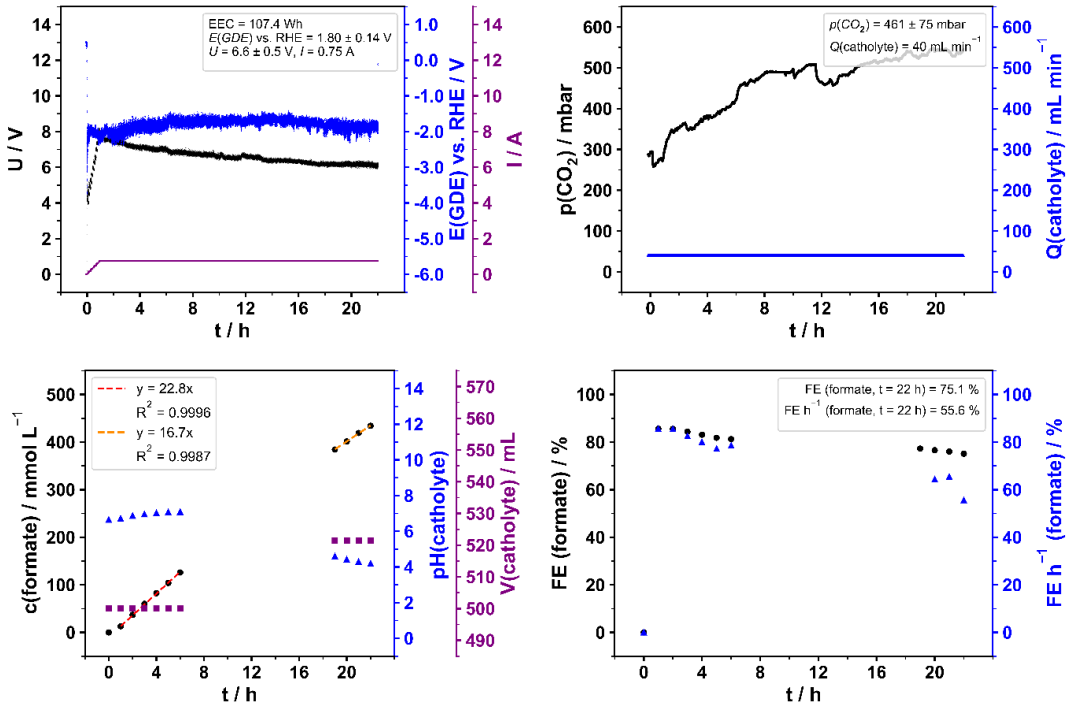

Figure S18: Supporting data for Electrolysis (B6), experimental details are provided in section 1.4 and results in Table S12 and Table S13.

3.1.3 Electrolyte (C) 0.2 M NaH_2PO_4 / Na_2HPO_4

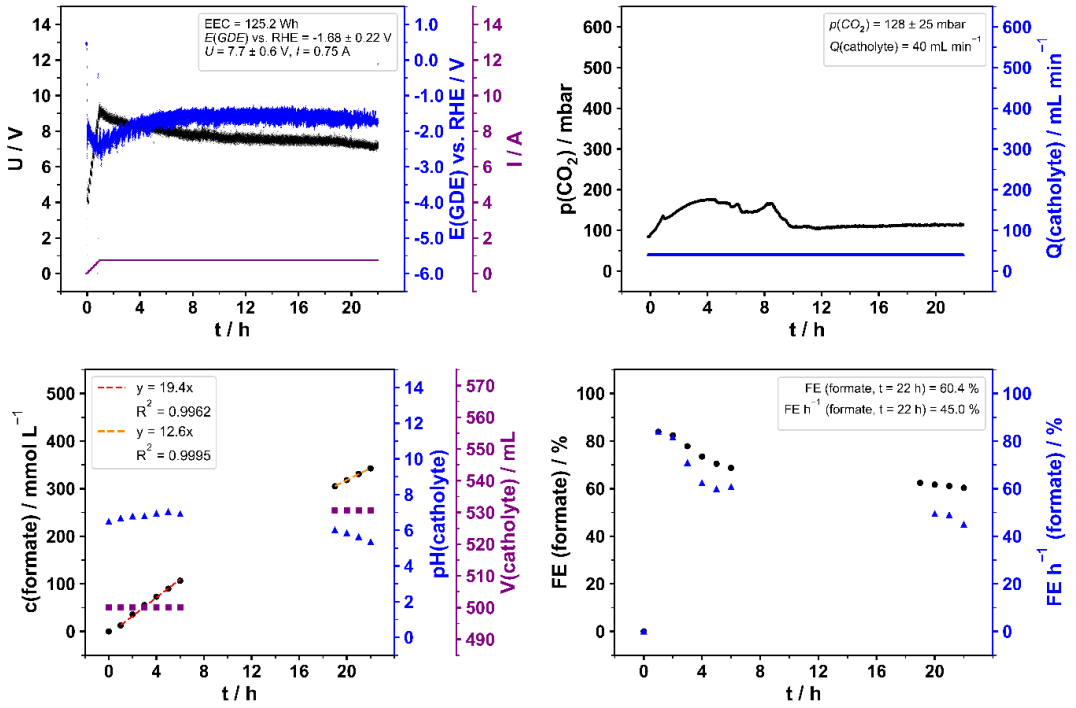

Figure S19: Supporting data for Electrolysis (C1), experimental details are provided in section 1.4 and results in Table S12 and Table S13.

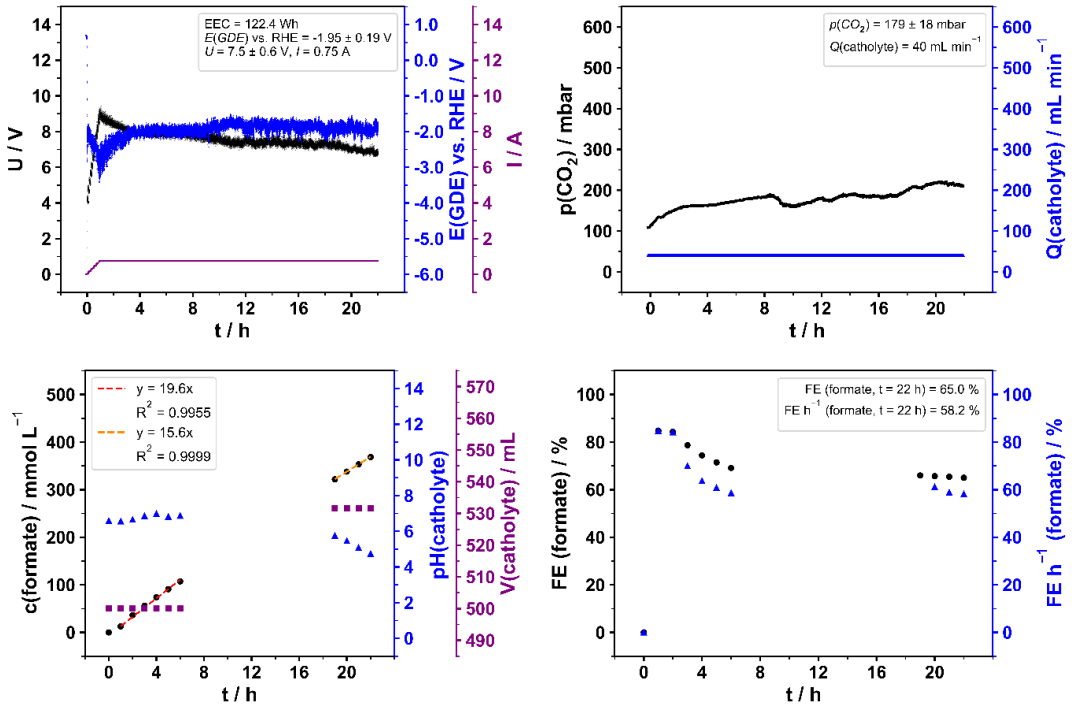

Figure S20: Supporting data for Electrolysis (C2), experimental details are provided in section 1.4 and results in Table S12 and Table S13.

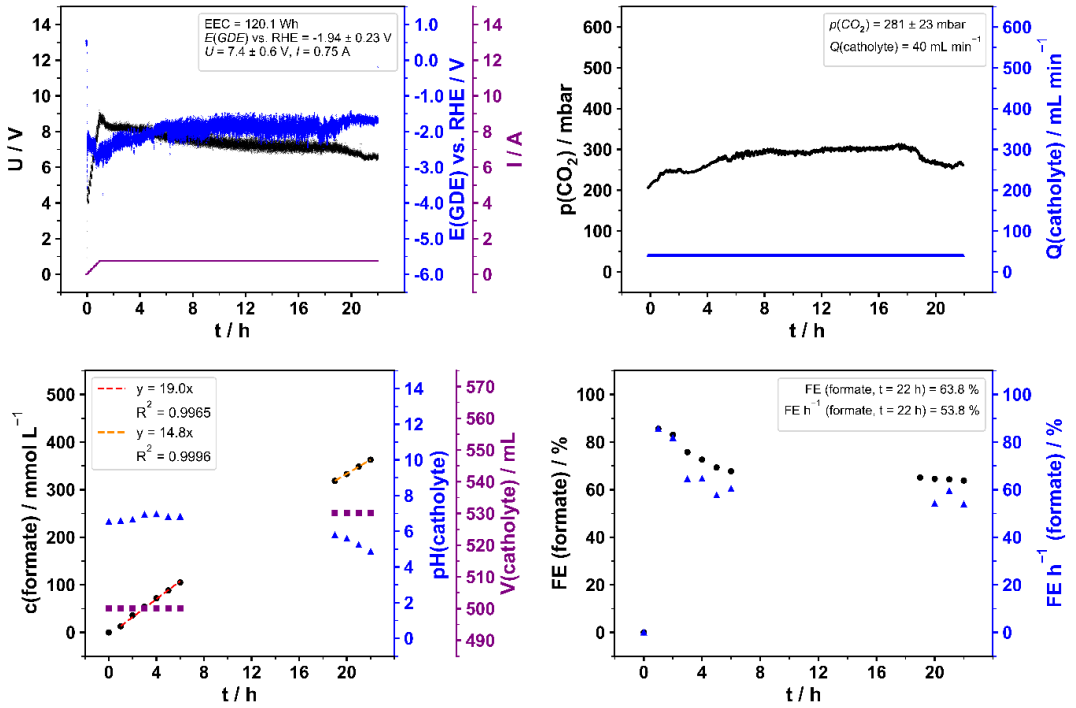

Figure S21: Supporting data for Electrolysis (C3), experimental details are provided in section 1.4 and results in Table S12 and Table S13.

3.2 Photographs of GDE before and after electrolysis

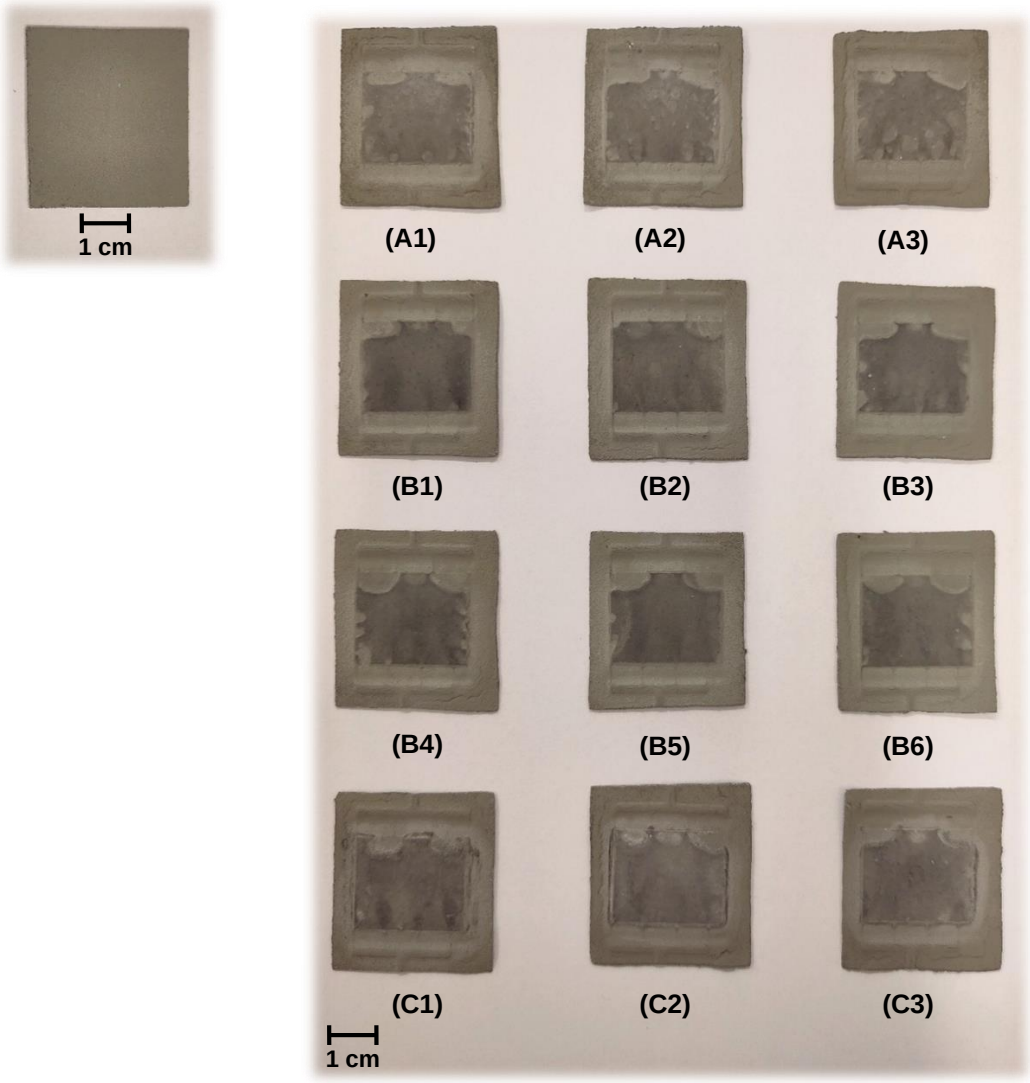

Figure S22: Exemplary photograph of a self-fabricated GDE before electrolysis (left). Photograph of the GDEs after electrolysis (right). Details of the fabrication process are provided in section 1.2, details on the electrolysis conditions in section 1.4.

3.3 SEM images of GDE before and after electrolysis

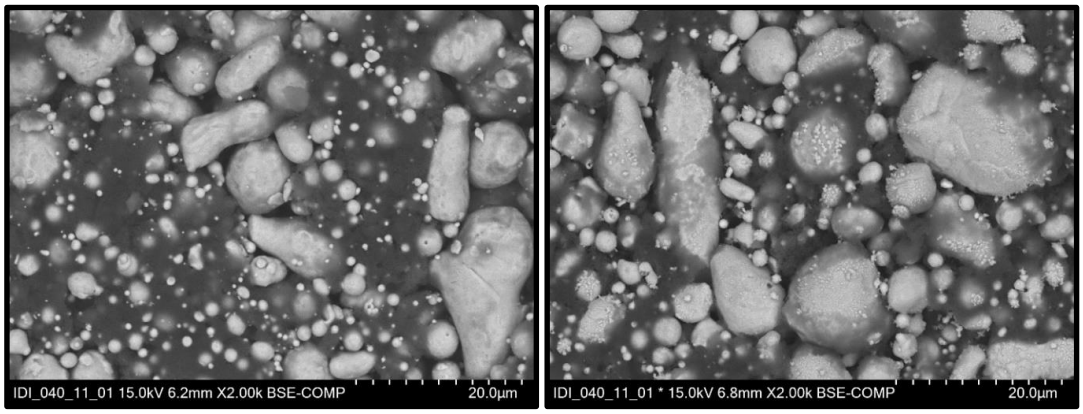

Figure S23: SEM image (BSE detected, bright particles are Sn, section 1.5) of the GDE before (left) and after (right) electrolysis (A1).

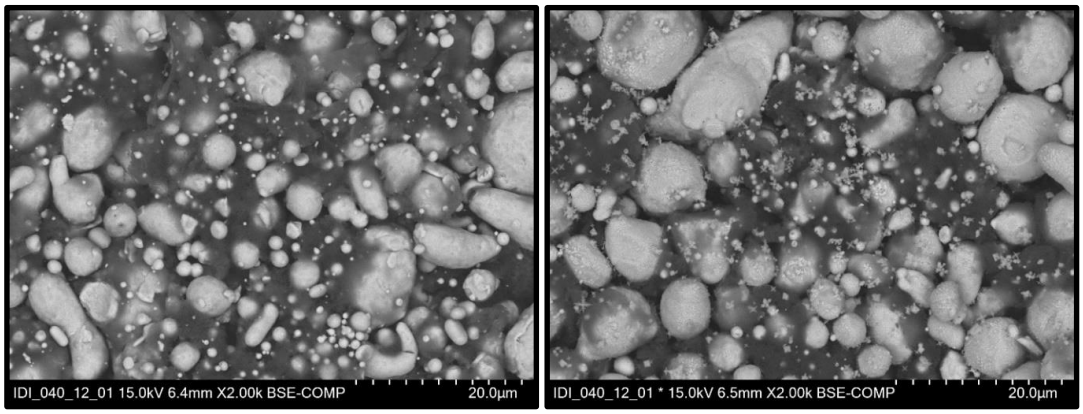

Figure S24: SEM image (BSE detected, bright particles are Sn, section 1.5) of the GDE before (left) and after (right) electrolysis (A2).

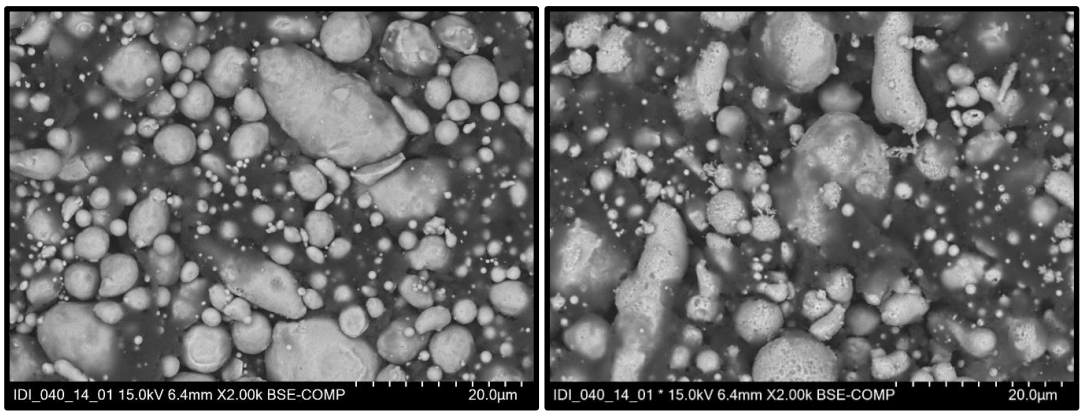

Figure S25: SEM image (BSE detected, bright particles are Sn, section 1.5) of the GDE before (left) and after (right) electrolysis (A3).

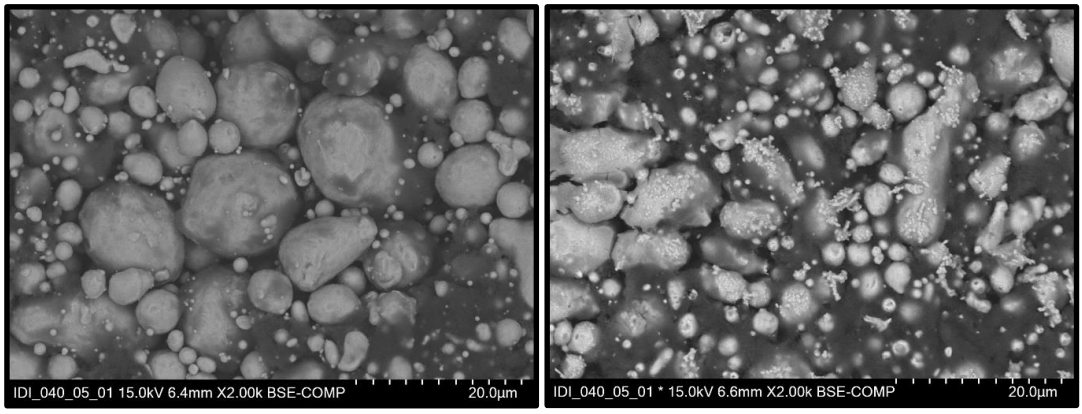

Figure S26: SEM image (BSE detected, bright particles are Sn, section 1.5) of the GDE before (left) and after (right) electrolysis (B1).

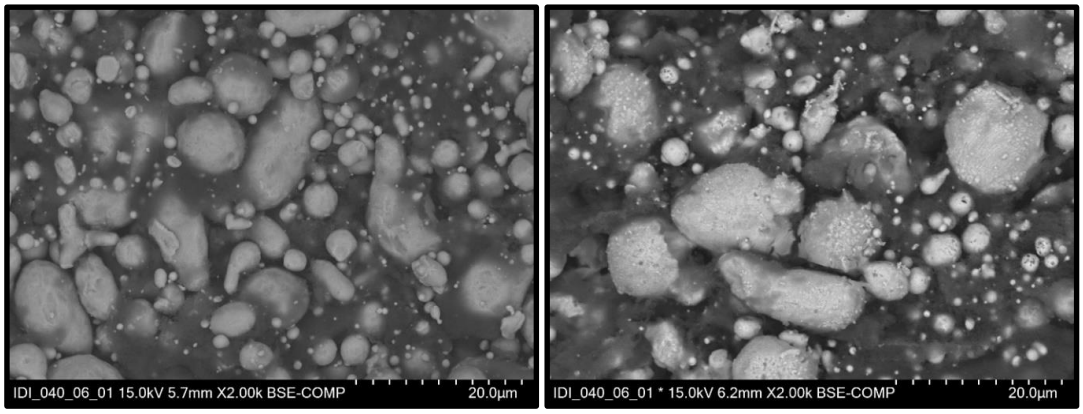

Figure S27: SEM image (BSE detected, bright particles are Sn, section 1.5) of the GDE before (left) and after (right) electrolysis (B2).

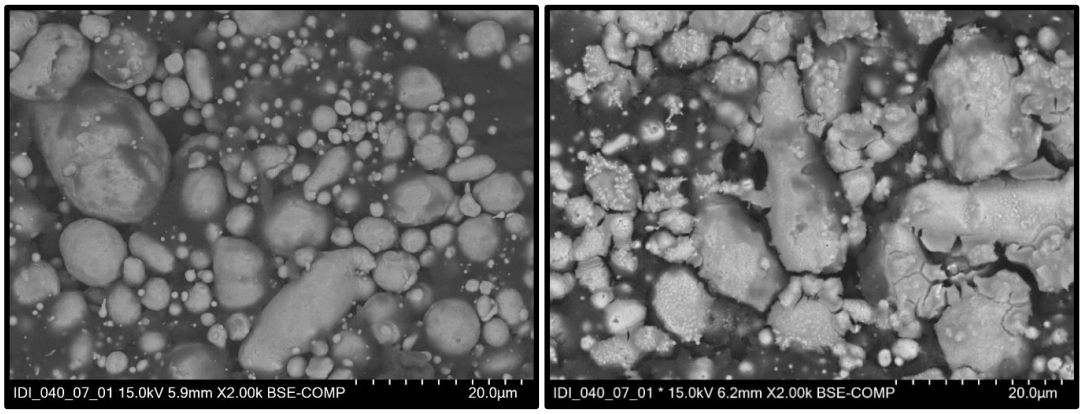

Figure S28: SEM image (BSE detected, bright particles are Sn, section 1.5) of the GDE before (left) and after (right) electrolysis (B3).

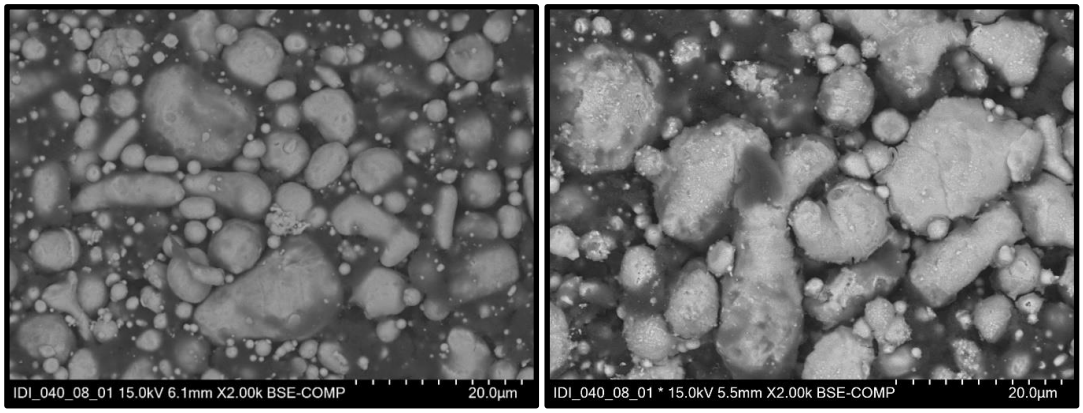

Figure S29: SEM image (BSE detected, bright particles are Sn, section 1.5) of the GDE before (left) and after (right) electrolysis (B4).

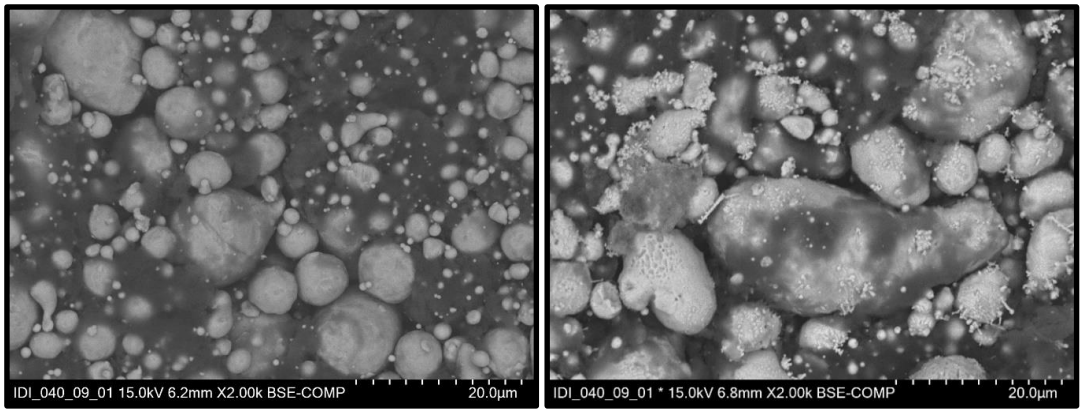

Figure S30: SEM image (BSE detected, bright particles are Sn, section 1.5) of the GDE before (left) and after (right) electrolysis (B5).

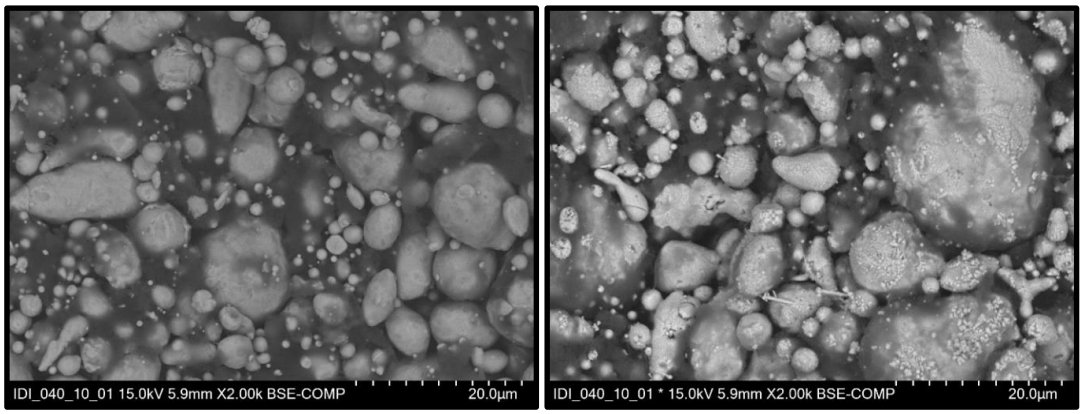

Figure S31: SEM image (BSE detected, bright particles are Sn, section 1.5) of the GDE before (left) and after (right) electrolysis (B6).

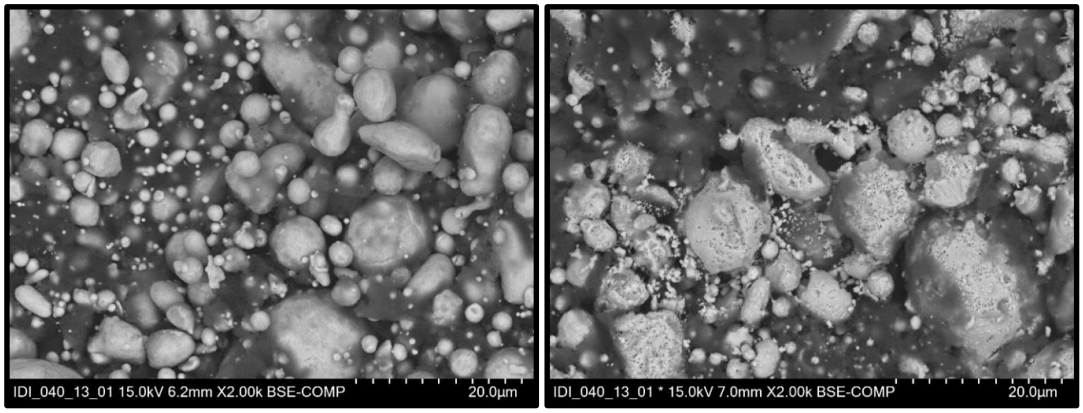

Figure S32: SEM image (BSE detected, bright particles are Sn, section 1.5) of the GDE before (left) and after (right) electrolysis (C1).

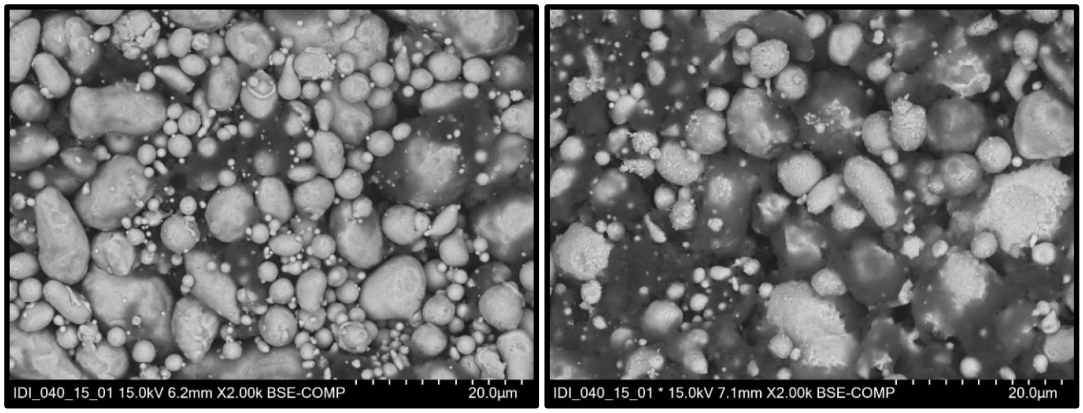

Figure S33: SEM image (BSE detected, bright particles are Sn, section 1.5) of the GDE before (left) and after (right) electrolysis (C2).

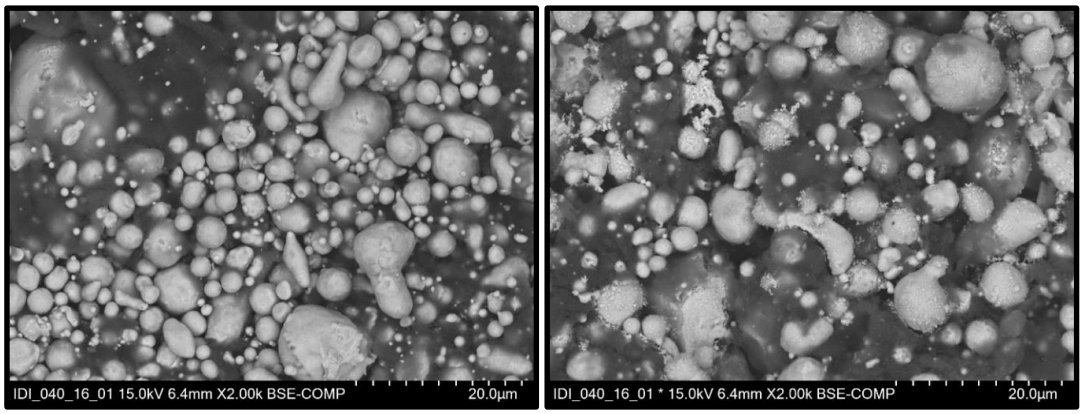

Figure S34: SEM image (BSE detected, bright particles are Sn, section 1.5) of the GDE before (left) and after (right) electrolysis (C3).

3.4 Microbial PHB synthesis in shaking flasks

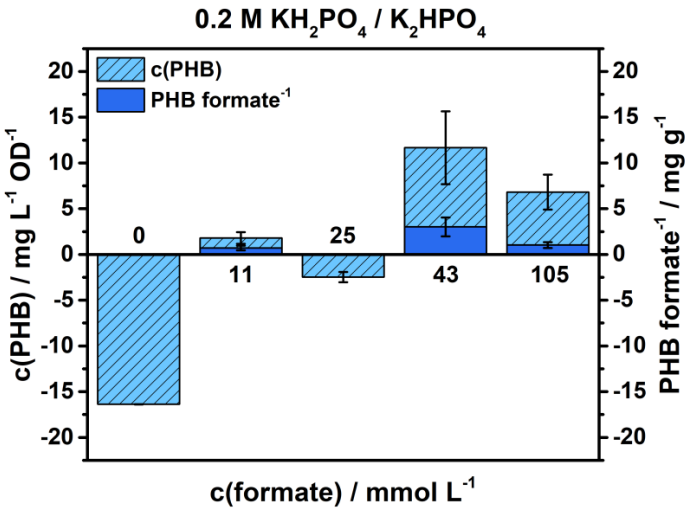

Figure S35: Comparison of c(PHB) normalised to initial OD_{600} (column, line pattern, blue) and PHB formate^{-1} (column, solid, light blue) during PHB synthesis with *C. necator* (resting cells) in shaking flasks with variable initial c(formate) specified at the columns in phosphate buffer (A) 0.2 M KH_2PO_4 / K_2HPO_4. Incubation conditions (n = 3): *C. necator* (resting cells), Initial OD_{600} ≈ 0.2, V = 75 mL, Duration = 4 h, T = 30 °C, Shaking = 180 rpm. The plotted data has been summarised in Table S14.

Table S14: PHB synthesis in shaking flasks with variable initial c(formate). Incubation conditions (n = 3): *C. necator* (resting cells), Medium = (A) 0.2 M KH_2PO_4 / K_2HPO_4 Initial OD_{600} ≈ 0.2, V = 75 mL, Duration = 4 h, T = 30 °C, Shaking = 180 rpm.

Initial OD_{600}	Initial c(formate) / mmol L^{-1}	Final c(formate) / mmol L^{-1}	q(formate) / mmol L^{-1} h^{-1} OD^{-1}	c(PHB) / mg L^{-1} OD^{-1}	PHB formate^{-1} / mg g^{-1}
0.13	0	0	0	−16.38 ± 0.03	0
0.17	11.1	1.60 ± 0.04	37 ± 3	1.8 ± 0.7	0.7 ± 0.3
0.14	25.0	15.6 ± 0.2	16.9 ± 0.3	−2.5 ± 0.6	0
0.16	42.7	28.89 ± 0.08	21.5 ± 0.2	11.7 ± 4.0	3.0 ± 1.0
0.15	105.2	82.8 ± 1.3	37.3 ± 2.2	6.8 ± 2.0	1.0 ± 0.4

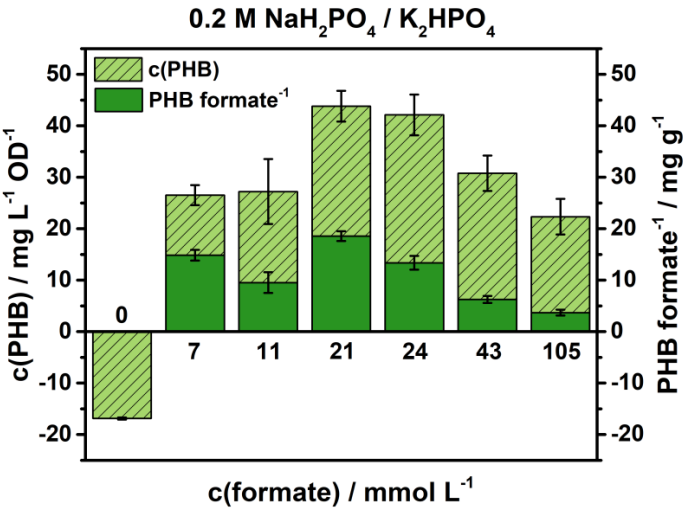

Figure S36: Comparison of c(PHB) normalised to initial OD_{600} (column, line pattern, green) and PHB formate^{-1} (column, solid, light green) during PHB synthesis with *C. necator* (resting cells) in shaking flasks with variable initial c(formate) specified at the columns in phosphate buffer (B) 0.2 M NaH_2PO_4 / K_2HPO_4. Incubation conditions (n = 3): *C. necator* (resting cells), Initial OD_{600} ≈ 0.2, V = 75 mL, Duration = 4 h, T = 30 °C, Shaking = 180 rpm. The plotted data has been summarised in Table S15.

Table S15: PHB synthesis in shaking flasks with variable initial c(formate). Incubation conditions (n = 3): *C. necator* (resting cells), Medium = (B) 0.2 M NaH_2PO_4 / K_2HPO_4 Initial OD_{600} ≈ 0.2, V = 75 mL, Duration = 4 h, T = 30 °C, Shaking = 180 rpm.

Initial OD_{600}	Initial c(formate) / mmol L^{-1}	Final c(formate) / mmol L^{-1}	q(formate) / mmol L^{-1} h^{-1} OD^{-1}	c(PHB) / mg L^{-1} OD^{-1}	PHB formate^{-1} / mg g^{-1}
0.17	0	0	0	−16.9 ± 0.3	0
0.17	7.2	0.45 ± 0.03	9.93 ± 0.05	26.5 ± 2.0	14.8 ± 1.0
0.15	11.4	1.96 ± 0.18	15.8 ± 0.4	27.2 ± 6.3	9.5 ± 2.0
0.18	21.3	11.9 ± 0.2	13.1 ± 0.2	43.8 ± 3.0	18.6 ± 1.0
0.14	24.4	14.6 ± 0.2	17.5 ± 0.4	42.1 ± 4.0	13.4 ± 1.3
0.15	42.8	26.4 ± 0.1	27.4 ± 0.2	30.8 ± 3.4	6.2 ± 0.7
0.17	104.9	82.0 ± 0.7	33.6 ± 1.0	22.3 ± 3.5	3.7 ± 0.6

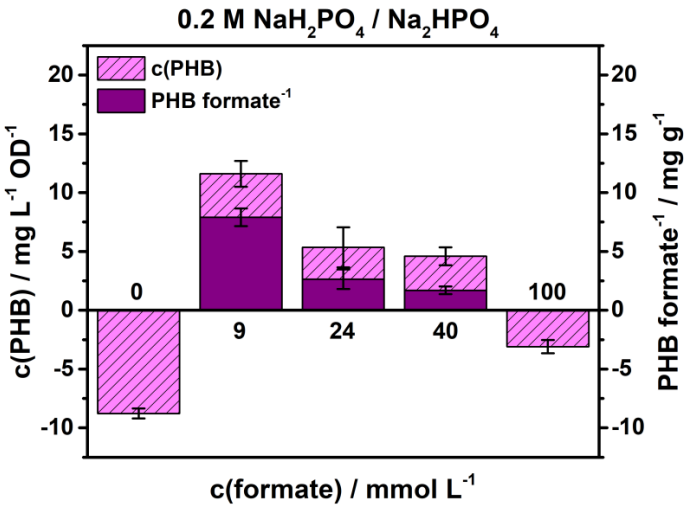

Figure S37: Comparison of c(PHB) normalised to initial OD_{600} (column, line pattern, purple) and PHB formate^{-1} (column, solid, light purple) during PHB synthesis with *C. necator* (resting cells) in shaking flasks with variable initial c(formate) specified at the columns in phosphate buffer (C) 0.2 M NaH_2PO_4 / Na_2HPO_4. Incubation conditions (n = 3): *C. necator* (resting cells), Initial OD_{600} ≈ 0.2, V = 75 mL, Duration = 4 h, T = 30 °C, Shaking = 180 rpm. The plotted data has been summarised in Table S16.

Table S16: PHB synthesis in shaking flasks with variable initial c(formate). Incubation conditions (n = 3): *C. necator* (resting cells), Medium = (C) 0.2 M NaH_2PO_4 / Na_2HPO_4 Initial OD_{600} ≈ 0.2, V = 75 mL, Duration = 4 h, T = 30 °C, Shaking = 180 rpm.

Initial OD_{600}	Initial c(formate) / mmol L^{-1}	Final c(formate) / mmol L^{-1}	q(formate) / mmol L^{-1} h^{-1} OD^{-1}	c(PHB) / mg L^{-1} OD^{-1}	PHB formate^{-1} / mg g^{-1}
0.18	0	0	0	−8.8 ± 0.5	0
0.17	8.6	3.0 ± 0.2	8.2 ± 0.2	11.6 ± 1.1	7.9 ± 0.8
0.18	23.7	15.58 ± 0.04	11.27 ± 0.06	5.4 ± 1.7	2.6 ± 0.9
0.14	40	30.84 ± 0.12	16.4 ± 0.3	4.6 ± 0.8	1.7 ± 0.3
0.15	100	90.4 ± 0.4	16.0 ± 0.7	−3.1 ± 0.6	0

Exemplarily, the best conditions of buffer (B) were also examined with its inverse Na^+ / K^+ ratio (2:1). For this purpose, PHB synthesis was carried out in 0.2 M KH_2PO_4 / Na_2HPO_4 (equimolar) at 25 mmol L^{-1} formate. In this case, only 29.8 ± 2.2 mg L^{-1} OD^{-1} (n = 3) PHB corresponding to 9.1 ± 0.6 mg g^{-1} (n = 3) PHB per formate with 18.1 ± 0.3 mmol L^{-1} h^{-1} OD^{-1} (n = 3) as average formate consumption rate were obtained. Generally, more formate was consumed while less PHB was generated at the inverse Na^+ / K^+ ratio (2:1).

3.5 Microbial PHB synthesis in parallel, semi-automated bioreactors

Table S17: PHB synthesis of *C. necator* resting cells in semi-automated bioreactors with e-formate stock solution feed (n = 4) shown in Figure 4 of the main article. Incubation conditions: Buffer = 0.2 M NaH_2PO_4 / K_2HPO_4 (equimolar), T = 30 °C, Initial e-formate feed = 6.9 mL h^{-1} (adjusted during runtime), c(e-formate) of feed = 441 mmol L^{-1}, Runtime = 7.5 h.

t / h	V(feed) / mL h^{-1}	V(reactor) / L	Initial OD_{600}[a]	c(Formate) / mmol L^{-1}	Consumed n(Formate) / mmol	c(PHB) / mg L^{-1} OD^{-1}	PHB $formate^{-1}$ / mg g^{-1}
0.0	0	0.340	1.80	16.3	0	19.5	0
0.5	6.9	0.343	1.78	8.2 ± 0.9	4.3 ± 0.3		
1.0	6.9	0.346	1.76	2.6 ± 0.4	6.2 ± 0.2		
1.5	30.9	0.359	1.69	11.5 ± 1.0	9.8 ± 0.4		
2.0	30.9	0.374	1.62	18.1 ± 1.1	14.0 ± 0.4	38.6 ± 4.1	17.8 ± 3.7
2.5	28.2	0.377	1.56	25.8 ± 2.2	17.3 ± 0.9		
3.0	28.2	0.391	1.50	29.4 ± 1.5	21.9 ± 0.6		
3.5	0	0.391	1.50	22.9 ± 2.2	24.4 ± 0.9		
4.0	0	0.390	1.50	15.1 ± 1.1	27.4 ± 0.5	55 ± 7	15.9 ± 3.0
4.5	0	0.378	1.50	11.7 ± 0.7	28.9 ± 0.3		
5.0	0	0.377	1.50	5.6 ± 1.4	31.2 ± 0.6		
5.5	17.3	0.384	1.46	11.2 ± 1.0	32.8 ± 0.4		
6.0	17.3	0.392	1.43	12.8 ± 2.4	35.8 ± 0.9	71 ± 12	16.9 ± 3.8
6.5	25.8	0.393	1.38	23.8 ± 1.3	37.0 ± 0.5		
7.0	25.8	0.404	1.33	29.2 ± 2.0	40.1 ± 0.8		
7.5	7.5	0.407	1.32	26.3 ± 1.7	42.8 ± 0.7	83 ± 16	16.5 ± 4.0

[a] The initial OD_{600} used for normalisation was mathematically corrected for the volume change due to e-formate feeding and sampling throughout incubation.

Supporting Information

All Electrochemical Synthesis of Performic Acid Starting from CO_2, O_2 and H_2O

I. Dinges, M. Pyschik, J. Schütz, S. Schneider, E. Klemm, S. R. Waldvogel, M. Stöckl*

Content

1 Experimental protocols and analytical methods

1.1 General Information

Selected chemical compounds and details on employed equipment are listed in this section (cf. Table S1, Table S2). All chemicals were used without further purification and all solutions were prepared using high purity H_2O (0.055 µS cm^{-1}, 25 °C, PURELAB Ultra).

Table S1: Selected chemical compounds (Purity grade, supplier, charge number).

Compound	Purity grade	Supplier	Charge
KH_2PO_4	>99% (p.a.)	Carl Roth, Karlsruhe / Germany	453340544
K_2HPO_4	>99% (p.a.)	Carl Roth, Karlsruhe / Germany	024350089
HCOOK	99% (p.a.)	Alfa Aesar, Haverhill / USA	10183323
HCOONa	≥99% (p.a.), ACS	Merck, Darmstadt / Germany	A0703243 608
NaCl	≥99.5% (p.a.), ACS, ISO	Carl Roth, Karlsruhe / Germany	238269100
KCl	≥99.5% (p.a.), ACS, ISO	Carl Roth, Karlsruhe / Germany	392328190
H_2SO_4	75%, pure	Carl Roth, Karlsruhe / Germany	262322778
HNO_3	69%, ROTIPURAN Supra	Carl Roth, Karlsruhe / Germany	1121091
$HClO_4$	60%, EMSURE®, ACS	Merck, Darmstadt / Germany	MB2171818
KI	≥99% (p.a.)	Carl Roth, Karlsruhe / Germany	182313120
Starch solution	1%, w/v aqueous solution	Carl Roth, Karlsruhe / Germany	24011166
Ferroin solution	1/40 mol L^{-1} in ethanol	VWR, Radnor / USA	23032448
$(NH_4)_6Mo_7O_{24}\cdot 4H_2O$	≥99% (p.a.)	Carl Roth, Karlsruhe / Germany	262325940
$Na_2S_2O_3$ titrimetric solution	0.01 mol L^{-1} standard solution	Carl Roth, Karlsruhe / Germany	24022325
$Ce(SO_4)_2$ titrimetric solution	0.1 mol L^{-1} standard solution	Carl Roth, Karlsruhe / Germany	24021136
HCOOH	≥98%, for synthesis	Carl Roth, Karlsruhe / Germany	083329609
KOH	≥85%,EMSURE®, pellets for analysis	Merck, Darmstadt / Germany	B1876233
H_3PO_4	75%	VWR, Radnor / USA	17H304001

Table S2: Equipment / device, function and manufacturer.

Equipment / device	Function / use	Manufacturer
PURELAB Ultra	High purity H_2O	ELGA LabWater, High Wycombe / United Kingdom
A 10 basic	Knife mill	IKA, Staufen / Germany
LaboPress P200S	Heat press	VOGT Labormaschinen, Berlin / Germany
Perkin Elmer 062566	Hydraulic press	Bodenseewerk Perkin-Elmer, Überlingen / Germany
MicroMahr E 40	Thickness measurement	Mahr, Göttingen / Germany
Sartorius 1712004	Analytical scale (0.00000 g)	Sartorius Lab Instruments, Göttingen / Germany
Entris 3202I-1S	Scale (0.00 g)	Sartorius Lab Instruments, Göttingen / Germany
NGP804	Power supply	Rohde & Schwarz, Munich / Germany
HMC8043	Power supply	Rohde & Schwarz, Munich / Germany
CEBO-LC (CESYS C028152)	Analog data logging	CESYS, Herzogenaurach / Germany
GMH 3151	Pressure meter	GHM Messtechnik, Regenstauf / Germany
GMSD 2 BR - K31	Differential pressure sensor	GHM Messtechnik, Regenstauf / Germany
Transferpette® S	Pipetting, sampling (100-1000 µL, 500-5000 µL, 1000-10000 µL)	BRAND, Wertheim / Germany
InLab micro	pH electrode coupled with SevenCompact pH/Cond S213	Mettler Toledo, Columbus / USA
SevenCompact pH/Cond S213	pH meter	Mettler Toledo, Columbus / USA
ECOLINE VC–MS/CA8-6	Peristaltic pump	ISMATEC Laboratoriums-technik, Wertheim / Germany

1.2 Fabrication of GDE

1.2.1 GDEs for formate electrosynthesis

The gas diffusion electrodes (GDE) were fabricated by pressing a Bi_2O_3 based catalyst mixture onto Ni foam as support material and current collector with a heat press. The catalyst mixture (30.00 g) consisted of Bi_2O_3 (87.5 wt%, 26.25 g, purity 99.9%, particle size approx. 80 nm, US Research Nanomaterials, Houston / USA) and polytetrafluoroethylene (PTFE) powder (12.5 wt%, 3.75 g, Dyneon™ PTFE TF 2072Z, 3M, Saint Paul / USA). The catalyst mixture was homogenised in a knife mill (A 10 basic). The mixing (30 s, 25000 rpm) was carried out twice and lead to a temperature increase of the mixture (T >35 °C). After cooling to room temperature (RT), the catalyst mixture (4.00 g) was equally distributed onto Ni foam (d = 1.4 cm, 3.5 cm x 4.0 cm ≙ 14 cm^2, Ni-5763, density 420 - 450 g m^{-2}, Recemat BV, Dodewaard / Netherlands) with a sieve (Stainless-steel wire mesh, mesh size = 500 µm, ISO 3310-1, Retsch / Verder Scientific, Haan / Germany) and a stencil (Cut-out 3.5 cm x 4.0 cm). The GDE blank was placed in between two pieces of ordinary baking sheet in the heat press (LaboPress P200S) and compressed (plate temperature 120 °C, pressure 10 bar, 60 s). After compressing excess material at the GDE edges was removed with a scalpel. The GDE's catalyst loading *b* was determined by differential weighing (Sartorius 1712004) and its thickness *d* was measured at the centre point (Micromar 40 ER). In total, three GDEs were fabricated with a catalyst loading of *b* (Bi_2O_3, wt%) = 65.7 ± 0.7 mg cm^{-2} and *d* = 523 ± 11 µm for the electrosynthesis of formate within this study.

1.2.2 GDEs for H_2O_2 electrosynthesis

The GDEs for the (electro)synthesis of H_2O_2 and PFA were prepared by pressing a mixture containing carbon black as catalyst and PTFE as hydrophobic binder onto a stainless steel mesh as support material.

First, the catalyst mixture (3.00 g) consisting of the carbon catalyst (65.5 wt%, 1.97 g, Acetylene Black, 100% compressed, >99.9%, S.A. 75 m^2 g^{-1}, bulk density 170 - 230 g L^{-1}, Lot: Z10G042, Alfa Aesar, Haverhill / USA) and the PTFE powder (34.5 wt%, 1.03 g, Dyneon™ PTFE TF 2072Z, 3M, Saint Paul / USA) was mixed twice (each 30 s, 25000 rpm) in a knife mill (A 10 basic). Part of the mixture (500 mg) was then placed in a cylindrical mask (*d* = 40 mm) containing a stainless steel mesh (Material 1.4301, mesh size = 0.5 cm, *d* = 240 µm, 3.2 cm x 3.2 cm, Haver & Boecker, Oelde / Germany) and compressed (pressure 3.5 t, 60 s, RT followed by pressure 7 t, 180 s, RT) using a hydraulic press (Perkin Elmer 062566). After trimming the edges, the raw electrodes were treated in a heat press (plate temperature 120 °C, 10 bar, 180 s) to improve their mechanical stability.

In total, eight GDEs were fabricated with a catalyst loading of b = 26.1 ± 0.5 mg cm^{-2} and a thickness of d ≈ 600 ± 10 µm for the (electro)synthesis of H_2O_2 and PFA within this study.

1.3 Electrochemical flow reactor and electrolysis set-up

Detailed descriptions of the electrochemical flow reactor and the electrolysis set-up have already been provided in a previous publication (https://doi.org/10.1002/cssc.202301721). The same electrochemical flow reactor and electrolysis set-up have been employed for both formate and H_2O_2 electrosynthesis herein.

1.4 Electrosynthesis of formate

Electrosynthesis of formate using CO_2 was carried out with self-fabricated Bi_2O_3 based GDEs (cf. section 1.2) in a flow reactor (cf. section 1.3), whereby the GDEs were only used once per experiment.

All electrosyntheses were performed for 22 h. A power supply unit (NGP804) was employed to run the electrolysis, it recorded cell voltage (U), current (I) and power (P). Furthermore, the electrode potential of the GDE was referenced to a RHE (CEBO-LC) without compensation of iR losses. The electrosynthesis started with a current ramp (30 s), in which the current density (j) reached 150 mA cm^{-2} (750 mA in total), which was maintained for the runtime.

CO_2 (N4.5) was supplied to the GDE at a flow rate of 10 - 15 mL min^{-1} (Float-type flow meter, Wagner Mess- und Regeltechnik, Offenbach / Germany) and an initial overpressure in range of 110 - 150 mbar relative to ambient pressure. The pressure was recorded (every 2 s) during the running electrolysis (CEBO-LC).

The phosphate-based buffer 0.2 mol L^{-1} KH_2PO_4 / K_2HPO_4 (equimolar) served as electrolyte for all three electrolyses. For each electrolysis, anolyte and catholyte had a starting volume of 500 mL (Volumetric flask, ISO 1042). Anolyte and catholyte were circulated continuously at a flow rate of approx. 40 mL min^{-1} between flow reactor compartment and reservoir, respectively. Furthermore, the catholyte reservoir was equipped with a pH electrode (EGA142, Xylem Analytics Germany Sales, Weilheim / Germany). The catholyte's pH was recorded (every 2 s) during the running electrolysis (CEBO-LC). During the electrolysis, catholyte samples (1 mL, Transferpette® S) were taken hourly in the first five (t = 0 - 5 h) and the last three (t = 20 - 22 h) hours to monitor formate concentration and calculate the corresponding Faradaic efficiency (FE). After electrolysis, the catholyte volume was determined by its weight (Entris 3202I-1S) and density. Therefore, the density was calculated by taking samples (1 mL, n = 3, Transferpette® S) and weighing them (Sartorius 1712004). Catholyte containing electrochemically generated formate was stored at 5 °C until its application for (electro)synthesis of H_2O_2 and PFA. The GDE was rinsed with H_2O and dried at RT.

Detailed information on the experimental parameters and results for all individual formate electrosyntheses are provided in section 3.1.

1.5 Electrosynthesis of H_2O_2

The (electro)synthesis of H_2O_2 and PFA using O_2 was carried out with self-manufactured carbon black based GDEs in the same reactor type as the formate electrosynthesis, whereby the GDEs were only used once per experiment.

The duration of each electrolysis was 6 h. A power supply unit (HMC8043) was employed to run the electrolysis, it recorded cell voltage (*U*), current (*I*) and power (*P*). Furthermore, the electrode potential of the GDE was referenced to a RHE (CEBO-LC) without compensation of *iR* losses. The current density was 150 mA cm^{-2} (750 mA in total), which was reached by a ramp (10 s) at the beginning of the electrolysis. Catholyte and anolyte had a starting volume of 50 mL each (Measuring cylinder, 100 mL, ISO 4788) and were continuously circulated at a flow rate of approx. 40 mL min^{-1} between the flow reactor and the reservoir. Pure O_2 (N4.6) was supplied to the GDE with a flow rate of 20 mL min^{-1} and an initial overpressure of approx. 90 mbar relative to ambient pressure. For the determination of H_2O_2 / PFA concentrations and pH, 1.0 mL of the electrolytes were sampled every 1.5 h. The catholyte's volume was determined at the end of the experiments in the same manner as described above (cf. section 1.4). The catholyte did not show any gas evolution indicating H_2O_2 / PFA decomposition during or after electrolysis.

Two different phosphate-based buffers containing formate were used as catholytes: (F) The catholyte containing formate originating from formate electrosynthesis and (R) a reference electrolyte based on (F) for comparison. For all electrolyses, 0.5 mol L^{-1} perchloric acid ($HClO_4$) was used as an anolyte. Four experiments were carried out for each catholyte.

Reference electrolyte (R): 0.2 mol L^{-1} KH_2PO_4 / K_2HPO_4 (equimolar) and 0.5 mol L^{-1} HCOOK / HCOOH (equimolar) in 1 wt% H_3PO_4. The electrolyte was adjusted to pH = 4.13 ± 0.05 using KOH pellets.

1.6 Titration

The concentrations of H_2O_2 and PFA in the samples were determined using a two-step titration method similar to the procedure described by Greenspan and Mackellar (DOI: 10.1021/ac60023a020). Firstly, the concentration of H_2O_2 was determined by cerimetry using $Ce(SO_4)_2$ (c = 0.01 mol L^{-1}). For this purpose, 5 drops of H_2SO_4 (c = 5 mol L^{-1}) and 70 µL ferroin (c = 0.025 mol L^{-1} in ethanol) as an indicator were added to the sample solution. The orange solution was titrated until a light blue colour was observed. The concentration of PFA was then determined via iodometry with $Na_2S_2O_3$ (c = 0.01 mol L^{-1}). To the light blue solution, 0.1 mL of a KI solution (c = 0.48 mol L^{-1}) and a spatula tip of $(NH_4)_6Mo_7O_{24}{\cdot}4H_2O$ were added.

After 15 minutes, the resulting reddish-brown suspension was slowly titrated until the colour changed to light brown. Then 2 - 3 drops of starch solution (1 wt%/v) were added and titration continued until the colour changed back to orange and no precipitates remained. The sample volumes were 0.2 mL (after 1.5 h), 0.1 mL (after 3.0 h) and 0.075 mL (after 4.5 h and 6.0 h). Each titration was carried out in triplicates (n = 3) for the specified time and experiment. Furthermore, results of the triplicates had statistically distributed values and did not show declining trends, which would have indicated H_2O_2 / PFA decomposition.

1.7 X-ray diffraction (XRD)

X-ray diffraction analysis was performed employing a D8 Advance XRD (Bruker, Billerica / USA), which was operated by *DIFFRAC.Measurement Center* (Version 6.5.0). Cu Kα radiation with a power of 1200 W was used, the split aperture was fixed at 2 mm, the increments were set to 0.020° and the measurement time per step was 1.0 s. XRD data was analysed with *Match!* (Version 4.0). XRD data was measured on the GDE's catalyst coated side at its geometrical centre point. Results before and after electrolysis are provided in section 3.6.

1.8 Scanning electron microscopy (SEM)

SEM imaging was performed employing the Flex SEM 1000 II (cf. Table S3), operated by *FlexSEM1000* (Version 2.3).

Table S3: Conditions for SEM imaging performed on Flex SEM 1000 II (Hitachi, Tokyo / Japan).

Conditions		Conditions	
Operation mode	Composition	Viewing height	6-8 mm
Pressure	High vacuum	Spot size	40
Accelerating voltage	15 kV	Cathode	Tungsten
Magnification	x2000, x4000	Detector	Secondary electrons (SE) and Back-scattering electrons (BSE)

Images of the GDEs were taken at the centre point of the geometrical GDE surface (2 cm x 2.5 cm) exposed within the reactor before and after application for formate and H_2O_2 / PFA (electro)synthesis. Prior to imaging, the GDEs were rinsed (H_2O) and dried (RT, 24 h). Exemplary SEM images are provided in section 3.4.

1.9 Determination of contact angle

The images for contact angle θ determination were taken with the OCA 15 plus (DataPhysics Instruments, Filderstadt / Germany), which was operated by *SCA20* (Version 4.4.1).

All measurements were carried out using the sessile drop method, a H_2O droplet (50 µL, Transferpette® S) was placed at the GDE's centre point. Contact angles were calculated by fitting the droplet edges with a Young-Laplace model using the operating software. Exemplary contact angle images are provided in section 3.5.

1.10 Determination of density

The densities of GDE were determined with the gas pycnometer BELPYCNO L (cf. Table S4), which was operated via *BELPycno-L* (Version 3.1.4).

Table S4: Volume / density measurement conditions performed on BELPYCNO L (Microtrac Retsch, Haan / Germany).

Conditions		Conditions	
Carrier gas	Helium	Restriction delta pressure	2.00000 bar
Temperature	20.00 °C	Equilibrium delta pressure	0.00020 bar
Reference volume	I	Equilibrium delta time	15 s
Flow cleaning time	0 s	Standard deviation (max.)	10%
Number of cleaning cycles	10	Nr. of good measurements	10
Sample cleaning time	5 s	Nr. of max. measurements	10
Atm. stabilisation time	15 s	High precision mode	Disabled

The reference volume chamber I was calibrated with steel calibration sphere S using the instrument's standard protocol. All samples were measured (n = 3) in sample chamber S (20 cm^3) using glass beads (⌀ = 2.85 - 3.45 mm, charge 381176662, Carl Roth, Karlsruhe / Germany) as filler volume (approx. 50%). The sample weights (Sartorius 1712004) were used to calculate the densities from the measured volumes. To measure the GDE after electrolysis, the area exposed in the reactor during electrolysis was cut out (5 cm^2). As the sample volumes were relatively small compared to the sample chamber despite the filler, the GDE for the electrosynthesis of formate and H_2O_2 were measured together in order to minimise relative errors. The results are summarised in Table S5.

Table S5: Volume and density results for Bi_2O_3 and carbon based GDE before and after electrolysis.

Sample	Electrolysis	Volume / cm^3	Density / g cm^{-3}
Bi_2O_3 based GDE	-	0.2275 ± 0.0001	7.060 ± 0.002
Bi_2O_3 based GDE	(F1), (F2), (F3)	0.3122 ± 0.0002	6.631 ± 0.004
Carbon based GDE	-	0.2634 ± 0.0003	3.094 ± 0.004
Carbon based GDE	(P1), (P2), (P3), (P4)	0.5444 ± 0.0002	3.270 ± 0.001
Carbon based GDE	(R1), (R2), (R3), (R4)	0.5144 ± 0.0002	3.363 ± 0.002

1.11 Inductively coupled plasma optical emission spectroscopy (ICP-OES)

ICP-OES measurements were performed on Agilent 5800 ICP-OES equipped with an SPS 4 Autosampler, a borosilicate double-pass spray chamber and a Seaspray concentric glass nebulizer (cf. Table S6). The system was operated via *ICP Expert* (Version 7.6.3.12735).

Table S6: ICP-OES measurement conditions performed on Agilent 5800 ICP-OES (Agilent Technologies, Santa Clara / USA).

Conditions		Conditions	
Replicate count	5	Viewing mode	Axial
Pump speed	12 rpm	Viewing height	-
Sample uptake time	25 s	Nebulizer flow	0.7 mL min^{-1}
Stabilization time	15 s	Plasma flow	12 mL min^{-1}
Read time	5 s	Aux Flow	1 mL min^{-1}
Rinse time	30 s	Oxygen content	0%
RF power	1.2 kW	IntelliQuant	Enabled

In between samples, autosampler and measurement system were rinsed with 2 wt% HNO_3 (prepared from 69 wt% HNO_3, Supra Quality, cf. Table S1).

All samples were measured without dilution except for acidification to 2 wt% HNO_3 (using 69 wt% HNO_3). In initial qualitative tests using an IntelliQuant screening, no elements of interest were detected in the anolyte samples. Consequently, only catholyte samples were examined further.

Standards to determine the concentrations of Bi^{3+} (λ = 223.061 nm), Cr^{3+} (λ = 205.560 nm), Fe^{3+} (λ = 238.204 nm) and Ni^{2+} (λ = 231.604 nm) were prepared by a dilution series of a stock solution (16 mg L^{-1}). The stock solution was prepared by combining the respective standards (10 mL each, cf. Table S7) in a volumetric flask (100 mL, ISO 1042) using 2 wt% HNO_3 for dilution. Afterwards, the solution was diluted further with 2 wt% HNO_3 to 16 mg L^{-1} in a volumetric flask (50 mL, ISO 1042). This was followed by a dilution series by factor 2. Finally, each standard (0.125, 0.25, 0.5, 1, 2, 4, 8, 16 mg L^{-1}) was diluted again by factor 2 with a matrix solution (0.4 mol L^{-1} KH_2PO_4 / K_2HPO_4, 0.5 mol L^{-1} HCOOH, 0.5 mol L^{-1} HCOOK in 2 wt% HNO_3). Thereby, a set of standards with a matrix based on the catholyte's composition was obtained. In the following, the calibrations for each targeted analyte with either catholyte matrix or 2 wt% HNO_3 matrix are presented. The calibration with catholyte matrix was used to calculate the results for the catholyte samples.

Table S7: Single Element ICP-Standard-Solutions used for analyte quantification (Element, Concentration, Supplier, Lot. No.).

Element	Concentration	Supplier	Lot. No.
Bi	1000 mg L^{-1}	Carl Roth, Karlsruhe / Germany	794591
Cr	1000 mg L^{-1}	Carl Roth, Karlsruhe / Germany	797239
Fe	1000 mg L^{-1}	Carl Roth, Karlsruhe / Germany	786848
Ni	1000 mg L^{-1}	Carl Roth, Karlsruhe / Germany	974203

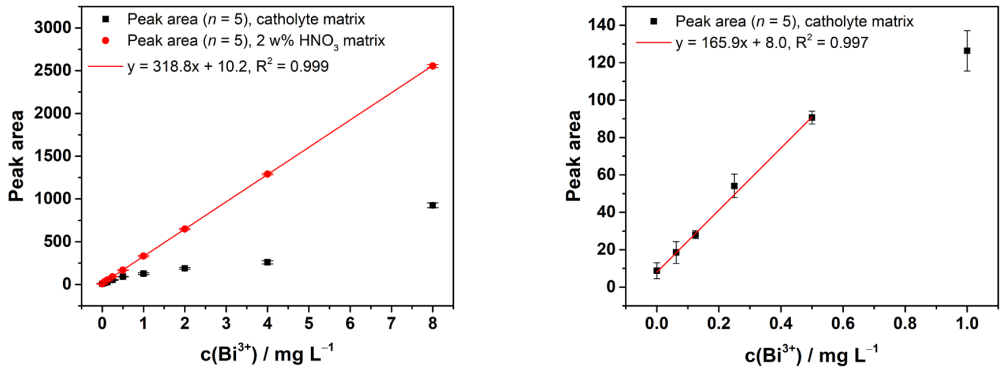

Figure S1: Calibration for Bi^{3+} (λ = 223.031 nm) via ICP-OES measurement with catholyte and 2% HNO_3 matrix**.** Plot of Bi^{3+} concentration (0, 0.0625, 0.125, 0.25, 0.5, 1, 2, 4, 8 mg L^{-1}) against the peak area of the measured signal (*n* = 5) with a linear fit, respectively.

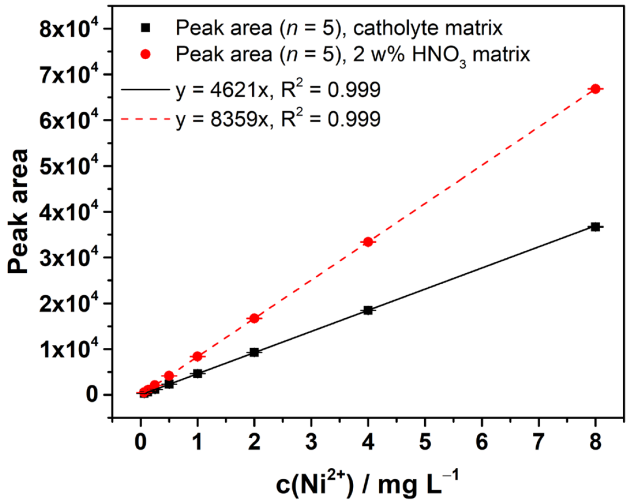

Figure S2: Calibration for Ni^{2+} (λ = 231.604 nm) via ICP-OES measurement with catholyte and 2% HNO_3 matrix**.** Plot of Ni^{2+} concentration (0.0625, 0.125, 0.25, 0.5, 1, 2, 4, 8 mg L^{-1}) against the peak area of the measured signal (*n* = 5) with a linear fit forced through zero, respectively.

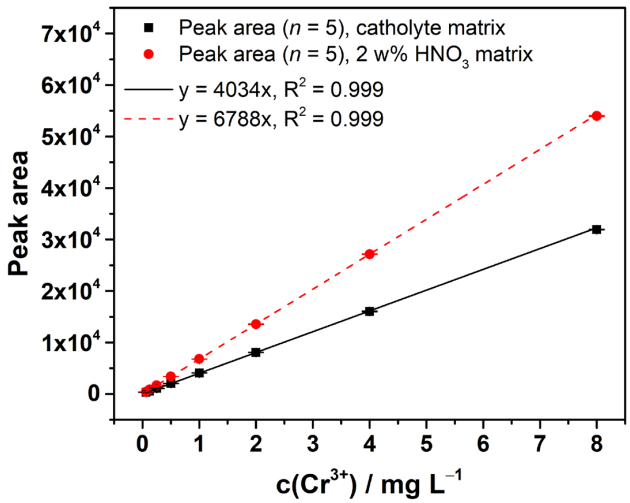

Figure S3: Calibration for Cr^{3+} (λ = 205.560 nm) via ICP-OES measurement with catholyte and 2% HNO_3 matrix**.** Plot of Cr^{3+} concentration (0.0625, 0.125, 0.25, 0.5, 1, 2, 4, 8 mg L^{-1}) against the peak area of the measured signal (*n* = 5) with a linear fit forced through zero, respectively.

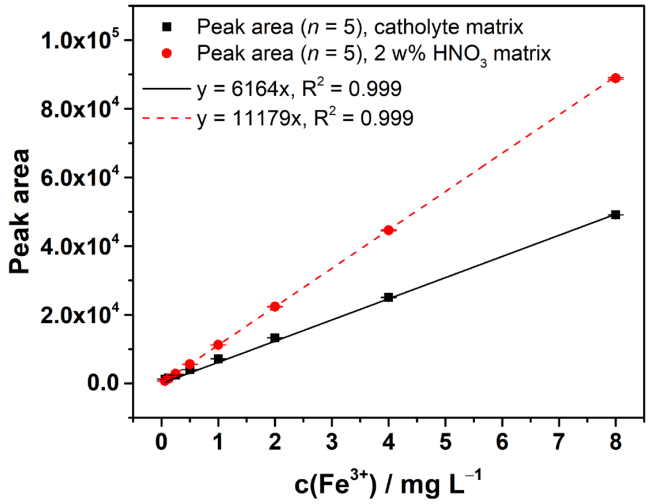

Figure S4: Calibration for Fe^{3+} (λ = 238.204 nm) via ICP-OES measurement with catholyte and 2% HNO_3 matrix**.** Plot of Fe^{3+} concentration (0.0625, 0.125, 0.25, 0.5, 1, 2, 4, 8 mg L^{-1}) against the peak area of the measured signal (*n* = 5) with a linear fit forced through zero, respectively.

Table S8: ICP-OES results for Bi^{3+}, Cr^{3+}, Fe^{3+} and Ni^{2+} concentrations in the catholyte samples.

Electrolysis	$c(Bi^{3+})$[c] / µg L^{-1}	$c(Cr^{3+})$ / µg L^{-1}	$c(Fe^{3+})$ / µg L^{-1}	$c(Ni^{2+})$ / µg L^{-1}
(F0)[a]	0	14.0 ± 0.7	151 ± 3	7.6 ± 1.9
(F1)	68 ± 25	12 ± 3	87.1 ± 0.9	19.3 ± 1.6
(F2)	98 ± 34	11.8 ± 1.7	102.6 ± 0.5	35.4 ± 1.0
(F3)	195 ± 35	11.4 ± 1.0	90.8 ± 0.6	17.1 ± 1.4
(P1)	24 ± 12	11.1 ± 2.1	99.0 ± 1.3	29.3 ± 0.6
(P2)	35 ± 20	12.6 ± 0.7	104.7 ± 1.8	49 ± 3
(P3)	54 ± 21	10.5 ± 0.9	94.3 ± 1.4	25 ± 3
(P4)	39 ± 39	14.4 ± 1.1	111.9 ± 0.7	27.1 ± 0.7
(R0)[b]	0	15.4 ± 0.5	165.7 ± 1.6	12.7 ± 1.3
(R1)	0	14.7 ± 0.7	151.2 ± 1.5	29.0 ± 1.5
(R2)	0	15.9 ± 1.2	141.2 ± 1.8	25.4 ± 1.9
(R3)	0	14.7 ± 0.4	153 ± 2	19.6 ± 1.8
(R4)	0	15.4 ± 0.5	159 ± 4	20.0 ± 0.8

[a] The phosphate buffer (0.2 mol L^{-1} KH_2PO_4 / K_2HPO_4) serving as supporting electrolyte for formate electrosynthesis was measured prior to electrolysis for comparison.

[b] The reference electrolyte (cf. section 1.5) serving as catholyte for H_2O_2 / PFA (electro)synthesis was measured prior to electrolysis for comparison.

[c] The Bi contents were below the limit of quantification (LOQ, approx. 250 µg L^{-1}) and close to the limit of detection (LOD, approx. 62.5 µg L^{-1}), which resulted in relative high standard deviations / relative errors.

1.12 Ion chromatography (IC)

IC measurements were carried out with two different IC units to determine the cation and anion concentrations in the electrolyte samples (cf. Table S9). Both units were operated with *Chromeleon* (Version 7).

Table S9: IC measurement conditions for K^+ and PO_4^{3-} analysis performed on two different IC units (Thermo Fisher Scientific, Waltham / USA).

Conditions	K^+	PO_4^{3-}
IC Unit	Dionex™ ICS-5000$^+$ DC, ICS-5000$^+$ SP, VWD, AS-AP autosampler	Dionex™ Aquion™ system, AS-DV autosampler
Pre column	Dionex™ IonPac™ CG17	Dionex™ IonPac™ AS22 IC column (4 x 50 mm)
Column	Dionex™ IonPac™ CS17 (Analytical 2 x 250 mm)	Dionex™ IonPac™ AS22 IC column (4 x 250 mm)
Suppressor	CERS 500 (2 mm)	ACRS 500 Suppressor (4 mm)
Eluent	6 mmol L^{-1} CH_3SO_3H (MSA)	4.5 mmol L^{-1} Na_2CO_3 / 1.4 mmol L^{-1} $NaHCO_3$
Flow rate	0.1 mL min^{-1}	1.2 mL min^{-1}
Method	gradient 1. −5 - 0 min, 1.5 mmol L^{-1} MSA 2. 0 - 25 min, 1.5 - 2.1 mmol L^{-1} MSA 3. 25 - 40 min, 6 mmol L^{-1} MSA 4. 40 - 60 min, 1.5 mmol L^{-1} MSA	isocratic
Injection volume	10 µL	250 µL
Sample dilution factor	500	250
Detector	Conductivity cell	Conductivity cell
Retention time	34.87 min	9.28 min
Duration	60 min	15 min

Samples were diluted by factor 250 in a volumetric flask (50 mL, ISO 1042) for PO_4^{3-} quantification. The samples were diluted further by factor 2 for K^+ quantification.

Standards to determine the concentrations of K^+ were prepared by a dilution series of a stock solution. The stock solution was prepared with KCl (1.221 g ≙ 640 ppm K^+) in a volumetric

flask (1 L, ISO 1042). The stock solution was first diluted by 10, followed by a dilution series with the dilution factor 2 (cf. Figure S5).

The PO_4^{3-} standards were prepared from an anion multi-element standard (Certipur, Anion multi-element standard I, 1000 ppm F^-, PO_4^{3-}, Br^-, Merck, Darmstadt / Germany, HC17168637) by a dilution series (cf. Figure S6).

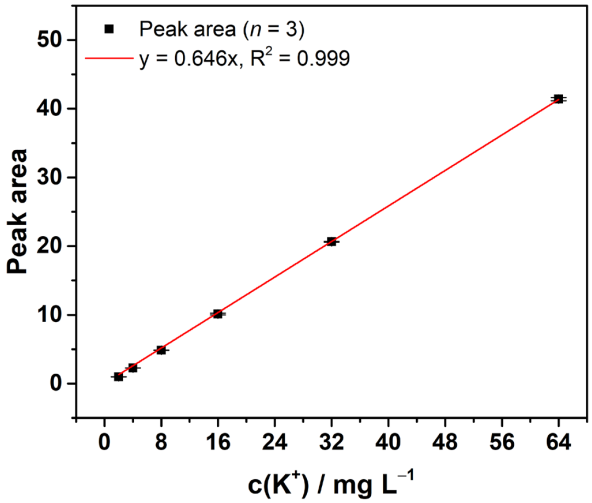

Figure S5: Calibration for K^+ quantification via IC measurement**.** Plot of K^+ concentration (2, 4, 8, 16, 32, 64 ppm) against the peak area of the measured signal (n = 3) with a linear fit forced through zero.

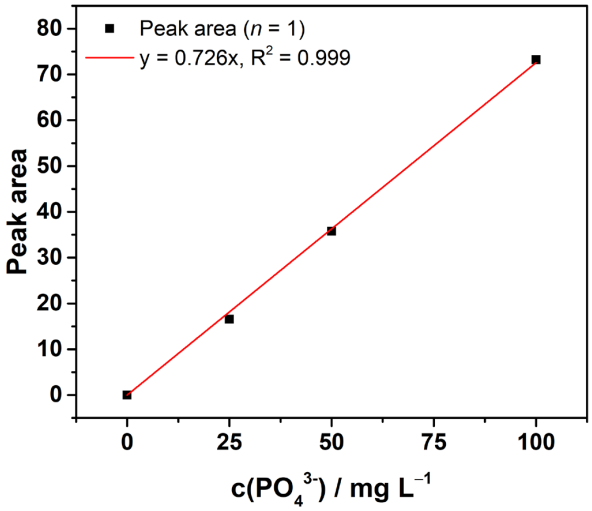

Figure S6: Calibration for PO_4^{3-} quantification via IC measurement**.** Plot of PO_4^{3-} concentration (0, 25, 50, 100 ppm) against the peak area of the measured signal (n = 1) with a linear fit forced through zero.

Table S10: Concentrations of K^+ and PO_4^{3-} determined by IC in catholyte and anolyte after electrolysis (6 or 22 h, 150 mA cm^{-2}) with different catholytes: 0.2 mol L^{-1} KH_2PO_4 / K_2HPO_4, (F) Combined catholytes containing formate, (R) Reference electrolyte (cf. section 1.5).

Electrolysis	c(K^+) / mmol L^{-1}		c(PO_4^{3-}) / mmol L^{-1}	
	Catholyte	Anolyte	Catholyte	Anolyte
(F0)[a]	286.2	286.2	197.5	197.5
(F1)	548.0	3.0	183.6	209.8
(F2)	540.4	2.7	183.5	210.3
(F3)	537.9	3.4	183.0	206.1
(P1)	383.4	13.2	133.5	0.8
(P2)	448.0	14.8	154.7	0.3
(P3)	433.9	11.6	150.8	0.4
(P4)	425.8	10.9	148.2	0.4
(R0)[b]	672.2	-	288.6	-
(R1)	533.2	12.9	238.0	0.4
(R2)	550.5	12.8	245.2	0.4
(R3)	532.5	12.2	236.1	0.4
(R4)	529.3	13.2	237.7	0.3

[a] The phosphate buffer (0.2 mol L^{-1} KH_2PO_4 / K_2HPO_4) serving as supporting electrolyte for formate electrosynthesis was measured prior to electrolysis for comparison.

[b] The reference electrolyte (R, cf. section 1.5) serving as catholyte for H_2O_2 / PFA (electro)synthesis was measured prior to electrolysis for comparison.

1.13 High-performance liquid chromatography (HPLC)

The quantification of formate was carried out via HPLC (cf. Table S11), the system was operated with the software *LabSolutions* (Version 5.93).

Table S11: HPLC measurement conditions for formate and PHB analysis performed on an HPLC unit (LC-20AD, SIL-20AC HT, CBM-20A, CTO-20AC, SPD-M20A - Shimadzu, Kyoto / Japan).

Conditions	Formate
Eluent	5 mmol L^{-1} H_2SO_4
Flow rate	0.6 mL min^{-1}
Pressure	30 ± 1
Column oven	35 °C
Column	Rezex ROA- Organic Acid (8%), 300 mm × 7.8 mm, Phenomenex, Torrance / USA
Injection volume	10 µL
Detector	Photodiode array (PDA)
Wavelength λ	194 nm
Retention time	14.9 min
Duration	25 min

Formate standards were prepared from a stock solution by a dilution series with the dilution factor 2. The stock solution was prepared with HCOONa (3.482 g, 51.2 mmol) in a volumetric flask (100 mL, ISO 1042).

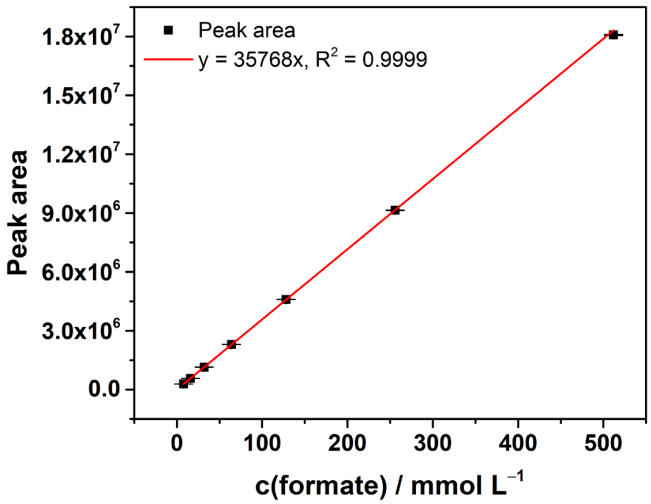

Figure S7: Calibration for formate quantification via HPLC measurement**.** Plot of formate concentration (8, 16, 32, 64, 128, 256, 512 mmol L^{-1}) against the peak area of the measured signal (n = 3) with a linear fit forced through zero.

2 Calculations

2.1 Faradaic efficiency (FE)

The FE for formate and H_2O_2 were calculated based on the determined amount of electrosynthesised components using equation (1).

$$FE = \frac{F \cdot z \cdot n}{I \cdot t} \cdot 100\% \quad (1)$$

With FE = Faradaic efficiency / %, F = Faraday constant / A s mol^{-1}, z = Number of transferred electrons (z = 2), n = Amount of synthesised formate or H_2O_2 / mol, I = Current / A, t = Electrolysis runtime / s.

The results for the different catholytes were averaged and their standard deviation was provided as uncertainty.

The indirect FE for PFA was determined under the assumption that formic acid reacted equimolar in a chemical reaction with the electrochemically generated H_2O_2 to PFA using equation (2).

$$H_2O_2 + HCOOH \rightleftharpoons HCOOOH + H_2O \quad (2)$$

The combined concentrations and FE of H_2O_2 and PFA were calculated by addition of the individual mean values. The errors were determined using their standard deviations and Gaussian error propagation using equation (3).

$$\sigma_{\text{combined}} = \sqrt{{\sigma_{\text{H}_2\text{O}_2}}^2 + {\sigma_{\text{PFA}}}^2} \quad (3)$$

3 Results

This chapter contains detailed data for formate electrosynthesis in section 3.1 and for H_2O_2 / PFA electro(synthesis) in section 3.2. Furthermore, GDE photographs are provided in section 3.3, which is followed by SEM images in section 3.4 and contact angle photographs in section 3.5 of the self-fabricated GDEs before and after electrolysis, respectively.

3.1 Electrosynthesis of formate

The operational electrolysis parameters have been summarised in Table S12, further electrolysis results have been collected in Table S13. Moreover, detailed courses of each individual electrolysis are provided.

Table S12: Overview of operational electrolysis parameters of the formate electrosynthesis using 0.2 mol L^{-1} KH_2PO_4 / K_2HPO_4 as electrolyte. All values are given as average with standard deviation for the 22 h electrolysis duration, excluding the absolute electric energy consumption (EEC).

Electrolysis	OCP vs. RHE / V[a]	$E(GDE)$ vs. RHE / V	U / V	EEC / Wh	$p(CO_2)$ / mbar
(F1)	0.67 ± 0.03	−1.25 ± 0.12	5.6 ± 0.4	92.2	292 ± 29
(F2)	0.273 ± 0.002	−1.20 ± 0.14	5.9 ± 0.4	96.9	263 ± 44
(F3)	0.268 ± 0.004	−1.19 ± 0.10	6.0 ± 0.5	98.9	272 ± 33

[a] Average with standard deviation measured for 5 min prior to electrolysis.

Table S13: Overview of volume, formate concentration, formate FE and pH determined *n* = 3 after 22 h electrolysis in the catholyte of formate electrosynthesis with 0.2 mol L^{-1} KH_2PO_4 / K_2HPO_4 as starting electrolyte.

Electrolysis	V / mL	c(formate) / mmol L^{-1}	FE(formate) / %	pH
(F1)	529.4 ± 0.6	501.6 ± 0.3	86.34 ± 0.06	4.12 ± 0.05
(F2)	531.5 ± 0.7	501.0 ± 0.4	86.50 ± 0.13	4.12 ± 0.05
(F3)	529.5 ± 0.7	499.8 ± 0.6	86.0 ± 0.3	4.10 ± 0.05

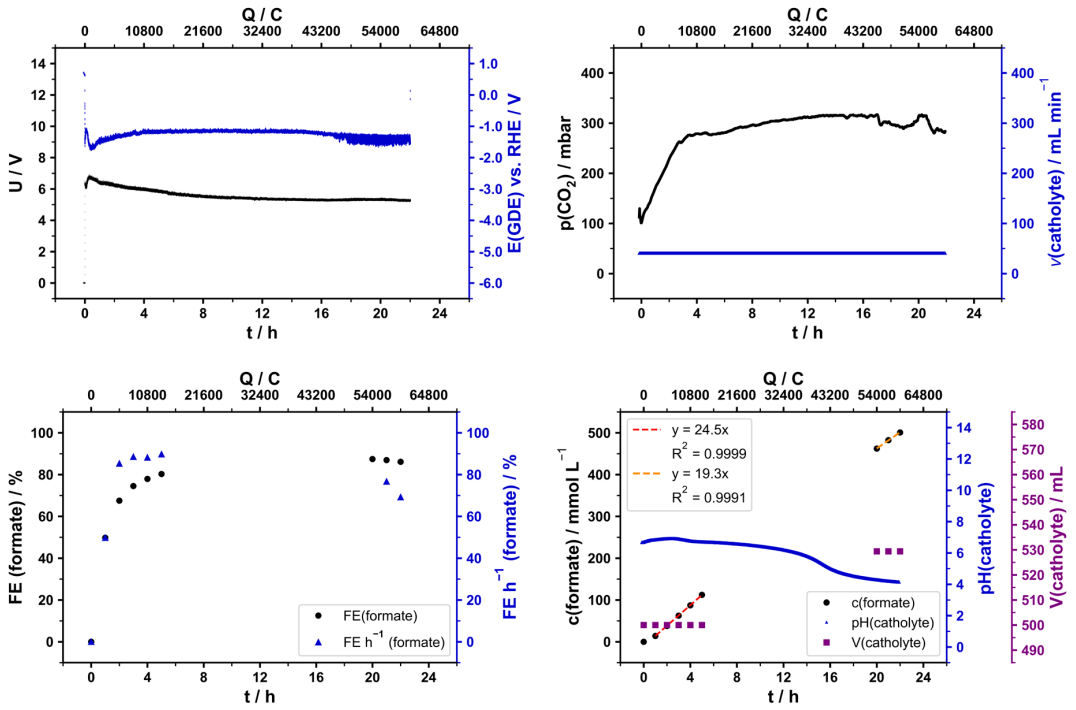

Figure S8: Data for Electrolysis (F1), experimental details are provided in section 1.4 and results in Table S12 and Table S13.

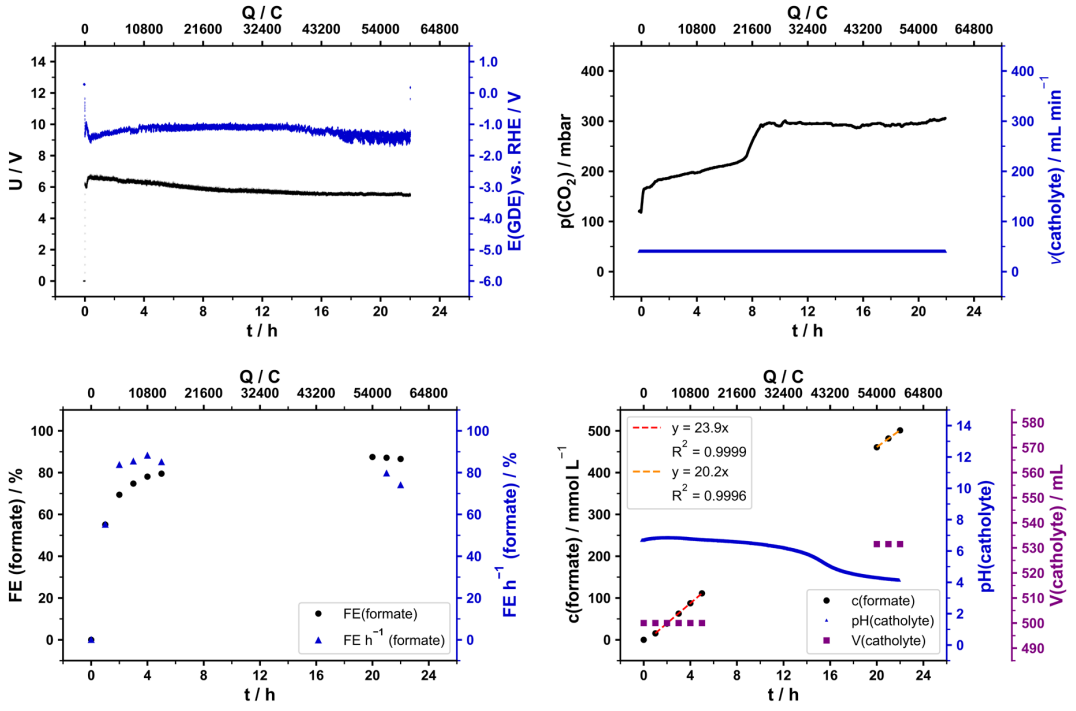

Figure S9: Data for Electrolysis (F2), experimental details are provided in section 1.4 and results in Table S12 and Table S13.

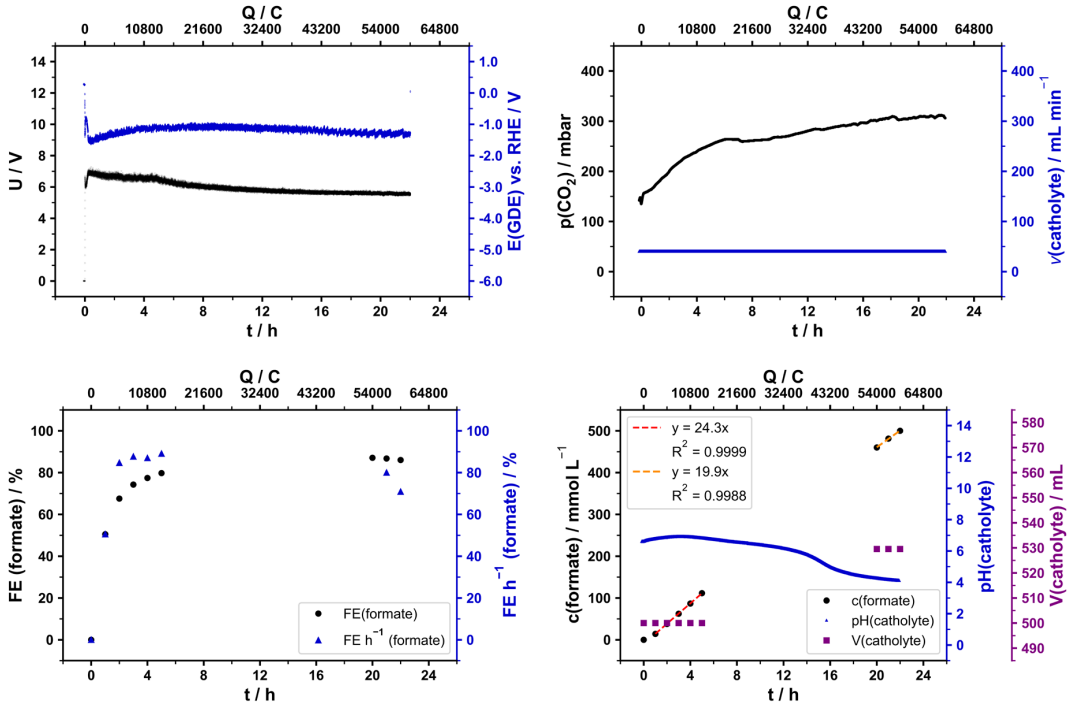

Figure S10: Data for Electrolysis (F3), experimental details are provided in section 1.4 and results in Table S12 and Table S13.

3.2 Electrosynthesis of H_2O_2

The operational electrolysis parameters have been summarised in Table S14, further electrolysis results have been collected in Table S15. Moreover, detailed courses of each individual electrolysis are provided.

Table S14: Overview of operational electrolysis parameters of the H_2O_2 / PFA (electro)synthesis using (F) or (R) as starting electrolyte (cf. section 1.5). All values are given as average with standard deviation for the 6 h electrolysis duration, excluding the absolute electric energy consumption (EEC).

Electrolysis	$E(GDE)$ vs. RHE / V	U / V	EEC / Wh	$p(O_2)$ / mbar
(P1)	−1.75 ± 0.36	4.7 ± 0.2	21.2	111 ± 22
(P2)	−0.68 ± 0.23	4.7 ± 0.2	21.2	121 ± 18
(P3)	−1.52 ± 0.32	4.8 ± 0.2	21.6	132 ± 38
(P4)	−1.59 ± 0.62	4.9 ± 0.2	22.1	146 ± 44
(R1)	−1.75 ± 0.30	4.7 ± 0.1	21.2	184 ± 33
(R2)	−1.44 ± 0.29	4.8 ± 0.1	21.6	193 ± 33
(R3)	−1.40 ± 0.33	4.4 ± 0.2	19.8	210 ± 56
(R4)	−1.40 ± 0.32	4.7 ± 0.1	21.2	174 ± 50

Table S15: Overview of volume, H_2O_2 / PFA concentrations, H_2O_2 / PFA FE and pH determined n = 3 after 6 h electrolysis in the catholyte of H_2O_2 / PFA (electro)synthesis with (F) or (R) as starting electrolyte (cf. section 1.5).

Electrolysis	V / mL	c(H_2O_2) / mol L^{-1}	FE(H_2O_2) / %	c(PFA) / mmol L^{-1}	FE(PFA) / %	pH
(P1)	52.3 ± 0.1	1.1855 ± 0.0051	73.8 ± 0.4	70.7 ± 2.7	4.4 ± 0.2	3.92 ± 0.05
(P2)	53.1 ± 0.2	1.3700 ± 0.0122	86.6 ± 0.8	78.7 ± 11.4	5.0 ± 0.8	3.93 ± 0.05
(P3)	54.1 ± 0.2	1.2600 ± 0.0034	81.2 ± 0.3	81.3 ± 4.7	5.2 ± 0.3	3.93 ± 0.05
(P4)	52.0 ± 0.2	1.2756 ± 0.0051	79.0 ± 0.4	96.4 ± 2.8	6.0 ± 0.2	3.92 ± 0.05
(R1)	54.0 ± 0.2	1.2389 ± 0.0084	79.6 ± 0.6	69.3 ± 4.7	4.5 ± 0.5	3.94 ± 0.05
(R2)	54.3 ± 0.3	1.0311 ± 0.0070	66.7 ± 0.5	64.4 ± 3.9	4.2 ± 0.3	3.96 ± 0.05
(R3)	54.8 ± 0.3	1.1722 ± 0.0051	76.5 ± 0.4	72.9 ± 0.8	4.8 ± 0.1	3.98 ± 0.05
(R4)	54.4 ± 0.2	1.0833 ± 0.0034	70.2 ± 0.3	67.6 ± 0.8	4.4 ± 0.1	4.00 ± 0.05

3.2.1 Catholyte (F) containing formate from formate electrosynthesis

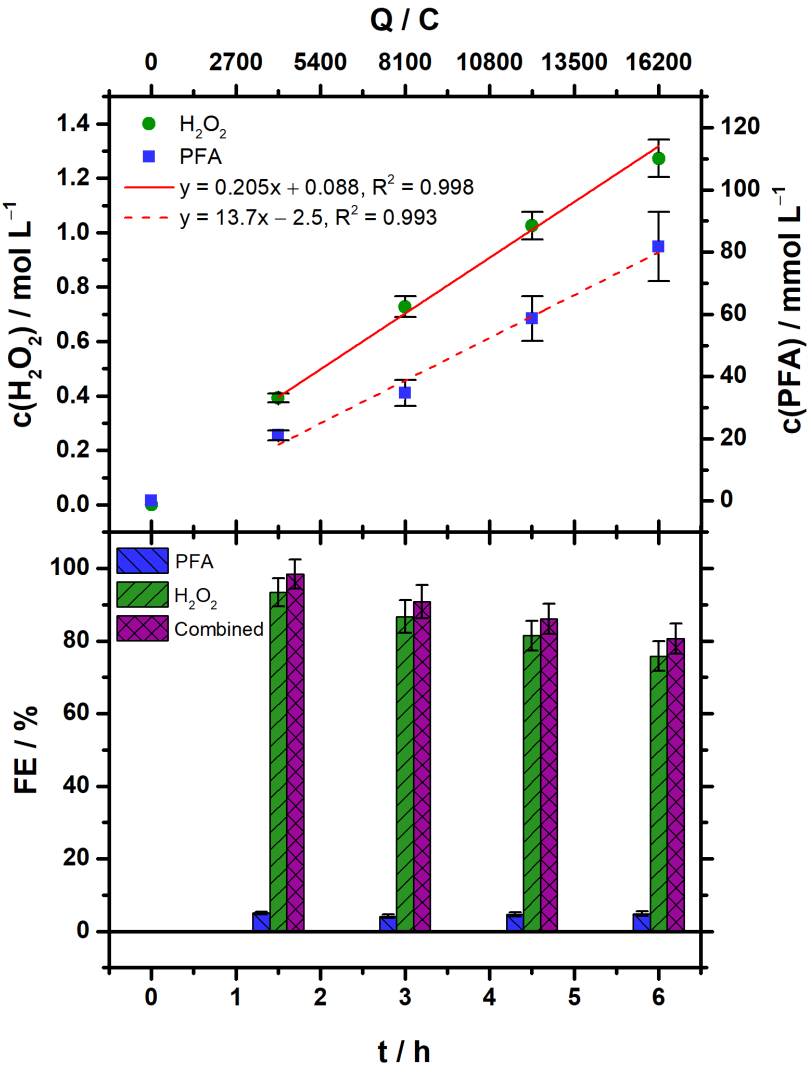

Figure S11: Concentration and Faradaic efficiency (FE) course of H_2O_2 and PFA for H_2O_2 / PFA (electro)synthesis (n = 4). Electrolysis parameters: Constant current density j = 150 mA cm^{-2}, Runtime = 6 h (≙ 16200 C), Catholyte = Formate containing catholyte originating from formate electrosynthesis (50 mL), Anolyte = 0.5 mol L^{-1} $HClO_4$ (50 mL), Cathode (GDE) = 65.5 wt% Acetylene Black, 34.5 wt% PTFE on stainless steel mesh, Reference electrode = Reversible hydrogen electrode (RHE), Anode = Mixed Ir-oxide on a Ti-grid (Platinode EP, Type 177, Umicore).

Table S16: Concentration and Faradaic efficiency (FE) of H_2O_2 and PFA in the catholyte for electrolysis (P1) with 0.2 mol L^{-1} KH_2PO_4 / K_2HPO_4 containing formate originating from formate electrosynthesis as starting electrolyte (cf. Figure S12).

t / h	c(H_2O_2) / mol L^{-1}	FE(H_2O_2) / %	c(PFA) / mmol L^{-1}	FE(PFA) / %
1.5	0.3729 ± 0.0008	88.8 ± 0.2	23.0 ± 0.5	5.5 ± 0.2
3	0.6758 ± 0.0029	80.5 ± 0.4	31.7 ± 0.5	3.8 ± 0.5
4.5	0.9544 ± 0.0020	75.8 ± 0.2	64.0 ± 1.1	5.1 ± 0.9
6	1.1855 ± 0.0051	70.6 ± 0.3	70.7 ± 2.7	4.2 ± 0.2

Table S17: pH for electrolysis (P1) with 0.2 mol L^{-1} KH_2PO_4 / K_2HPO_4 containing formate originating from formate electrosynthesis as starting electrolyte.

t / h	pH (catholyte)	pH (anolyte)
0	4.11 ± 0.05	0.39 ± 0.05
1.5	3.92 ± 0.05	0.38 ± 0.05
3	3.93 ± 0.05	0.38 ± 0.05
4.5	3.93 ± 0.05	0.33 ± 0.05
6	3.92 ± 0.05	0.34 ± 0.05

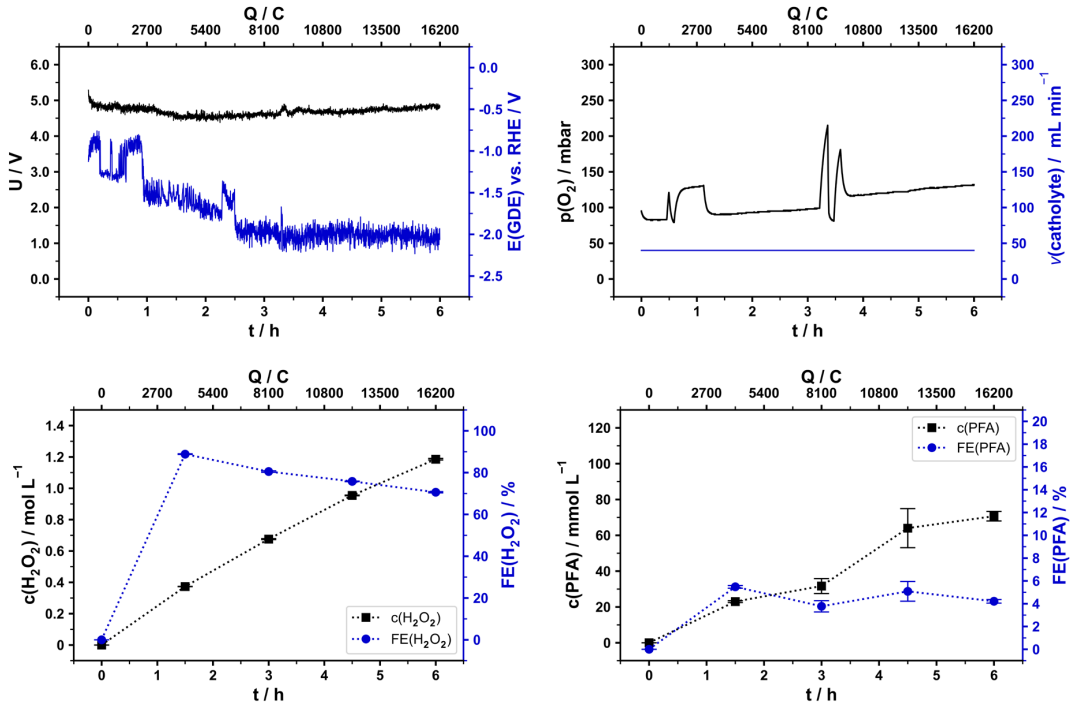

Figure S12: Data for electrolysis (P1), experimental details are provided in section 1.5 and results in Table S14 and Table S15.

Table S18: Concentration and Faradaic efficiency (FE) of H_2O_2 and PFA in the catholyte for electrolysis (P2) with 0.2 mol L^{-1} KH_2PO_4 / K_2HPO_4 containing formate originating from formate electrosynthesis as starting electrolyte (cf. Figure S13).

t / h	c(H_2O_2) / mol L^{-1}	FE(H_2O_2) / %	c(PFA) / mmol L^{-1}	FE(PFA) / %
1.5	0.4158 ± 0.0015	99.1 ± 0.4	19.8 ± 0.3	4.7 ± 0.1
3	0.7775 ± 0.0025	92.6 ± 0.3	34.7 ± 1.2	4.1 ± 0.2
4.5	1.0911 ± 0.0051	86.6 ± 0.5	56.9 ± 8.8	4.5 ± 0.7
6	1.3700 ± 0.0122	81.6 ± 0.8	78.7 ± 11.4	4.7 ± 0.7

Table S19: pH for electrolysis (P2) with 0.2 mol L^{-1} KH_2PO_4 / K_2HPO_4 containing formate originating from formate electrosynthesis as starting electrolyte.

t / h	pH (catholyte)	pH (anolyte)
0	4.10	0.38
1.5	3.93	0.29
3	3.93	0.30
4.5	3.92	0.27
6	3.93	0.23

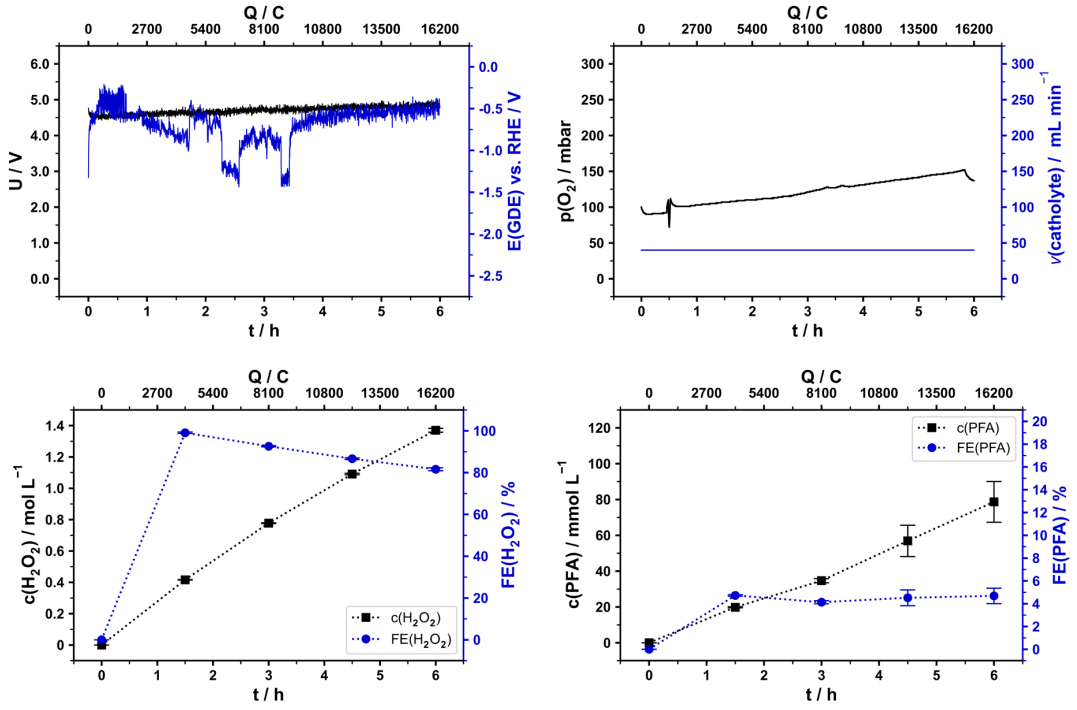

Figure S13: Data for electrolysis (P2), experimental details are provided in section 1.5 and results in Table S14 and Table S15.

Table S20: Concentration and Faradaic efficiency (FE) of H_2O_2 and PFA in the catholyte for electrolysis (P3) with 0.2 mol L^{-1} KH_2PO_4 / K_2HPO_4 containing formate originating from formate electrosynthesis as starting electrolyte (cf. Figure S14).

t / h	c(H_2O_2) / mol L^{-1}	FE(H_2O_2) / %	c(PFA) / mmol L^{-1}	FE(PFA) / %
1.5	0.3846 ± 0.0020	91.6 ± 0.5	19.8 ± 0.2	4.7 ± 0.3
3	0.7217 ± 0.0015	86.0 ± 0.2	32.0 ± 1.0	3.8 ± 0.2
4.5	1.0189 ± 0.0020	80.9 ± 0.2	55.6 ± 4.3	4.4 ± 0.4
6	1.2600 ± 0.0034	75.0 ± 0.2	81.3 ± 4.7	4.8 ± 0.3

Table S21: pH for electrolysis (P3) with 0.2 mol L^{-1} KH_2PO_4 / K_2HPO_4 containing formate originating from formate electrosynthesis as starting electrolyte.

t / h	pH (catholyte)	pH (anolyte)
0	4.00	0.33
1.5	3.96	0.33
3	3.95	0.32
4.5	3.94	0.28
6	3.93	0.24

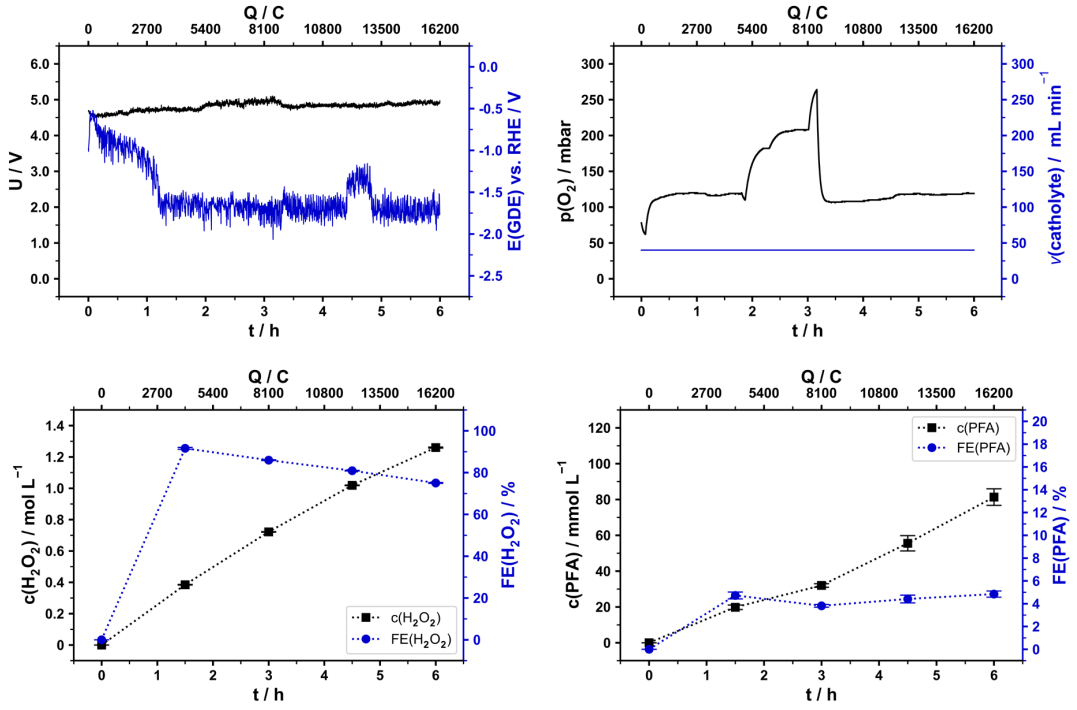

Figure S14: Data for electrolysis (P3), experimental details are provided in section 1.5 and results in Table S14 and Table S15.

Table S22: Concentration and Faradaic efficiency (FE) of H_2O_2 and PFA in the catholyte for electrolysis (P4) with 0.2 mol L^{-1} KH_2PO_4 / K_2HPO_4 containing formate originating from formate electrosynthesis as starting electrolyte (cf. Figure S15).

t / h	c(H_2O_2) / mol L^{-1}	FE(H_2O_2) / %	c(PFA) / mmol L^{-1}	FE(PFA) / %
1.5	0.3950 ± 0.0013	94.1 ± 0.3	21.7 ± 1.2	5.2 ± 0.3
3	0.7367 ± 0.0015	87.8 ± 0.2	40.3 ± 2.1	4.8 ± 0.3
4.5	1.0378 ± 0.0020	82.4 ± 0.2	58.2 ± 2.8	4.6 ± 0.3
6	1.2756 ± 0.0051	76.0 ± 0.4	96.4 ± 2.8	5.7 ± 0.2

Table S23: pH for electrolysis (P4) with 0.2 mol L^{-1} KH_2PO_4 / K_2HPO_4 containing formate originating from formate electrosynthesis as starting electrolyte.

t / h	pH (catholyte)	pH (anolyte)
0	3.99	0.34
1.5	3.95	0.34
3	3.94	0.34
4.5	3.94	0.30
6	3.92	0.27

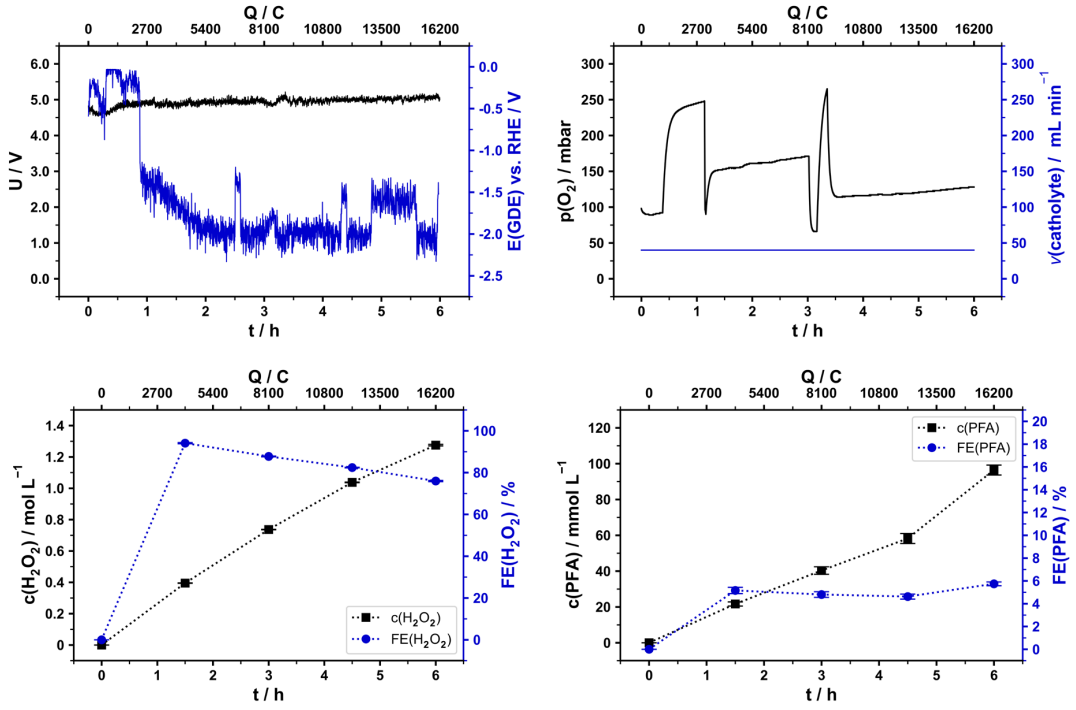

Figure S15: Data for electrolysis (P4), experimental details are provided in section 1.5 and results in Table S14 and Table S15.

3.2.2 Reference electrolyte (R) containing 0.5 mol L^{-1} HCOOK / HCOOH as catholyte

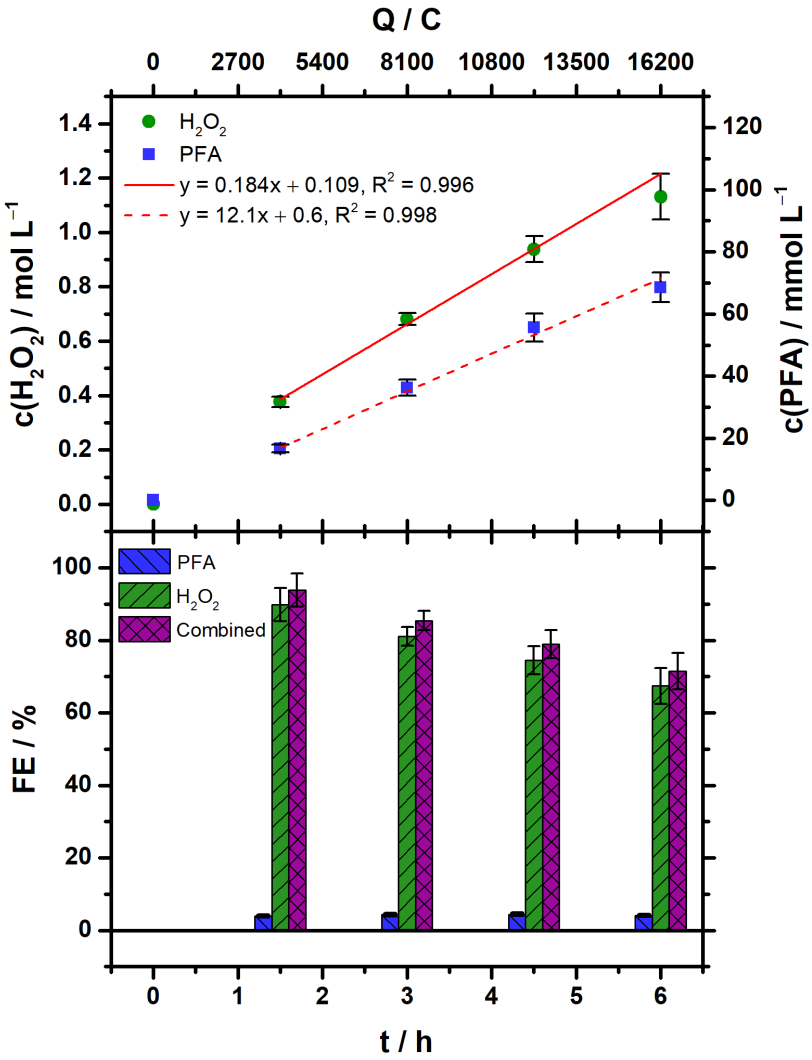

Figure S16: Concentration and Faradaic efficiency (FE) course of H_2O_2 and PFA for H_2O_2 / PFA (electro)synthesis (n = 4). Electrolysis parameters: Constant current density j = 150 mA cm^{-2}, Runtime = 6 h (≙ 16200 C), Catholyte = 0.2 mol L^{-1} KH_2PO_4 / K_2HPO_4 (equimolar) and 0.5 mol L^{-1} HCOOK / HCOOH (equimolar) in 1 wt% H_3PO_4 (50 mL, reference electrolyte (R), cf. section 1.5), Anolyte = 0.5 mol L^{-1} $HClO_4$ (50 mL), Cathode (GDE) = 65.5 wt% Acetylene Black, 34.5 wt% PTFE on stainless steel mesh, Reference electrode = Reversible hydrogen electrode (RHE), Anode = Mixed Ir-oxide on a Ti-grid (Platinode EP, Type 177, Umicore).

Table S24: Concentration and Faradaic efficiency (FE) of H_2O_2 and PFA in the catholyte for electrolysis (R1) with 0.2 mol L^{-1} KH_2PO_4 / K_2HPO_4 containing 0.5 mol L^{-1} HCOOK / HCOOH in 1 wt% H_3PO_4 as starting electrolyte (cf. Figure S17).

t / h	c(H_2O_2) / mol L^{-1}	FE(H_2O_2) / %	c(PFA) / mmol L^{-1}	FE(PFA) / %
1.5	0.4067 ± 0.0060	96.9 ± 1.5	17.0 ± 2.0	4.1 ± 0.5
3	0.7142 ± 0.0063	85.1 ± 0.8	35.3 ± 2.1	4.2 ± 0.3
4.5	1.0333 ± 0.0034	79.7 ± 0.3	51.1 ± 2.1	4.1 ± 0.2
6	1.2389 ± 0.0084	73.8 ± 0.5	69.3 ± 4.7	5.1 ± 0.3

Table S25: pH for electrolysis (R1) with 0.2 mol L^{-1} KH_2PO_4 / K_2HPO_4 containing 0.5 mol L^{-1} HCOOK / HCOOH in 1 wt% H_3PO_4 as starting electrolyte.

t / h	pH (catholyte)	pH (anolyte)
0	4.07	0.35
1.5	3.96	0.32
3	3.94	0.29
4.5	3.93	0.28
6	3.94	0.27

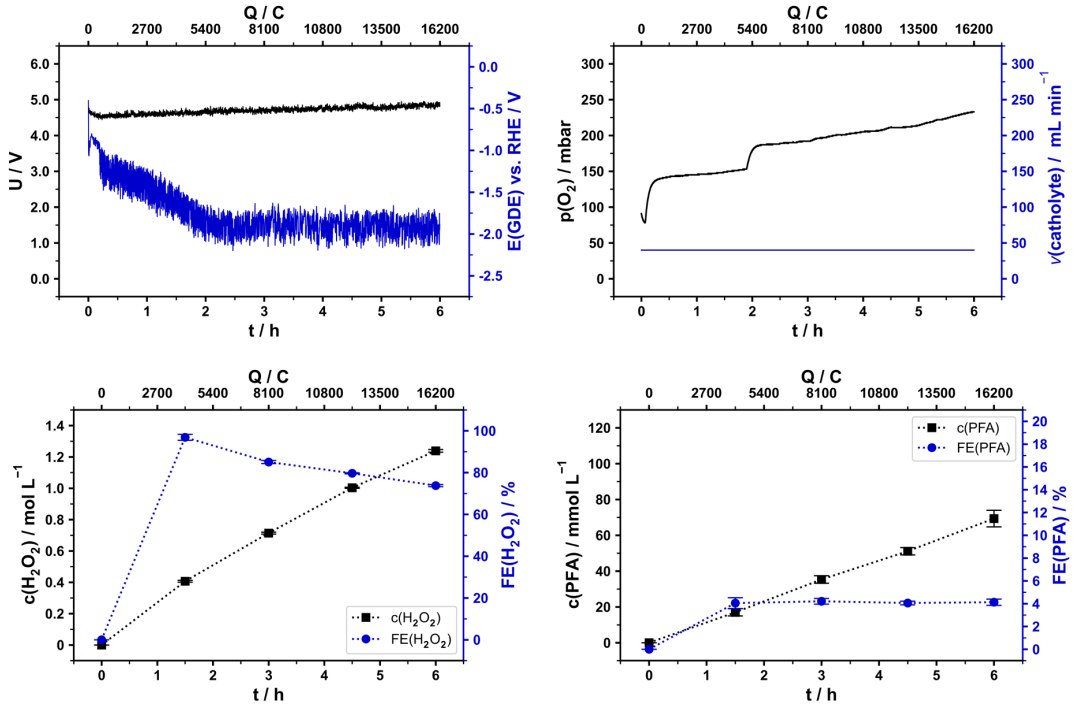

Figure S17: Data for electrolysis (R1), experimental details are provided in section 1.5 and results in Table S14 and Table S15.

Table S26: Concentration and Faradaic efficiency (FE) of H_2O_2 and PFA in the catholyte for electrolysis (R2) with 0.2 mol L^{-1} KH_2PO_4 / K_2HPO_4 containing 0.5 mol L^{-1} HCOOK / HCOOH in 1 wt% H_3PO_4 as starting electrolyte (cf. Figure S18).

t / h	c(H_2O_2) / mol L^{-1}	FE(H_2O_2) / %	c(PFA) / mmol L^{-1}	FE(PFA) / %
1.5	0.3763 ± 0.0013	89.6 ± 0.3	16.7 ± 1.1	4.0 ± 0.3
3	0.6733 ± 0.0015	80.2 ± 0.2	34.3 ± 2.1	4.1 ± 0.3
4.5	0.8867 ± 0.0034	70.4 ± 0.3	52.0 ± 2.4	4.1 ± 0.2
6	1.0311 ± 0.0070	61.4 ± 0.5	64.4 ± 3.9	3.8 ± 0.3

Table S27: pH for electrolysis (R2) with 0.2 mol L^{-1} KH_2PO_4 / K_2HPO_4 containing 0.5 mol L^{-1} HCOOK / HCOOH in 1 wt% H_3PO_4 as starting electrolyte.

t / h	pH (catholyte)	pH (anolyte)
0	4.05	0.33
1.5	4.01	0.30
3	3.97	0.29
4.5	3.96	0.28
6	3.96	0.27

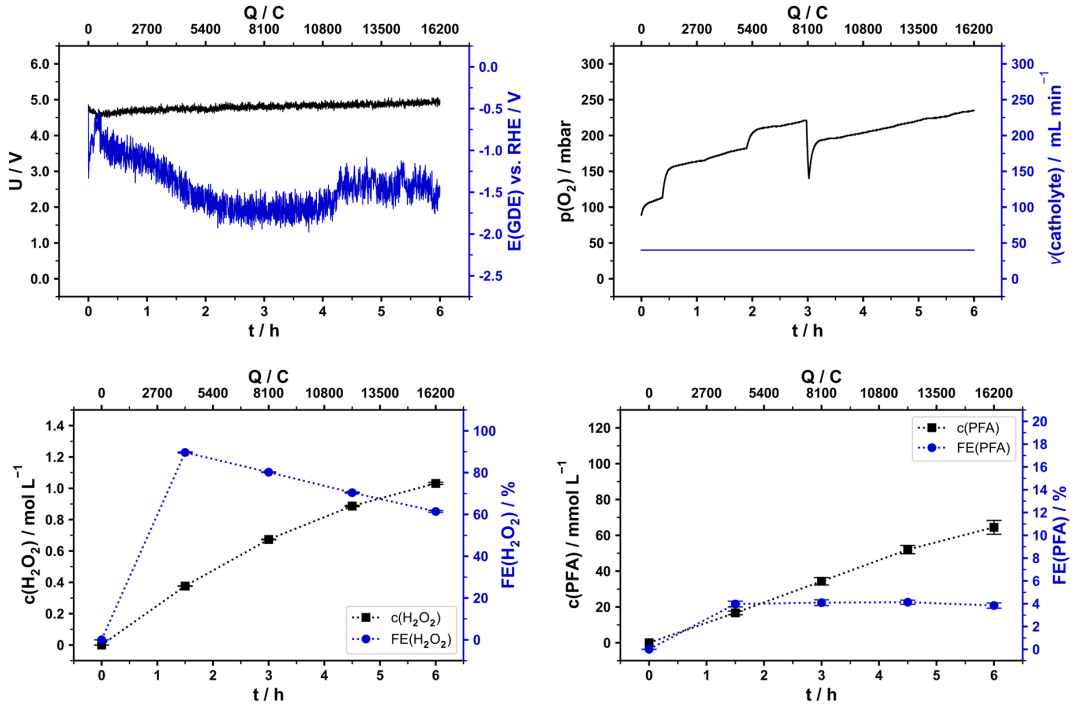

Figure S18: Data for electrolysis (R2), experimental details are provided in section 1.5 and results in Table S14 and Table S15.

Table S28: Concentration and Faradaic efficiency (FE) of H_2O_2 and PFA in the catholyte for electrolysis (R3) with 0.2 mol L^{-1} KH_2PO_4 / K_2HPO_4 containing 0.5 mol L^{-1} HCOOK / HCOOH in 1 wt% H_3PO_4 as starting electrolyte (cf. Figure S19).

t / h	c(H_2O_2) / mol L^{-1}	FE(H_2O_2) / %	c(PFA) / mmol L^{-1}	FE(PFA) / %
1.5	0.3654 ± 0.0008	87.1 ± 0.2	15.5 ± 0.5	3.7 ± 0.2
3	0.6767 ± 0.0011	80.6 ± 1.3	39.0 ± 3.0	4.6 ± 0.4
4.5	0.9578 ± 0.0039	76.1 ± 0.4	59.6 ± 1.6	4.7 ± 0.2
6	1.1722 ± 0.0051	69.8 ± 0.4	72.9 ± 0.8	4.3 ± 0.1

Table S29: pH for electrolysis (R3) with 0.2 mol L^{-1} KH_2PO_4 / K_2HPO_4 containing 0.5 mol L^{-1} HCOOK / HCOOH in 1 wt% H_3PO_4 as starting electrolyte.

t / h	pH (catholyte)	pH (anolyte)
0	4.08	0.34
1.5	4.03	0.33
3	3.99	0.30
4.5	3.99	0.29
6	3.98	0.27

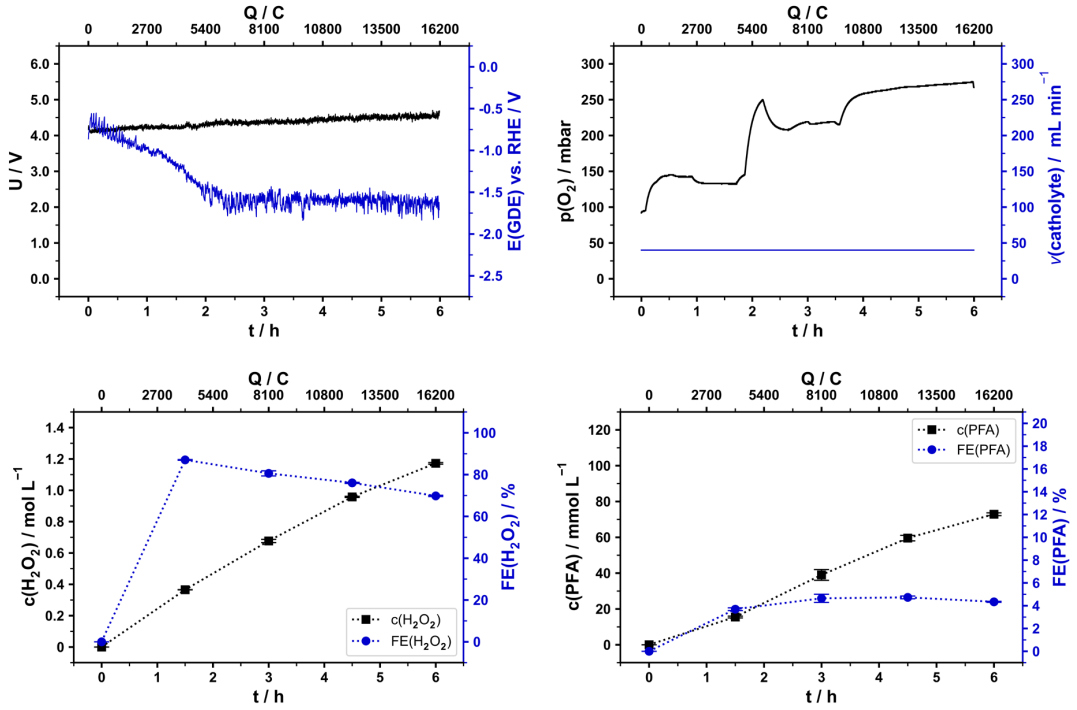

Figure S19: Data for electrolysis (R3), experimental details are provided in section 1.5 and results Table S14 and Table S15.

Table S30: Concentration and Faradaic efficiency (FE) of H_2O_2 and PFA in the catholyte for electrolysis (R4) with 0.2 mol L^{-1} KH_2PO_4 / K_2HPO_4 containing 0.5 mol L^{-1} HCOOK / HCOOH in 1 wt% H_3PO_4 as starting electrolyte (cf. Figure S18).

t / h	c(H_2O_2) / mol L^{-1}	FE(H_2O_2) / %	c(PFA) / mmol L^{-1}	FE(PFA) / %
1.5	0.3600 ± 0.0013	85.8 ± 0.3	17.7 ± 0.8	4.2 ± 0.2
3	0.6583 ± 0.0039	78.4 ± 0.5	36.3 ± 1.2	4.3 ± 0.2
4.5	0.9044 ± 0.0039	71.8 ± 0.4	59.6 ± 2.1	4.7 ± 0.2
6	1.0833 ± 0.0034	64.5 ± 0.2	67.6 ± 0.8	4.0 ± 0.1

Table S31: pH for electrolysis (R4) with 0.2 mol L^{-1} KH_2PO_4 / K_2HPO_4 containing 0.5 mol L^{-1} HCOOK / HCOOH in 1 wt% H_3PO_4 as starting electrolyte.

t / h	pH (catholyte)	pH (anolyte)
0	4.07	0.35
1.5	4.02	0.33
3	3.98	0.31
4.5	3.99	0.31
6	4.00	0.27

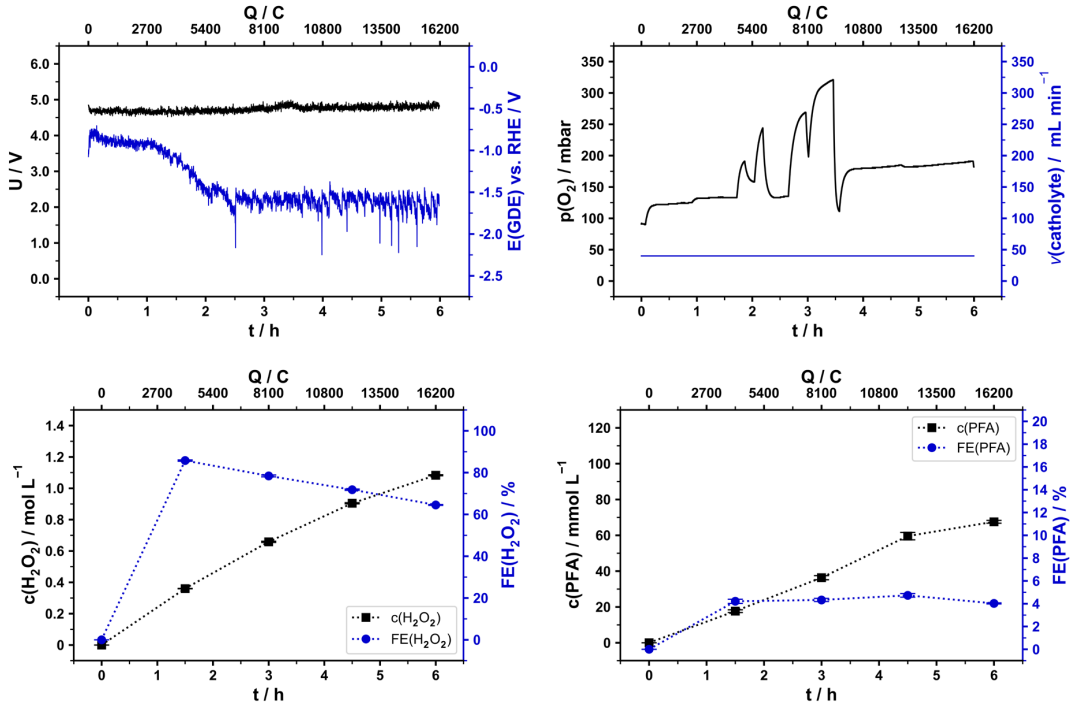

Figure S20: Data for electrolysis (R4), experimental details are provided in section 1.5 and results in Table S14 and Table S15.

3.3 Pictures of GDE before and after electrolysis

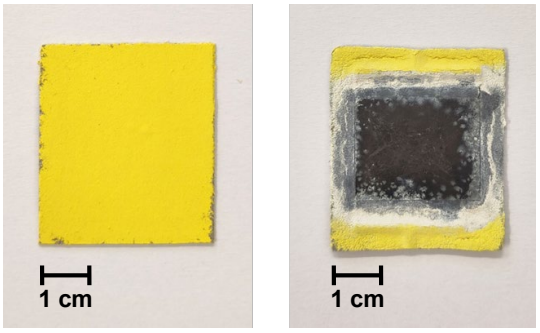

Figure S21: Exemplary pictures of a self-fabricated Bi_2O_3 based GDE before (left) and after (right) electrolysis. Details of the fabrication process are provided in section 1.2.1, details on the electrolysis conditions in section 1.4.

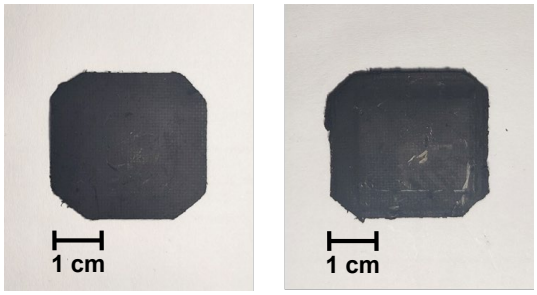

Figure S22: Exemplary pictures of a self-fabricated Carbon based GDE before (left) and after (right) electrolysis. Details of the fabrication process are provided in section 1.2.2, details on the electrolysis conditions in section 1.5.

3.4 SEM images of GDE before and after electrolysis

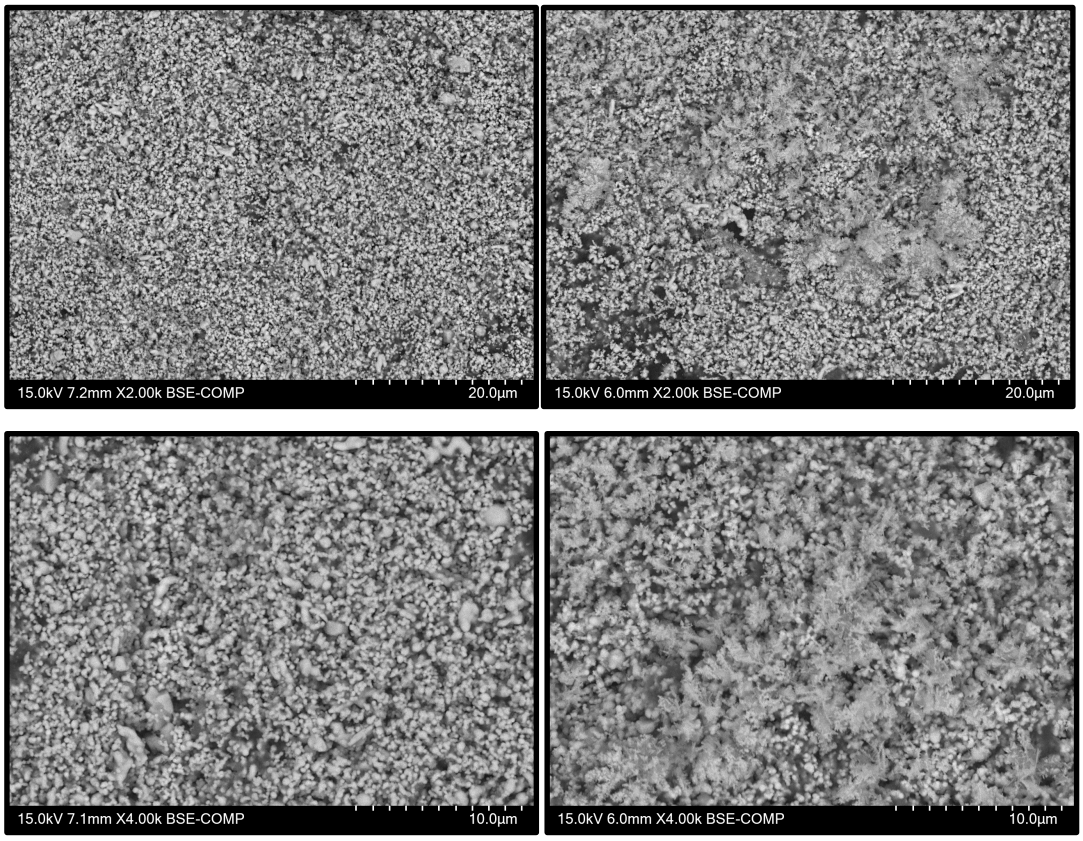

Figure S23: Exemplary SEM images (BSE, bright particles are Bi, section 1.8) of the GDE for formate electrosynthesis before (left) and after (right) electrolysis.

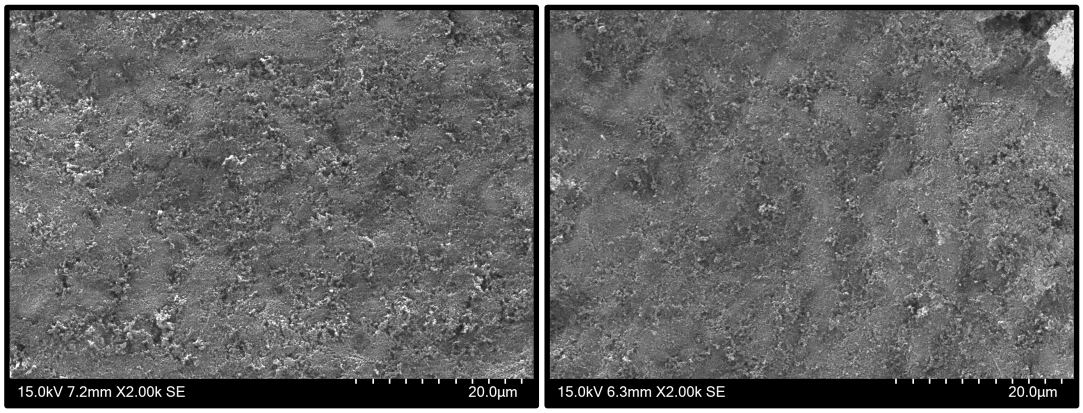

Figure S24: Exemplary SEM image (SE, cf. section 1.8) of the GDE for H_2O_2 / PFA (electro)synthesis before (left) and after (right) electrolysis.

3.5 Contact angle of GDE before and after electrolysis

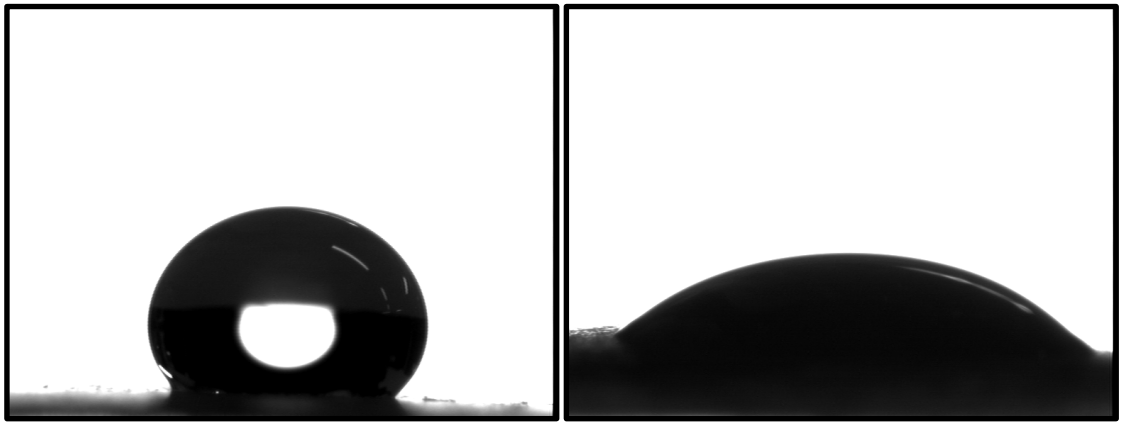

Figure S25: Exemplary images for contact angle θ determination (cf. section 1.9) of the Bi_2O_3 based GDE for formate electrosynthesis before (left) and after (right) electrolysis (cf. Table S32).

Table S32: Exemplary contact angles θ of a Bi_2O_3 based GDE before and after application for formate electrosynthesis**.**

	θ (left) / °	θ (right) / °	θ (average) / °
Before electrolysis	136.34	136.02	136.2 ± 0.3
After electrolysis	46.26	48.71	47.5 ± 1.8

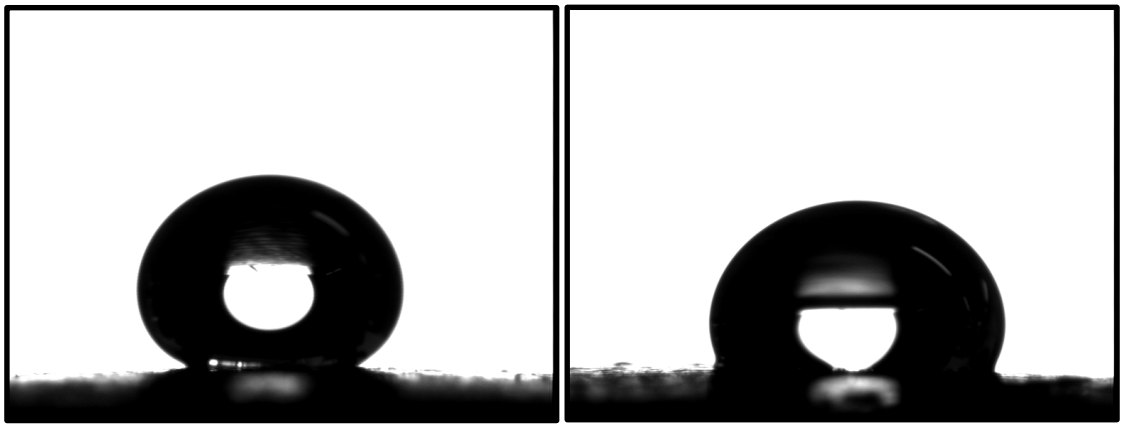

Figure S26: Exemplary images for contact angle θ determination (cf. section 1.9) of the carbon based GDE for H_2O_2 / PFA (electro)synthesis before (left) and after (right) electrolysis (cf. Table S33).

Table S33: Exemplary contact angles θ of a carbon based GDE before and after application for H_2O_2 / PFA (electro)synthesis**.**

	θ (left) / °	θ (right) / °	θ (average) / °
Before electrolysis	142.77	142.66	142.72 ± 0.08
After electrolysis	116.24	116.52	116.4 ± 0.2

3.6 X-ray diffraction of GDE before and after electrolysis

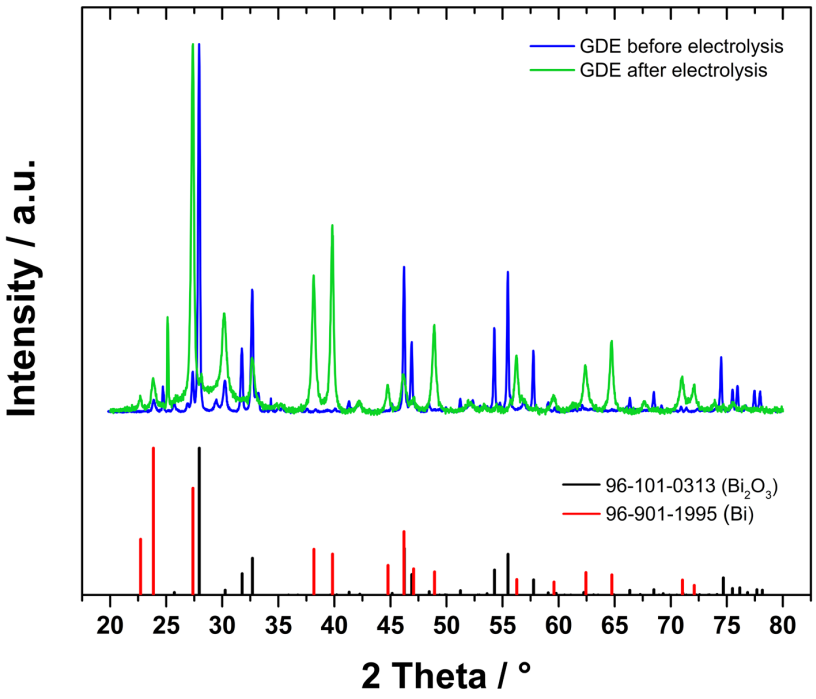

Figure S27: XRD data of the Bi_2O_3 based GDE for formate electrosynthesis before and after electrolysis as well as peak positions of Bi_2O_3 (96-101-0313) and Bi (96-901-1995) from the PDF-2 database (International Centre of Diffraction Data - ICDD) for comparison.

Curriculum Vitae

Not included in the electronic version for data protection reasons.